Phase Transformations in Ti-Mo Alloys

by

SABEENA.M
Enrollment No: PHYS02 2010 04004
Indira Gandhi Centre for Atomic Research, Kalpakkam,
Tamil Nadu, India.

A thesis submitted to the
Board of Studies in Physical Sciences

In partial fulfillment of requirements
for the Degree of

DOCTOR OF PHILOSOPHY
of
HOMI BHABHA NATIONAL INSTITUTE
Mumbai, India

May, 2016

Homi Bhabha National Institute[1]

Recommendations of the Viva Voce Committee

As members of the Viva Voce Committee, we certify that we have read the dissertation prepared by **Sabeena. M** entitled **"Phase Transformations in Ti-Mo Alloys"** and recommend that it may be accepted as fulfilling the thesis requirement for the award of Degree of Doctor of Philosophy.

Chairman –	Dr. G. Amarendra	G. Amarendra	**Date:** Aug 24, 2016
Guide / Convener -	Dr. M. Vijayalakshmi	~~Dr.~~ M. Vijayalakshmi	**Date:** 24/8/16
Examiner -	Dr A. K. Singh		**Date:** 24/08/2016
Member 1-	Dr. Saroja Saibaba	S. Sai	**Date:** 24/08/2016
Member 2-	Dr. Ashok Arya	N.V. Cha[illegible] (Dean)	**Date:** 24/08/2016
Member 3-	Dr. A.K Bhaduri	AK Bhaduri	**Date:** 24/8/2016
Member 4-	Dr. A. Bharathi	A. Bharathi	**Date:** 24/08/2016
Technology advisor	Mr. E. Mohandas		**Date:** 24/8/2016

Final approval and acceptance of this thesis is contingent upon the candidate's submission of the final copies of the thesis to HBNI.

I/We hereby certify that I/we have read this thesis prepared under my/our direction and recommend that it may be accepted as fulfilling the thesis requirement.

Date: 24.8.16

Place: IGCAR, Kalpakkam

M. Vijayalakshmi

<signature>

Guide

---

[1] This page is to be included only for final submission after successful completion of viva voce.

STATEMENT BY AUTHOR

This dissertation has been submitted in partial fulfillment of requirements for an advanced degree at Homi Bhabha National Institute (HBNI) and is deposited in the Library to be made available to borrowers under rules of the HBNI.

Brief quotations from this dissertation are allowable without special permission, provided that accurate acknowledgement of source is made. Requests for permission for extended quotation from or reproduction of this manuscript in whole or in part may be granted by the Competent Authority of HBNI when in his or her judgment the proposed use of the material is in the interests of scholarship. In all other instances, however, permission must be obtained from the author.

Sabeena

Sabeena.M

Kalpakkam,
May, 2016.

DECLARATION

I, hereby declare that the investigation presented in the thesis has been carried out by me. The work is original and has not been submitted earlier as a whole or in part for a degree/diploma at this or any other Institution / University.

Sabeena

Sabeena.M

Kalpakkam,
May, 2016.

LIST OF PUBLICATIONS ARISING FROM THE THESIS

I. Published

1. “Microstructural characterization of transformation products of bcc β in Ti- 15Mo alloy”, M. Sabeena, Alphy George, S. Murugesan, R. Divakar, E. Mohandas and M. Vijayalakshmi- *Journal of alloys and compounds*, **2016**, *658*,301-315.
2. “Thermodynamic basis of non equilibrium phase transformations of bcc- β phase in Ti-Mo system”, M. Sabeena, R. Mythili, Joysurya Basu, and M. Vijayalakshmi, *Transactions of the Indian Institute of Metals,* **2013**, 66, 401-407.
3. “Studies on ω phase formation in Ti-Mo alloys using Synchrotron XRD”, M. Sabeena, S. Murugesan, R. Mythili, A.K Sinha, M. N Singh, M. Vijayalakshmi, and S. K Deb. *Transactions of the Indian Institute of Metals*, **2015**, *68(1)*, 1-6.

II. Manuscript under revision

1. Crystal Structure and Bonding Characteristics of Transformation Products of BCC β in Ti-Mo Alloys”, M. Sabeena, S. Murugesan, P. Anees, E. Mohandas and M. Vijayalakshmi- *Journal of alloys and compounds.*

III. Manuscript under preparation

1. “Competing Phase Transformation Mechanisms and Products in Ti-Mo Alloys”, M. Sabeena, R. Mythili, Pradyumna Kumar Parida, S. Murugesan, E. Mohandas and M. Vijayalakshmi. (to be communicated)

IV. Conference proceedings

1. “Influence of Mo in phase stability of Ti-Mo System: Synchrotron based XRD studies”, Sabeena M, Murugesan S, Mythili R, Sinha A K, Singh M N, Vijayalakshmi M, Deb S K, *AIP Conference Proceedings*, **2014**, *1591*, 119-121.

V. Conference presentations

1. "Thermodynamic Basis of Non-equilibrium Phase Transformations of bcc β-phase in Ti-Mo System", *Presented in ISRS 2012 held at IIT, Madras on Dec 13-15, 2012.*
2. "Influence of Mo in phase stability of Ti-Mo system: Synchrotron based XRD studies", Presented in *DAE- SSPS* 2013 held at Thapar University, Patiala, Punjab on Dec 17-21, 2013.
3. Neutron Activation Analysis of Ti-xMo alloys", J.S. Brahmaji Rao, M. Sabeena, G. V. S. Ashok Kumar, R. Kumar, M. Vijayalakshmi and C.R. Venkata Subramani, CTAC 2015, May 26-29, at BARC.
4. High Resolution Phase Contrast Microscopy of athermal ω in Ti-15 wt%Mo Alloy", Alphy George, M. Sabeena, R. Divakar, E. Mohandas and M. Vijayalakshmi, EMSI 2015.

Sabeena

Sabeena. M.

DEDICATED

TO

MY FAMILY

ACKNOWLEDGEMENTS

This thesis is the result of selfless support of many people to my obsession towards scientific research. I take advantage of this opportunity to acknowledge and thank all those who contributed to this thesis and supported me along my graduation.

First of all, I would like to express my sincere gratitude to my research supervisor, Dr. M Vijayalakshmi, for giving me the opportunity to work with her in the Physical Metallurgy Group. Without her guidance, supervision and constant academic and personal support, this thesis would not have been successful. I am very grateful for her efforts to improve my scientific knowledge, academic skills and personal qualities. She has been a good guide, teacher and above all an accommodating personality that I could always count on.

I am very thankful to Dr. R. Mythili for her collaboration and continuous support throughout my graduation. I always enjoyed a friendly personal relationship with her and I extremely benefited from her support in the scientific and personal life.

My sincere thanks to Dr. S. Murugesan for his collaboration in XRD studies. His expertise and dedication towards our projects has been vital in our investigations.

I would like to thank Dr. S. A. V. Satya Murty, director of IGCAR and the former director, Dr. P. R. Vasudeva Rao for the excellent research facilities I enjoyed at IGCAR. I thank Dr. N. V. Chandra Shekar, Dean of Physical Science and the former Dean, Dr. B.V.R Tata for the pleasant academic and research atmosphere.

Scientific discussions with E. Mohandas at PMG have been invaluable in establishing my basic knowledge and improving the concepts in X-ray diffraction techniques. I thank him for all the helps and for the precious time he dedicated to me.

I thank the Doctoral committee members, Dr. G. Amarendra, Dr. A. Bharathi, Dr. Saroja Saibaba, Dr. Ashok Arya, and Dr. A. K. Bhaduri for their guidance and supervision.

I thank my close collaborators Prof. M. C. Valsa Kumar at IIT Palakkad and my friend Anees P. at MSG for the collaboration in the DFT calculations. I also thank Dr. S. V. M. Satyanarayana and Mr. Asweel at Pondicherry University and Prof. K. P. N. Murthy at University of Hyderabad for theoretical support.

I acknowledge DAE/IGCAR for financial support. I thank Kalaimagal and Shanmugham for helping me through administrative jobs. I thank Dr. M. Sai Baba, for facilitating a pleasant boarding in the township.

I thank all the PMG members for the pleasant academic and friendly atmosphere I enjoyed in the group. Many thanks to Dr. R Divakar, Dr. Karthikeyan and Dr. Thomas Paul for academic discussions. Special thanks to my friend Alphy George for the collaboration in HRTEM studies and her boundless support during the difficult days in my personal life. I thank Pradyumna Kumar Parida for his active involvement in EBSD studies. I thank my friends, Shabana khan, Thangam, Chanjal Gosh, Raghavendra, Dr. Ravi Kirana, Pragna, Prashanti, Manmadh Kumar Dash for their friendship and academic discussions.

My research and life at IGCAR was possible due to the endless support from my family. First of all I thank my parents for their unconditional support and help in developing a career of my choice. I cannot leave without a special mention to my mother whose vision and encouragement made me a self-reliant person. I thank Ameen Poyli, my husband, for his companionship and support. Kisses to our daughter Amelia for the cheerful lovely moments, especially along the stressful final months of my PhD. I am obliged to my parents-in-law for the helps and support they extended to me. I extend my gratitude to all my family members for their love and personal support.

I owe a lot to my good friends in the township for the pleasant life at Kalpakkam. I thank Nishad, Abhilash, Srikant, Aiswarya, Meera, Priyada, Rajani and Rashmi among many, who are numerous to mention in this limited space.

Sabeena M.
May 2016, Kalpakkam.

Contents

INTRODUCTION

EXPERIMENTAL AND MODELING DETAILS

INFLUENCE OF Mo ON TRANSFORMATION PRODUCTS OF HIGH TEMPERATURE PARENT BCC β PHASE IN Ti-Mo ALLOYS

VARIANT SELECTION MECHANISM DURING TRANSFORMATIONS OF β PHASE IN Ti-Mo ALLOYS

CHARACTERISTICS OF $\beta \rightarrow \omega$ TRANSFORMATION IN Ti-15Mo ALLOY

SUMMARY

SYNOPSIS

The thesis on “Phase Transformations in Ti-Mo Alloys”, which is Part II of the PhD programme of Sabeena.M deals with study of non-equilibrium transformation mechanisms and products in four alloys of Ti-Mo system, under different thermal treatments. The study has employed mainly Rietveld refinement methodology of X-ray diffraction results, in addition to microscopy techniques like optical, scanning electron and transmission electron microscopy, including recently emerging orientation imaging microscopy in SEM and TEM.

The thesis is organized into eight chapters as given below, of which five (chapter 3 to 7) describe the main results of the study:

1	Introduction
2	Experimental and modeling details
3	Influence of Mo on transformation products of high temperature parent bcc β phase in Ti-Mo alloys
4	Crystal structure and bonding characteristics of transformation products of bcc β in Ti-Mo alloys
5	Competing phase transformation mechanisms and products in Ti-Mo alloys
6	Variant selection mechanism during transformations of β in Ti-Mo alloys
7	Microstructural characterization of athermal and isothermal ω in Ti-15Mo alloy
8	Summary and scope for future work

The introduction presents the diverse application sectors for which titanium alloys have been developed in the last six to seven decades. It is shown that the ease with which the titanium alloys are found suitable in various application sectors is due to many of the beneficial characteristics of titanium alloys like specific weight, corrosion properties and mechanical properties [1-3]. The maneuverability of titanium alloys is shown to be due to the various types of phase transformation mechanisms, different combination of metastable products and their morphology. Accordingly, the titanium alloys are classified into α, $\alpha + \beta$ and β alloys, which is discussed based on the alloying additions. The literature on phase transformations in titanium alloys in general and Ti-Mo in particular are described, followed by the scope of the present thesis.

The second chapter is followed by the details of experimental and modeling methodologies used in the study. The procedure of preparation of alloys, determination of the chemical composition, the details of the thermal treatments and sample preparation methods for various techniques are described in the first part. The main part of the chapter, deals with each of the experimental techniques like Instrumental Neutron Activation Analysis (INAA) for chemical analysis, X-ray diffraction and microscopy techniques. The major experimental method employed in the thesis is X-ray diffraction using conventional XRD and synchrotron XRD systems. The data analysis pertains to detailed Rietveld refinement to obtain crystal structure parameters, electron charge density distribution and 3D strain distribution. The microscopy techniques included Visible light microscopy, Scanning Electron Microscopy (SEM)/EDX, Transmission Electron Microscopy (TEM) and High Resolution TEM (HRTEM). The orientation imaging microscopy analysis using Precession Electron Diffraction (PED)/TEM and EBSD/SEM is described. In addition to that, the hardness has been studied with Vickers hardness tester the details of which are stated. For each of the experimental technique, the following aspects are discussed: the principle, the information obtained, the operation parameters, calibration procedures, method of analysis, accuracy, sources of error, estimation and minimization of error. The details of the computational/simulation method i.e., the Miedema model, DFT first principle calculation and JMAT Pro calculations are given. The basic principle, the inputs used, the boundary conditions and the errors are presented of each method.

The **Chapter 3** on "*Influence of Mo on transformation products of high temperature parent bcc β phase in Ti-Mo alloys*", reports the influence of Mo on the transformation products of ice water quenched parent bcc β into hcp α′, base centered orthorhombic α″, and hexagonal omega (ω) and retention of higher temperature bcc β for four different alloys of Ti-Mo[4-6]. Synchrotron XRD was found to be extremely useful in identifying low amounts of secondary phase of ω (see figure 1). In addition to that, to understand the thermodynamic rationale behind this transformation, Miedema calculation was carried out for entire range of Mo concentration. An attempt has been made to provide a thermodynamic basis to understand the influence of Mo on the stability of phases.

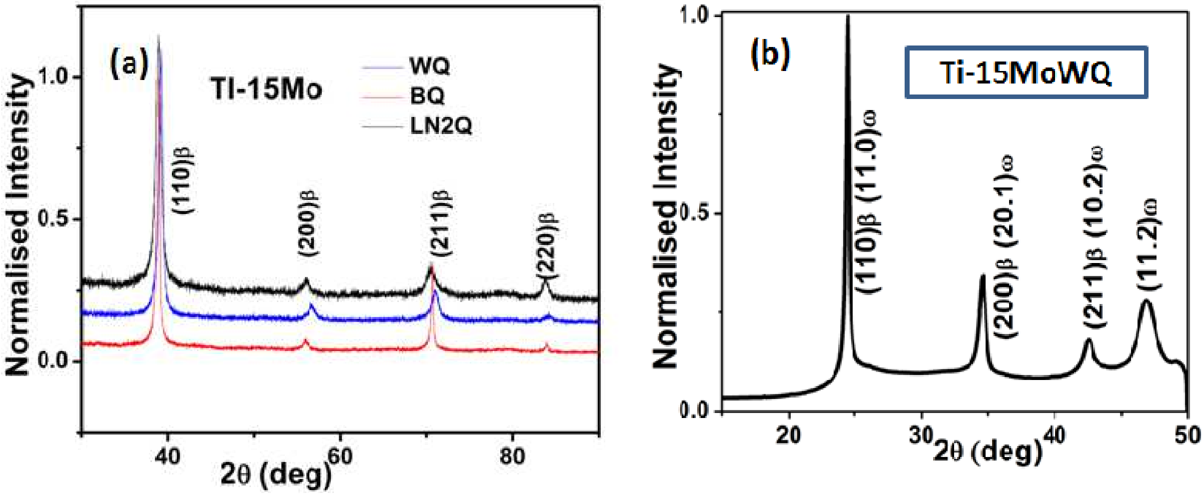

Figure 1 The absence of unique ω peak in (a) conventional XRD and its presence in (b) Synchrotron XRD.

Chapter 4 on *"Crystal structure and bonding characteristics of transformation products of bcc β in Ti-Mo alloys"*, highlights the crystal structure details of all the product phases, in addition to bonding characteristics. Rietveld refinement of X-ray diffraction patterns of α', α″ and β phases of four alloys of Ti-Mo has been carried out to arrive at their crystal structure parameters and bonding nature. The addition of molybdenum to titanium is found to shift the stability of crystal structure from hcp to orthorhombic to bcc. The unit cell dimensions and the atomic positions of α', α″ and β phases were evaluated, with reliability indices lower than those reported so far in titanium alloys. The reduction in unit cell dimensions and its volume, bond length and co-ordination number with addition of molybdenum is consistent with the reduced size of solute (Mo) atom. The orthorhombic α″ phase, a transition phase with a minor distortion of hcp α', is found to be closer to α' than β phase, based on the orthorhombicity (b/a), c/a the volume of equivalent orthorhombic unit cells of the phases and the atomic shuffle 'y' in 4c Wyckoff positions along 'b' axis of α″ phase. The Fourier electron density contour maps suggest that the bonding in all phases is predominantly metallic. The charge density plot obtained using first principle DFT calculation is also in agreement with the above findings. However, addition of molybdenum delocalizes the spatial distribution of charge density, suggesting an enhancement of metallic character. Anisotropy in charge density was observed along <100> and <110> type directions in {100} family of planes in orthorhombic α″ phase of Ti-7Mo alloy. This offers the direct evidence for the origin of anisotropy in the values of elastic constants, reported in literature.

Chapter 5 on *"Competing phase transformation mechanisms and products in Ti-Mo alloys"*, focuses on the influence of cooling rate on the mechanism of phase transformation and the final products during decomposition of β in Ti-1Mo and Ti-7Mo alloys. The transformation mechanism and products of β phase for both the Ti-Mo alloys are summarized in micro structural map. The experimental evidences are in agreement with the predictions based on JMatPro calculations of the amount of phase formation at various temperatures, for the two alloys. The difference in transformation mechanism is understood in terms of thermodynamic and kinetic factors, in relation to the driving force for each transformation and the residence time at various temperature zones. The room temperature microstructure is understood in terms of events that take place in three different temperature zones (figure 2.).

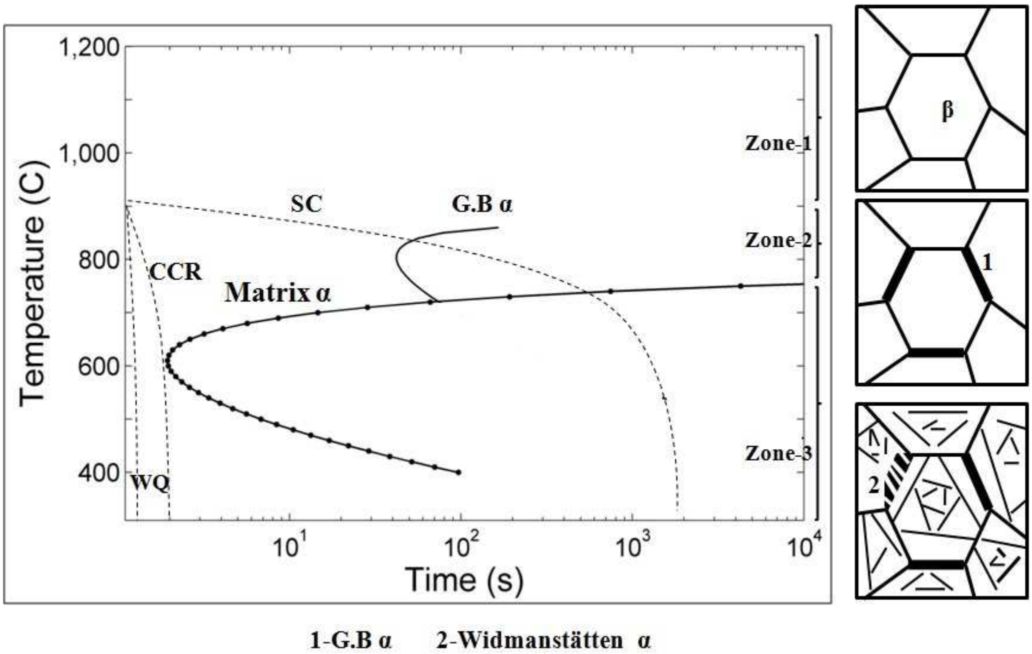

Figure 2 The temperature zones and sequence of transformation mechanism in Ti-1 and 7 Mo on cooling from β phase.

Rietveld refinement of XRD data could provide, for the first time, crystallographic details about the orthorhombic α″ in Ti-7Mo system, in addition to unit cell dimensions, atom positions and amount of all other phases α', ω and β in the two alloys for different cooling rates. The crystal structure parameters like the unit cell dimension of product phases and micro-chemistry of co-existing phases are consistent with expectation based on variation with amount of solute Mo in the product phases. Variations in the hardness with cooling conditions are consistent with the nature of phase transformation.

Chapter 6 on *"Variant selection mechanism during transformations of β in Ti-Mo alloys"*, presents the results on the study of variant selection mechanism during martensitic and Widmansttätten transformation in Ti-1Mo and Ti-7Mo, using emerging techniques like orientation imaging microscopy in EBSD in SEM and Precession Electron Diffraction in TEM (figure 3). It was found that none of the treatments i.e., different cooling rate for Ti-

1Mo and Ti-7Mo during β→α'/α″ promoted variant selection mechanism, which is understood in terms of absence of mechanical strain, which is required for selection of variants. The very low "transformation strain" which is clearly confirmed by low hardness and strain distribution maps is yet another reason for absence of variant selection mechanism during transformations from β phase.

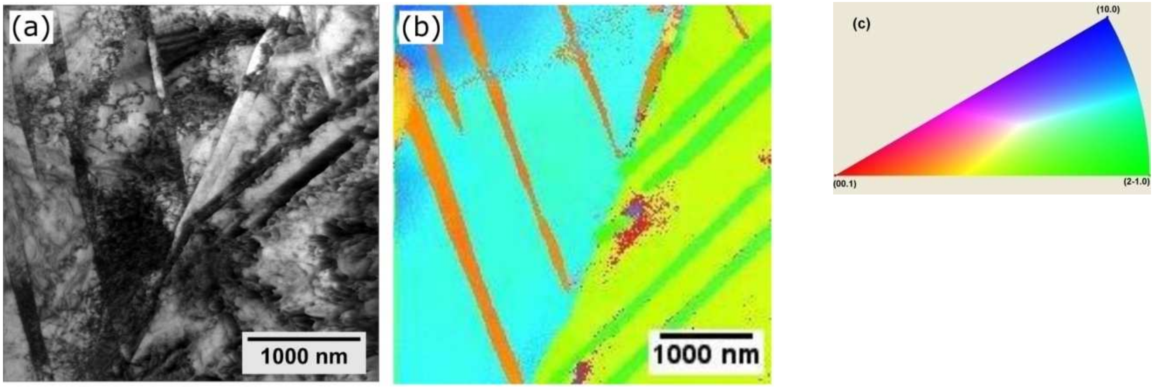

Figure 3 Precession electron diffraction of water quenched Ti-1Mo alloy.

Chapter 7 on **"***Microstructural characterization of athermal and isothermal ω in Ti-15Mo alloy"*, deals with the β→ω transformation in Ti-15 wt% Mo and its absence in Ti-25 wt % Mo alloy. The Rietveld analysis of XRD patterns using Synchrotron / or Cu-Kα sources and phase contrast microscopy of product phases of high temperature bcc β phase in Ti-15 wt% Mo alloy, after quenching the β phase at different cooling rates and isothermal exposure at 748K are presented. The comparison of the characteristics of ω^{ath} and ω^{iso}, the nature of bonding in ω^{iso} and the strengthening mechanism by the formation of ω are highlighted based on unit cell dimensions, interatomic distances, 3-D strain distribution, electron density distribution maps and atomic column contrast images from hcp α, bcc β and hexagonal ω. The characteristics of ω^{ath} and ω^{iso} are compared with respect to the extent of displacement (figure 4) during the 'lattice collapse mechanism', symmetry of the phases and morphology, using Fourier filtering technique to image atomic column contrast, for the first time in literature. Identification of ‘graphite-like’ bonding in ω^{iso} based on the interatomic distances and electron density distribution is another novelty[7] of the chapter.

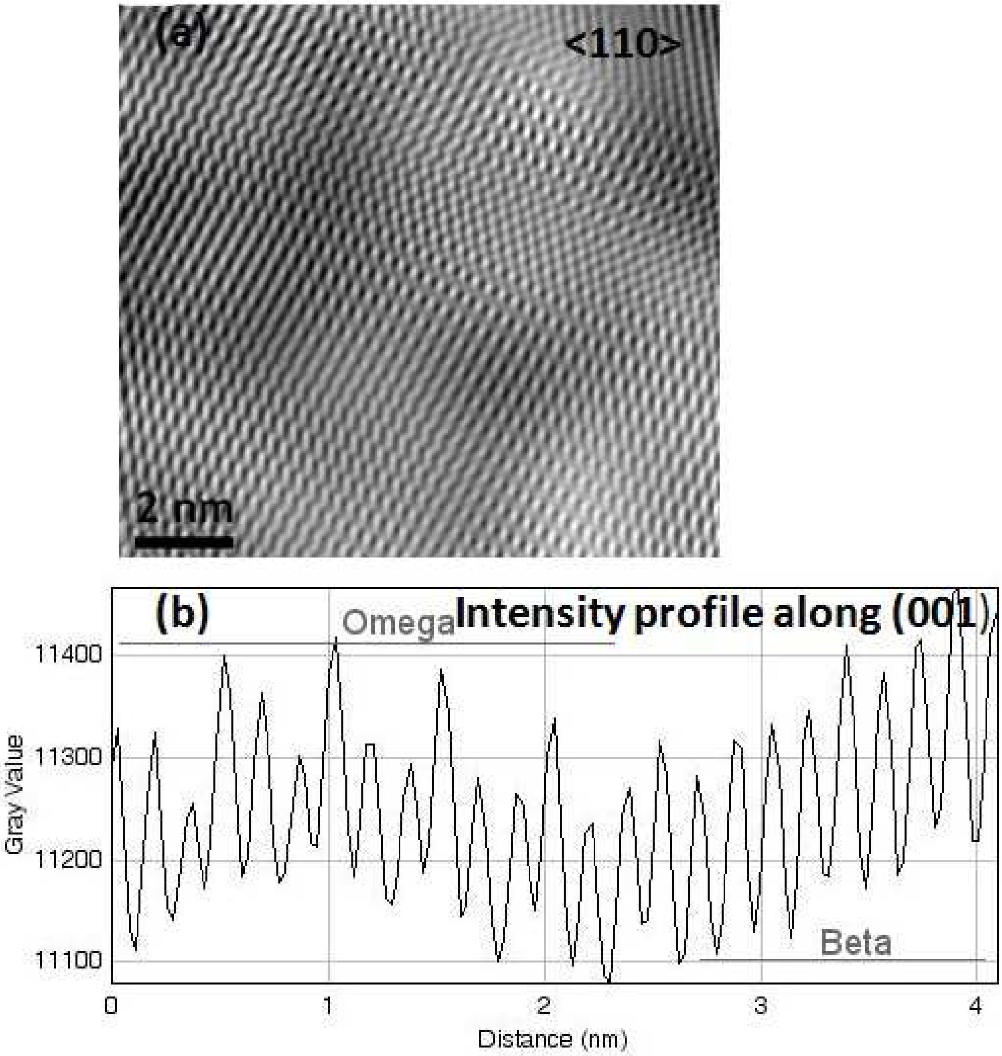

Figure 4 (a) Atomic column contrast of ω in β lattice, using image analysis procedure and (b) intensity profile along <110>.

identified. JMatPro calculations and principles of thermodynamics and kinetics supports the conclusion derived. The newly emerging Orientation imaging microscopy in SEM and TEM have been used to examine if variant selection mechanism is operative in Ti-1Mo and Ti-7Mo alloys during martensitic and widmansttätten transformations. The systematics of β→ω phase transformation, with respect to deviation from ideality, degree of ‘lattice collapse’ and crystallographic details have been studied using HRTEM and conventional and Synchrotron XRD.

References

1. Banerjee, S. and P. Mukhopadhyay, *Phase transformations: examples from titanium and zirconium alloys*. Vol. 12. 2010: Elsevier.
2. Banerjee, D. and J.C. Williams, *Perspectives on Titanium Science and Technology.* Acta Materialia, 2013. **61**(3): p. 844-879.
3. Geetha, M., *et. al.*, *Ti based biomaterials, the ultimate choice for orthopaedic implants – A review.* Progress in Materials Science, 2009. **54**(3): p. 397-425.
4. Sabeena, M., et al., *Thermodynamic Basis of Non-equilibrium Phase Transformations of bcc β-Phase in Ti–Mo System.* Transactions of the Indian Institute of Metals, 2013. **66**(4): p. 401-407.
5. Sabeena, M., et al. *Influence of Mo in β phase stability of Ti-Mo system: Synchrotron based XRD studies*. in *solid state physics: Proceedings of the 58th DAE Solid State Physics Symposium 2013*. 2014. AIP Publishing.
6. Sabeena, M., et al., *Studies on ω Phase Formation in Ti-Mo Alloys Using Synchrotron XRD.* Transactions of the Indian Institute of Metals, 2015. **68**(1): p. 1-6.
7. Sabeena, M., et al., *Microstructural characterization of transformation products of bcc β in Ti-15 Mo alloy*. Journal of Alloys and Compounds, 2016. **658**: p. 301-315.

LIST OF FIGURES

LIST OF TABLES

LIST OF SYMBOLS

Symbol	Expansion
A'	Activity of a sample
λ	Decay constant
N_t	Number of target atoms
ϕ	Neutron flux
t	Time period
m	Mass
σ	Cross section
γ	Gamma ray
A'_{std}	Activity of standard
A'_{sample}	Activity of sample
N_{std}	Number of atoms present in the standard at a time t
N_{sample}	Number of atoms present sample at a time t
A'_0	Activity at time t=0
A'_d	Activity at time $t=t_d$
t_c	Counting time
t_d	decay time
cps	Counts per second
t_d	Decay time
d	Inter-planar spacing
θ	Angle of diffraction
λ	Wavelength
n	Order of diffraction
A	Mass absorption coefficient
F	Fluorescence
$\mathbf{k_0}$	Incident beam of wave vector
Q(i)	Correlation index
$P(x_j,y_j)$	Intensity function of the experimental spot pattern at $(x_j,y_j$
$T_i(x_j,y_j)$	Intensity function of the template
ΔH^{sol}	Enthalpy of solid solution
ΔH^{c}	Chemical enthalpy
ΔH^{e}	Elastic enthalpy
ΔH^{s}	Structural enthalpy
X_A	Mole fraction of element A
X_B	Mole fraction of element B
Δh^{Sol}	Enthalpy of solution of one element in to another at infinite dilution
V_i	Molar volume of solute
V_j	Molar volume of solvent
μ_j	Shear modulus of solvent

K_i	Compressibility of solute
ΔH_{AB}^{am}	Enthalpy of formation of amorphous phase
$\bar{T}_m$	Melting point of alloy
$E_t[n(r)]$	Total energy of the system of non interacting particle
$T[n(r)]$	Kinetic energy
$E_H[n(r)]$	Hatree Folk Functional
$E_{ext}[n(r)]$	Nucleus-core electrons interaction
$E_{xc}[n(r)]$	Exchange correlation functional
I_o	Total normalized profile intensity of xrd pattern
wRp	Weighted reliability indices
Rp	Unweighted reliability indices
$\rho^{e}(x,y,z)$	Electron charge density distribution
Ω	Number of states
S	Entropy
k	Boltzmann constant
ω^{ath}	Athermal ω phase
ω^{iso}	Isothermal ω phase
α'	hcp martensite
α″	Base centered orthorhombic martensite
$\hat{H}$	Hamiltonian
$\hat{T}_e$	Kinetic energy operator (electron)
$\hat{T}_i$	Kinetic energy operator (ion)
V_{ee}	Potential energy operator (electron and electron interaction)
V_{ei}	Potential energy operator (electron ion interaction)
V_{ii}	Potential energy operator (ion-ion interaction)
$v_{coul}^{e}(r)$	Coulombs potential
$v_{xc}(r)$	Exchange correlation function
v_{ext}	External potential
Ћ	Planks constant
l_i	Distance from the central atom to the ith coordinating atom
l_{av}	Weighted average of bond length
U^{iso}	Isotropic temperature factor
I_{cal}	Calculated intensity
I_{obs}	Observed intensity
ψ_{nk}	Plane wave
hkl	Miller indices
α	hcp equilibrium phase
B	Bcc phase
ω	Hexagonal omega phase
K	Kelvin
S	Second

(hkl)	Plane corresponding to the miller indices h,k,l
$\mathbf{g}_{hk}$	Reciprocal lattice vector
a,b,c	Lattice parameter
F_o	Observed structure factor
F_c	Calculated structure factor

LIST OF ABBREVIATIONS

Abbreviation	**Expansion**
XRD	X-ray Diffraction
DFT	Density Functional Theory
VASP	Vienna Ab-initio Simulation Package
INAA	Instrumental Neutron Activation Analysis
OM	Optical Microscopy
SEM	Scanning Electron Microscopy
TEM	Transmission Electron Microscopy
ATEM	Analytical Transmission Electron Microscopy
HRTEM	High Resolution Transmission Electron Microscopy
OIM	Orientation imaging microscopy
PED	Precession Electron Diffraction
EBSD	Electron Back Scatter Diffraction
EDX	Energy Dispersive X-ray Spectroscopy
e/a	electron to atom
WQ	ice water quenching
BQ	Brine quenching
LN_2Q	Liquid Nitrogen quenching
FC	Furnace cooling
AC	Air cooling
Ti-xMo	Ti-xwt%Mo
OPS	Oxide Polishing Suspension
GSAS	General Structure Analysis System
ICDD	International Centre for Diffraction Data
2D	2 Dimensional
3D	3 Dimensional
e.m	Electro magnetic
W	Tungsten
LaB_6	Lanthanum hexaboride
FEG	Field Emission Gun
Z	Atomic number
I	X-ray intensity
Nm	Nanometer
ED	Electron Diffraction
SAD	Selected Area Diffraction
keV	Kilo electron volt
R	reliability index
LDA	Local Density Approximation
GGA	generalized Gradient Approximation
PAW	Projected Augmented Wave

PW	Perdew-Wang
CW	constant wavelength
FWHM	Full Width at Half Maximum
hcp	Hexagonal close packed structure
bcc	Body centered cubic
bco	Base centered orthorhombic
BL	Bond Length
ECN	Effective Co-ordination Number
LN_2	Liquid Nitrogen
TOF	Time of flight
FESEM	Field Emission Scanning Electron Microscope
DC	Decay correction
CC	Counting correction
IPF	Inverse pole figure
K.E	Kinetic Energy
GOF	goodness of fit
std	Standard

CHAPTER 1

INTRODUCTION

CHAPTER 1

INTRODUCTION

1.1 Introduction

Development of titanium alloys has taken rapid strides in various industrial sectors in the last six to seven decades. The versatile application of Ti is due to its unique combination of properties. It is as strong as steel, as light and ductile as aluminium and as passive as noble metals. Titanium alloys have high specific strength, excellent corrosion resistance, bio compatibility and mechanical properties [1-3]. This has been possible in titanium alloys due to a variety of phase transformation mechanisms, different combinations of metastable products and their morphology, which influence their properties. The phase transformations are influenced by alloying additions and thermo-mechanical/chemical processing. This chapter discusses the literature on phase transformations in titanium alloys in general and Ti-Mo in particular, followed by the scope of the present thesis.

1.2 Role of titanium and its alloys in industrial sectors

The vibrant growth of titanium industry, catalyzed by the invention of Kroll process began only in later half of the last century, despite its discovery 200 years ago. Titanium, one of the most abundant metals in the earth's crust (0.6%), is present in igneous rocks and their sediments. Ti occurs in minerals rutile (TiO_2) and ilmenite ($FeTiO_3$), and is present mainly as titanates. The strong affinity of titanium to oxygen makes the production and separation of pure titanium rare and expensive. Extensive research in the last century has demonstrated the indispensability of titanium and its alloys in aerospace, petrochemical and biomedical industries. Presently, Ti has successfully (figure1.1) made its way into aerospace industry, chemical processing industry, power generating industry and desalination, architectural and civil engineering, automotive industry, consumer goods, health and sports sectors. Titanium has also assumed strategic importance following its proven performance in military and off-shore applications.

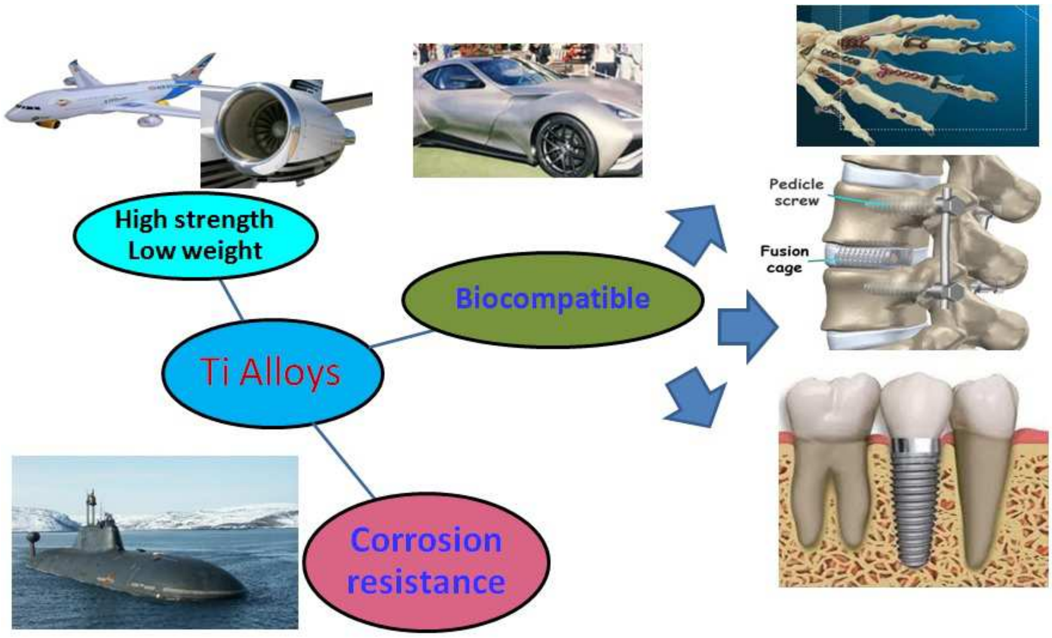

Figure 1.1 Application of Ti alloys in various sectors ranging from aerospace industry to biomedical field.

Lower density of Ti alloys (~4.5 g/cm^3) in comparison with steels and Ni based super alloys, leading to high strength to weight ratio in addition to excellent corrosion resistance has made Ti alloys most suitable in aerospace industry for manufacturing airframe, engine, and various parts of helicopter. The reduction in the weight of the various parts of engine without compromising its strength and other properties reduces the fuel consumption to a larger extent. Suitability for high temperature application, corrosion resistance, galvanic compatibility with polymer matrix composites and need for miniaturization of components promoted Ti alloy as a substitute for steels, Al and Ni based super alloys in aircraft and engine materials .

As a structural biomaterial, Ti plays a crucial role for the manufacturing of artificial valves in the heart, cardiac simulator, urinary track reconstruction, and replacements in dental structures, knee, shoulders, hip etc [3]. It is interesting to note that the Young's modulus of Ti alloys (55-110GPa) [3] is close to human bone (4-30GPa) [3] and far less than that of steels (~206 GPa) and Co based (~240 GPa) alloys [4]. Young's modulus, hardness, biocompatibility with human tissue, excellent corrosion resistance in the body fluids and high strength to weight ratio [2-8] are the relevant parameters, which make Ti alloys most suitable for biomedical applications.

Titanium alloys are classified into α, α + β and β alloys, depending on the phase at room temperature, as dictated by the nature and concentration of different alloying additions. Currently, α-Ti and α+β alloys of Ti are being used for the fabrication of bio-implants, despite their modulus being very high (~100 GPa) [3, 4, 6, 7]. Initially, Ti-6Al-4V based alloy was the widely used Ti based biomaterial. Mitsuo Niinomi *et. al.* [4] reported no variations in the Vickers hardness and fracture toughness of bio implant materials (Ti-6Al-4V ELI, Ti-5Al-2.5Fe) before and after implantation in living rabbit. However, during prolonged use of this alloy, the classic Ti-6Al-4V alloy posed health hazards [4, 5], due to the presence of toxic elements like Al and V. These reasons had motivated development of Ti alloys, without toxic elements, with elastic modulus matching with bone. Addition of elements like Zr, Nb, Ta and Mo are more suitable for developing Ti based implant materials [4], since they are non-toxic and reduces the Young s modulus than α/α + β alloys. So, research has been focused on β or near β alloys of Ti with biocompatible additions like Mo, Nb and Ta. Wrought Ti-13Nb-13Zr, Ti-12Mo-6Zr-2Fe, Ti-35Nb-7Zr-5Ta, Ti-29Nb-13Ta-4.6Zr, Ti-15Mo-5Zr-3Al, Ti-Mo are few among the current generation bio implants [3].So, there is a surge of R&D activities directed [1,3,4] towards developing next generation implant materials: Ti-Mo/Ti-Nb based β alloys, with better bio compatibility and lower modulus [5] than α, α+β based Ti alloys [3, 4].

A clear understanding on the principles of alloy design for each application of Ti has emerged based on the extensive studies on processing-structure-property correlations. The study of instability of high temperature bcc β phase and consequent transformation to either the hexagonal ω or hcp α phases has led to a unified theory of transformation of bcc to hcp. Ti has offered a unique platform to study a myriad of phase transformations: diffusionless martensitic, Widmanstätten, order-disorder and diffusional nucleation and growth mechanisms. The consequent differences in the product phases and their morphology, have led to widely varying properties – mechanical and chemical, reviewed in detail in literature [1-3, 5, 6, 9, 10].

1.3 Phase transformations in titanium and its alloys

Titanium exists as hcp (α) structure at room temperature transforms to bcc (β) structure above 1155K, which is termed as the β transus temperature. α ↔β phase transformation in Ti is dictated by various factors like , temperature, pressure or by alloying elements. The details about each are explained briefly in the present section.

Temperature dependence of the entropy term in the Gibb’s free energy plays a crucial role in the stabilization of α and β phases in elemental titanium. As the temperature increases, the vibrational entropy of the system increases. Since the bcc structure is more open and loosely packed in comparison with hcp structure, the increase in the vibrational entropy with temperature is higher in bcc structure. So, the decrease in the total free energy is more rapid in bcc structure with increase in temperature and so, Ti and its alloys prefers bcc structure at higher temperature [1].

The ideal c/a ratio of hcp structures, when atoms are assumed to be perfectly spherical, can be shown to be 1.633. This ratio is observed only for one hcp metal, Mg (1.623). Elements like zinc have c/a~1.856, while titanium has a value of ~1.587-3% less than ideal. The implied compression of atoms along ‘c’ axis is attributed to a slight covalent component in its bonding.

The α→β phase transformation in elemental titanium can occur at room temperature at higher pressure. However, the lower compressibility and the difficulty to achieve a higher pressure has limited the experimental observation of the same [1]. Another interesting pressure induced transformation in elemental titanium is the ω phase transformation. At room temperature and a pressure of ~ 2 GPa, α phase of Ti transforms to ω structure and retains it until 87 GPa. The possible reason attributed for this transformation is the transfer of electron from sp to d bands due to pressure [11].

In addition to temperature and pressure, the phase stabilities in titanium, can be altered significantly by alloying addition. The contribution of electronic structure to internal energy is known to dictate the crystal structure of elements in the periodic table. Similar factor is found to be valid for the influence of alloying additions in titanium alloys to stabilize α or β. Those solutes which enhance the d band occupancy in the anti-bonding states are found to stabilize β phase.

An alloying element is classified as either α or β stabilizer, based on whether it increases/decreases the α→β transformation temperature of pure Ti. Alloying Ti with non-transition metals/interstitial elements like Al, Zr, Sn, and O increases the β transus temperature transformation temperature and α phase is stabilized even above 882°C. Hence, these alloying additions are called as α stabilizer. Such alloys exist either fully or predominantly as hcp α structure at room temperature. Ti-alloys belonging to this category generally exhibit high strength, toughness, creep resistance and weldability. Elements like Mo, Nb, V, W, Cr, Ni, Mn, Co, Fe are called β stabilizers [1]. Addition of transition elements with more d electrons promotes Ti to gain the structure of next group to the right of periodic table, *i.e*, bcc structure. They reduce the β transus temperature, hence retaining its higher temperature bcc structure below the critical temperature of transformation. The β alloys are heat treatable and have better strength and formability than α alloys. However, they are prone to ductile to brittle transformation and exhibit a lower creep resistance. Additionally, the multi component alloys consisting both α and β stabilizers, can exist as α+β alloys, with high maneuverability to achieve the required combination of properties. Among this category, there are subclasses like near α and near β depending on the composition which make them near α/α+β or α+β/β respectively. The stabilization effect of each alloying element for various phases in multi component alloys is expressed based on the equivalence of 'Al' and 'Mo' content. The calculation [1] of the same is given as equation (1.1) and (1.2),

$$[\mathrm{Al}]_{\mathrm{eq}} = [\mathrm{Al}] + \frac{Zr}{3} + \frac{[\mathrm{Sn}]}{3} + 10[\mathrm{O}] \tag{1.1}$$

$$\begin{aligned}[\mathrm{Mo}]_{\mathrm{eq}} = [\mathrm{Mo}] + \frac{Ta}{5} + \frac{[\mathrm{Nb}]}{3.6} + \frac{[\mathrm{W}]}{2.5} + \frac{[\mathrm{V}]}{1.25} + 1.25[\mathrm{Cr}] + 1.25[\mathrm{Ni}] + 1.7[\mathrm{Mn}] \\ + 1.7[\mathrm{Co}] + 2.5[\mathrm{Fe}]\end{aligned} \tag{1.2}$$

1.4 Metastable phase transformation mechanisms and products

In addition to the equilibrium phases, Ti and its alloys mainly undergo following types of phase transformations resulting in many metastable products: (1). Diffusionless or military or shear and (2) diffusional phase transformations. The non equilibrium, shear transformations include martensitic and ω phase transformations. The diffusional transformations involve formation of various morphologies of α through different mechanism. They are formed as grain boundary allotriomorphs or primary / secondary α plates or as massive/Widmanstätten α. Since the final property of titanium alloys depend not only on the end product, but also the morphology of the product phases, i.e., the mechanism through which β has transformed, different transformation mechanisms in titanium alloys are briefly described below.

1.4.1 Diffusionless transformation

The Ti-X alloys undergo martensitic transformation [12] above a critical cooling rate (CCR) for a specific range of alloying element concentration. In contrast to steels, only a low super cooling of 50K below the β transus temperature is required for the martensitic transformation in titanium alloys. The difference between martenstitic start temperature (M_s) and martensitic finish temperature (M_f) is ~25K in Ti based alloys. Two types of martensitic transformation product reported in Ti based alloys namely hcp α’ [13, 14] and base centered orthorhombic α″ [15, 16]. Lower concentration of β stabilizing elements promote the formation of hcp α’ [14] and a higher concentration of the same leads to the formation of centered orthorhombic α″.

Extensive literature is available with respect to various aspects of these phase transformations [1, 17, 18] and their influence on the hardness, modulus and other mechanical properties of the Ti-X systems [10, 19-21]. Variation in the lattice parameter with alloying element has been reported in Ti-Nb alloys by detailed Rietveld refinement [15] and first principle calculations [16].

Another mode of non diffusional transformation is the formation of athermal ω phase. The transformation involves shuffle of atoms from their equilibrium position and retains its parent composition. Athermal ω phase formation does not require long range diffusion of atoms, but involves either atomic shuffle or co-ordinate atom movement. There is a specific orientation relation between the parent β and product ω phase. The athermal ω phase formation competes with the martensitic transformation in a narrow range of composition for specific thermodynamic conditions. The ω phase transformation can occur either by the application of static pressure or due to quenching (athermal ω) or aging (isothermal ω). The transformation proceeds *via* “lattice collapse mechanism”, illustrated in figure 1.2. This mechanism involves collapse of alternate $(222)_\beta$ plane of bcc lattice to intermediate position retaining the hexagonal symmetry [1]. Athermal transformation involves either complete or incomplete collapse of $\{111\}_\beta$ planes depending on alloying concentration and cooling rate. Based on degree of collapse, ω retains either hexagonal (P6/mmm) or trigonal (p-3mI) structure. The complete collapse results in the relation $a_\omega=\sqrt{2}\ a_\beta$, $c_\omega=(\sqrt{3}/2)\ a_\beta$ [1, 22].

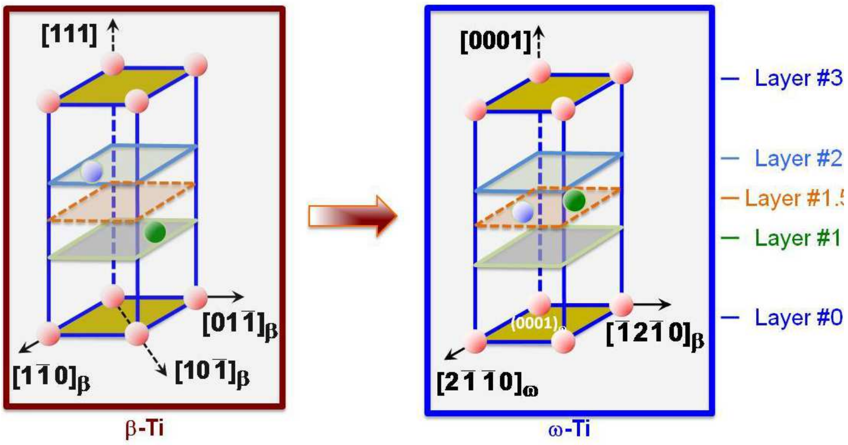

Figure 1.2 Schematic of lattice collapse mechanism for the β→ω transformation [23].

1.4.2 Diffusional Phase Transformation

Ti alloys display a wide variety of morphology and mechanisms of formation of diffusional α phase from β phase [24-26]. α phase forms on isothermal aging in the two phase field. Additionally, during cooling from the β phase, system traverses the two phase α+β region, where the β phase starts transforming to α phase. Depending upon the nucleation site and the mode of transformation, the phases are classified as grain boundary allotriomorph, inter granular α and intra granular α, primary/secondary α and massive or Widmanstätten α.

During cooling, just below the β transus, equilibrium α nucleates heterogeneously at the β grain boundary and then preferentially grows along the grain boundary. It is called grain boundary allotriomorph α. However, during further cooling, if the alloy is held at a specific temperature for long time in the $\alpha+\beta$ region, primary α (α_p) forms along with equilibrium β phase. The α_p can have plate/polygonal shape and forms either along the grain boundary or inside the grain. It follows the equilibrium composition corresponding to annealing temperature. A further cooling of the equilibrium β phase leads to formation of α called secondary α plate, which involves both diffusion and shear transformation. So secondary α plates strictly do not follow the equilibrium composition. Compared to secondary α, primary α plate are coarser. Since α_p is a diffusion controlled transformation, it does not, generally, follow any strict orientation relationship with the parent β phase. However, the secondary α follows an orientation relation with the parent β phase. The grain boundary allotriomorph, primary α plates and secondary α are relevant in the present study, which have been reported in many Ti alloys [24, 26-28].

In addition to the complete diffusional transformation, Ti-X systems are also known to undergo Widmanstätten transformation on slow cooling from the β phase field [24, 27, 29] or on aging in the $\alpha+\beta$ phase field [19, 30]. In Widmanstätten transformation, the system spends enough time in the temperature range where the β to $\alpha+\beta$ transformation takes place. Hence, diffusion and shear act together to yield Widmanstätten products of α and β, with specific orientation relation between product and parent. Since limited diffusion is allowed, Widmanstätten products grow by diffusion across the $\beta/\beta+\alpha$ boundary layer, in a cooperative manner. Hence, the product always assumes morphology of alternate lamellae of α and β [24, 31]. The composition of products in many situations does not reach the equilibrium value, due to limited diffusion. This property, along with the characteristic morphology of products distinguishes diffusional equilibrium α in β matrix, from Widmanstätten α and β. Depending on cooling rate, Widmanstätten structure can either retain a lamellar colony structure of coarse α and β plates arising from β grain boundary or the basket wave micro structure or a mixture of two, with fine plates of α and β phases [32]. The former has a single variant and occurs on very slow cooling rate and is growth dominated. The basket wave micro structure forms inside the grain and forms at a higher cooling rate and hence nucleation dominated. An intermediate cooling rate promotes a mixture of this microstructure.

Another diffusional transformation, the massive transformation is reported in several Ti based alloys, for medium cooling rates, which is too slow for martensitic transformation and too fast for long range diffusional transformations. The short range thermally activated atomic jumps across the interface of parent and product facilitates composition invariance. The thermally activated jumps cause re arrangement of atoms in the α/β interface and cause the nucleation of α phase at the grain boundary. The growth is as fast as the nucleation of α and demands large driving force. The growth kinetics, morphology and orientation relationship during massive transformation is reported in titanium aluminide [33]. Ahmed *et. al.* [34] reported the range of cooling rate required for various modes of transformations like martensitic, massive, and diffusional in Ti-Al-4V. A cooling rate above 410°C/s cause complete martensitic transformation and a cooling rate of 410°C/s to 20°C/s cause massive transformation. A further reduction from 20°C/s, causes the alloy to undergo Widmanstätten transformation.

Isothermal ω forms during aging below the ω start temperature 'ω_s'. The isothermal ω formation is a diffusional transformation involving out-diffusion of β stabilizing solutes, leading to compositional change during the ω precipitation. The reported temperature range of ω_s for β Ti alloys are between 150-500 ^{o}C [35]. However, the exact temperature range varies with alloys system [36]. During the athermal and isothermal ω formation, the product phase follows an orientation relation with the parent which is given below.

$$\{111\}_\beta \| (0001)_\omega , < 1\bar{1}0 >_\beta \; \| < 11\bar{2}0 >_\omega$$

The characteristics of these transformations are discussed in detail in the chapter 7.

1.5 Phase Transformation in Ti-Mo based alloys

The phase diagram of Ti-Mo is well established (figure 1.3) for titanium rich side and the composition ranges and temperature limits for various phase domains are known fairly well. The system offers excellent scope for the study of phase transformation mechanisms in view of the existence of wide spectrum of transformation modes. Several experimental/theoretical studies are still being carried out on various aspects of phase transformations in Ti-Mo alloys. These include study of the nature of phase transformations of the high temperature β phase during both equilibrium thermal exposure conditions and non- equilibrium cooling conditions. The equilibrium phase transformations in Ti-Mo alloys are well studied and documented [1]. Aging always promotes the formation of diffusional α+β structure in Ti-Mo alloys.

There are several studies regarding the nature of transformation products for different amount of Mo concentration, for a particular cooling condition. Generally, slow cooling rates promote the Widmanstätten transformation in Ti-Mo alloys. The transformation product consists of alternate lamellae of α and β structure. The fast quenching always promotes the martensitic transformation. Two types of martensitic structures are reported in Ti-Mo alloys; the hcp α′ and orthorhombic α″[1]. The formation of hcp α′ phase and orthorhombic α″ phase is reported in Ti-Mo alloys for a concentration of 0-4 wt% and 4-9 wt% of Mo [10, 13, 14]. On the other hand, bcc β phase is retained for a Mo concentration of 10wt% [14]. A measured lower cooling rate called CCR is reported for the martensitic transformation. The CCR rate is 3000 K/s for pure Ti and decreases due to alloy addition from 420 K/s to 70 K/s for a composition of 1 to 8 wt% Mo [13]. A very high cooling rate of 11000 K/s could not suppress martensitic transformation in Ti-Mo alloys [1]. There are reports mentioning the formation of athermal or isothermal ω phase, for a concentration ranging from 10 to 18 wt%

of Mo. However, there is no agreement among the reported values of Mo concentration for the complete retention of bcc phase. Several reports mention the upper limit as 10 wt % Mo [10, 37]. However, detailed microscopy studies confirm [9, 22, 23, 38-40] that it is above this value. The complete retention of β phase on quenching is reported for alloys of Ti-Mo for a concentration above 15 wt% [9, 38, 39].

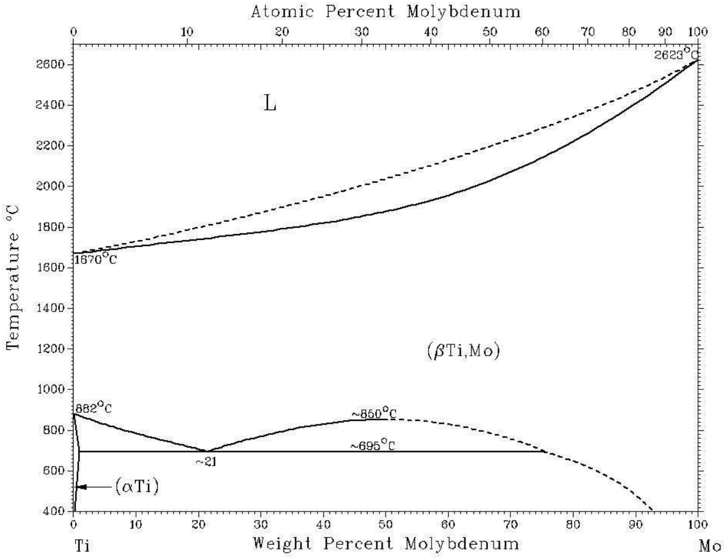

Figure 1.3 Phase diagram of binary Ti-Mo alloy.

The influence of each phase transformation on the mechanical and physical properties is well studied in literature [9, 10]. The details about each phase transformation are discussed in the respective chapters of the thesis.

1.6 Organization of the present thesis on "Phase Transformations in Ti-Mo alloys"

A detailed study has been carried out in Ti-Mo alloys to study the various aspects of phase transformation, which includes both diffusional and non diffusional phase transformation. The major part of the study deals with the identification of transformation products with conventional and synchrotron X-ray Diffraction (XRD). In addition to mere identification of crystal structure, detailed Rietveld refinement has been carried out to retrieve crystal structure details like lattice parameter, atom positions, coordination number, bond length, 3-D strain distribution and the bonding characteristics. Detailed microstructural characterization was carried out using Optical Microscopy (OM), Scanning Electron Microscopy (SEM), Transmission Electron Microscopy (TEM), and Orientation Imaging Microscopy (OIM) which include Electron Backscatter Diffraction (EBSD) and Precession Electron Diffraction (PED). The signatures of athermal and isothermal ω are identified. Additionally, the competing phase transformations and possibility of variant selection mechanism is analyzed for Ti-1Mo and Ti-7Mo alloys at various cooling conditions. The present thesis "Phase transformations in Ti-Mo alloys" is organized as follows in Table 1.1.

Table 1.1 Organizations of thesis chapters

Chapter No:	Title	Content
1	Introduction	Literature survey, existing gaps, contributions of the present study and organization of the thesis.
2	Experimental and modeling details	Theory and Principle, experimental details, calibration, error and accuracy of investigation methods.
3	Influence of Mo on transformation products of high temperature parent bcc β phase in Ti-Mo alloys	Identification of non-equilibrium transformation products *via* conventional/Synchrotron XRD and TEM/SAD.
4	Crystal structure and bonding characteristics of transformation products of bcc β in Ti-Mo alloys	Rietveld analysis of X-ray diffraction patterns of α', α″ and β phases of four alloys of Ti-Mo for crystal structure parameters and first principle DFT calculations to benchmark bonding nature.
5	Competing phase transformation mechanisms and products in Ti-Mo alloys.	Influence of cooling rate on the mechanism of phase transformation of β in Ti-1Mo and Ti-7Mo alloys is studied using experimental and JMatPro calculations.
6	Variant selection mechanism during transformations of β in Ti-Mo alloys.	Variant selection mechanism during the martensitic and Widmanstätten phase transformation of Ti-xMo (x-1,7 wt%) for various cooling conditions, using orientation imaging microscopy in SEM and TEM.
7	Study of β → ω transformation in Ti-15 wt% Mo	Characteristics of athermal and isothermal ω in Ti-15 Mo established.
8	Summary and scope for future work	

As has already been presented earlier, extensive research work has already been carried out on various aspects of Ti-Mo alloys. Most of the studies on phase transformations are based on electron diffraction and microscopy. The X-ray diffraction has been used mainly as preliminary identification of the product phases. However, the details of product phases beyond crystal structure, like atom positions, co-ordination number, bond length, charge density distribution and 3-D distribution of lattice strain have not been so far reported. Present thesis has made an effort to fill this gap. Another interesting debate in literature has been about the bonding nature of the ω phase, in Ti/Zr alloys, which is mainly based on interatomic distances and band structure calculations. The present work has for the first time provided confirmation of graphite like bonding in ω in Ti-Mo system, based on evaluation of interatomic distances in various planes of ω using detailed analysis of XRD results. Application of synchrotron XRD for detection of minor phases, orientation imaging microscopy in TEM and SEM and Fast Fourier Transformation (FFT)/Inverse FFT for elucidating atomic column contrast in ω are some of the additional contributions of the thesis.

References

[1] S. Banerjee, P. Mukhopadhyay, Phase transformations: examples from titanium and zirconium alloys, Elsevier, **2010**.

[2] D. Banerjee, J.C. Williams, *Acta Materialia* **2013**, 61, 844.

[3] M. Geetha, A.K. Singh, R. Asokamani, A.K. Gogia, *Progress in Materials Science* **2009**, 54, 397.

[4] M. Niinomi, *Materials Science and Engineering: A* **1998**, 243, 231.

[5] M.T. Mohammed, Z.A. Khan, A.N. Siddiquee, *International Journal of Chemical, Nuclear,Materials and Metallurgical Engineering* **2014**, 8, 1123.

[6] M. Long, H. Rack, *Biomaterials* **1998**, 19, 1621.

[7] X. Liu, P.K. Chu, C. Ding, *Materials Science and Engineering: R: Reports* **2004**, 47, 49.

[8] J.I. Qazi, H.J. Rack, *Advanced Engineering Materials* **2005**, 7, 993.

[9] W. Ho, *Journal of Medical and Biological Engineering* **2008**, 28, 47.

[10] W. Ho, C. Ju, J.C. Lin, *Biomaterials* **1999**, 20, 2115.

[11] M. Pérez-Prado, A. Zhilyaev, *Physical review letters* **2009**, 102, 175504.

[12] S. Miyazaki, K. Otsuka, C.M. Wayman, *Acta Metallurgica* **1989**, 37, 1885.

[13] R. Davis, H. Flower, D. West, *Journal of Materials Science* **1979**, 14, 712.

[14] M. Sabeena, R. Mythili, J. Basu, M. Vijayalakshmi, *Transactions of the Indian Institute of Metals* **2013**, 66, 401.

[15] S. Banumathy, R. Mandal, A. Singh, *Journal of Applied Physics* **2009**, 106, 093518.

[16] A. Pathak, S. Banumathy, R. Sankarasubramanian, A. Singh, *Computational Materials Science* **2014**, 83, 222.

[17] R. Davis, H. Flower, D. West, *Acta Metallurgica* **1979**, 27, 1041.

[18] J. Hernandez, S. Li, E. Martinez, L. Murr, X. Pan, K. Amato, X. Cheng, F. Yang, C. Terrazas, S. Gaytan, *Journal of Materials Science & Technology* **2013**, 29, 1011.

[19] J.-W. Lu, Y.-Q. Zhao, P. Ge, H.-Z. Niu, *Materials Characterization* **2013**, 84, 105.

[20] Y. Mantani, Y. Takemoto, M. Hida, A. Sakakibara, M. Tajima, *Materials transactions* **2004**, 45, 1629.

[21] F.F. Cardoso, P.L. Ferrandini, E.S. Lopes, A. Cremasco, R. Caram, *journal of the mechanical behavior of biomedical materials* **2014**, 32, 31.

[22] M. Sabeena, A. George, S. Murugesan, R. Divakar, E. Mohandas, M. Vijayalakshmi, *Journal of Alloys and Compounds* **2016**, 658, 301.

[23] R. Banerjee, Phase Separation And Second Phase Precipitation In Beta Titanium Alloys, In, University Of North Texas, 2011.

[24] R. Mythili, V.T. Paul, S. Saroja, M. Vijayalakshmi, V.S. Raghunathan, *Materials Science and Engineering: A* **2005**, 390, 299.

[25] S. Semiatin, T. Bieler, *Acta materialia* **2001**, 49, 3565.

[26] R. Pederson, Microstructure and phase transformation in Ti-6Al-4V, Lulea,**2002**.

[27] H. Flower, *Materials Science and Technology* **1990**, 6, 1082.

[28] M. Behera, R. Mythili, S. Raju, S. Saroja, *Journal of Alloys and Compounds* **2013**, 553, 59.

[29] H. Flower, S. Henry, D. West, *Journal of materials science* **1974**, 9, 57.

[30] T. Furuhara, T. Makino, Y. Idei, H. Ishigaki, A. Takada, T. Maki, *Materials Transactions, JIM* **1998**, 39, 31.

[31] N. Kishore Babu, S. Ganesh Sundara Raman, R. Mythili, S. Saroja, *Materials Characterization* **2007**, 58, 581.

[32] R. Shi, Variant Selection during Alpha Precipitation in Titanium Alloys A Simulation Study, in, The Ohio State University, **2014**.

[33] R. Ramanujan, *Journal of materials science* **2002**, 37, 2203.

[34] T. Ahmed, H. Rack, *Materials Science and Engineering: A* **1998**, 243, 206.

[35] M. Lai, C.C. Tasan, J. Zhang, B. Grabowski, L. Huang, D. Raabe, *Acta Materialia* **2015**, 92, 55.

[36] S. K. Sikka, Y. K. Vohra, R. Chidambaram, *Progress in Materials Science* **1982**, 27, 245.

[37] D. Eylon, R.R. Boyer, D.A. Koss, Beta Titanium Alloys in the 1990's, in, Warrendale, PA (United States); Minerals, Metals and Materials Society, 1993.

[38] M. Sabeena, S. Murugesan, R. Mythili, A. K. Sinha, M. N. Singh, M. Vijayalakshmi, S. K. Deb, Influence of Mo in β phase stability of Ti-Mo system: Synchrotron based XRD studies, in: Solid State Physics: Proceedings of the 58th DAE Solid State Physics Symposium 2013, AIP Publishing, 2014, pp. 119.

[39] M. Sabeena, S. Murugesan, R. Mythili, A. K. Sinha, M. N. Singh, M. Vijayalakshmi, S. K. Deb, *Transactions of the Indian Institute of Metals* **2015**, 68, 1.

[40] A. Devaraj, S. Nag, R. Srinivasan, R. Williams, S. Banerjee, R. Banerjee, H. Fraser, *Acta Materialia* **2012**, 60, 596.

CHAPTER 2

EXPERIMENTAL AND MODELING DETAILS

CHAPTER 2

EXPERIMENTAL AND MODELING DETAILS

2.1 Introduction

The current thesis “Phase Transformations in Ti-Mo Alloys” focuses on the influence of chemistry and thermal history on the nature of equilibrium and non-equilibrium transformation mechanisms and products of β phase in Ti-xMo (x=1,7,15,25) alloys. The study establishes the microstructural and crystallographic details, atom positions, co-ordination number, bonding nature and strain distribution of the transformation phases α, α', α", ω, and β, employing various microscopy and X-ray Diffraction (XRD) techniques. Additionally, several computational methods have also been employed, namely Miedema model for energetics and Density Functional Theory (DFT) calculations using Vienna Ab-initio Simulation Package (VASP) for charge density distributions.

The current chapter gives the details of the procedure adopted for each of the technique employed in the present study. The section 2.2 describes the procedure of preparation of alloys, followed by determination of the chemical composition using Neutron Activation Analysis (INAA). Details of various sets of thermal treatments carried out for study of different types of phase transformations are presented in section 2.3. This is followed by the methodology adopted for sample preparation for various techniques. Section 2.4 deals with the major techniques used for understanding the various aspects of phase transformations in Ti-Mo alloys. The conclusions of the study are mainly based on results from X-ray diffraction using both lab XRD and Synchrotron XRD. Detailed Rietveld analysis of the XRD data forms major part of the present study.

Microstructural characterization to study phase transformation mechanisms was carried out using microscopy techniques ranging from OM, SEM to TEM. TEM studies include the following: (a) analytical TEM (ATEM) for micro structural, micro chemical and crystal structure details, (b) high Resolution TEM (HRTEM) for atomic column contrast studies, (c) OIM using PED technique in TEM and EBSD technique in SEM. In addition, mechanical property like hardness has been studied using Vickers microhardness tester.

For each of the experimental technique, the following aspects are discussed: the principle of operation, the information that can be obtained, the operation parameters employed in the study, calibration procedures, and method of analysis of results, accuracy of results and error.

Section 2.5 deals with details of the computational technique/Miedema model, the principle of the computational method, the inputs, the boundary conditions and the errors are presented. Finally, Section 2.6 briefly summarizes the details presented in the chapter.

2.2 Experimental Techniques: Alloy preparation and chemical analysis

2.2.1 Alloy preparation

The compositions of the alloys were selected based on the literature, the electron to atom (e/a) ratio and the phase diagram. It has been shown that e/a ratio dictates the phase stability in Ti-Mo alloys: 4-4.07 for α', 4.07-4.17 for α'', for 4.06-4.14 for ω and 4.2 or above for retention of β. Generally, a concentration of Mo up to 4 wt% promotes the hcp α' phase during quenching. Further increase in the alloying element of Mo up to 8wt% promotes the formation of an intermediate orthorhombic α'' structure. The propensity of the formation of athermal/isothermal ω phase is reported for a concentration of Mo of 9-18wt% in the binary Ti-Mo alloys. Detailed discussion on these aspects are provided in Chapters.3, 4, and 7. The compositions of the alloys chosen were 1, 7, 15, 25 wt% of Mo. The details of alloy preparation and chemical analysis are described below.

Pure metals of 99.95% purity Mo and 99.99% purity Ti from M/s. Sigma Aldrich were used. Ti and Mo rods were made into very small pieces for ensuring better mixing during alloy preparation. The required amounts of Ti and Mo corresponding to each composition of the alloy were weighed using Mettler AE 163 balance, with an accuracy of 0.1 mg. Before melting, the metals of specified weight were manually mixed and kept in the water cooled Cu hearth of the vacuum arc furnace supplied by M/s. Vacuum Techniques, Bangalore. The empty Cu hearth was filled with Ti sponges, to minimize O_2 pick up during melting. Diffusion pump in combination with primary rotary pump was used for the generation of vacuum of ~10^{-6} mbar. Once the pressure of the order of 10^{-6} mbar was obtained, chamber was purged with high purity Ar gas. The process was repeated twice to ensure minimum contamination in the chamber. Finally, chamber was maintained at a pressure of ~2×10^{-6} mbar, to ensure minimum O_2 pickup. Tungsten electrodes were used for plasma generation. Even though, 15A current is used for initial arc generation, during melting this was increased up to 220A. The current was selected in order to ensure proper mixing of both the elements in the liquid state. The visual examination of the flow of the liquid metal in the Cu hearth confirmed the proper mixing of both the elements. Melting was carried out repeatedly, ~7-20 times depending on the nature of the sample to ensure homogeneity. Before each remelting, the oxide layer present on the alloy surface was removed manually using grit paper. The alloy was cut again into pieces before the final melting. After each melting, micro chemistry of several regions was evaluated using SEM/EDX, to check for contamination and homogeneity of composition. If surface contamination of Cu, W were present, it was removed mechanical grinding or drilling before the next melting. The process was repeated till the alloy of homogeneous composition was obtained.

2.2.2 Chemical Analysis

The homogeneity of the alloy composition and presence of impurities after each melting were analyzed using SEM / EDX and the accurate chemical analysis was carried out using Neutron Activation Analysis.

2.2.2.a Energy Dispersive X-ray Spectroscopy (EDX)

The operating voltage used in SEM was 25 kV during EDX experiments. The chemical composition of the alloy used for present studies are given in Table 2.1.

Table 2.1 Chemical composition of Ti-Mo alloys obtained using EDX.

No	Alloy	Ti (wt%)	Mo (wt%)
1	Ti-1Mo	98.67 ± 0.32	1.32 ± 0.32
2	Ti-7Mo	92.64 ± 0.13	7.35 ± 0.13
3	Ti-15Mo	84.92 ± 0.24	15.08 ± 0.24
4	Ti-25Mo	75.19 ± 0.28	24.80 ± 0.28

2.2.2.b Neutron Activation Analysis (INAA)

The Ti-xMo (x=1, 7, 15, 25) alloys were analyzed by Instrumental Neutron Activation Analysis (INAA) using KAMINI research reactor at IGCAR, Kalpakkam. Presences of impurities like Fe, W, Co and Cu have been analyzed.

Reasons for the choice of INAA

Even though widely accepted methods of chemical analysis ranging from wet chemical analysis to spectroscopic techniques like Atomic absorption Spectroscopy, Inductively Coupled Plasma Optical Emission Spectroscopy (ICP-OES) and Inductively Coupled Plasma Mass Spectrometry (ICP-MS) are available, INAA was chosen in the present study, due to the following reasons: Most of the spectroscopic techniques require proper dissolution of the constituent element of the material in suitable solvents and so, is destructive by nature. The highly oxidizing nature of Ti poses difficulties for dissolution of Ti in proper solvents with minimum error in the measurements. In addition, INAA requires minimum amount of sample and is non-destructive in nature.

Principle of INAA

The interaction of the incident, energetic neutron from a nuclear reactor, with matter generates radioactive isotopes.

1. The radioactive isotopes emit γ rays with specific energy, during its radioactive decay. The energy of γ thus emitted is characteristic for each element.
2. Detection and quantification of γ rays enable the identification of constituent elements.

The schematic diagram of INAA is given in figure 2.1.

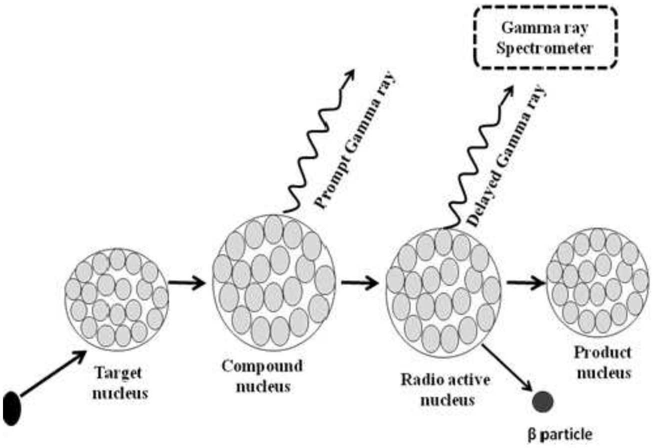

Figure 2.1 A schematic diagram illustrating the process involved in Neutron activation Analysis.

Principle of quantitative analysis

The activity (A') of a sample, having decay constant λ for a nuclear reaction with cross section

σ and number of target atoms N_t (the composition, that is being analyzed) irradiated with a neutron flux ($\emptyset$) for a time period (t) is given by the following equation.

$$A' = N_t \sigma \emptyset \left[1 - e^{-\lambda t}\right] \tag{2.1}$$

So by measuring activity (A') followed by the proper substitution of the above parameters, the number of atoms in the sample, i.e., the composition can be calculated.

However, absolute values of σ and ∅ are neutron energy dependent. So it is difficult to evaluate its values. Also due to the uncertainties with the absolute values of thermal, epithermal and neutron cross section, a relative method has been adopted for deriving the elemental constitution of present alloys. Here the standard samples along with the alloys of interest are irradiated and their activities are measured in identical conditions. The basic equation governing the analysis is as follows:

$$\frac{A' std}{A' sample} = \frac{N\ std}{N\ sample} \tag{2.2}$$

where A'_{std} and A'_{sample} are the activity (counts per second, cps) of the standard and sample, N_{std} and N_{sample} are the number of atoms present in the standard and sample at a time t. Normally it is the time just after the completion of irradiation. The irradiation of the sample and standard can be done at same time. However, the γ ray counting can be done one after other for standard and the sample of interest. So the corresponding error; the 'decay correction' and 'counting correction' ha to be introduced in the above equation.

$$Decay\ correction, DC, A'_d = A'_0 \times e^{-\lambda t_d} \tag{2.3}$$

$$Counting\ correction, CC = \frac{1 - e^{-\lambda t_c}}{\boldsymbol{\lambda} t_c} \tag{2.4}$$

Here λ→decay constant, t_d →decay time, A'_d→ Activity at time $t=t_d$, A'_0→ activity at time t=0, t_c →counting time. So final equation for atomic weight (m) of the sample is

$$\Rightarrow m\ sample = m\ std \times \frac{cps\ sample}{cps\ std} \times \frac{(DC \times CC)std}{(DC \times CC)sample} \tag{2.5}$$

The activity, cps (count rate) of the sample and standard is identified as

$$cps = \frac{peak\ area}{time} \tag{2.6}$$

Thermal neutrons have more activation cross section compared to high energy neutrons. So, for present INAA analysis, thermal neutrons (Kinetic Energy, K.E < 0.5 eV) are used. The epithermal (K.E - 0.5 eV to 0.5 MeV) and high energy neutrons (K.E > 0.5 MeV) are filtered out using suitable B or Cd filters.

Experimental procedure:

1-2 mm small pieces of samples weighing minimum 1.3mg to maximum 8mg were washed with DM water and acetone and dried. The samples were packed in double polythene covers and heat sealed. The high purity standard chemicals were used as elemental relative standards, the details of which are given in Table 2.2. For Ti standard, TiO_2 of Spec-pure from Jhonson & Mathey Company, England was used. The sealed sample and standard were placed in irradiation capsule and irradiated at the power of 5 kW in Pneumatic Fast Transfer System (PFTS) position of KAMINI reactor for 5mins. ^{233}U-Al alloy is used as fuel for neutron generation in the reactor. For present INAA analysis, thermal neutrons (K.E < 0.5 eV) are used due to its higher activation cross section in comparison to high energy neutrons. The irradiated sample and standard were assayed immediately by high-resolution γ ray spectrometry using Eurisys HP Ge detector coupled to 8k Aptec MCA card and its acquisition software. The energy calibration of γ ray spectrometry multi channel analyzer is carried out using ^{152}Eu. Since the present study adopted relative method for quantification of the elements, efficiency calibration was not carried out.

Table 2.2 Details about the elements, standards used for the INAA analysis of Ti-Mo alloys.

Sl. No	Alloy	Weight of sample given for analysis	Analyzed elements	Standards used
1	Ti-1MoWQ	6.9 mg	Ti, Mo, Fe, W, Co, Cu	TiO_2 standard, Ferro molybdenum (12.33 mg), Ferro Tungsten(5.25 mg), Lead brass (6.22 mg), Co foil (4.2 mg)
2	Ti-7MoWQ	10 mg		
3	Ti-15MoWQ	10 mg		
4	Ti-25MoWQ	7.895 mg		

Figure 2.2 shows the γ ray spectrum corresponding to Ti-1Mo alloy. The peaks, corresponding to 320.1KeV of Ti and 739.5KeV of Mo are used for the calculation of the concentration of the respective elements. All the short duration irradiations of the samples

were done independently and counted immediately. The same samples were used for long duration irradiation.

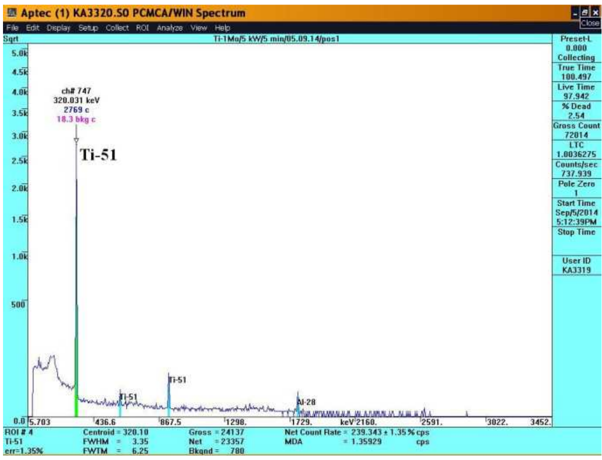

Ti-1Mo/5 kW/5 min/05.09.14/pos1

Preset-L
0.000
Collecting
True Time
100.497
Live Time
97.942
% Dead
2.54
Gross Count
72014
LTC
1.0036275
Counts/sec
737.939
Pole Zero
1
Start Time
Sep/5/2014
5:12:39PM
Stop Time
User ID
KA3319

ROI # 4
Ti-51
err=1.35%
Centroid = 320.10
FWHM = 3.35
FWTM = 6.25
Gross = 24137
Net = 23357
Bkgnd = 780
Net Count Rate = 239.343 ± 1.35 % cps
MDA = 1.35929 cps

Figure 2.2 γ Spectrum of irradiated Ti-1Mo alloy.

Samples were allowed for decay of the short lived activation products and one set of samples was used after 6 days and another set was used after 30 days. Each set of samples and standards were prepared and irradiated for 6h at the same PFTS position of reactor at 20kW. The samples were opened after overnight cooling and counted at different intervals. All the samples were counted long time for better counting statistics. The gamma activities of the activation products of 6 hours irradiated samples and standards were measured using BSI p-type HP Ge detector with 30% relative efficiency and 2.1 keV energy resolution at 1332.5 keV of ^{60}Co, coupled with ITECH Instruments quad ADC 8k MCA module and Inter-winner 7.0 MCA software. The selection of relative method in the present study for elemental quantification minimized the possible errors expected from the neutron flux measurement. In addition to that, the decay and counting corrections during the γ ray measurement have been taken into account in the calculation. The above methods minimized the error bar of INAA as low as ±5%. The results of chemical analysis of the alloys used in the present study are given in Table 2.3.Based on the above analysis, hereafter, the four alloys will be referred as given in column 1 of Table 2.3.

Table 2.3 Amount of Ti, Mo and W in Ti-xMo alloy samples

Sample	Ti (wt.%)	Mo (wt.%)	W (ppm)
Ti – 1Mo	98.99 ± 0.36	0.91 ± 0.01	717.1 ± 0.6
Ti – 7Mo	93.46 ± 0.32	7.41 ± 0.04	945.1 ± 13.8
Ti – 15Mo	84.87 ± 1.33	16.60 ± 0.10	369.2 ± 8.7
Ti – 25Mo	74.47 ± 0.48	24.00 ± 0.14	734.1 ± 6.3

2.3 Heat treatment and specimen preparation for various experiments

2.3.1 Heat treatment

Heat treatments were carried out in a tubular furnace, fitted with proportional temperature controller. The hot zone of the furnace was ~12 cm, at the centre of the furnace tube. The temperature was measured and controlled using calibrated Chromel -Alumel thermocouple. Figure 2.3 shows a typical calibration curve for a furnace.

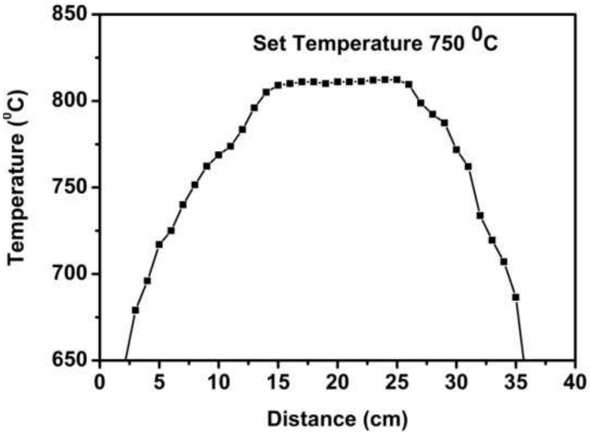

Figure 2.3 Furnace calibration curve.

During homogenization, ingots of dimensions ~2.5x1x1cm were used. For quenching and aging experiments, specimens of dimensions ~1.5x1x0.2 cm were used. The samples were vacuum sealed with Ti sponge at ~10^{-6}mbar pressure in quartz tube to ensure minimum O_2 pick up during heat treatments.

Prior to various quenching experiments, the vacuum sealed samples were kept at 1173K for another 2 hour. This is followed by fast cooling in the quench bath like ice water (temp ~273K), ice brine (temp ~263K) and liquid N_2 (77K). During the quenching process, the glass tube was broken just before dropping into the bath. The cooling rate could not be measured.

However, based on visual observations, it appeared that achieving bath temperature during LN_2 quenching was slow, in comparison with the other two, due to the possible formation of N_2 gas around the sample surface. In all cases, a colored oxide layer was formed on the surface of alloy. Six different heat treatments were carried out on the four alloys, for different themes of studies, which are listed in Table 2.4.

Table 2.4 Heat treatment details of Ti-Mo alloys.

No.	Heat treatment (β solutionising temperature)	Alloys used	Temperature of bath/outside	Theme of the study
1.	WQ(1173K)	Ti-1Mo, Ti-7Mo, Ti-15Mo, Ti-25Mo	273K	Identification of transformation products of high temperature β phase
2.	LN_2Q(1173K)	Ti-15Mo, Ti-25Mo	77K	Confirmation of presence/absence of ω phase. Identification of lattice parameter of ω phase.
3.	BQ(1173K)	Ti-15Mo, Ti-25Mo	263K	
4.	WQ(1173K)+Aging at 753K	Ti-15Mo, Ti-25Mo		
5	AC(1173K)	Ti-1Mo, Ti-7Mo	293K	To study the influence of cooling rate on the transformation mechanism and to study the variant selection mechanism
6	FC(1173K)			
WQ→ ice water quenching, BQ→ Brine quenching, LN_2Q → Liquid Nitrogen quenching, FC→ Furnace cooling, AC→ Air cooling				

The furnace and air cooling experiments of Ti-xMo (x=1, 7 wt%) alloys were carried out using the furnace manufactured by Vacuum technologies Private Limited, Bengaluru, in the UGC-DAE-CSR facility. Prior to cooling, the sample was kept at 1173K for 1 hr at 10^{-6} m bar pressure. The cooling curve plotted based on temperature Vs time data for both furnace and air cooling experiments is given in figure 2.4. The cooling rate calculated from 900°C to 500 °C is 3.3°C/s for air cooling, where as it was 0.13°C/s for furnace cooling. The temperature is measured using calibrated Chromel Alumel thermo couple.

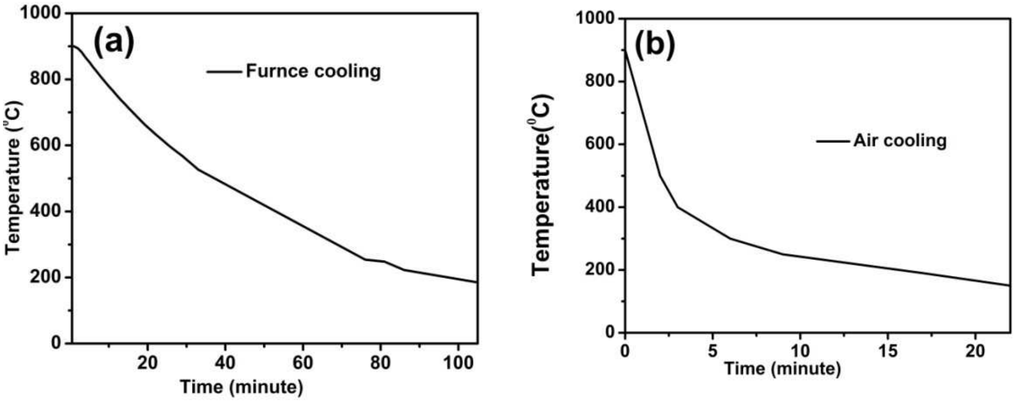

Figure 2.4 Experimentally measured cooling curve for Ti-1Mo and Ti-7Mo alloys during (a) furnace cooling and (b) Air cooling.

2.3.2 Specimen Preparation

Conventional metallographic methods of sample preparation were followed for optical microscopy, Scanning Electron Microscopy, Microhardness, laboratory and synchrotron XRD studies. Samples were polished using emery sheets of successive grades upto 4000 grit paper. This was followed by polishing using Oxide Polishing Suspension (OPS) solution. Mechanical polishing was finally followed by electro polishing for EBSD analysis. Electro polishing was carried out using solution containing methanol (99.95 %) and Perchloric acid (60 wt %) in the ratio 9:1 at temperature below 245K, using a voltage of 20V and a current of ~2A. For SEM and OM, etching of the samples was carried out using 2% HF solution / Kroll's reagent (70ml Distilled water+25ml HNO3+5ml HF). Observations and recording of images were carried out soon after the sample preparation.

Transmission Electron microscopy requires samples of 50-100 nm thickness to ensure electron transparency for 200kV incident electron beam. Hence, after mechanical polishing up to 1200 grit paper to about 120 μm, the samples were electro polished using 10% Perchloric acid in Methanol with Struers Tenupol-5 jet polishing unit. Electro polishing was carried out at a voltage -15V and at a temperature of -28 to 30^{0}C. The samples for HRTEM analysis, which need to be even thinner than conventional TEM, were made using ion milling.

2.4 Experimental Methods

Many experimental methods were employed for the study of phase transformations in Ti-Mo alloys: conventional and synchrotron XRD, microscopy techniques and Vickers microhardness tester. The details of each technique are given below.

2.4.1 X-ray Diffraction

In order to retrieve information regarding crystal structure, unit cell dimensions, atom positions, co-ordination number, 3-D strain distribution and charge density distribution, conventional and Synchrotron X- ray diffraction experiments were carried out.

Principle:

When X-rays of wavelength similar to the interatomic spacing interact with this natural grating setup, diffraction occurs and form diffraction maxima and minima. This diffraction pattern is specific to each material and so, is a finger print of the crystal. The main attempt is to arrive at various features as given below.

For a known wavelength λ, the inter planar distance, 'd' can be identified from the Braggs diffraction condition

$$2d \sin\theta = n\lambda \qquad (2.7)$$

A schematic XRD pattern is nothing but the line position '2θ' Vs intensity 'I' plot and is given in figure 2.5.

The absence/presence of diffraction maxima, following the "extinction rules", provides a clue about the crystal structure. The direct substitution of angle of diffraction, "2θ" position in Bragg's law yields the experimentally determined interplanar spacing'd'. Comparison of the experimental'd' values with ICDD data for an anticipated crystal system, as it happened in present study, provides information regarding the crystal structure and indexing of the peaks.

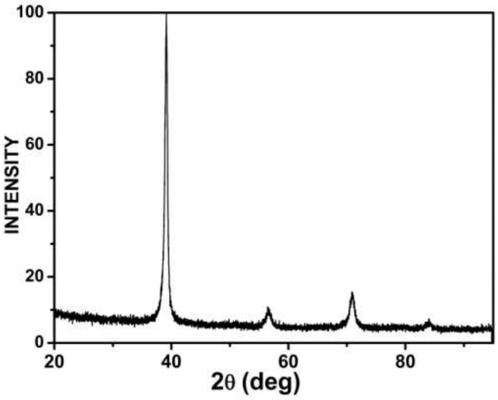

Figure 2.5 Schematic XRD pattern showing the I vs 2θ data

The intensity values of the XRD pattern carry accurate information about the structure factor of the lattice, which yields valuable information about the atomic co-ordinates and electron density distribution. But the experimentally measured intensity is directly influenced by many other factors [1]: (1) polarization factor, (2) multiplicity factor, (3) temperature factor, (4) Lorentz factor, and (5) absorption factor. Careful separation of structure factor contribution from other factors is carried out using detailed analysis of the XRD pattern. The third useful parameter in the XRD pattern is the Full Width at Half Maximum (FWHM), which yields information about the strain and particle size.

2.4.1.a Conventional X-ray Diffraction

Experimental details

An XRD instrument contains three major parts: a source producing the X- ray beam, sample and the detector. Various sources are available like Cu Kα (λ=1.5405 Å), Mo Kα (λ=0.711Å), Co Kα (λ=1.790Å) Cr Kα (λ=2.291 Å), and Fe Kα(λ=1.937 Å) [1]. The choice of the source depends on the required range of 2θ, expected angular separation between closely lying peaks and possibility of fluorescence. With these criteria, Cu Kα is used for present XRD studies.

INEL XRG 3000 XRD spectrometer was used at an operating voltage of 40kV and a current of 30 mA. Acquisition of the diffraction data was carried out in parallel beam geometry, with monochromatic incident beam of CuKα radiation of wave length, λ=1.54056 Å. The size of the incident, rectangular X-ray beam was 4mm/125 μm. The measurements were carried out using samples, which were rotated at room temperature. The data corresponding to 2θ=10° to 95° was recorded using a curved position sensitive detector, with step size of 0.012°. Calibration of the diffractometer, for getting accurate distance between sample surface and detector, was carried out using standard Si powder from National Physical Laboratory, New Delhi.

Method of Analysis of XRD

Rietveld refinement of the XRD pattern was carried out using General Structure Analysis System (GSAS) [2]. VESTA software [3] was used for plotting the calculated charge density distribution.

The various steps used in the above analysis are the following: (1) generation of experimental as well as calculated XRD pattern. The basic input parameters like space group, lattice parameter and atom positions were obtained from ICDD data and available literature. Si standard from the National Physical Laboratory, New Delhi, was used for generating the calibration data, to correct for shift in 2θ and instrumental broadening. TOF profile function 4 was used to generate the model profile. (2) The elimination of back ground noise of the intensity data was carried out using shifted Chebyschev function. The best fit was identified by trial and error method among the available background functions. (3) Next, the refinement of 2θ and the (4) intensity values were carried out using Lorentian and Guassian part of the pseudo-Voigt function, to incorporate broadening due to microstructural features. (5) The contributions due to polarization factor, zero correction, texture and thermal vibrations were taken into account for the refinement. Each step in this refinement was continued until the convergence was obtained for all parameters. Improved matching for experimental and calculated profile was ensured during the refinement of each parameter. In addition to that, trend in the unweighted and weighted reliability 'R' indices (wRp, Rp) and goodness of fit (GOF) were checked, during the refinement of each parameter in order to ensure an optimum fitting.

The refined peak intensities of XRD pattern were used for arriving at the structure factor values. The calculated structure factors from available (hkl)'s were used for evaluating the electron density distribution using Fourier method. The 2D and 3D electron density distribution maps within the unit cells of all product phases in each alloy were plotted using VESTA software.

2.4.1.b Synchrotron X-ray Diffraction

It is difficult to detect low amount of product phase in conventional X-ray systems, due to low current. Synchrotron X- ray sources overcome this limitation, by using intense, tunable, collimated, X-ray source, with brilliance 10 orders of magnitude, higher than the conventional sources [4] making it possible to detect even a low intensity peak of low volume fraction phase, like 'ω' in the present studies.

Principle

The schematic diagram of synchrotron X-ray beam line is given in figure 2.6.

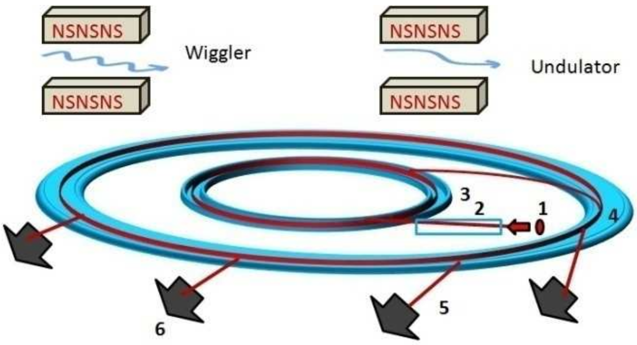

1-*electron from an electron gun*
2-lenear accelerator
3-booster ring
4-storage ring with bending magnets, wigglers & undulators
5-beam line
6-experimental stations

Figure 2.6 Schematic diagram of synchrotron X-ray beam line.

The electrons are accelerated to ~3Gev, which further enter the storage ring. The storage ring contains bending magnets and many other components.

For diffraction experiments, the incident white X-ray source is collimated using appropriate filters, to get single monochromatic X-ray beam with high brilliance. The XRD experiments can be carried out in reflection mode. The 2 dimensional MAR Research Image plate is used as detector for the same.

The quality of the synchrotron X-ray source is superior over the conventional method due to its high brilliance. Generally, the 'figure of merit' of the X-ray sources is compared with the term 'brilliance' [4] and is defined as follows.

$$Brilliance = \frac{Photons/second}{(mrad)^2\ (mm^2\ source\ area)(0.1\%BW)} \qquad (2.8)$$

Experimental details

Synchrotron XRD experiments were carried out using angle dispersive x-ray diffraction beam line (BL-12) at Indian Synchrotron Source (Indus 2), facility at RRCAT Indore. Monochromatic x-ray beam of energy 13.081KeV (λ=0.9478 Å) was used. The calibration of wavelength was done using XRD pattern of NIST LaB_6 powder in transmission mode. However, the actual experiments in synchrotron XRD of Ti-Mo alloys were carried out in the reflection mode using MAR Research image plate (MAR 345 DTB). Also due to certain experimental difficulties, sample had to be kept stationary during the data acquisition. The data acquisition was carried out till the saturation of detector, which is within few seconds. Image plate data was converted to I vs 2θ plot using FIT2D software [5]. Generally, the accuracy of the measurement of synchrotron XRD is as small as 0.03°. However, in the present case it was as high as 0.2°, due to the above mentioned difficulties.

The experiments were repeated for the identification of ω phase and determination of its unit cell parameters accurately. Si powder from NIST was used as internal standard. Prior to analysis, the peaks corresponding to internal standard has been subtracted out. This was used for I Vs 2θ plot. Further indexing was carried out as in conventional XRD analysis.

2.4.2 Microscopy Techniques

Microstructural analysis of Ti-Mo alloys was carried out with various microscopy techniques like optical microscopy, scanning electron microscopy, and transition electron microscopy. In addition to the microstructure, information about the micro-chemistry was obtained by EDS (Energy Dispersive Spectrometry) analysis in SEM and TEM, while micro-texture was studied using Automated Orientation Imaging in SEM and TEM.

2.4.2.a Optical Microscopy

Experimental details

Preliminary microstructural characterization was carried out using LEICA MeF4A visible light microscope fitted with a Leica digital camera along with image analysis software QWin. The magnification calibration of the objective lenses was carried out with a standard micrometer stage insert with 1000 lines/mm. In certain circumstances, polarized light was used with the choice of appropriate polarizer and analyzer lenses, to enhance contrast among the fine features.

2.4.2.b Scanning Electron Microscopy (SEM)

SEM is used to study the surface topography, micro chemistry and micro texture. Incident electron beam, with energy around 10 to 30 keV is generated by thermionic emission using W or LaB_6 and field emission process in FEG guns. The intensity of the incident beam increases by an order of magnitude from W to LaB6 to FEG. The incident beam scans the surface of the sample, using a scanning coil. The signals used in the SEM are secondary electrons for surface topography, backscattered electrons for Z contrast, X-rays for micro chemistry and Kikuchi pattern for orientation. The appropriate signals are detected using suitable detectors.

The semi-quantitative chemical analysis is carried out using characteristic X-rays generated from the specimen due to incident electron beam interaction. The energy of the X-ray emitted from the signal is characteristic of the Z of the element and the intensity of a peak is proportional to the amount of the element present in the sample.

Qualitatively, amount of an element (C) in the sample can be calculated, by comparing with X-ray intensity (I) in standard sample, using following equation:

$$\frac{C_{sample}}{C_{std}} = \frac{I_{sample}}{I_{std}} \qquad (2.9)$$

However quantification of the above values requires ZAF correction to be applied, due to the following factors: (a) Atomic number ‘Z’ to account for the higher yield of X-rays from elements with higher Z, (b) absorption (A) factor to account for the change in intensity due to mass absorption co-efficient and the path length in denser material and (c) Fluorescence (F) to account for the secondary fluorescence due to X-rays of neighboring elements, in addition to the X-rays generated by incident electron beam.

So quantitative analysis of the material can be calculated using the following equation.

$$\frac{C_{sample}}{C_{std}} = \frac{I_{sample}}{I_{std}} \, . [ZAF]_{sample} \qquad (2.10)$$

The *C* and *I* represent the composition and the measured intensity respectively.

Experimental Details

Calibration of magnification of SEM has been carried out with standard cross grating sample of 20 lines /mm and 2160 lines per mm. Acceleration voltage ranging from 20-30 KV is used. For chemical composition and homogeneity analysis, Energy Dispersive Spectrometry (EDS) analysis in SEM was carried out in either Philips XL-30 SEM, or Helios NanoLab- 600i Dual

Beam Field Emission Scanning Electron Microscope (FESEM). Calibration for the same was carried out using standard Cu grid. Energy resolution of EDX was 30 eV at Mn Kα.

2.4.2.c Transmission Electron Microscopy (TEM)

Both Analytical TEM (ATEM) and High Resolution TEM (HRTEM) have been used in the present study. ATEM is equipped with attachments for EDS and Orientation imaging analysis. .

Principle

An incident electron beam of energy 100 to 300 KeV passes through the sample of thickness ~10-50nm and forms image of the sample on a screen with desired magnification and far superior resolution, since resolution is given as

$$r_{min} \approx 0.91(C_s\,\lambda^3)^{1/4} \qquad (2.11)$$

r_{min}→minimum disc radius, C_s→Spherical aberration coefficient, λ→wave length of incident electron beam. Electron diffraction patterns provide crystallographic information form nm sized regions. In conventional TEM, contrast is achieved by either absorption from Mo rich regions or diffraction, from regions which are Bragg oriented. High resolution lattice fringe image is obtained by interference between various diffraction peaks. The sample acts as a “pure phase object” and introduces only phase change to the incident beam. The image generated using only this change is referred to as “lattice image” or “phase contrast image”.

Experimental details

Morphology, micro structure, orientation and atomic column alignment of various products phases have been carried out using Transmission Electron Microscopy (TEM). Among this, detailed microstructural analysis of transformation products of all Ti-xMo alloys has been carried out using CM 200 analytical TEM operated at 200kV. Magnification calibration has been carried out using cross grating of 2160 lines/mm with a separation of 469 nm between lines. Standard nanocrystalline oriented gold in holy carbon film is used for calibration of camera length and high resolution test with a line resolution of 2.3Å. Using Selected Area Diffraction (SAD), crystal structures of various product phases were confirmed. In order to identify the distribution of various phases in the sample, selected area diffraction and dark field microscopy has been carried out. An aperture of size 10µm was used for the same. The post imaging processing has been carried out using image J software for quantitative analysis.

β→ω transformation was mainly studied using high resolution transmission electron microscopy FEI Tecnai F30 G2 TEM at 300 kV. At imaging mode, for low magnification conditions (5to 100 kX at 300kV) calibration has been carried out using standard grating of 2160 lines/mm corresponding to 463 nm. The high magnification calibration has been carried out using standard polycrystalline Au#646 specimen for (111) plane at a d spacing of 0.2355nm. In the diffraction mode, camera length calibration was carried out using standard Au-613. The post imaging processing has been carried out using Gatan Digital Micrograph and the simulation of diffraction pattern is done with JEMS software version 4.2.

2.4.3 Orientation Imaging Microscopy

The orientation imaging microscopy at two levels of resolution was carried out using EBSD in SEM and scanning Precession Electron Diffraction patterns in TEM.

Principle

Electron Back Scattered Diffraction (EBSD) in SEM makes use of “Kikuchi Pattern” to identify the orientation of the crystal, on which the beam is incident. The incident, parallel 30 keV electron beam, gets back scattered from the first few µm layer of the polished sample. The back scattered beam is incident on certain planes of the crystal at Bragg angle, satisfying diffraction condition. The diffracted beam produces the “Kikuchi pattern” containing the information about the orientation of the region of interest. A typical experimental set up and the Kikuchi pattern is shown in figure 2.7.

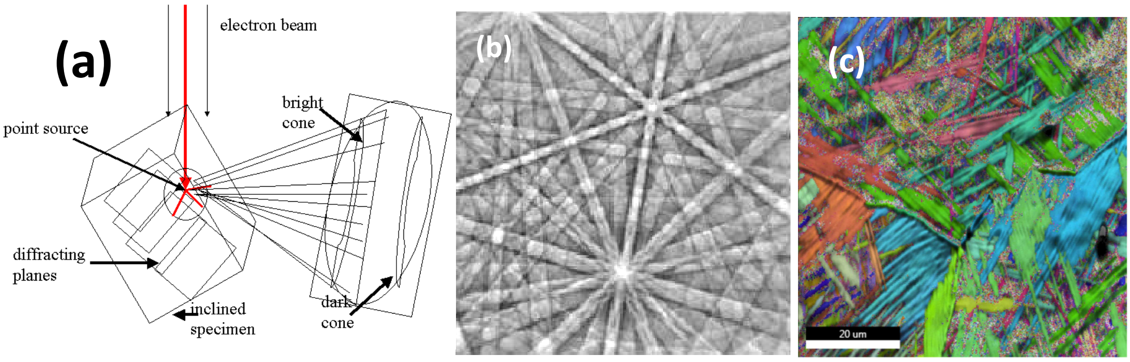

Figure 2.7 (a) Typical experimental set up in SEM/EBSD and (b) Kikuchi Pattern. (c) An orientation micrograph.

The region of interest in the sample is scanned by the incident beam and the orientation in each pixel is recorded using the Kikuchi pattern. Finally, mapping of the orientation of individual pixels in the selected region of interestis mapped using an appropriate colouring scheme. Orientation imaging map is thus generated, a typical image of which is shown in figure 2.8(c).

The orientation imaging studies were carried out using Electron Back Scatter Diffraction (EBSD) attached with FEI make Helios NanoLab- 600i Dual Beam Field Emission Scanning Electron Microscope (FESEM) at an operating voltage of 20kV and current of 2.7nA at a working distance of 6mm. The indexing of Kikuchi pattern was carried out using the library data available with the EBSD software.

In addition to that, an automated orientation imaging analysis was carried out with the ASTAR system with Precession Electron Diffraction (PED), from N/s. Nanomegas SPRL, Belgium. The principle of this method is illustrated in figure 2.8. The high energy (200keV) incident beam [figure 2.8 (a)] is precessed around the optic axis [figure 2.8(b)], in the region of interest [figure 2.8(c)], followed by scanning. Within the residence time of the incident beam in each pixel, the electron pattern is collected, recorded and stored. This process is repeated for each pixel, for the entire area of interest, using the scanning device. The experimentally obtained electron diffraction pattern from each pixel [figure 2.8(c)], is compared with library functions, to identify the zone axis of each pixel, which carries the information about the orientation of the region [figure 2.8(d)].

The conditions for acquisition of orientation maps acquired in the present study, using ASTAR system attached to the PHILIPS CM 200 TEM are given in Table 2.5. The micro-diffraction and precession was controlled by a dedicated external device. The diffraction patterns at the determined step size for the area of interest were recorded with a fast acquisition CCD camera of large dynamical range, fitted externally on the viewing screen of the TEM. The precessing angle was restricted to less than 0.5° to avoid beam broadening due to precession. Prior to acquisition of diffraction patterns of the sample, diffraction pattern from a standard [001] oriented gold specimen was used for the calibration of angle of precession and camera length.

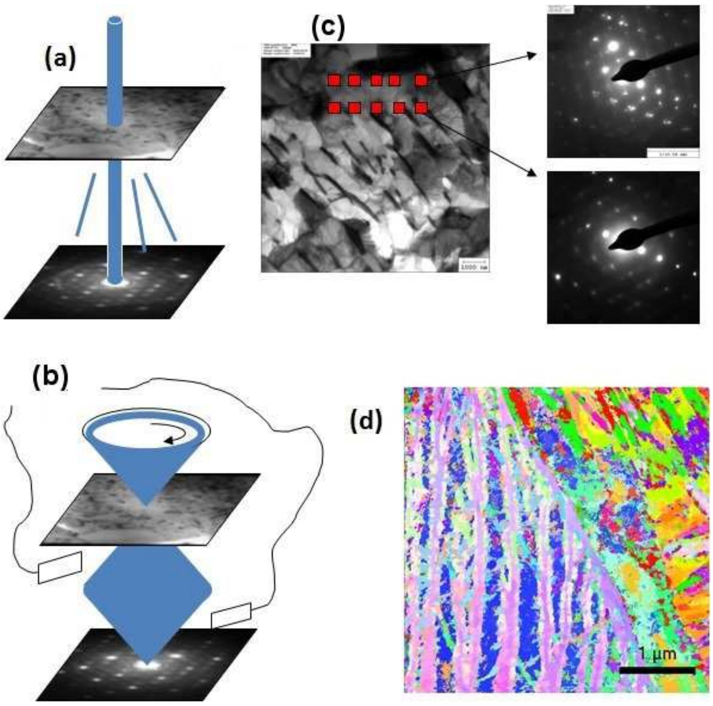

Figure 2.8 Experimental set up in Orientation imaging in TEM.

Table 2.5 Conditions for acquisition of OIM maps

Parameter	**Value**
Operating voltage	200kV
Precession angle	0.4°
Beam size	15-55nm
Step size	8-25 nm
Condenser aperture size	50 μm
Diffraction pattern acquisition rate	25-30 frames per second
Camera length	12 to 17 cm
Magnification	8800 X

The area of the region of interest was calibrated with the image of the scanned region acquired with an on-axis camera. After the acquisition of the diffraction patterns, they were indexed using a template matching procedure by generating the diffraction patterns along various zone axes for the expected phases with known crystallographic details like the lattice parameters and the space group. The degree of matching of the experimental pattern with a theoretically generated template is characterized by cross correlation index, which is defined as

$$Q(i) = \frac{\sum_{j=1}^{m} P(x_j, y_j)\, T_i(x_j, y_j)}{\sqrt{\left[\sum_{j=1}^{m} P^2(x_j, y_j)\right]}.\sqrt{\left[\sum_{j=1}^{m} T_i^2\,(x_j, y_j)\right]}} \qquad (2.12)$$

where, Q(i) is called the correlation index, $P(x_j,y_j)$ is the intensity function of the experimental spot pattern at (x_j,y_j), while $T_i(x_j,y_j)$ is the intensity function of the template. Based on the Q(i) values, the index map is generated. The reliability of a particular solution in case more than one template is matched is given by R, reliability index, which is defined to be

$$R = \left[1 - {Q_2}/{Q_1}\right].100 \tag{2.13}$$

where, Q_1 and Q_2 are the index values of 2 nearly matching solutions. The value of R is minimum if more than one solution is possible, like on a grain boundary or inter phase. An R value of 15 and above is generally accepted to be reliable. The map generated for the spatial distribution of the R values is called the reliability map. The orientation map generated based on the template matching of the constituent phases includes all the values of reliability indices. However, a superposed image of the orientation image and the reliability map helps to identify points of low reliability.

2.4.4 Vickers Microhardness tester

The microhardness testing was carried out using LEITZ Miniload-2 microhardness tester. A static load of 100g is used for making an indentation mark on each material using the diamond tip of the Vickers pyramidal indenter. In order to minimize the error, experiments were repeated for 10 times for each alloy and average is taken. The microhardness tester was calibrated using the standards provided along with LEITZ Miniload-2 microhardness tester.

2.5 Computational Method

2.5.1 Miedema model

Using Miedema approach [6, 7], an attempt has been made to find out the relative stability of metastable phases over the solid solution phase. The stability of a phase at a particular composition range can be predicted based on the lowest enthalpy of formation. This is merely based on the calculation of formation enthalpy of solid solution and amorphous phases. The process involves mixing of solute atom in the solvent matrix by equalizing the potential gradient. During this stabilization process, the difference in the electron negativity, atomic size, crystal structure and valence electrons of both solvent and solute atom play a major role.

According to this model, the enthalpy of a solid solution (ΔH^{sol}) is the sum of chemical (ΔH^{c}), elastic (ΔH^{e}) and structural (ΔH^{s}) enthalpy [6, 7].

$$\Delta H^{sol} = \Delta H^{c} + \Delta H^{e} + \Delta H^{s} \tag{2.14}$$

The chemical term originate due to the variation in electro negativity and electron density at the surface of Wiegner seitz unit cell. The elastic enthalpy term is related to lattice mismatch energy and is calculated based on the atomic size difference between solute and solvent atoms. However, the structural contribution indicates the preference of the transition metal to attain any of the bcc, hcp, or fcc phase based on the valence electrons. But the contribution from the structural part is negligible comparing the other two. So, it is assumed constant lattice stability throughout the system. So for simplification 'ΔH^{s}' is considered to be zero. So,

$$\Delta H^{sol} = \Delta H^{c} + \Delta H^{e} \tag{2.15}$$

The chemical enthalpy of mixing can be calculated as

$$\Delta H^{c} = X_A X_B [X_A \Delta h^{sol}_{B\ in\ A} + X_B \Delta h^{sol}_{A\ in\ B}] \tag{2.16}$$

X_A and X_B represent the mole fraction of corresponding atoms. Δh^{Sol} is the enthalpy of solution of one element in to another at infinite dilution. The elastic enthalpy originated from the lattice size mismatch can be calculated as

$$\Delta H^{e} = X_A X_B [X_A \Delta h^{e}_{B\ in\ A} + X_B \Delta \tag{2.18}$$

$$\Delta h^{e}_{i\ in\ j} = \frac{2\mu_j (V_i - V_j)^2}{V_j (3 + 4\mu_j \mathrm{K}_i)} \tag{2.19}$$

where, V_i and V_j are the molar volume of solute and solvent and $\mu_j and\ \mathrm{K}_i$ represents shear modulus of solvent and compressibility of solute respectively. For amorphous phase, due to the lack of periodicity, atoms have no constrained to fit in to a specific volume. So, elastic contribution of enthalpy is absent. So, chemical enthalpy with enthalpy of fusion of constituent atoms dictates the enthalpy of formation of amorphous phase (ΔH_{AB}^{am}).

$$\Delta H_{AB}^{am} = \Delta H^{c} + 3.5\,\bar{I} \tag{2.20}$$

Here $\bar{T}_m$ is nothing but the melting of alloy. This can be represented by the combination of individual melting point of solvent and solute. So,

$$\Delta H_{AB}^{am} = \Delta H^{c} + 3.5\,[X_A T_A^{m} + X_B T_B^{m}] \tag{2.21}$$

2.5.2 First principle calculation using Density Functional Theory (DFT)

DFT is a quantum mechanical computational modeling method which identifies the ground state properties of a many electron system like atoms, molecules, metals, and insulator by solving the corresponding Schrodinger equation governing the system dynamics. In order to understand the electron charge density distribution of various transformation products of Ti-Mo alloys, first principle calculations has been carried out using Vienna Ab-initio Simulation Package (VASP)[8]. The theory behind this method is briefly discussed below.

The system is described using a suitable many-body non relativistic Hamiltonian ($\widehat{H}$).

$$\widehat{H} = \widehat{T}_e + \widehat{T}_i + V_{ee} + V_{ii} + V_{ei} \tag{2.22}$$

The parameters $\widehat{T}_e, V_{ee}, V_{ei}$ represents kinetic energy operator corresponding to electron, potential energy operator corresponding to electron-electron interaction and electron-ion interaction respectively. It is possible to consider the kinetic energy term of nuclei ($\widehat{T}_i$) in the Hamiltonian to be zero and the potential energy operator of ion-ion interaction (V_{ii}) constant, based on the well established Born- Oppenheimer approximation . The total energy is expressed as a unique function of electron density, based on the Hohenberg-Kohn theorem [9], which helps us to replace the wave function by electron charge density. This approximation is used to express the Hamiltonian in terms of its energy functional, in which the term related to exchange correlation functional is not exactly known. Generally, Local Density Approximation (LDA) and generalized Gradient Approximation (GGA) are the two most commonly used exchange correlation functional. In the former approximation, the electron density is considered to be purely local; the contribution at each point (**r**) is independent of other. The GGA is a modified version of LDA where in addition to the local electron density its gradient is also taken into consideration.

The core electrons are tightly bound to the nuclei and do not participate in bonding. Hence most of the physical properties of solids depend on valance electron than the core-electron. Thus near the core region the strong electron-nuclei potential is replaced by a pseudo-potential, which will same behavior of total potential outside the core region [10]. There are different approaches to construct pseudo-potentials; Projected *Augumented Wave* (PAW) [11] method employed in VASP has been selected in the present study. In summary the Schrödinger equation with K-S Hamiltonian can be written as

Non relativistic LDA, GGA

$$\left(-\frac{\hbar^2}{2m}\nabla^2 + v_{ext}(r) + v_{coul}^{e}(r) + v_{xc}(r)\right)\psi_{nk}(r) = E_{nk}\psi_{nk}(r) \tag{2.23}$$

Pseudo potential (PAW) VASP-uses-plane waves

The functional/potential used for present studies are marked in the equation. The basic idea behind solving a problem using DFT is to identify the solution of Kohn-Sham equation. The total energy $'E_t[n(r)]'$ of the system of non interacting particle can be re written in terms of electron density as given below

$$E_t[n(r)] = T[n(r)] + E_{ext}[n(r)] + E_H[n(r)] + E_{xc}[n(r)] \tag{2.24}$$

$T[n(r)]$ represents the summation of kinetic energies of individual electrons moving in the field of all other electrons. $E_H[n(r)]$ is the Hatree Folk Functional. The potentials due to the ‘nucleus-core electrons’ interaction is represented by a pseudo potential ‘$E_{ext}[n(r)]$’ and $E_{xc}[n(r)]$ is the exchange correlation functional in the DFT calculation.

Computational details

All simulations are done using VASP package, which employs the PAW pseudo-potentials. PAW potential helps to not only helps to reduce the size of basis set, but also incorporates the accuracy of all electron calculations. The systematic procedure adapted is as follows

1. **Selection of exchange correlation functional:** The suitability of exchange correlation functional from LDA and GGA are checked for Ti and Mo atoms. For GGA approximation analysis, both PBE [12] and PW-91 (Perdew-Wang) are used. The results were analyzed with the experimental lattice parameter (see Table 2.5). The lattice parameter calculated using PBE functional is less deviated from the experimental lattice parameter in comparison with other potential. Hence PBE is selected for further calculations.

Table 2.6 comparison of lattice parameter of Ti obtained via VASP calculations for various exchange correlation functional and with the Rietveld refined parameter.

No	Exchange correlation functional		Calculated lattice parameter (Å)	Experimental lattice parameter (Å)	Variations in the lattice parameter (Å)
1	LDA		a= 2.8536 c=4.5180	a= 2.9514 c=4.6814	Δa=0.0978 Δc=0.1634
2	GGA	PW-91	a=2.9199 c=4.6188		Δa=0.0315 Δc=0.0626
		PBE	a=2.9239 c=4.6240		Δa=0.0275 Δc=0.0574

2. **Optimization cut of energy (ENCUT) and K point mesh size:** In-order to fix the size of plane wave basis set and k-point mesh a series of convergence test has been made. Kinetic energy cut-off energy has to be defined, to truncate the size of plane wave basis set. The kinetic energy varied for 250 eV-1000 eV, and found a convergence of the order of (7.25×10^{-4} meV/atom) from 700 eV onwards. The k-point mesh size governs the sampling in

the reciprocal space, and its convergence has been tested. A Monkhorst-pack[13] pack grid of size 17x17x11 k for Ti and 17x17x17 k for Mo is finalized (see figure 2.9)

3. Geometry relaxation: After fixing all these values, geometry relaxation has been carried out for each structure. For Bulk Ti and Mo atom the volume relaxation scheme is adopted. For the Ti-Mo alloy the ions position and cell shapes were relaxed. During this process we ensured a force on atoms of the order of 10^{-4} eV/atoms and the external pressure is zero.

4. Generation of Ti-25Mo alloy: For that, a super cell has generated by taking in to consideration the alloy composition. For eg: The atom percent of Mo in Ti-25Mo alloy is ~14. It exists as bcc structure. So, for that, a super cell of 2x2x2 is generated. Out of the 16 lattice position of this bcc structure, 2 are occupied by Mo atoms. For incorporating the Mo in various lattice positions, Site Occupancy Disorder (SOD) technique [14] is used.

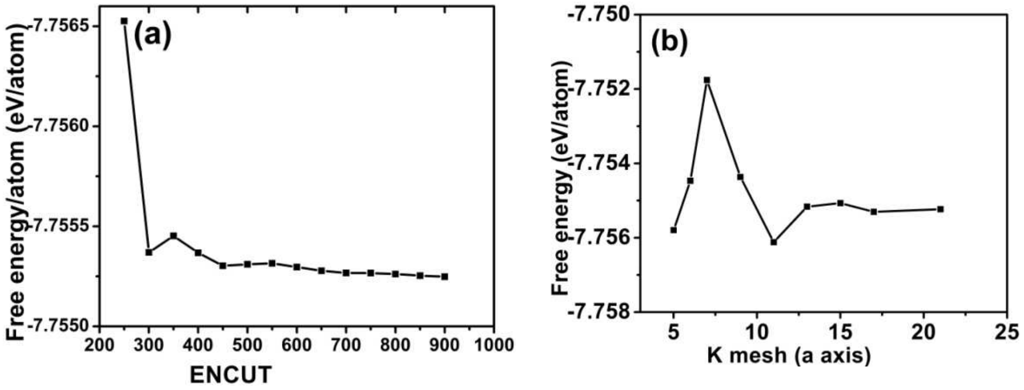

Figure 2.9 Optimization of (a) energy cut of value and (b) k mesh for Ti.

The technique allows the non periodic occupation of Mo and Ti atoms in the crystal lattice by taking the advantage of crystal symmetry. For the present alloy system, 4 in equivalent configurations are generated using the SOD technique and is given in figure 2.10. DFT calculations are carried out by taking the optimized values of Ti/Mo for defining plane wave basis sets, pseudo potential, and exchange correlation functional. After getting the charge density for each configuration, averaging has been over all configurations done to get a final charge density which will be close to the random solid solution of Ti-Mo alloy. The average charge density obtained from all these configurations is used for further comparison with the experimental results. The summary of the same is given in figure 2.11.

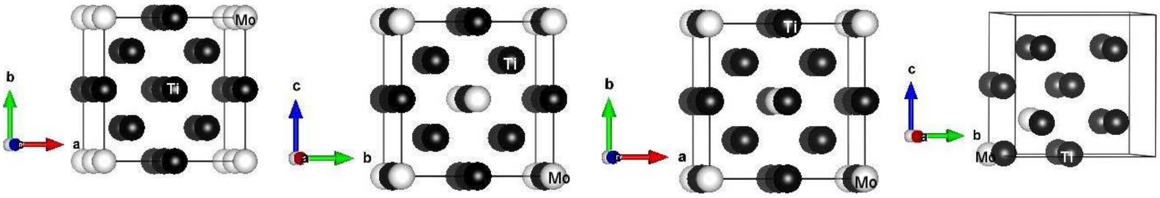

Figure 2.10 The four in equivalent configuration of Ti-25Mo alloy super cell generated by SOD technique.

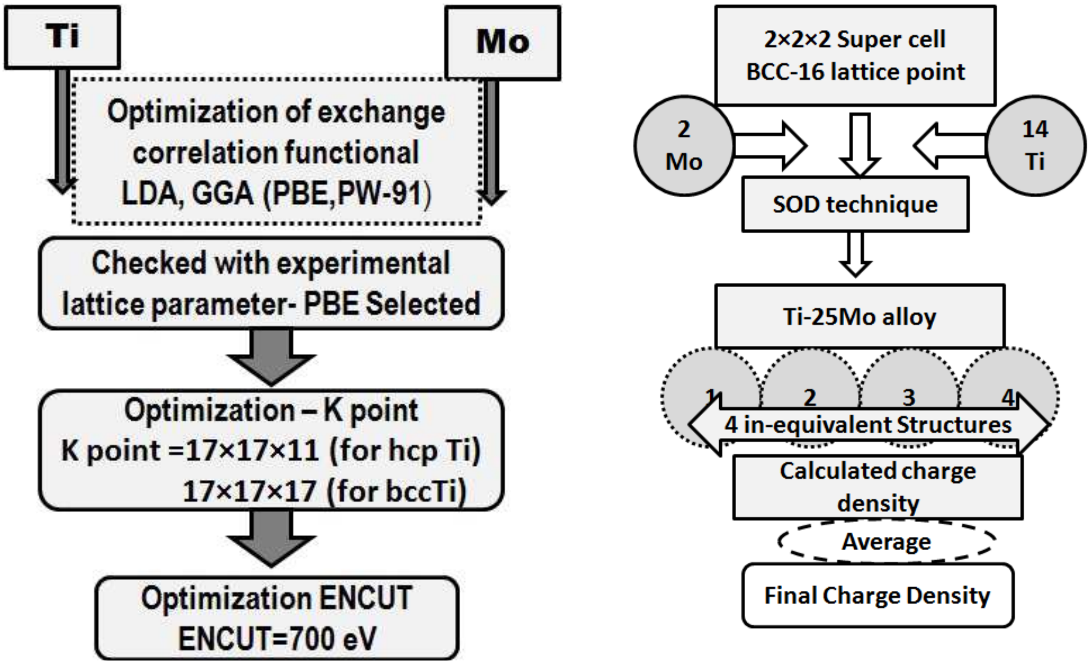

Figure 2.11 Overview of major steps involved in the DFT calculation using VASP for the identification of electronic charge density distribution of Ti, Mo and Ti-25Mo alloy.

2.6 Summary

The chapter 2 has presented the details of the various techniques used in the study: X-ray diffraction, range of microscopy methods for structure, chemistry and orientation, Miedema model and DFT calculations. The principle, operating parameters, calibration methods, and analysis procedures along with source of errors are described.

References

[1] B. Cullity, S. Stock, Elements of X-ray Diffraction, *Addison Wesley, **1956**.*

[2] A.C. Larson, R.B. Von Dreele General structure analysis system (GSAS), Los Alamos National Laboratory Report LAUR 86, **1994**.

[3] K. Momma, F. Izumi, *Journal of Applied Crystallography* **2011**, 44, 1272.

[4] J. Als-Nielsen, D. McMorrow, Elements of modern X-ray physics, John Wiley & Sons, **2011**.

[5] A. Hammersley, S. Svensson, M. Hanfland, A. Fitch, D. Hausermann, *International Journal of High Pressure Research* **1996**, 14, 235.

[6] S. Ghosh, J. Basu, D. Ramachandran, E. Mohandas, M. Vijayalakshmi, *Intermetallics* **2012**, 23, 148.

[7] J. Basu, B. Murty, S. Ranganathan, *Journal of Alloys and Compounds* **2008**, 465, 163.

[8] G. Kresse, J. Hafner, *Physical Review B* **1993**, 47, 558.

[9] P. Hohenberg, W. Kohn, *Physical review* **1964**, 136, B864.

[10] W.E. Pickett, *Computer Physics Reports* **1989**, 9, 115.

[11] G. Kresse, J. Furthmüller, *Physical Review B* **1996**, 54, 11169.

[12] J.P. Perdew, K. Burke, M. Ernzerhof, *Physical review letters* **1996**, 77, 3865.

[13] H.J. Monkhorst, J.D. Pack, *Physical Review B* **1976**, 13, 5188.

[14] R. Grau-Crespo, S. Hamad, C. Catlow, N. De Leeuw, *Journal of Physics: Condensed Matter* **2007**, 19, 256201.

CHAPTER 3

INFLUENCE OF Mo ON TRANSFORMATION PRODUCTS OF HIGH TEMPERATURE PARENT BCC β PHASE IN Ti-Mo ALLOYS

CHAPTER 3

INFLUENCE OF Mo ON TRANSFORMATION PRODUCTS OF HIGH TEMPERATURE PARENT BCC β PHASE IN Ti-Mo ALLOYS

3.1 Introduction

It is well established that there are a large number of metastable and stable phases in titanium based alloys. The nature and composition of the solutes dictate the choice of the particular phase in which the alloy exists. The energetic competition between the phases and the electronic structure variations during the alloying dictates [1] the stability of phases. During the addition of non transition elements like Al in the Ti matrix, most of the electrons prefer the lower energy band and not the Fermi level. Hence, the Ti atoms try to avoid the Al atoms creating a dilution effect and hence preserve the directionality of pre-existing Ti-Ti bond and the hcp crystal structure [2]. However addition of transition elements to Ti matrix enhances the concentration of conduction electron and so, the screening of ion cores. As a consequence, system prefers more symmetrical cubic structure. In addition, due to lattice vibration at higher temperature, the system goes through the same steps. This is the possible reason of the stabilization of bcc structure at higher temperature [2]. Thus, alloying followed by suitable heat treatments can stabilize equilibrium phases like bcc β or hcp α. Generally, the α alloys have good strength, toughness, weldability and creep resistance [1, 2]. The absence of ductile to brittle transformation makes them a suitable candidate in cryogenic applications [2].

Many studies have also reported non equilibrium phases like martensite or hexagonal omega (ω) on quenching the high temperature bcc β phase. Two types of martensites with different crystal structures namely hcp (α') and orthorhombic (α″) have been reported in Ti alloys on fast cooling from β phase field, depending on the concentration of β stabilizing solute. Generally, a concentration of Mo up to 4 wt% [3-6] promotes the hcp α' phase during quenching. Further increase in the alloying element of Mo up to 8 wt% promotes the formation of an intermediate orthorhombic structure in the binary Ti-Mo alloys [3-5, 7]. It is well established that the propensity of non diffusional transformations in Ti alloys like martensite and omega (ω) depends on the average group number or the electron/atom (e/a) ratio [8].

Another interesting athermal transformation in titanium alloys is the β→ω transformation. Of various types of transformations, the ω phase formation has been the subject of vibrant studies, due to the complex nature of the transformation and its technological importance. Depending on the mode of transformation, the ω phase can either be classified as athermal ω or isothermal ω. The reported range of ω phase formation is 10 to 18 wt% [1, 4, 9-14] in Ti-Mo alloy. The precipitation of ω increase the hardness and Young's modulus of the alloy [1, 4, 9, 15, 16] and so, normally avoided during the development of bio implant material.

Extensive literature is available with respect to the mechanism, thermodynamics, kinetics and structure–property correlation for each of the phase transformation in Ti alloys [1, 3, 4, 7-9, 12-14, 17-23]. Similar studies have been carried out in Ti-Mo system [3, 4, 7, 10, 12, 13, 17-19, 24], especially in the context of development of biomedical implants. Ti when alloyed with Mo exhibits a plethora of phase transformations upon change in cooling rate during solidification and subsequent heat treatment. The sequence and the nature of the phase transformations are altered depending upon composition and thermal treatment [1]. In this connection, development of a thermodynamic rationale to explain the phase transformation behavior is extremely important. The electron per atom is a dictating parameter for the stabilization of various non equilibrium phases like hcp α', base centered orthorhombic α" and hexagonal omega (ω) and retention of higher temperature bcc β in this alloy. Specific composition, *i.e.,* electron to atom ratio (e/a) range is reported for each type of these non equilibrium phase transformation [4, 12, 13, 18, 19]. The α′ exists for an e/a ratio of 4- 4.07 and α" up to 4.1. It is reported that the athermal ω phase is favored for e/a around 4.13 ± 0.03, and above 4.2 β phase is stabilized [1, 8]. So, based on the e/a ratio, composition is selected in order to study the non equilibrium phase transformation of Ti-Mo alloys.

The present chapter reports the influence of Mo on the transformation products of ice water quenched parent bcc β into hcp α', base centered orthorhombic α" and hexagonal omega (ω) and retention of higher temperature bcc β for four different alloys of Ti-Mo. Synchrotron XRD, which has not been extensively used in literature, was found to be useful in identifying low amounts of secondary phase like ω phase. Also, Miedema calculation was carried out for entire range of Mo concentration, to examine the stability of solid solution.

3.2 Stability of solid solution phase over amorphous phase-Miedema calculation

As has been explained in introduction, the plethora of phase transformation products of high temperature bcc β phase in Ti alloys has been understood based on various stability criteria. Several theoretical methodologies to examine the stability of phases on alloying titanium have been carried out, ranging from simple calculation of free energy of various phases to recent trends of DFT calculations [25]. In order to capture the basic concept of almost all these calculations, namely the minimization of free energy dictating the stability of a particular phase, the most fundamental, earliest model has been used in the present study. Miedema calculations have been carried out to get a preliminary idea about the stability of solid solution phase, which is presented in this section.

Miedema calculation was carried out mainly to understand (1) the thermodynamic criterion for the stability of crystalline structure of the solid solution against the amorphous phase of Ti-Mo alloy and (2) the role of Mo in stabilizing the solid solution. The formation enthalpy of crystalline structure was calculated as the sum of chemical, structural, and elastic contributions. As the amorphous phase has no crystal structure, the structural and elastic contribution to enthalpy is neglected. Instead, the enthalpy is considered as the sum of chemical enthalpy and enthalpy of fusion. The basic principle and the relevant equations for the calculation of enthalpy of formation of both amorphous and crystalline phases were discussed in chapter 2. Based on these assumptions the formation enthalpy is calculated for solid solution and amorphous phase for Ti-Mo alloy and is given in figure 3.1(a).

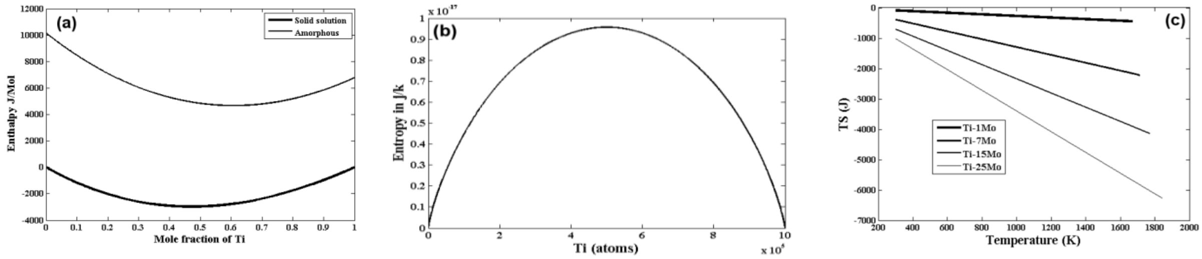

Figure 3.1 (a) Enthalpy calculation curve showing the stability of crystalline phase over amorphous phase (b) Entropy vs composition diagram showing the maximum at Ti-50Mo% and (c) Temperature Vs TS curve showing increase in slope with Mo concentration

It is observed (figure 3.1(a)) that the enthalpy of the crystalline state is always more negative than the amorphous state over the entire composition range. This necessarily means that even under the extreme conditions of cooling, crystalline phase will be stabilized over the amorphous phase. There is no tendency for formation of inter metallic compounds.

In order to assess the relative stability of different crystalline phases, an atomic array of total number of N atoms have been considered, out of which the *n* atoms of the alloying elements have been calculated and replaced in order to build the crystalline state. The mathematical representation of the statistical entropy for Ω number of available state is given by the equation.

$$S = -k \ln \Omega \tag{3.1}$$

where, *k* is Boltzmann constant.

A plot of the equation (3.1) (Figure 3.1(b)) indicates that the entropy-composition diagram is parabolic with maximum around 50 at% Mo composition. This necessarily means that with lesser and lesser alloying, second derivative of the entropy-composition curve becomes more and more positive. This is reflected in figure 3.1(c), in which it is observed that entropy diverges in the T-TS space. The difference in entropy can be taken into consideration to assess the relative stability of the phases. However, certain crystallographic order would result in similar entropy. In this case, the relative stability would strongly depend on the enthalpy, which basically originates from the change in coordination between Ti and Mo atoms. The stability of solid solution β with Mo content is experimentally evaluated in four alloys, which is discussed in detail below.

3.3 Experimental details

In order to verify stability of solid solution and absence of intermetallic compound and higher stability of β with Mo content, ice water quenching (WQ) experiments were carried out from 1173K to ~273K in Ti-xMo (x=1,7,15,25) alloys. For the confirmation of formation of ω phase, further heat treatments like quenching in ice brine solution(BQ) and Liquid Nitrogen (LN_2Q) have been carried out in addition to aging experiments at 548K for ice water quenched alloys of Ti-xMo(x=15,25wt%).

3.4 Transformation mechanisms & products in Ti-Mo alloys

3.4.1 Preliminary studies of water quenched alloys

The average grain size of Ti-xMo (x=1,7wt%) alloys is identified using stereo micrograph given in Figure 3.2 (a) and (b) respectively. Homogenization at 1173K for 6 days resulted in the formation of large β grains in ice water quenched Ti-1Mo and Ti-7Mo alloys. In both cases, the grains of the order of mm (Table 3.1) have been formed. Similar trend (Table 3.1) is noticed in Ti-15Mo and Ti-25Mo alloys at various heat treatment conditions. The unusually large β grains in Ti alloys are well documented and attributed to the low activation energy (20kJ/mol) for grain growth [26]. It is known that self diffusion is one of the factors that dictate grain growth in a system. The self diffusion coefficient of Ti in β Ti lattice is known to be very high due to the high binding energy of Ti with vacancy (2eV), low formation energy for vacancies (0.2eV) and high mobility of Ti-vacancy complex. In addition as the Mo concentration increases from 1 wt% to 25 wt% (Table 3.1), the average grain size reduces from 1.8 mm to 0.4 mm. The observed reduction in grain size is probably a manifestation of the reduction in the diffusion coefficient of Ti due to addition of Mo. Addition of Mo is known to reduce the diffusion rates [27].

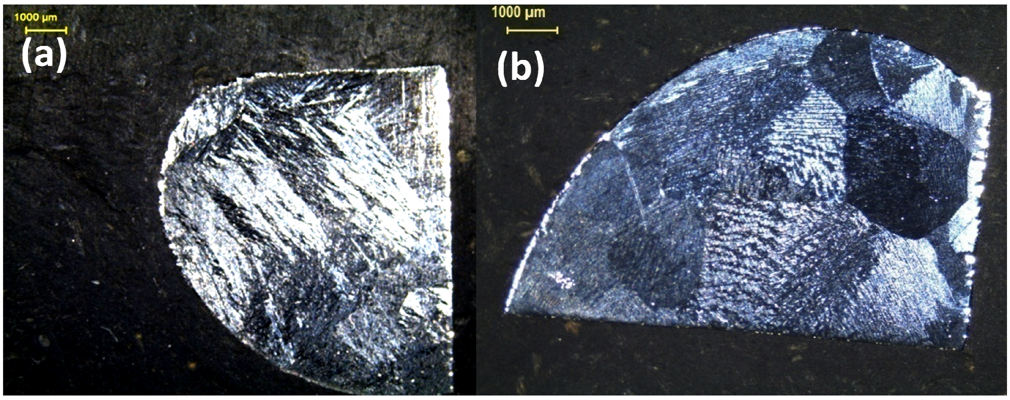

Figure 3.2 Stereo micrographs of (a) Ti-1Mo and (b) Ti-7Mo alloys showing presence of large β grains.

Table 3.1 Variation of β grain size and hardness with Mo concentration.

No.	Alloy	Grain Size(mm)	Hardness (VHN)	product
1	Ti-1Mo	1.8±0.6	188	Martensite, hcp α′
2	Ti-7Mo	1.2±0.2	244	Martensite, bco ″
3	Ti-15Mo	0.6±0.2	295	bcc β+ω
4	Ti-25Mo	0.4±0.1	250	bcc β

Optical microscopy analysis of the above samples has been carried out. Figure 3.3 shows the distribution of acicular structure consisted of plates with twin like features in the β grains of Ti-xMo(x=1,7 wt%). The absence of α precipitate along the grain boundary [figure 3.3(a)] as well as the observation of acicular martensitic structure inside the grain supports the displacive, non diffusional transformation of bcc β phase in Ti-1MoWQ and Ti-7MoWQ alloys. The size of the acicular maternsitic product also shows a gradual decrease with increase in Mo concentration from 1 to 7 wt% Mo. It is known [5] that the morphology and substructure of Ti martensites are sensitive to the concentration of the β stabilizer, which changes from lath with dislocations to plates with twins as the concentration of β stabilizer increases. The observation of plate martensite in all the alloys suggests that even a concentration of 1wt% Mo is sufficient to form a plate martensite.

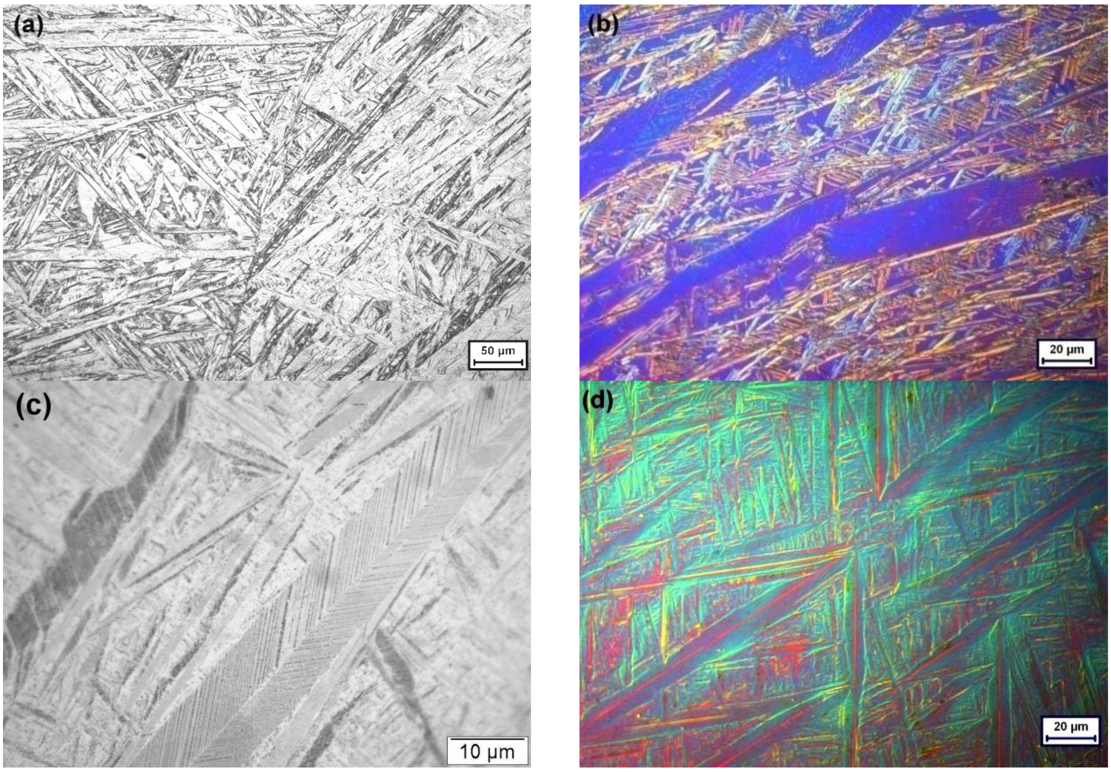

Figure 3.3 Microstructure of Ti-1MoWQ alloy β quenched from 1173K (a) with normal illumination and (b) with polarized incident light, showing fine acicular structures within large β grains. Microstructure of Ti-7Mo WQ alloy, β quenched from 1173K (c) with normal illumination and (d) in the polarized light showing twin martensitic structure. The anisotropy in the orientation of various features of martensitic structure is visible in the polarized light.

Additionally, the morphology of transformation products of Ti-7Mo alloy was also studied in detail with similar cooling rate. The ice water quenching (900K/s) promotes the formation of complete martensitic structure in this alloy as in Ti-1Mo alloy under similar cooling rate. Twin martensite formation was observed in this alloy, which is shown in figure 3.3. Similar analysis has been carried out in Ti-xMo (x=15,25 wt%)WQ alloys too (figure 3.4). However, the microstructural examination shows retention of β grains and absence of martensitic structures in these alloys. Retention of β phase above 10 wt %Mo is reported in literature [4, 12, 28].

3.4.2 Identification of transformation products of Ti-Mo alloys

In order to identify the crystal structure of transformation products, X-ray diffraction studies were carried out in Ti-xMo(x=1, 7, 15, 25)WQ alloys. Figure 3.5 (a-d) shows the X-ray diffraction (XRD) pattern of Ti-xMo(x=1, 7, 15, 25) WQ Ti-Mo alloys. An unambiguous confirmation of hcp phase in the Ti-1Mo alloy and base centered orthorhombic in Ti-7Mo alloys is evident. The results are in agreement with e/a ratio discussed in section 3.1 and the reported literature [4, 5, 12].

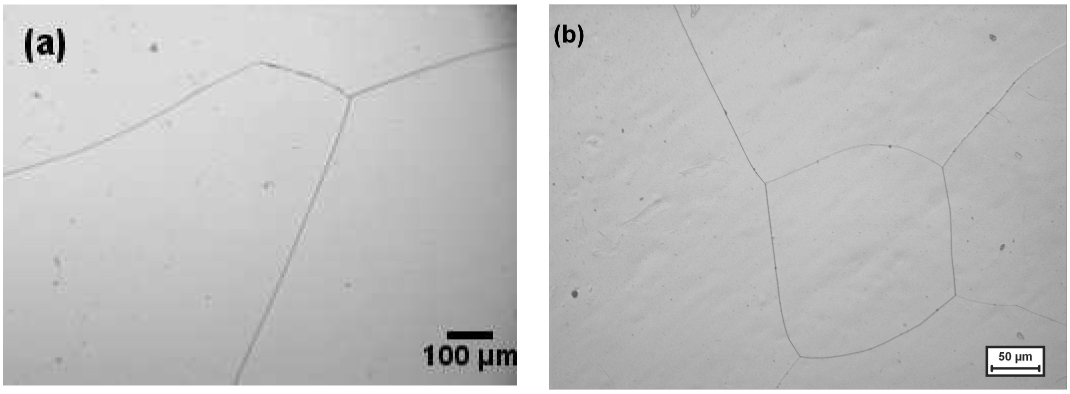

Figure 3.4 Presence of retention of bcc β grains and absence of plate like morphology in (a)Ti-15Mo WQ and (b) Ti-25MoWQ alloys.

In Ti-15Mo and Ti-25Mo water quenched alloys (figure3.5), all peaks of β phase in the range of $2\theta=20^0$ to 90^0 are present. So, presence of bcc β structure is confirmed in both these alloys. However, there is no clear distinct XRD peak of ω present in the pattern. The possibility of existence of ω phase has been predicted along with retained β structure in Ti-15Mo alloys on fast quenching experiments [4, 13, 14, 17-19], though, it is difficult to confirm experimentally the presence of ω phase in this composition range,. The challenges are due to its low amount and overlapping of strongly diffracting peaks with those of bcc β phase [4, 18, 19]. The unique peaks of ω phase distinct from the β phase are of low intensity and difficult to be observed with conventional XRD. There is hardly any literature based on conventional X-ray diffraction studies for the confirmation ω phase formation in Ti-15Mo water quenched alloys, since many reports define 15wt% as the upper limit for formation ω phase. So, the volume fraction of ω phase formed in this composition range is low. Generally TEM is preferred for the study of ω phase [1, 4, 8, 10, 13, 14, 17]. In certain cases, synchrotron based XRD is employed, to identify the ω phase in Ti alloys [18-20]. However, athermal and isothermal transformation of β→ω in Ti-15Mo alloy has not been studied so far using synchrotron based XRD. In order to promote β→ω transformation, the parent β phase was cooled at faster rates, like brine water and liquid nitrogen quenching. Present study employs synchrotron based XRD to examine the formation of ω phase and β phase stability in Ti-15 and 25 wt% Mo alloys with quenching medium as ice water, brine and LN_2 .

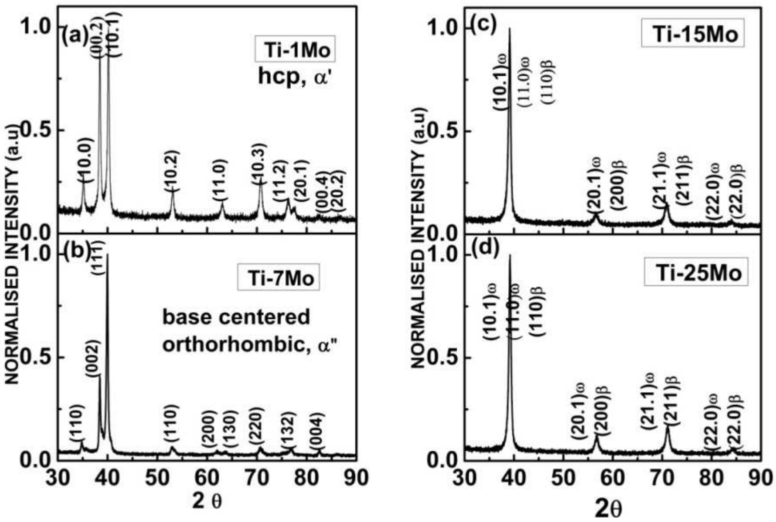

Figure 3.5 XRD patterns of β quenched (a) Ti-1Mo confirming the presence of hcp α' structure and (b) Ti-7Mo showing the presence of bco α" phase(c) Ti-15Mo and (d) Ti-25Mo showing the presence β phase.

In most cases, TEM/SAD analysis is resorted to [4], for the identification of ω. However, if the crystal structure parameters have to also be estimated, XRD is a more appropriate characterization method, especially using synchrotron XRD, which is discussed in section 3.5.

For further confirmation of finer micro structural/ crystal structure details, TEM/SAD analysis was carried out for all water quenched alloys of present interest. Figure 3.6 shows the TEM micrograph along with the SAD analysis Ti-1MoWQ alloy. The TEM micrograph is shown figure 3.6(a) further confirms the formation of twin martensite in the Ti-1MoWQ alloys. The SAD pattern (figure 3.6(b) confirms formation of hcp α′ structure. The matrix as well as twin spots are clearly visible in the micrograph. Formation of hcp α' martensite phase is in agreement with the XRD analysis and the reported literature [4, 5].

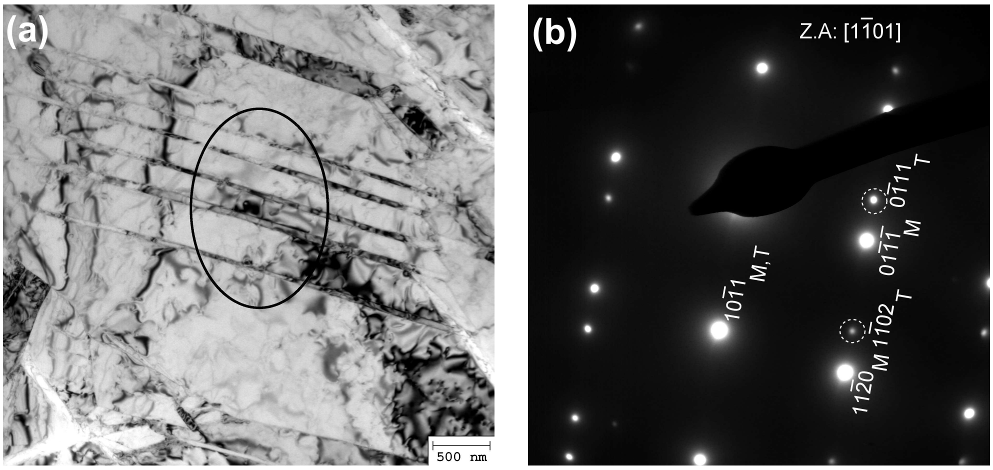

Figure 3.6(a) TEM micrograph of β quenched Ti-1Mo alloy showing plate martensite with twins(circled) and (b) SAD pattern along [1-101] zone axis of hcp (α′) structure.

TEM/SAD analysis is carried for Ti-7MoWQ alloy for further confirmation of micro structural details and phase identification. Transmission electron micrograph and Selected Area Diffraction (SAD) pattern of β quenched Ti-7Mo alloy are shown in Figure 3.7(a) and (b) respectively. Martensitic structures are visible in the TEM micrograph shown in figure 3.7(a). The SAD analysis confirmed formation of orthorhombic martensite (α″). The analysis of SAD in figure 3.7(b) confirmed the presence of α″ along [1-10] zone axis. Both these results are in agreement with conventional XRD analysis and optical microscopy studies.

Davis *et. al.* [5] reported the variations in the morphology of martensitic structures in Ti-Mo alloy.

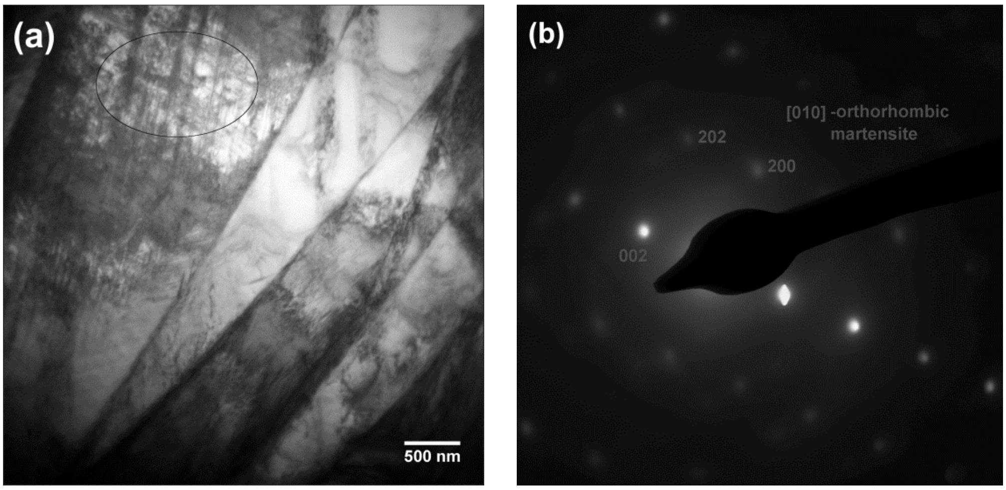

Figure 3.7(a) TEM micrograph of β quenched Ti-7Mo alloy showing plate martensite with twins(circled) and (b) SAD pattern along [010] zone axis of orthorhombic (α″) structure

Similar analysis is carried out for Ti-15Mo and Ti-25Mo alloys too. The result is shown in figure 3.8 and 3.9 respectively. TEM micrograph (figure 3.8 (a)) shows fine plate like structures. However, XRD analysis ruled out possibility of formation of such martensitic structures in Ti-15Mo alloys and Ti-25Mo alloys. So, detailed analysis was carried out using selected area diffraction to understand the system in detail. The analysis of SAD in figure 3.8(b) confirmed the presence of β phases along [013] zone axis. However, the microstructure shows the possibility of formation of α″ phase along [1-10] zone axis too. Intense diffuse scattering is observed in the SAD pattern of Ti-15Mo, in addition to the well defined spots of β. A detailed analysis of the diffuse scattering was carried out using HRTEM. The details of which will be discussed in the chapter 7. This type of diffuse scattering is well established to be characteristic of athermal ω, in many Ti and Zr based alloys [1, 4, 14, 17]. It has been understood based on “lattice collapse mechanism” and the diffuse scattering is shown to be an indication of incomplete collapse of bcc β plane. This can happen if the composition of the alloy was slightly shifted from the region corresponding to ideal ω formation. The transformation product in β quenched Ti-25Mo alloy is shown in figure 3.9(a) and (b). The bright field image is similar to that of figure3.8(a), but the plates are finer. Analysis of SAD pattern [figure 3.8(b)] confirmed the presence of β phase along [001] zone axis. It is observed that streaking in the SAD pattern continues to be present, however, to a lesser extent than in Ti-15Mo alloy. Since there is no clear distinct peak/spots in the XRD pattern analysis / SAD pattern, the unambiguous confirmation of ω phase is difficult in the Ti-15Mo alloy. For the unambiguous confirmation of expected ω phase in Ti-15Mo and for the identification of plate morphology observed in TEM micrograph, synchrotron XRD experiments were carried out.

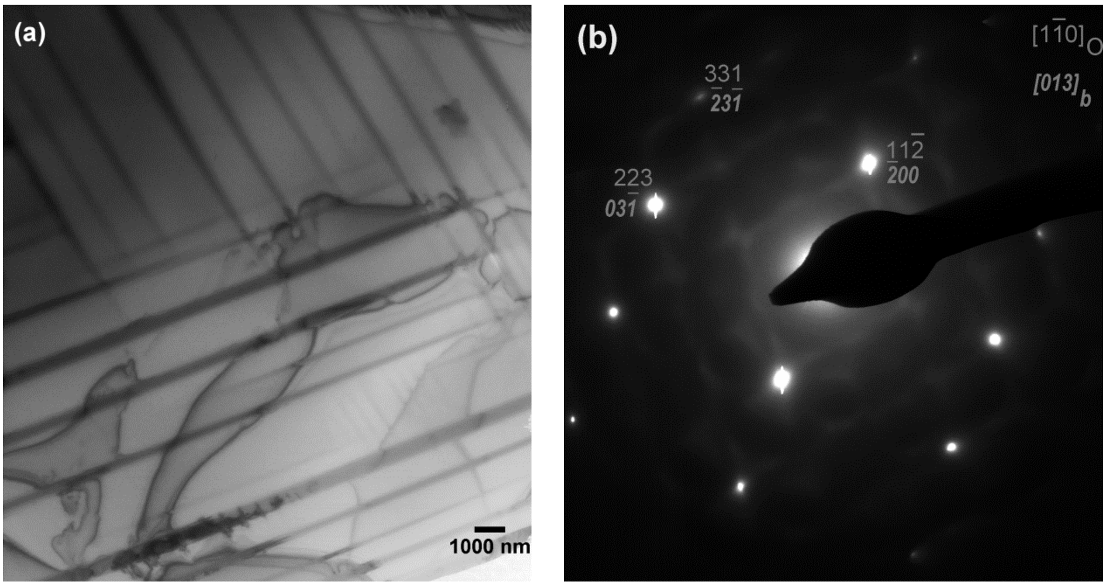

Figure 3.8 (a) TEM micrograph of β quenched Ti-15Mo alloy showing fine plate of α″ and (b) SAD pattern along $[1\text{-}10]_{\alpha''}$ *and* $[013]_{\beta}$ *zone axis and curvilinear streaking due ω phase.*

The brilliance of synchrotron source is ~ 10 orders of magnitude higher than the conventional source [29], enabling the identification of phases of volume fraction less than 1%. Synchrotron XRD pattern of Ti-15MoWQ alloy is given in figure 3.10 (a) confirms the presence of ω phase. The unique peak of ω corresponding to (11.2) plane is clearly visible in the pattern. However, there is no such indication of ω phase formation in Ti-25MoWQ alloy. Also, there is no signature for the presence of phases like orthorhombic α″ as suspected from the TEM and SAD analysis. Reason for the martensitic structures in the TEM/SAD analysis is discussed in section 3.5.4.

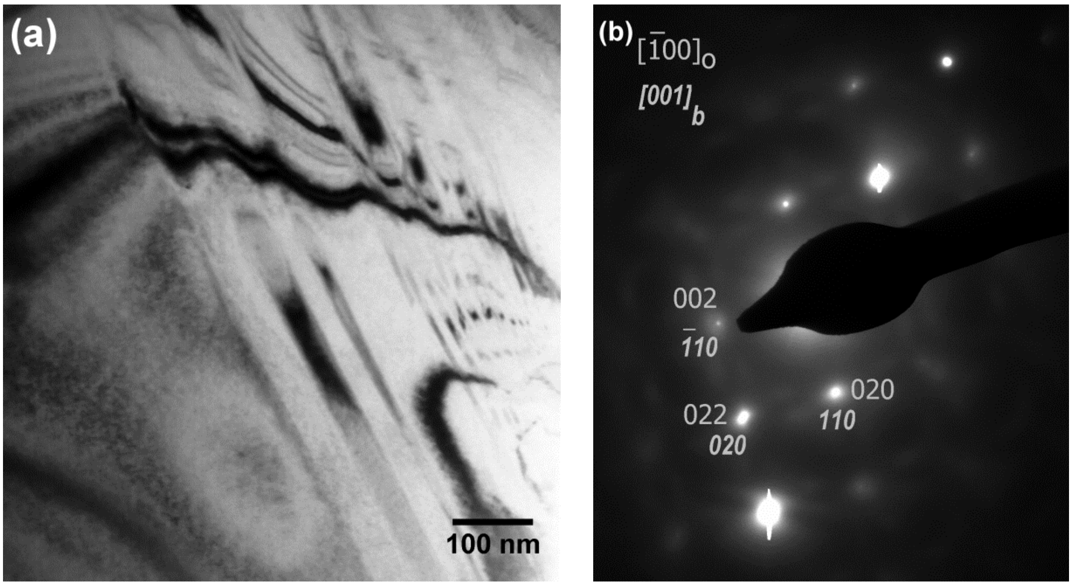

Figure 3.9 (a)TEM micrograph of β quenched Ti-25Mo alloy showing fine plate of α″ and (b) SAD pattern along [-100]$_{\alpha''}$ and [001]$_{\beta}$ zone axis and streaking due ω phase to a lesser extent than figure 3.4(b)

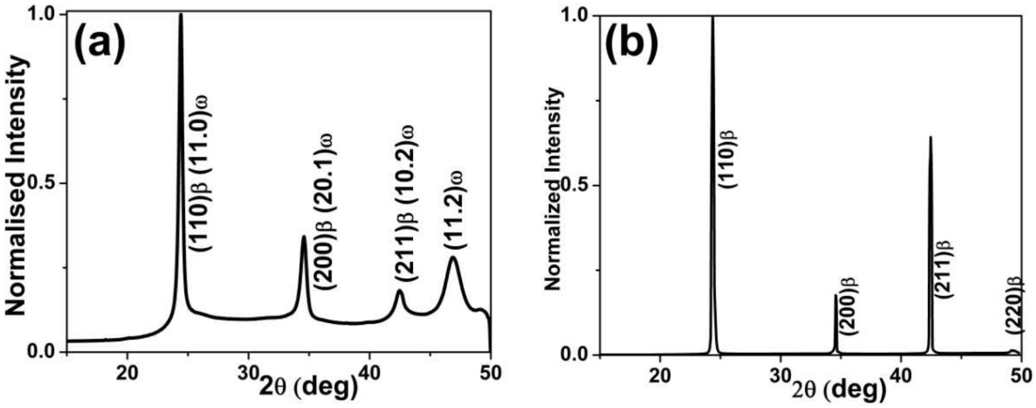

Figure 3.10 Synchrotron XRD pattern showing the formation ω phase in (a) Ti-15MoWQ alloy and its absence in (b) Ti-25MoWQ alloy with bcc β phase. No indication for the formation of orthorhombic α″ structure in both the alloys.

3.5 Effect of heat treatment on the ω phase formation.

Further quenching experiments were carried out for Ti-xMo alloys (x=15, 25wt%) to answer the following questions

- Does ω phase formation occur in Ti-xMo (x=15,25) alloys on various quenching conditions?
- Does ageing promote the formation of ω?
- Does concentration of Mo and quenching conditions influence the ω phase formation?
- Does any martensitic transformation occur in Ti-xMo (x=15, 25 wt%) alloys as observed in TEM micrograph in any of the heat treatment conditions?

3.5.1 Influence of quenching condition on the ω phase formation

For the confirmation of β phase stability in Ti-xMo(x=15, 25wt%) and to verify if β→ω transformation is influenced by the rate of cooling, the experiment was repeated by increasing the cooling rate through quenching the alloys from the β phase field in iced brine (NaCl + H2O) solution and liquid nitrogen (LN_2). In addition, aging experiments in the α+β phase field at 748K/1day was carried out for ice water quenched alloy.

Figure 3.11 (a) shows the optical micrograph of Ti-15MoLN$_2$Q alloy. β grains of order of ~ mm are visible in the micrograph. Conventional XRD experiments were carried out for identification product phases. The data acquisition is extended to 3 h for the identification of low intensity peaks. However, XRD pattern given in figure 3.11 (b) shows no clear evidence for the formation of ω phase. No unique peaks of ω are identified in the lab XRD pattern. So, synchrotron XRD experiments were carried out. The synchrotron XRD pattern of Ti-15MoLN$_2$Q alloy is given in figure 3.11(c) confirms the unique ω reflections corresponding to (00.1), (11.1), (00.2), (11.2) planes.

The conventional XRD results in Ti-Mo alloys reported in literature have not been able to confirm the β→ω transformation in compositions around 15 Mo [4, 12, 13]. Earlier literature reported retention of β phase alone in as cast structure of Ti-xMo (x=15, 20 wt%) [3, 21], and the quenched samples of Ti-xMo (x=10 to 20 wt%) [12]. In fact, Mo equivalent of a Ti alloy is defined based on a critical concentration of 10 wt% of Mo to completely stabilize β phase on β quenching [28]. However, Ying Long Zhou *et. al.* [22] reported the presence of ω phase in the quenched sample of Ti-10Mo and its absence in Ti-20Mo using conventional XRD. Wen Fu Ho[12] studied Ti-xMo (x=7.5, 9, 10, 12.5, 15, 17.5, 20) alloys in detail using conventional XRD and TEM. They could confirm the presence of ω phase in Ti-xMo (10,12.5 wt%) and its absence above 15 wt% of Mo using conventional XRD. But, detailed electron diffraction analysis of the above mentioned alloys confirmed the presence of sharp ω reflections in Ti-10Mo and diffuses streaking in Ti-20Mo [13]. Devraj *et. al.* [10] reported presence of ω phase in Ti-9 at.% Mo in as quenched as well as annealed samples. In most cases, conventional XRD analysis is not sufficient for unambiguous identification of ω phase. Therefore, electron diffraction is resorted to.

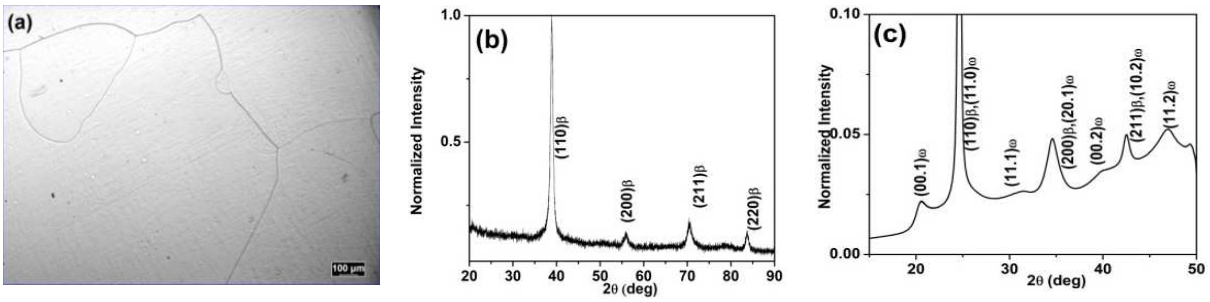

Figure 3.11 (a) Optical micrograph showing large β grains and (b) conventional lab XRD pattern showing the absence of unique ω peaks (c) Synchrotron XRD pattern confirming the formation of ω phase in Ti-15MoLN$_2$Q alloy.

Quenching experiments are carried out in Ti-15Mo alloys again with brine solution. The trend was observed to be similar. As in ice water quenched and LN2Q Ti-15Mo alloy, optical micrograph showed large β grains. No clear evidence for the formation of ω phase in conventional lab XRD pattern [figure 3.12(a)]. Only synchrotron XRD experiments could confirm the formation of ω phase [figure 3.12 (b)]. The alloy shows unique peaks of ω phase corresponding to (00.2), (11.2) planes in addition to the overlapping peaks with β phase.

From these three results, it can be concluded that irrespective of quenching conditions, a low volume fraction of athermal ω phase formed in Ti-15Mo alloys, which could not be detected using conventional XRD . However, synchrotron XRD and TEM/SAD could provide evidence for formation of ω phase.

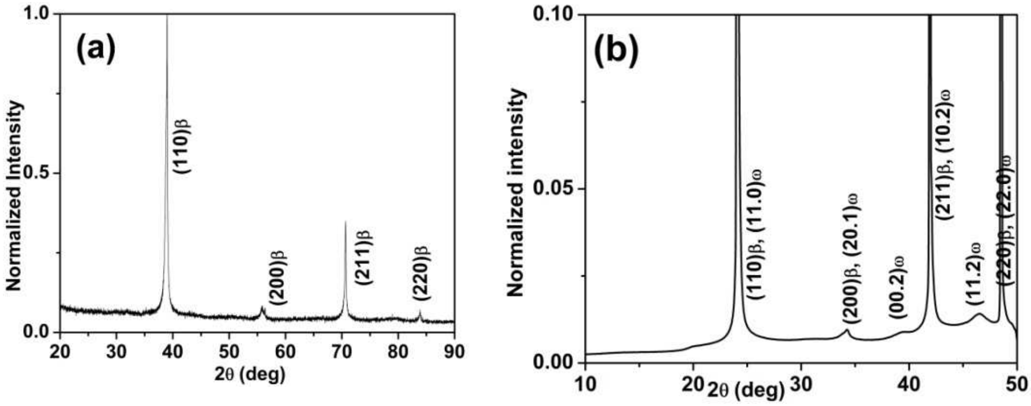

Figure 3.12 (a) Conventional XRD pattern showing the absence of ω phase and (b) Synchrotron XRD pattern confirming the formation of ω phase in Ti-15MoBQ alloy.

3.5.2 Effect of aging on the ω phase formation

In order to answer the second question, aging was carried out in Ti-15MoWQ alloy at 748K/24hours. Figure 3.12 (a) and (b) shows the optical micrograph and conventional lab XRD pattern respectively in Ti-15Mo alloy after aging. Optical micrograph in figure 3.13 (a) shows the presence of α plate. The conventional XRD analysis unambiguously confirmed the formation of ω phase along with α and β phases. This suggests the formation of higher volume fraction of ω phase in the aged alloy in comparison to quenched Ti-15Mo alloy. The thermal activation due to aging promotes the kinetics and β→ω transformation. Detailed study is carried out to understand the bonding and crystallographic details of constituent phases and is discussed in detail in chapters 4 and 7.

The synchrotron XRD results [figure 3.13(c)] are also in agreement with the above findings. More number of unique diffraction peaks of ω (11.1), (11.2), (30.1) is observed in the XRD pattern, in contrast to the results of quenched alloys discussed earlier. This observation suggests that ageing promotes the growth of ω phase, as reported in literature, based on electron microscopy studies in Ti-Mo system [1, 8, 10].

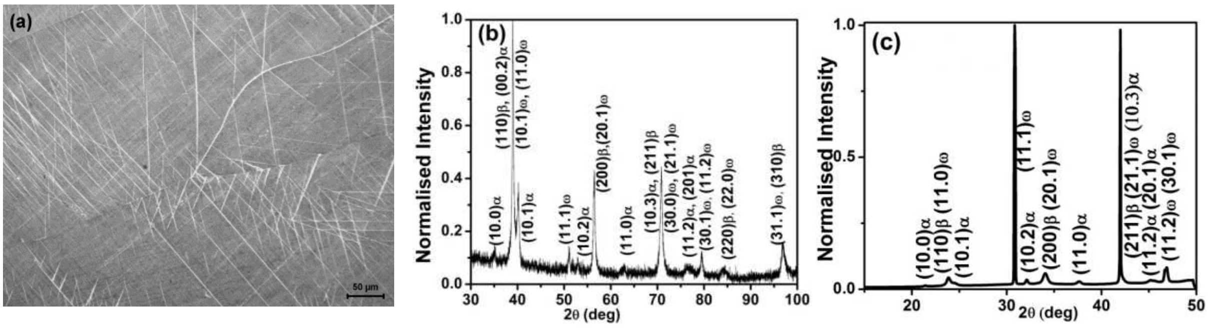

Figure 3.13 (a) Optical micrograph of Ti-15Mo alloy aged 748K/24 hours after ice water quenching showing the presence of α plate. (b) Conventional and (c) synchrotron XRD pattern of the same alloy showing the formation of α, β and ω phases.

The intensity ratio of peaks in synchrotron XRD pattern was found to be not following the ratios reported in ICDD even in the alloy with single phase of α or β, which could be due to the larger grain size of the alloys than the beam size, texturing and static sample during data acquisition. Estimation of the low volume fractions of ω phase requires controlled experiments with optimized geometry of the samples, and recording of diffracted intensity. Hence, quantification of the ω phase volume fraction was not attempted in this study for any of the alloys. In addition to that, no conclusion has been arrived out based on the intensity values of synchrotron XRD peak other than the mere identification of various phases present in the each sample with Δθ allowance of 0.2°, for peak identification.

3.5.3 Influence of Mo concentration and heat treatment on ω phase formation.

Conventional and synchrotron XRD experiments were carried out in Ti-25Mo alloys also for various quenching and aging conditions in order to identify the possibility of formation of ω phase. Both conventional and synchrotron XRD analysis shown in Figure 3.14 (a and b) suggest only the presence of β phase and ω phase was not observed in brine quenched, LN_2Q and aged alloys. From this analysis, it can be concluded that irrespective of heat treatment (WQ, BQ, LN_2Q or aging at 748K/24hours), ω phase formation occurs in Ti-15Mo alloy along with β phase. In contrast, the β phase is fully stable in Ti-25Mo alloy.

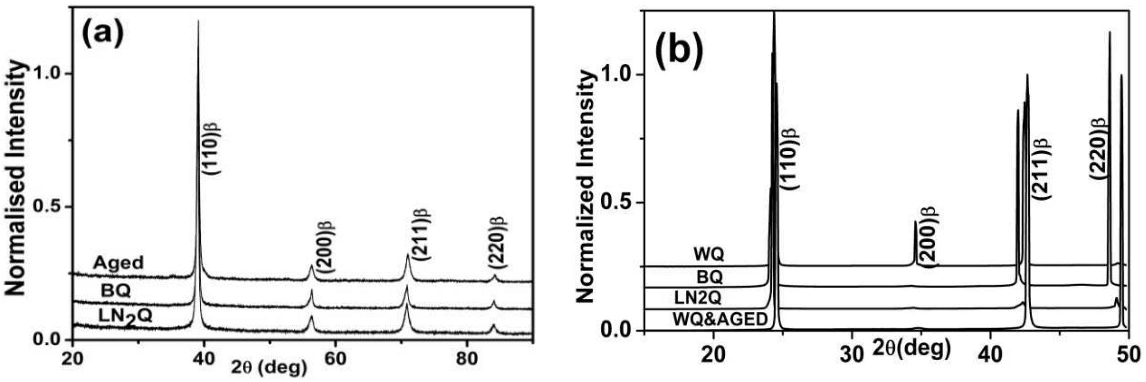

Figure 3.14 (a) Conventional (b) Synchrotron XRD pattern of Ti-25Mo alloy for various quenching and aging conditions confirming 100% retention β phase and absence of ω phase formation.

3.5.4 Martensitic transformation in Ti-15Mo and Ti-25Mo alloys

The fourth point addressed in this experiment is the identification of the possibility of formation of martensitic structures in Ti-xMo (x=15, 25wt%) alloys which is observed in TEM/SAD analysis. In both Ti-x Mo(x=15, 25 wt%) alloys, fine plate like features were visible in TEM micrograph. However, the conventional and synchrotron XRD experiments did not confirm the possibility of formation of the same. So, experiments were repeated for Ti-15MoWQ alloys. During the certain attempts, the optical micrograph could identify regions with plate like morphology (see figure 3.15). Detailed analysis of the plate like structure in TEM micrograph was carried out. We could index SAD pattern for both fcc as well as base centered orthorhombic structure. Hammod and Kelly [30] reported formation of such strain induced martensite in the thin TEM samples of Ti-Mo alloys. Such formation of fcc martensite with a ~4.5 Å has been reported [30] to be observed in TEM studies of quenched Ti-20%V, Ti-11.6% -15%Mo and Ti-6%-20%Cr alloys, all of which are β or β+ω alloys in the bulk form as revealed by XRD. In such cases, they have reported formation of fine features on the optical micrograph of the thin foil around the thinned edges of the material. Present examinations also revealed the same. So, the fine structures in the TEM micrograph is an artifact formed during the sample preparation, which were minimized with more care during specimen preparation.

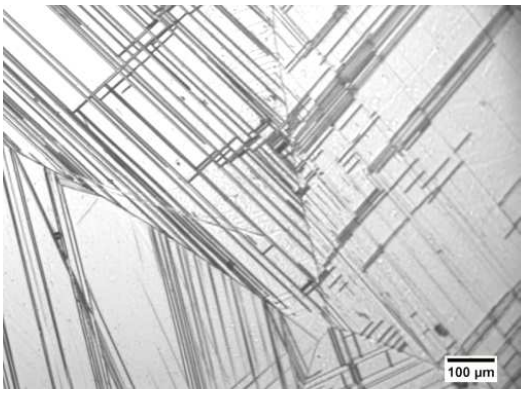

Figure 3.15 Plate like morphology observed in Ti-15MoWQ alloy.

3.6 Influence of Mo concentration and crystal structure on the microhardness of Ti-Mo alloys

Microhardness measurements were carried out in all the alloys of Ti-x Mo (x=1, 7, 15, 25 wt%) using an external load of 100g, to identify the contribution of transformation products and amount of Mo on the hardness values. Table 3.1 shows the microhardness of ice water quenched Ti- Mo alloys. Generally, a higher hardness is expected in martensite due to the presence of dislocations. But, present results do not follow the general trend. From Table 3.1, it is clear that there is a marginal increase in the microhardness values with Mo concentration, except in 15wt%Mo. The increase in hardness with Mo concentration is probably due to the reduction in grain size (see Table 3.1). The higher hardness in Ti-15Mo [13] alloy is due to the presence of fine ω phase formation[1, 4, 13]. This is in agreement with reported literature.

3.7 Summary

From the microstructual and XRD analysis of Ti-Mo alloys, the following conclusions have been arrived at.

1. Miedema calculation confirms the stability of solid solution over the amorphous phase, for all composition of Mo.

2. The higher solutionising treatment time of 6 days at a temperature of 1173K resulted in formation of coarse grains, with size of few mm in all the water quenched alloys of Ti-Mo.
3. The grain size shows a gradual decrease as the Mo content increases due to reduction in diffusion coefficient.
4. Martensitic structure is formed in Ti-1Mo and Ti-7Mo alloys at fastest cooling rate of 900K/s.
5. The synchrotron XRD experiments in Ti-15 and 25 % Mo alloys enabled the unambiguous identification of transformation products of high temperature bcc β phase.
6. These experiments confirmed the formation of both athermal and isothermal ω phases in Ti-15Mo.
7. Irrespective of heat treatment, β phase is stable in Ti-25Mo alloy.
8. The threshold concentration of Mo to stabilize bcc β phase is between 15 and 25 wt% of Mo.
9. The transformation products in Ti-Mo alloys during ice water quenching is as follows**.**

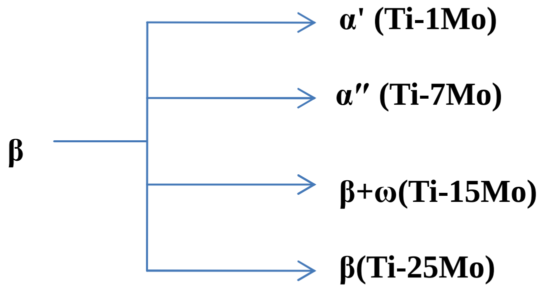

10. The transformation product in Ti-15Mo aged alloy is α+β+ω.
11. Due to decrease in grain size, a gradual increase in microhardness is noticed with respect to Mo concentration.
12. The highest hardness is observed in Ti-15Mo alloy due to ω phase formation.

References

[1] S. Banerjee, P. Mukhopadhyay, Phase transformations: examples from titanium and zirconium alloys, Elsevier, 2010.

[2] G. Welsch, R. Boyer, E. Collings, Materials properties handbook: titanium alloys, ASM international, 1993.

[3] N.T. Oliveira, G. Aleixo, R. Caram, A.C. Guastaldi, *Materials Science and Engineering: A* **2007**, 452, 727.

[4] M. Sabeena, R. Mythili, J. Basu, M. Vijayalakshmi, *Transactions of the Indian Institute of Metals* **2013**, 66, 401.

[5] R. Davis, H. Flower, D. West, *Journal of Materials Science* **1979**, 14, 712.

[6] H. Flower, S. Henry, D. West, *Journal of materials science* **1974**, 9, 57.

[7] Y. Mantani, Y. Takemoto, M. Hida, A. Sakakibara, M. Tajima, *Materials transactions* **2004**, 45, 1629.

[8] E.W Collings, Applied superconductivity, metallurgy, and physics of titanium alloys: Vol. 1: Fundamentals Pentium Press, New York, **1986**.

[9] D. Banerjee, J.C. Williams, *Acta Materialia* **2013**, 61, 844.

[10] A. Devaraj, S. Nag, R. Srinivasan, R. Williams, S. Banerjee, R. Banerjee, H. Fraser, *Acta Materialia* **2012**, 60, 596.

[11] A. Devaraj, R. Williams, S. Nag, R. Srinivasan, H. Fraser, R. Banerjee, *Scripta Materialia* **2009**, 61, 701.

[12] W. Ho, C. Ju, J.C. Lin, *Biomaterials* **1999**, 20, 2115.

[13] W. Ho, *Journal of Medical and Biological Engineering* **2008**, 28, 47.

[14] D. De Fontaine, N. Paton, J. Williams, *Acta Metallurgica* **1971**, 19, 1153.

[15] M. Geetha, A.K. Singh, R. Asokamani, A.K. Gogia, *Progress in Materials Science* **2009**, 54, 397.

[16] Y. Hao, S. Li, S. Sun, C. Zheng, R. Yang, *Acta biomaterialia* **2007**, 3, 277.

[17] M. Sabeena, A. George, S. Murugesan, R. Divakar, E. Mohandas, M. Vijayalakshmi, *Journal of Alloys and Compounds* **2016**, 658, 301.

[18] M. Sabeena, S. Murugesan, R. Mythili, A. Sinha, M. Singh, M. Vijayalakshmi, S. Deb, *Transactions of the Indian Institute of Metals* **2015**, 68, 1.

[19] M. Sabeena, S. Murugesan, R. Mythili, A. Sinha, M. Singh, M. Vijayalakshmi, S. Deb, Influence of Mo in β phase stability of Ti-Mo system: Synchrotron based XRD studies, in: Solid State Physics: Proceedings of the 58th DAE Solid State Physics Symposium 2013, AIP Publishing, 2014, pp. 119.

[20] F. Sun, J. Zhang, M. Marteleur, T. Gloriant, P. Vermaut, D. Laillé, P. Castany, C. Curfs, P. Jacques, F. Prima, *Acta Materialia* **2013**, 61, 6406.

[21] Y.-y. Chen, L.-j. Xu, Z.-g. Liu, F.-t. Kong, Z.-y. Chen, *Transactions of Nonferrous Metals Society of China* **2006**, 16, Supplement 2, s824.

[22] Y.-L. Zhou, D.-M. Luo, *Materials Characterization* **2011**, 62, 931.

[23] T. Ahmed, H. Rack, *Materials Science and Engineering: A* **1998**, 243, 206.

[24] J.R.S. Martins Jr, C.R. Grandini, *Journal of Applied Physics* **2012**, 111, 083535.

[25] J. Kohanoff, Electronic structure calculations for solids and molecules: theory and computational methods, Cambridge University Press, 2006.

[26] F. Gil, D. Rodriguez, J. Planell, *Scripta metallurgica et materialia* **1995**, 33, 1361.

[27] Y. Liu, L. Zhang, D. Yu, *Journal of phase equilibria and diffusion* **2009**, 30, 334.

[28] D. Eylon, R.R. Boyer, D.A. Koss, Beta Titanium Alloys in the 1990's, in, Warrendale, PA (United States); Minerals, Metals and Materials Society, 1993.

[29] J. Als-Nielsen, D. McMorrow, Elements of modern X-ray physics, John Wiley & Sons, 2011.

[30] C. Hammond, P. Kelly, *Acta Metallurgica* **1969**, 17, 869.

CHAPTER 4

CRYSTAL STRUCTURE AND BONDING CHARACTERISTICS OF TRANSFORMATION PRODUCTS OF BCC β IN Ti-Mo ALLOYS

CHAPTER 4

CRYSTAL STRUCTURE AND BONDING CHARACTERISTICS OF TRANSFORMATION PRODUCTS OF BCC β IN Ti-Mo ALLOYS

4.1 Introduction

Emergence of computational capabilities in recent years has enabled in-depth insight into the stability of crystal structure, bonding nature and their influence on mechanical properties in titanium alloys [1-3]. Initially, the stability of various phases with alloying addition was understood in terms of electrons to atom ratio (e/a) and d-electron occupancy. However, inability of e/a to capture the intrinsic mechanism of elastic behavior and the need for better description than e/a, were realized. Subsequently, in-depth understanding of role of solutes was achieved in terms of energetics, density of states, Fermi energy and Brillouin zone. First principle calculations [1] have provided further insight by relating the compromise between covalent and metallic bonding nature to be the origin of the stability of the metastable phases. It is demonstrated that bcc β phase is stabilized when d-electrons start filling the anti-bonding states, on adding solutes rich in d electrons. Criteria for the mechanical stability of phases and its correlation to e/a and the modulus, have been arrived at [2].

Experimentally, 3-Dimensional Atom Probe (3-DAP) [4], electron microscopy [5-8], Rietveld [9-12] analysis of XRD using conventional [7, 8, 10, 11, 13] and synchrotron radiation [14-18] and neutron diffraction [19] have been used extensively to study the structure and stability of crystal structure in titanium and its alloys. There are many overviews [5, 20, 21] and books [6] available on phase transformation mechanisms and structure-property correlation studies in titanium alloys.

Most of the studies are based on first principle calculations, with respect to bonding characteristics in titanium alloys. Saravanan *et. al.* [12] reported the bonding nature and charge density distribution of elemental Ti based on maximum entropy method (MEM). However, similar experimental reports explaining the role of alloying elements in altering the bonding characteristics of titanium alloys have not been reported so far to the best of the existing knowledge.

Of the various titanium alloys, Ti-Mo, alloy of interest to the present study, has been extensively studied in the recent past, due to its potential biomedical applications [2, 3, 13, 22-25]. Formation energy calculations for the all possible crystal structures, α', α″, ω and β in Ti-Mo system, have yielded ranges of molybdenum for stability of various crystal structures, which agree well with the experimental reports. First principle calculations have been carried out to evaluate the cohesive energy of formation, optimum volume and lattice parameter [2, 3] of equilibrium bcc β phase in Ti-Mo alloys. Criteria for the “mechanical stability” of the various phases has been arrived at, based on estimation of Young’s modulus and elastic constants for different molybdenum content. Structure-property correlations of β phase alloys of Ti-Mo system have been carried out mainly to evaluate their suitability for bio-medical applications [8, 13, 17, 22, 26, 27]. The relation between the low modulus and ductility to the charge density distribution has been established using first principles pseudo potential plane wave method [28] in β phase titanium alloys. Rietveld analysis of conventional and synchrotron XRD studies in Ti-Mo alloys has yielded information on unit cell dimensions of various phases [11] and micro structural parameters like domain size and micro-strain. However, detailed Rietveld analysis of the crystal structure and bonding characteristics in Ti-Mo alloys, have not been reported so far to the best of the author’s knowledge. Hence, the present chapter, attempts to evaluate unit cell dimensions, atom positions, bond length, co-ordination number and electron density distribution in the unit cell of hcp α', orthorhombic α″ and bcc β in four Ti-Mo alloys. In addition, the role of molybdenum on stability of the crystal structure and nature of bonding is understood in terms of the nature of Mo atoms.

The salient features of the present chapter are as follows: Rietveld analysis of X-ray diffraction patterns of α', α″ and β phases of four alloys of Ti-Mo has been carried out to refine their crystal structures and understand their nature of bonding. The addition of molybdenum to titanium is found to shift the stability of crystal structure from hcp to orthorhombic to bcc, as expected. The unit cell dimensions and the atomic positions of α', α″ and β phases were evaluated, with good reliability indices. The reduction in unit cell dimensions and its volume, bond length and co-ordination number with addition of molybdenum is consistent with the reduced size of solute atom. The orthorhombic α″ phase, a transition phase with a minor distortion of hcp α', is found to be closer to α' than β phase, based on the orthorhombicity (b/a) and the volume of equivalent orthorhombic unit cells of the phases and the atomic shuffle y in 4c Wyckoff positions along 'b' axis ([010] direction in (100) plane) of α″ phase. The Fourier electron density contour maps suggest that the bonding in all phases is predominantly metallic. However, addition of molybdenum delocalizes the spatial distribution of charge density, suggesting an enhancement of metallic character. Anisotropy in charge density was observed along <010> and <011> directions in (100) plane in orthorhombic α″ phase of Ti-7Mo alloy. This offers the direct evidence for the origin of anisotropy in the values of elastic constants, reported in literature.

The organization of the chapter is as follows. Section 4.2 discusses the detailed Rietveld refinement of conventional XRD of hcp α phase in Ti and Ti-1Mo (section 4.2.1), bcc β phase in Ti-15Mo and Ti-25Mo (section 4.2.2) and orthorhombic structure inTi-7Mo (section 4.2.3) to arrive at accurate crystal structure details: lattice parameters, atom positions, unit cell volume and density. In addition, section 4.2.4 discusses about the influence of molybdenum on bond length and co-ordination number of all these phases. The bonding characteristics in Ti-Mo alloys are discussed in Section 4.3 in the same order as above. The bonding nature in hcp α phase of Ti and Ti-1Mo is discussed in subsection 4.3.1, followed by bonding nature in bcc β phase of Ti-xMo (x=15, 25) in section 4.3.2 and that of orthorhombic α″ structure in Ti-7Mo in section 4.3.3. The role of molybdenum on structural parameters and bonding nature is discussed in section 4.3.4. The above results are discussed in section 4.4 in the light of three major themes:

(a) α″: transition phase of α' and β, in the section 4.4.1

(b) Influence of charge density distribution in anisotropy of orthorhombic α″ phase in section 4.4.2 and

(c) Influence of crystal structure and bonding on modulus of Ti-Mo alloys in section 4.4.3.

Section 4.5 summarizes the major findings of the present chapter on crystal structure and bonding of all product phases of bcc β phase in Ti-Mo system.

4.2 Crystal Structure analysis using Rietveld method

In chapter 3, using conventional and synchrotron XRD and TEM [7, 14, 15] the high temperature bcc β phase of four alloys of Ti-Mo, was reported to transform to several metastable product phases, during different types of treatments. The present chapter examines the crystallographic and bonding characteristics of the product phases. An attempt is made to understand the influence of addition of molybdenum in these characteristics.

4.2.1 α'-hcp phase in Ti and Ti-1Mo alloy

The equilibrium hcp phase in pure Ti and non-equilibrium hcp phase in Ti-1Mo are referred to as α & α′ respectively in literature. Since both are crystallographically similar, with small difference in unit cell dimensions, the hcp phases will be referred as α' hereafter in this chapter. The experimental XRD patterns from pure titanium and Ti-1Mo, both with hcp phase, were analysed as explained earlier. The initial structural model for the hcp α'- phase of pure Ti and Ti-1Mo are as follows (ICDD # 00-044-1294)[29]: space group symmetry: P63/mmc, Laue symmetry: 6/mmm, lattice parameters as a=b=2.9505 and c=4.6826Å and atomic position as 1/3, 2/3, 1/4. In Ti and Ti-1Mo, (00.2) peak was found to have high intensity due to preferred orientation and hence refinement was carried out using the March-Dollase formalism [30, 31]. Intensity of each (hk.l) plane was refined to account for texture in both elemental Ti and Ti-1Mo alloy. In the final cycle of refinements, the anisotropic temperature factor was also accounted for, with constrained model. In the constrained model, the atomic co-ordinates were occupied by "pseudo atom", whose proportion is same as at% of each element in the alloy. The thermal vibration of the most dominant element *i.e,* Ti is chosen as the basis for the calculation of isotropic temperature factor (U^{iso}) of pseudo atom. The refinement included presence of transformation strain also. However, it was found during refinement that the change in unit cell parameters with and without strain was not significant.

The typical experimental and refined profiles along with the difference map, for pure Ti and Ti-1Mo alloy water quenched from β phase field, are shown in figure 4.1(a) and (b). The accuracy of refinement is evident from the difference curve between the observed and calculated intensities, which is almost a straight line. However, the difference curve shows that there is a measurable residue around 35-40 degrees. Repeated refinements suggest that this is the best possible fit, as also revealed by fitness parameters. R indices of the refinement are as follows: Rp -5.87, wRp - 7.71, GOF-1.

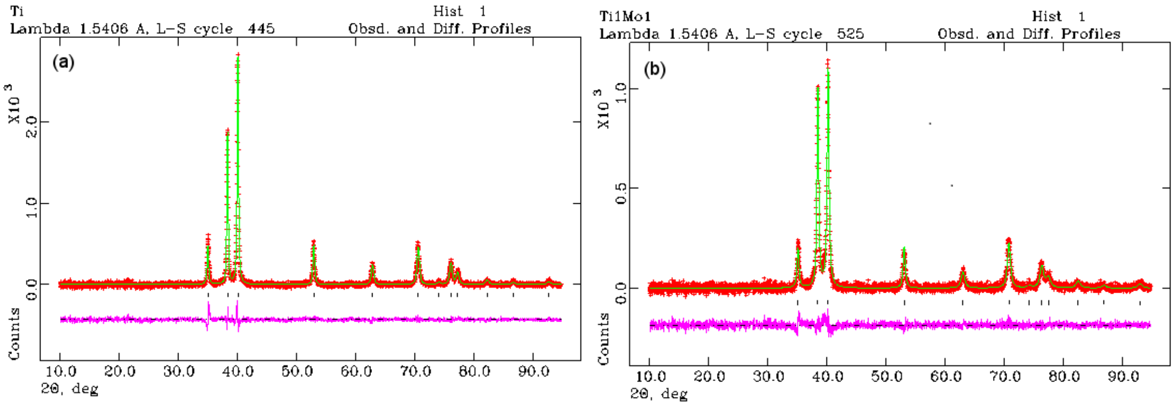

Figure 4.1 Rietveld plot of hcp α' in (a) Ti and (b) Ti-1Mo. The dots represent the experimental data and the solid lines show calculated profile. The small bars close to the profile indicates the Bragg peak positions. The difference plot is marked as the solid line in the lower part of the figure.

Table 4.1 lists the crystallographic data for elemental Ti and Ti-1Mo alloy. As expected [47], the *c/a* ratio of elemental titanium is 1.5877, which is less than the ideal value of 1.6333. It is observed that the addition of Mo to Ti further reduces the lattice parameters of hcp Ti. The reduction in the value of '*c* 'is more compared to '*a*'. While the '*c*' value has reduced by 0.86%, the '*a*' value is reduced only by about 0.39%. Consequently, the *c/a* ratio decreases from 1.5877 to 1.5853 by addition of 1wt% Mo to Ti, leading to compression of unit cell volume by 0.45%. The observed reduction in c/a in the present study is in agreement with the available literature of Ti based binary alloys using first principle calculations [1]. This can be understood directly as due to the smaller size of solute atom352 for pure Ti and Rp - 6.97, wRp - 9.00, GOF-1.13 for Ti-1Mo.

The estimation of unit cell dimensions for hcp α phase, in Ti based alloys [10, 32, 33] and Ti-Mo [11, 34-36] has been extensively carried out in literature (Figure 4.2). However, the detailed Rietveld analysis studies are much less [11, 19, 37, 38]. Of these, only few studies report the values of Rp and wRp in the range, 8.53 to 14.89 [11], *i.e.*, higher than those of present studies. The values of unit cell dimensions of different phases of Ti-Mo alloys from the present studies (Figure 4.2) compare reasonably well with reported values.

Table 4.1 Crystallographic parameters of product phases

Alloy	Lattice parameter			Atom position	unit cell volume (Å^3)	Density g/cm^3	U$_{iso}$ (Å^2)
	a(Å)	b (Å)	c (Å)	(x,y,z)			
hcp (α,α′)							
Ti	2.9514 (1)*	2.9514 (1)	4.6814 (2)	(1/3,2/3,1/4)	35.317 (5)	4.504	0.060 (2)
Ti-1Mo	2.9475 (2)	2.9475 (2)	4.6728 (4)		35.158 (8)	4.547	0.029 (4)
bcc (β)							
Ti-15Mo	3.2523 (4)	3.2523 (4)	3.2523 (4)	(000)	34.404 (15)	4.999	0.04 (1)
Ti-25Mo	3.2423 (3)	3.2423 (3)	3.2423 (3)		34.088 (11)	5.333	0.048 (6)
base centered orthorhombic(α″)							
Ti-7Mo	2.9867 (6)	5.0471 (21)	4.6672 (7)	(0,0.1862,0.25) (8)	70.355 (35)	4.686	0.089 (4)
* Number in parenthesis represents error.							

4.2.2 β bcc phase in Ti-xMo alloys (x=15, 25)

Figure 4.3(a) and (b) shows the experimental, calculated XRD patterns and the difference plot for Ti-15Mo and Ti-25Mo alloys. The ω phase was assumed to be absent, during the refinement of XRD pattern of Ti-15Mo alloy, despite our earlier observation of its presence, in studies using synchrotron XRD [7, 14, 15]. This assumption is valid, since the volume fraction of the ω phase is below the detection limit of conventional XRD. The inputs for the initial structural model (ICDD # 04-013-0263) [39] are as follows: bcc (β); space group Im-3m; Laue symmetry: m3m, lattice parameter, a=3.225 Å and atomic position (0, 0, 0). The preferred orientation index for bcc structure of Ti-15Mo and Ti-25Mo alloys was found to be unity, indicating the absence of texture. The refinement was continued until convergence was obtained with Rp-7.18, wRp-9.08, and GOF-1.141 for Ti-15Mo. The same input was used for the refinement of Ti-25Mo alloy and the corresponding R indices were Rp - 6.78, wRp - 8.77, and GOF-1.014. Similar values reported in literature, for β phase in Ti alloys, range from 8.53 to 14.89 [11].

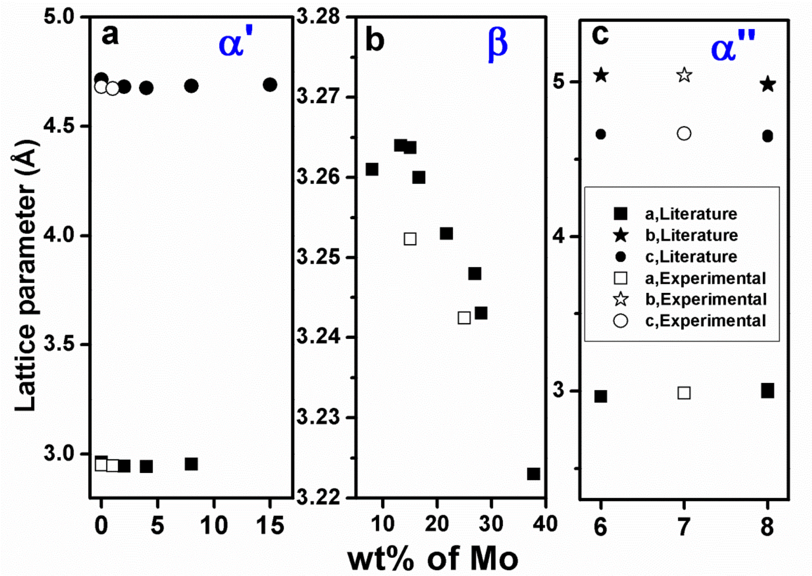

Figure 4.2 Comparison of unit cell dimensions of (a) α', (b) β and (c) α'' phases as a function of amount of Mo in Ti-Mo alloys. In the figure, 'Experimental' refers to current work. Literature refers to published data [11, 34-36].

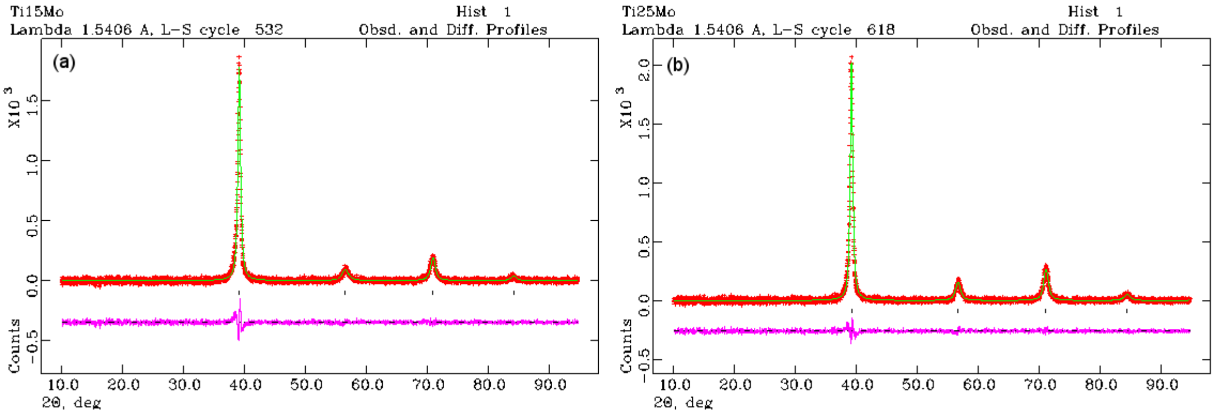

Figure 4.3 Rietveld plot of bcc β structure in (a) Ti-15Mo [14] and (b) Ti-25Mo alloys. The dots represent the experimental data and the solid lines show calculated profile. The small bars close to the profile indicates the Bragg peak positions. The difference plot is marked as the solid line in the lower part of the figure.

The unit cell dimensions, volume of the unit cell and the density have been calculated and are listed in Table 4.1. The error limits for the values of lattice parameter were obtained using non-linear least square fitting in GSAS. Volume of the bcc unit cell has reduced with increase in the amount of molybdenum in the alloy. This is a consequence of reduction in the unit cell parameter due to addition of undersized atoms, following Vegard's law. Similar observations have been already reported in literature [35, 36, 40]. The unit cell dimensions of bcc β phase of Ti-Mo system reported by many investigators are shown in figure 4.2(b). Our values agree well with the reported literature. Many first principle calculations have also shown that the formation energy in a given Ti-Mo alloy, is minimum for the equilibrium volume of the β phase [2] and the minimum value of volume [1] gets reduced due to addition of smaller Mo atoms.

4.2.3 Orthorhombic α″ phase in Ti-7Mo alloy:

Figure 4.4 shows the experimental, calculated XRD patterns from water quenched Ti-7Mo alloy, along with the difference plot.

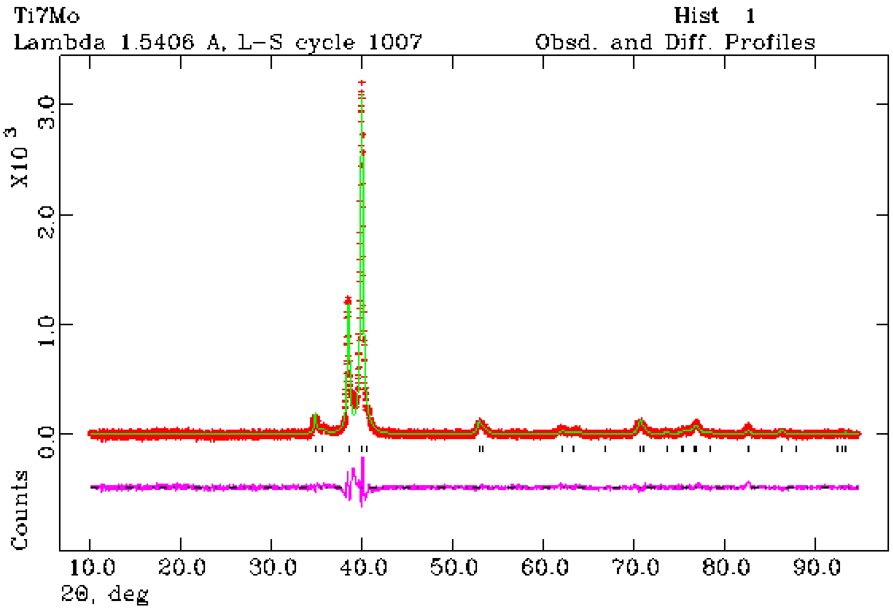

Figure 4.4 Rietveld plot of orthorhombic α″ phase in Ti-7Mo alloy. The dots and the small bars close to the profile are similar to figure 4.3. The difference plot is marked as the solid line in the lower part of the figure

Literature data [10] was used for the construction of the initial model due to the non-availability of ICDD data for orthorhombic α″ phase in Ti-Mo system. The inputs for the initial structural model are as follows: space group Cmcm, Laue symmetry – mmm, lattice parameters - a=2.9800, b=5.0761, c=4.6949 Å and atom position- 0, 0.1800, 1/4. Additionally, texture coefficients were refined using the March-Dollase function [30, 31].

This set of input data provided an excellent fit for the base centered orthorhombic (α″) structure with Rp - 7.72, wRp - 10.07, GOF-1.533.

The crystallographic structural details describing the unit cell of orthorhombic α″ are listed in Table 4.1 There are fewer reports [10, 32, 33] on the unit cell dimensions of the orthorhombic α″ phase in Ti alloys in general and Ti-Mo alloys in particular, in comparison to the other two phases. The limited data available on the lattice parameter values [Figure 2(c)] agree well with our results. During the refinement of atom position, a slight movement of atoms in the y direction parallel to b axis in the (100) plane, was observed for Ti-7Mo alloy. This is in agreement with the reported literature based on first principles calculations [1] of Ti-Mo and other Ti based alloys. However, there is no supporting experimental evidence [1], reported so far in Ti-Mo alloys. Banumathy *et. al.* [10] have reported similar observations in Ti-Nb alloys and pointed out that the atomic shuffle 'y' in α″ is a function of concentration of solute atom. Their reports are in good agreement with the first principle calculations [41] for orthorhombic Ti-Nb alloys. This atomic shuffle will be discussed later in the context of the relative stabilities of the product phases.

4.2.4 Influence of molybdenum on bond length and co-ordination number

It is seen from Table 4.1 that on addition of Mo, the density of pure titanium is increased from 4.504 g/cm^3 for pure titanium to 5.333 g/cm^3 for Ti-25Mo alloy, despite the expected 9% increase in packing fraction of close packed hcp compared to the open bcc structure. Mo is known to have higher density (~16.65 g/cm^3) [22], in comparison with elemental Ti. The observed increase in the density of the Ti-Mo alloys with Mo is understood in terms of the following factors: basic change in the product phase and hence the crystal structure, compression of the unit cell volume discussed earlier and addition of heavier Mo atom. The observed increase in density implies that the factors mentioned above offsets the anticipated decrease based on the difference in the packing fraction.

In addition to refinement, the crystal structures of the various metastable phases in Ti-Mo alloys and detailed analysis on the nature of co-ordination and bond length were also carried out using GSAS and VESTA, the results of which are discussed below.

The exact effective coordination number (CN) was determined, as per the standard procedure (equation 4. 1) adopted in VESTA [42].

$$CN = \sum_{\mathrm{i}} \exp\left[1 - \left(\frac{l_i}{l_{av}}\right)^6\right] \tag{4.1}$$

l_i is the distance from the central atom to the ith coordinating atom and l_{av} is the ‘weighted average of bond length’, details of which are given elsewhere [42]. The effective co-ordination number and the bond length of α″ are closer to α' than β phase, which has an implication on the relative stabilities of the phases.

Figure 4.5 shows the different bond lengths (BL1-shortest, BL2, BL3) selected for calculating the average bond length and co-ordination number, in the lattices of hcp α', orthorhombic α″ and bcc β phases. The ‘minimum’ bond lengths and effective co-ordination number were calculated and listed in Table 4.2. It is seen that within each phase field, hcp or bcc, bond length reduces marginally with increase in molybdenum. This could be due to the smaller size of molybdenum atoms. The reduction in bond length for a specific phase field, suggests an increase in bond strength, which is consistent with the increase in melting point and strength, with increase in molybdenum [6]. The reduction in these two parameters, bond length and effective co-ordination number is consistent with the expectation of influence of lower size of solute atoms.

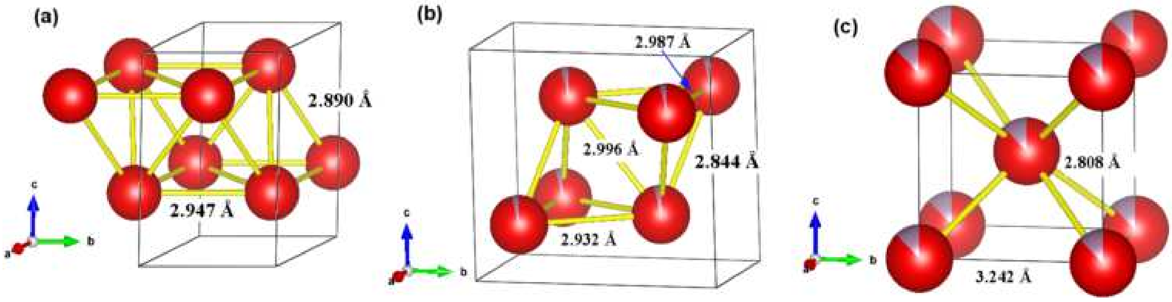

Figure 4.5 The effective bond length in the three crystal systems (a) hcp α' in Ti-1Mo, (b) base centered orthorhombic α" in Ti-7Mo and (c) β bcc in Ti-25Mo.

Table 4.2 Bond length and co-ordination number for unalloyed titanium and Ti-Mo alloys

Alloy	Minimum bond length, A	Effective co-ordination number (CN)
Ti	2.8952	11.96
Ti-1Mo	2.8904	11.95
Ti-7Mo	2.8443	11.79
Ti-15Mo	2.8166	8
Ti-25Mo	2.8079	8

4.3 Bonding Characteristics in Ti-Mo Alloys

The elastic properties and strength of β-phase Ti alloys, crucial for biomedical applications, are governed by the nature of bonding. Rietveld analysis of XRD patterns provides the best means of directly viewing the spatial distribution of charge density around atoms. Hence, the diffraction results of the present study from the three phases of Ti- Mo alloys have been further analysed to calculate electron density contour maps of α′,α″, and β lattices. The method of analysis is described in chapter 2. The results are presented below.

The refined intensities of the Bragg reflections of the individual phases in Ti and Ti-Mo alloys are used for deriving the geometrical structure factors, which in turn are converted to electron density (ρ^e) distribution using the equation 4.2:

$$\rho^e(x,y,z) = \frac{1}{V}\sum_h\sum_k\sum_l F_{(hkl)} \exp[-2\pi i(hx+ky+lz)] \tag{4.2}$$

As mentioned earlier, prior to the charge density distribution calculations, structure factor data has been corrected for texture and micro strain. These factors influence the structure factor values in reciprocal space. However, accurate refinement of the XRD data ensures that the charge density distribution finally arrived at, more or less represents the ideal crystal. The quantification of the influence of the charge density distribution due to texture and strain factor is not feasible, in the current study.

Additionally, the reliability of the electron density distribution data depends largely on the accuracy of the calculated structure factors, which in turn, depends on the number of peaks included for the calculation. The current data spanning over few peaks, therefore provides low resolution data. Hence, only gross qualitative details about nature of bonding have been inferred based on these data.

4.3.1 α'-hcp phase in Ti and Ti-1Mo Alloys

Elemental titanium is used as the reference sample. Table 4.3 shows the calculated and experimental intensity values (F_o^2 and $F_c^{2)}$ for all reflections of α'-hcp phase in Ti-1Mo. Similar values were obtained for Ti also. The multiplicity of each plane {hk.l} and the corresponding d-spacing are shown in Table 4.3. The experimentally observed intensity values I_{obs} agreed well with the intensity values I_{cal}, calculated after refining, as per the procedure explained in Chapter 2. The corresponding intensities, F_o^2 and F_c^2 and the contribution from the preferred orientation to the intensity of each (hk.l), during refining, are also included in the Table 4.3. Based on the history of the sample, the origin of texture can be traced back to the transformation of β→α' during quenching. Similar transformation texture in titanium based alloys has been reported earlier [19].

Table 4.3 Observed and calculated intensity values for (hkl) planes of all phases in Ti-Mo alloys

No	(hkl)	multiplicity	Value of ‘d’ (Å)	Intensity		Preferred orientation index
				F_o^2	F_c^2	
hcp α' structure Ti-1Mo						
1	(10.0)	6	2.5526	1.15E+04	1.08E+04	0.6139
2	(00.2)	2	2.3364	1.68E+05	1.62E+05	2.6534
3	(10.1)	12	2.2401	3.54E+04	3.45E+04	0.7741
4	(10.2)	12	1.7234	1.10E+04	1.09E+04	1.1425
5	(11.0)	6	1.4737	1.89E+04	1.76E+04	0.6139
6	(10.3)	12	1.3296	2.53E+04	2.32E+04	1.5219
7	(20.0)	6	1.2763	3.05E+03	3.03E+03	0.6139
8	(11.2)	12	1.2465	1.49E+04	1.46E+04	0.8228
9	(20.1)	12	1.2312	9.49E+03	8.68E+03	0.656
10	(00.4)	2	1.1682	3.30E+04	3.46E+04	2.6534
11	(20.2)	12	1.1200	3.16E+03	2.47E+03	0.7741
12	(10.4)	12	1.0622	4.98E+03	4.33E+03	1.8188
bcc β structure Ti-25Mo						
1	(110)	12	2.29272	8.48E+04	8.27E+04	1.0000
2	(200)	6	1.62119	4.43E+04	4.14E+04	1.0000
3	(211)	24	1.3237	2.35E+04	2.24E+04	1.0000
4	220)	12	1.14636	1.43E+04	1.28E+04	1.0000
5	(310)	24	1.02533	1.22E+04	7.65E+03	1.0000
base centered orthorhombic α˝ Ti-7Mo						
1	(110)	4	2.57037	9.08E+03	8.73E+03	0.7425
2	(020)	2	2.52356	2.50E+04	1.87E+04	0.4044
3	(002)	2	2.33361	1.74E+05	1.70E+05	2.6583
4	(111)	8	2.25151	1.17E+05	1.15E+05	2.2489
5	(021)	4	2.21984	1.96E+04	1.93E+04	0.5006
6	(112)	8	1.72776	5.56E+03	5.36E+03	1.1509
7	(022)	4	1.71333	1.45E+04	1.34E+04	0.7315
8	(200)	2	1.49336	1.43E+04	9.27E+03	0.6328
9	(130)	4	1.46582	1.44E+04	1.22E+04	0.4994
10	(131)	8	1.39847	9.89E+02	1.72E+03	0.5796
11	(113)	8	1.33094	1.07E+04	1.08E+04	1.1704
12	(023)	4	1.32431	7.83E+03	7.14E+03	1.0267
13	(220)	4	1.28519	3.41E+03	3.43E+03	0.7425
14	(040)	2	1.26178	1.11E+01	9.70E+00	0.4044
15	(202)	4	1.25785	6.68E+03	6.11E+03	0.9285
16	(132)	8	1.24126	8.69E+03	7.85E+03	0.7111
17	(221)	8	1.23907	5.50E+03	4.93E+03	1.2162
18	(041)	4	1.21805	8.56E+03	8.10E+03	0.4301
19	(004)	2	1.1668	2.27E+04	1.39E+04	2.6583
20	(222)	8	1.12575	3.91E+03	4.85E+03	2.2489
21	(042)	4	1.10992	1.01E+01	5.64E+00	0.5006
22	(133)	8	1.06686	8.17E+02	5.16E+02	0.7976
23	(114)	8	1.06246	9.05E+02	6.17E+02	1.4029
24	(024)	4	1.05908	2.69E+03	2.31E+03	1.3223

The electron density distribution within the unit cell of hcp for reference sample of titanium and Ti-1Mo alloy were calculated as stated above. Figure 4.6 (a) and (b) shows the 3-D unit cell of hcp α′ with the atoms at the appropriate positions. The uniform charge density distribution is shown by plotting an iso-surface of 1 e/Å.

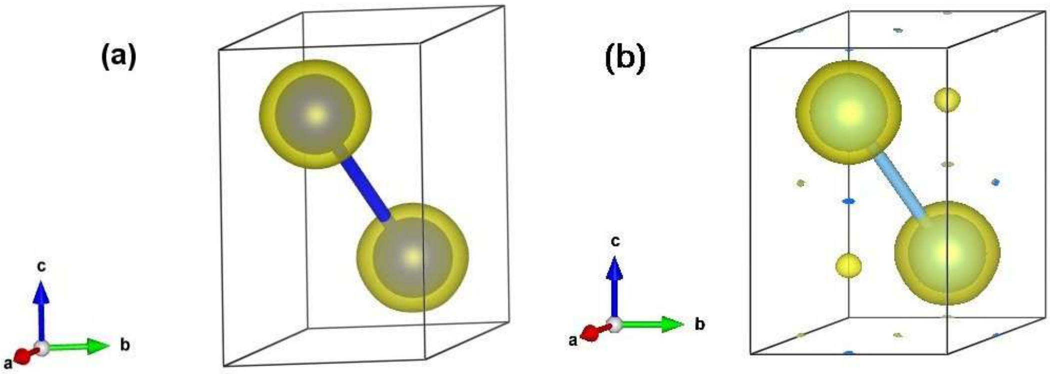

Figure 4.6. (a) 3D unit cell with atoms of pure titanium and (b). Ti-1Mo alloys showing the charge density distribution. The electron charge density iso surface value of 1 e/Å^3 is shown in the figures.

The charge density distribution along (11.0) crystallographic plane of Ti is shown in Figure 4.7. The electron density at any point in a given plane depends strongly on the distance of the chosen point from the atom positions in its neighborhood. It is clear from (11.0) plane that the distribution of electrons around the atomic centers is nearly spherical and it persists to be the same even up to fairly large distances. The uniform low density of charge in places other than atom centers is due to the free, valence electrons, confirming the metallic nature of bonding.

The above inference based on GSAS Fourier calculation for pure Ti is found to agree well with charge density of pure Ti calculated using VASP code (Figure 4. 7(b)) This qualitative observation would further be discussed by comparison of the mid-bond intensity in bonding and non-bonding directions, with and without molybdenum, in section 4.3.4. The investigations [12] on charge density distribution in literature, based on Rietveld analysis of XRD patterns, also suggest that the bonding in Ti is metallic.

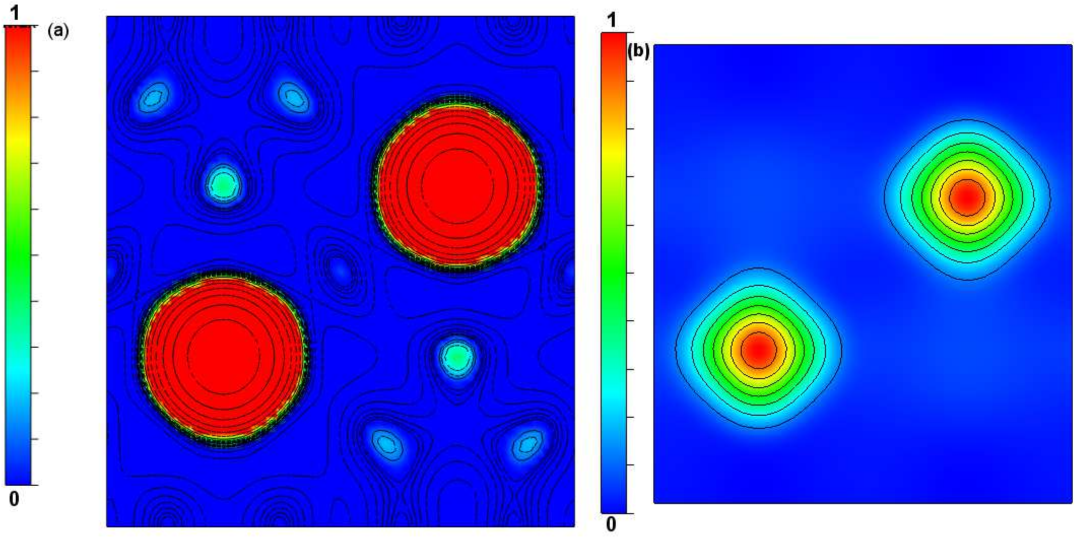

Figure 4.7 Charge density distribution in the (11.0) plane of hcp α titanium calculated by (a) X-ray diffraction Fourier method (the contour levels are set at 0 to 1 e/Å^3 saturation level for X-ray Fourier map) and (b) first principle calculations.

No significant change was observed in the electron density distribution between Ti and Ti-1Mo alloy, as can be seen from Figure 4.8 in the (00.4) plane, with the presence of atoms. Both show the core of the atom positions to have spherical distribution of electron density, while the intra spaces show concave nature. The additional charge density in the interatomic space in Ti-1Mo in contrast to elemental titanium, as seen in Figure 4.6 (b), is more likely to be an artifact rather than genuine effect. This is further supported by the fact that increase in Mo by 10 % in bcc β has not displayed similar additional charge density, as will be shown later.

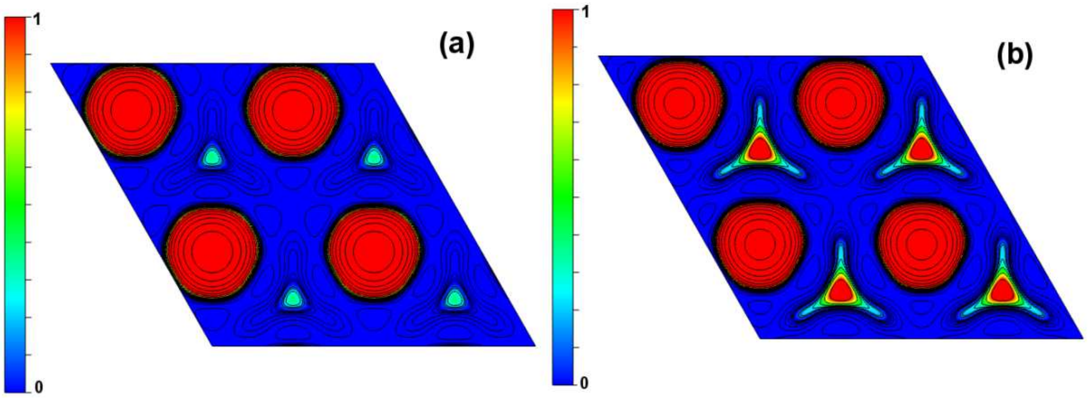

Figure 4.8. Charge density distribution in the (00.4) plane of hcp α in (a) pure Ti and (b)Ti-1Mo alloy viewed at 2x2 unit cells. The contour levels are set at 0 to 1 e/Å^3 saturation level.

4.3.2 β-bcc phase in Ti-15Mo and Ti-25Mo alloys

The calculated and experimental intensity values for all reflections of the bcc β phase in Ti-15Mo and Ti-25Mo alloys were obtained and those corresponding to Ti-25Mo are listed in Table 4.3. Figure 4.9(a) and (b) show the 3-D electron density distribution for the bcc β phase, consistent with the symmetry of the crystal, in both these alloys. Figure 4.9 also represents the atoms at the appropriate positions. The shaded portion of the atom represents the amount of molybdenum.

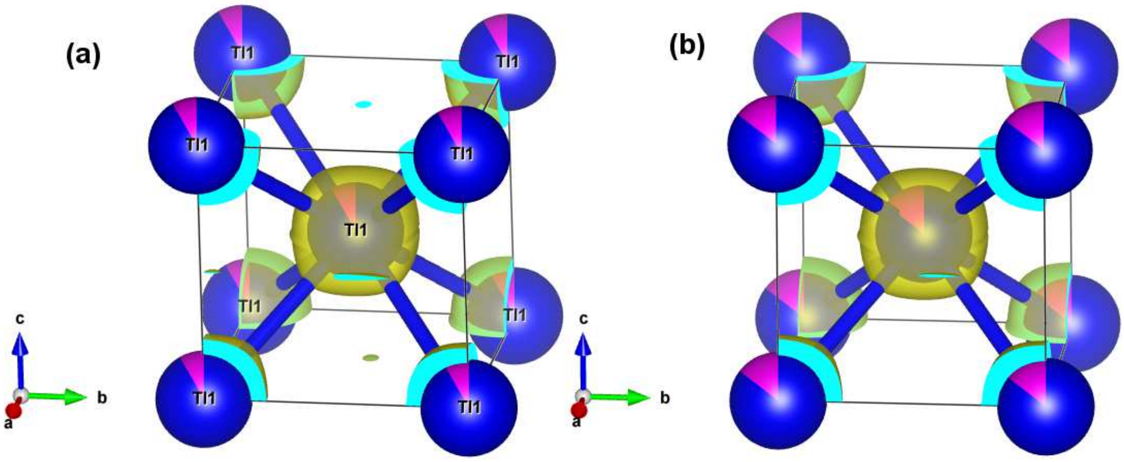

Figure 4.9 3D electron density distributions in (a) Ti-15Mo and (b) Ti-25Mo alloys. The electron charge density iso surface value is 1 e/Å^3 *saturation level*

Figure 4.10(a) shows the 2-D electron density distribution in (100) plane of the bcc lattice obtained from Rietveld data. The charge is found to be localized around atom centers, with a uniform smearing in-between the atom centers. The above observation, in Figure 4.10(a) was found to be in agreement with the results of VASP calculations, as shown in Figure 4.10(b).

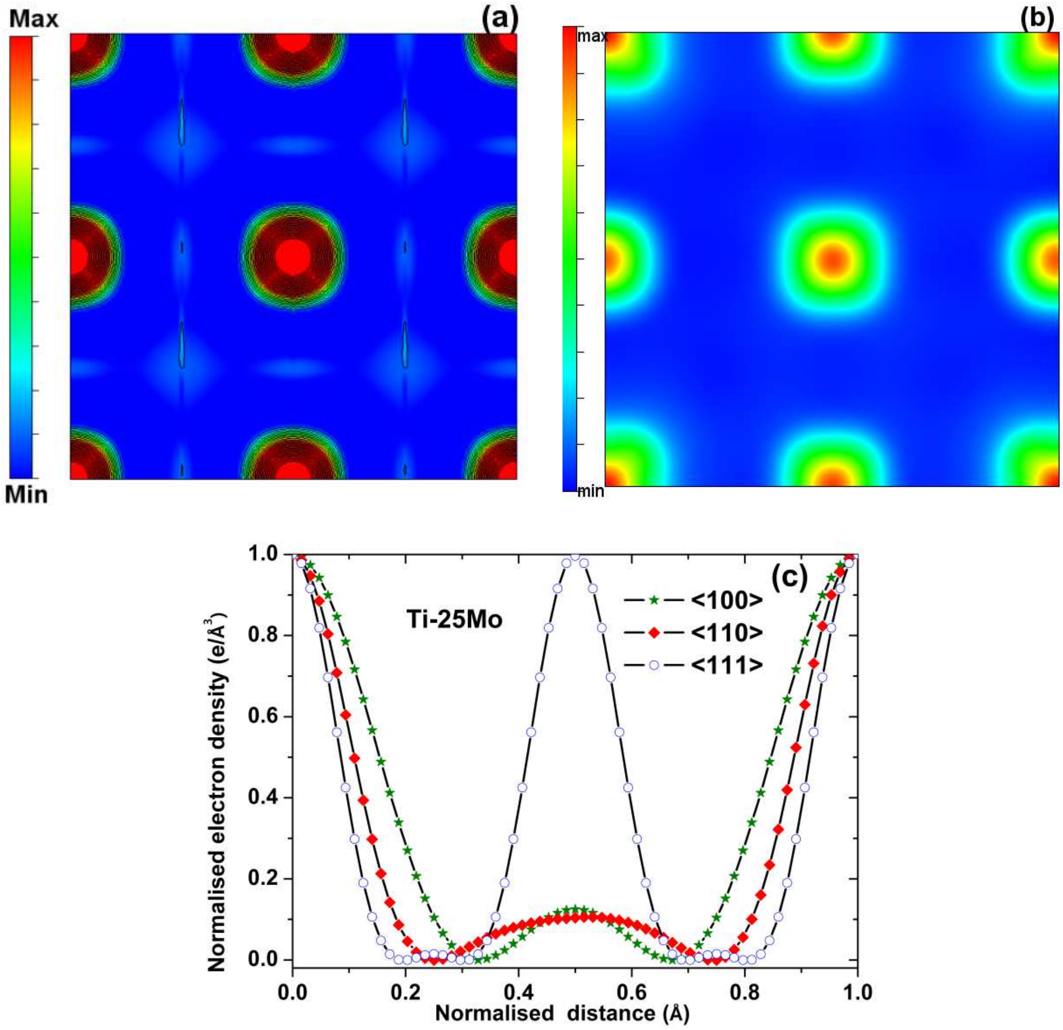

Figure 4.10 2-D Charge density distributions of bcc β in the plane (100) (a) calculated by XRD Fourier method with, the contour values are set as 0 to 10 e/Å^3 saturation levels, (b) 2-D Charge density distribution in the plane (100) of bcc β Ti-25Mo alloy calculated using VASP. (c) Line profile of same along <100>, <110> and <111> of bcc β of Ti-25Mo alloy.

The VASP calculations showed that the substitution of Mo atom does not change the metallic nature of bonding in Ti-Mo alloys. The localization of charge around atom centers and uniform smearing of charge in the region between the atomic centers suggests the strong metallic character of bonding in the bcc β phase. Figure 4.10(c), which is the line profile of charge density along <100>, <110> and <111> directions of bccβ, shows that there is no significant change in the mid-bond values.

In order to study the relative changes in ρ^e for different amounts of molybdenum, line profiles of ρ_e in all five systems, along shortest bond lengths is calculated and shown in Figure 4.11. The inset in Figure 4.11 shows that the degree of delocalization of electrons is higher in α″ and β phase than α' phase, suggesting that the addition of molybdenum tends to enhance the metallic nature of the alloys, which is in tune with literature. However, the inset shows that the trend is not observed in hcp α' phases of Ti and Ti-1Mo, the reason for which is unknown.

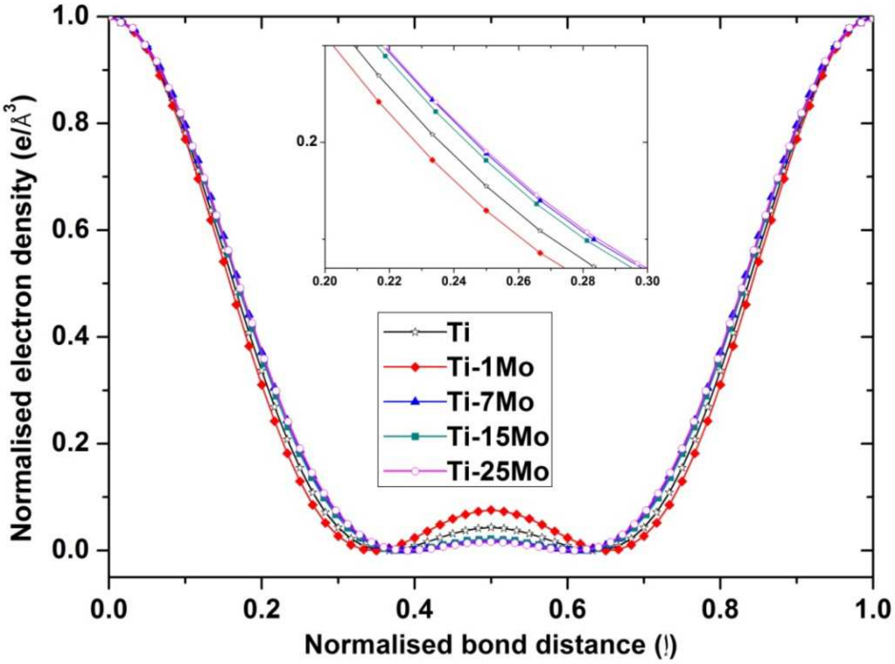

Figure 4.11 1-D line profile of ρ^e along the shortest bond lengths (co-ordinates of which are given in section 4.3.4) in all the five systems of interest. The inset shows the enlarged view of linear portion of the curve.

Similar studies in literature demonstrate [12] the qualitative metallic nature of bonding based on charge density distribution along [110], [001] and [100] directions. Based on the electronic structure of a large number of transition elements and the way the bonding and anti-bonding states are filled, it is deduced that increase in mid bond electron charge density (ρ^e_{mid}) in metals with covalent character is due to the addition of electrons in the bonding states. With increasing atomic number, once all bonding states are filled, anti-bonding states start getting filled, resulting in reduction of ρ^e_{mid} and consequent strengthening of metallic bonding nature. In contrast, some of the calculations have suggested [1] strong covalent nature in the α'-phase of titanium, based on the presence of pseudo-gap near the Fermi level in the density of states.

4.3.3 α″- orthorhombic phase in Ti-7Mo Alloy

Similar analysis for orthorhombic phase of Ti-7Mo alloy was carried out. Table 4.3 presents the values of intensities, while Fig. 4.12 shows the 3-D distribution of electron density within the unit cell. The observations with respect to charge density distribution are more or less similar to that of hcp (Ti and Ti-1Mo) and bcc (Ti-15 and 25Mo) alloys. The charge is isotropic, localized around the atom centers and weakly distributed uniformly in the space in-between. However, the cumulative charge along certain directions in some planes show anisotropy, which will be discussed section 4.4.2.

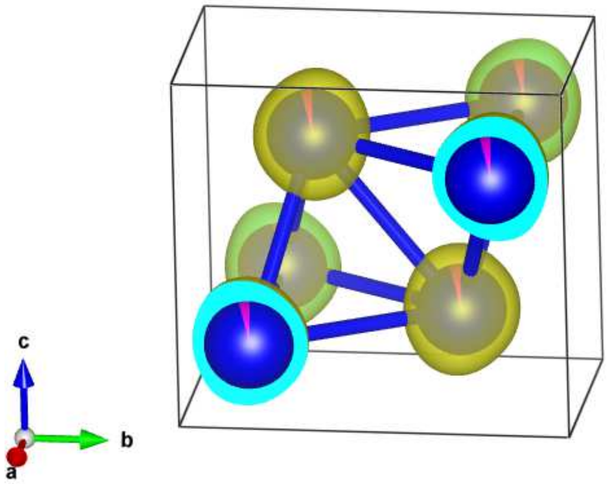

Figure 4.12 3D Electron density distributions in orthorhombic phase of Ti-7Mo alloy. The iso surface level is 1e/Å^3 saturation level.

4.3.4 Role of molybdenum in structural parameters and bonding nature

It has been shown in Table 4.1 that the unit cell dimensions of the given crystal, hcp or bcc reduce with addition of molybdenum. Correspondingly, the unit cell volumes also continue to decrease with addition of molybdenum. This is normally expected to be due to the reduction in the atomic size. In the present study, the effective atomic size after alloying is measured using the variation of charge density along the shortest bond length, as shown below.

Figure 4.13 shows the normalized electron density vs. distance along different bond lengths, calculated using VESTA code. The shortest interatomic distance in the four alloys was calculated using the profile along the shortest bond length directions (BL1) in Figure 4.13 and Figure 4.11, which correspond to the following: (0,0,0) and (1/2,1/2,1/2) along <111> of bcc, between (1/3, 2/3, 0.25) and (2/3, 1/3, 0.75) of hcp and (0.0000, 0.1862, 0.2500) and (0.5000, 0.3137, 0.7500) of orthorhombic system.

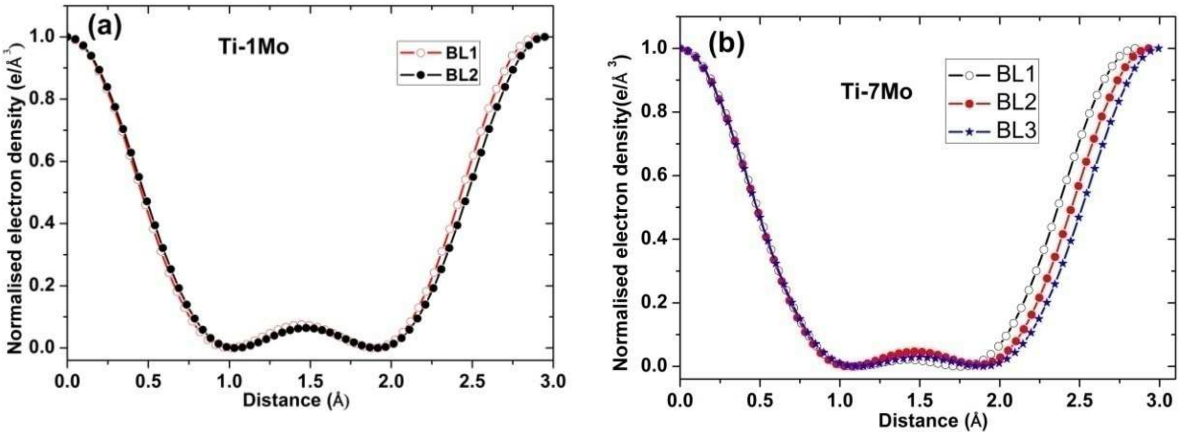

Figure 4.13 Normalised electron density vs. the mid bond distance along bond lengths of (a) Ti-1Mo and (b) Ti-7Mo alloys.

Shortest interatomic distance for the five alloys calculated based on the line profiles of charge density along close packed directions with amount of molybdenum is shown in *Figure* 4.14. Hence, the reduction in unit cell dimensions, unit cell volume, the effective bond lengths and co-ordination numbers with molybdenum discussed in section 4.2 is shown to be due to the associated reduction in atom size, determined using the charge density distribution of the alloys.

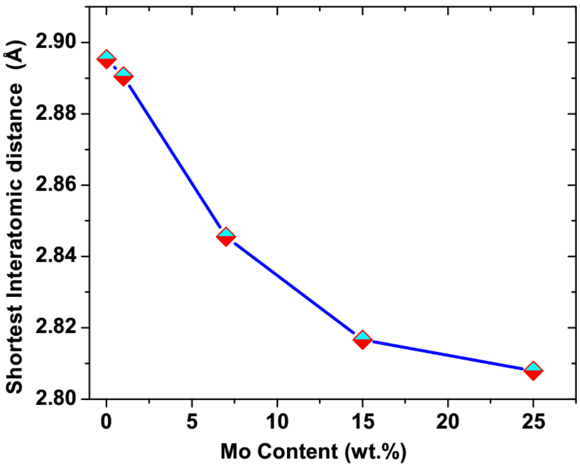

Figure 4.14 Shortest inter-atomic distance of Ti-Mo alloys, calculated along BL1

4.4 Discussion

Many studies have shown that an intermediate concentration of Mo in Ti-Mo alloy, promotes the stabilization of the transition phase. *i.e* base centered orthorhombic α″. Most of the papers in this field mainly discuss about the identification of transformation product and its influence of various thermo mechanical properties. However, the results reported in the present chapter include the crystal structure details of all these phases, in addition to bonding characteristics. On the basis of the results presented above, it has been possible to explain the following aspects:

- α″- a transition phase between α' and β, with addition of molybdenum
- Anisotropy of charge density distribution in α″ of Ti-7Mo and
- Influence of crystal structure and bonding on modulus of Ti-Mo alloys.

4.4.1 α″: transition phase of α' and β

Figure 4.15 shows the variation of e/a (valence electron per atoms) ratio of the four alloys studied and the reference titanium metal, with amount of molybdenum in the alloy. It is clear that e/a increases with addition of molybdenum shifting the stability of the phases from hcp to base centered orthorombic to bcc, in agreement with reported literature.

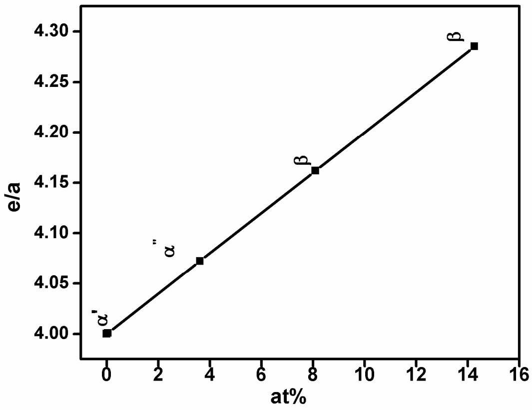

Figure 4.15 Variation of e/a ratio with amount of Mo and stability of different metastable states for Ti-Mo alloys

The results presented above were analyzed to identify the relative differences between the lattice of α″ from that of α′ and β phases of the four alloys. The stability of the base centered orthorhombic α″ phase depends basically on two fundamental parameters: the lattice parameter and the atomic position. Crystallographically, the orthorhombic structure has four independent parameters, that dictates its stability, like the orthorhombicity-b/a, c/a, volume of the unit cell and shuffle of atom position in the basal plane, y. The comparison of the relative change in α″ from the α' and β phases in the four alloys of interest, based on above parameters, is discussed below.

The volume, *b/a* and *c/a* were calculated using the values of the “orthorhombic” unit cells of the α', α″and β phases in the four alloys, reported in Table 4.4. The volume change is ‘ΔV’ calculated using the equation (4.3).

$$\Delta V = \frac{V_{(Ti-xMo)} - V_{\beta(Ti-25Mo)}}{V_{\beta(Ti-25Mo)}} \times 100 \qquad (4.3)$$

The method adopted for selection of the equivalent orthorhombic lattices of α' and β phases is the same as used before [34], which is based on the Burger’s orientation relation between the three lattices. Figure 16 shows the equivalent orthorhombic lattices of the three phases and Table 4.4 shows the variation of the unit cell dimensions of the α', α″ and β phases in the four alloys. It is clear that the unit cell of α″ is a simple distortion of the hcp α′ ($c_{\alpha''} = c_{\alpha'}$ (Δc = -0.005Å) $b_{\alpha''} < b_{\alpha'}$ (Δb = - 0.058 Å) $a_{\alpha''} > a_{\alpha'}$ (Δa = 0.039 Å)), with large contraction along b-axis, minor expansion along '*a*' axis and even lesser expansion along c axis, for the concentrations of Mo investigated in the present study. Purely based on geometrical considerations of the orthorhombic lattices of hcp and bcc phases, it is possible to show that the limiting values of orthorhombicity, b/a are √3 for hcp and √2 for bcc. It is seen that the b/a of Ti-7Mo alloy is closer to √3 than √2. This implies that the addition of 7wt%Mo is not sufficient enough to either dilate '*a*' or contract '*b*', to the required extent. The changes in volume and *c/a*, (Table 4.4) also suggest that the α″ phase is closer to α′ than β phase.

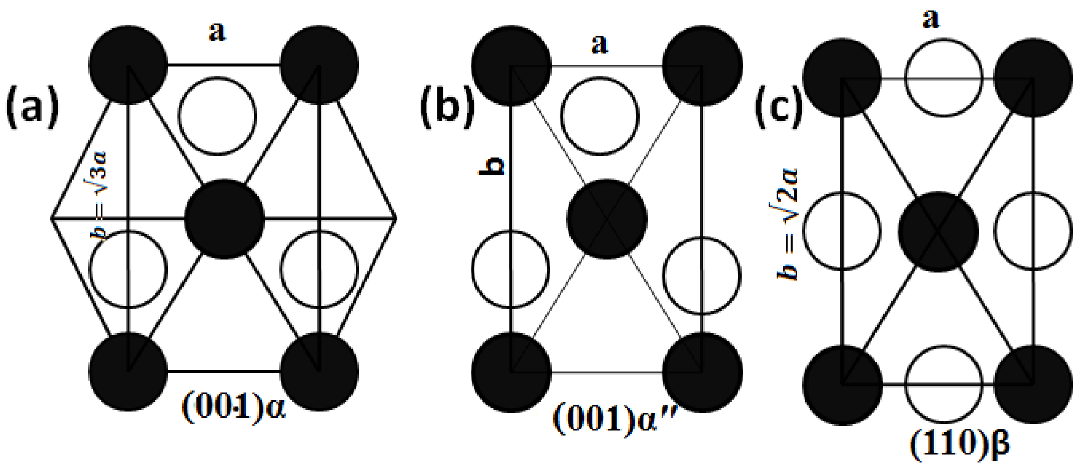

Figure 4.16. Equivalent orthorhombic lattices of (a) hcp α′, (b) orthorhombic α″ and (c) bcc β phases.

Table 4.4 Variation of the unit cell dimensions in the equivalent orthorhombic system, for the α, α″and β phases in the four alloys

Phase	a (Å)	b(Å)	c(Å)	Volume (Å)^3	b/a	c/a	Volume change (%)
	Considering as base centered orthorhombic						
α'(Ti)	2.9514	5.1119	4.6814	70.6295	1.7320	1.5861	3.6
α′(Ti-1Mo)	2.9475	5.1052	4.6728	70.3143	1.7320	1.5853	3.1
α″(Ti-7Mo)	2.9867	5.0471	4.6672	70.3541	1.6898	1.5626	3.2
β(Ti-15Mo)	3.2523	4.5994	4.5994	68.8007	1.4142	1.4142	0.9
β(Ti-25Mo)	3.2423	4.5853	4.5853	68.1692	1.4142	1.4142	---

The second basic parameter governing the stability of the α'' phase is the movement of atom along the ‘b’ axis, due to the shuffle introduced during the diffusionless transformation. Table 4.1 lists the atom positions of the α'' phase, in which it is clearly seen that the atom has moved along the ‘b’ axis to the final position of 0.1862 Å. The initial value of atom position (0.0, 0.20, 0.25) has site symmetry of *m2m* with multiplicity factor of 4. The titanium atom connected with the first two bond lengths, (four atoms at BL1=2.8455Å; four atoms at BL2=2.9318Å) shows distorted pseudo eight fold coordination, whereas, the Ti atom with next higher bond lengths, (BL3=2.9870Å and BL4=2.993Å) clearly shows the distorted 12 fold coordination. The change in co-ordination number and bond length, as a consequence of the movement of atom is calculated and listed in Table 4.2 The co-ordination number CN of α''(11.79) is closer to α'(11.95) than β phase (8).

Our results discussed above suggest that α'' in Ti-7Mo alloy, is an intermediate structure between hcp α' and bcc β phases. This does not imply that the parent β phase transforms to many intermediate phases before reaching the final phase. Since the Mo content is varying, these results do not throw any light on the transformation paths in an alloy of chosen composition. Another factor is the change in the phase field, itself, unlike the efforts in literature [10, 32]for Ti-Nb system, where in phase field is retained within α''. The base centered orthorhombic α'' phase can be viewed as a transition phase, obtained by only a very minor distortion of the hcp α phase and α'' is closer to α' than β phase. Amount of molybdenum (7wt %) in the present alloy is not sufficient enough to transform the system to retain β phase.

Many reports are available [32, 34] in the literature regarding the study of similarity of α'' phase to α and β phases, in titanium alloys. The orthorhombicity of α'' is reported to have limiting values ranging from b/a = 1.732 for hcp to 1.414 for bcc. Another signature is the shuffle in the y position of atoms parallel to b axis in the (100) plane. It is reported that the movement of atoms along ‘y’ direction is driven by the tendency of the system to achieve the eight-fold co-ordination of the bcc phase from the twelve fold co-ordination of hcp, with addition of β stabilizing solutes. The extent of ‘y’ is reported [1, 10, 32] to depend on the amount of the solute, with the permitted ranges (y=0 for bcc to y=0.18 for hcp) [1] dictated by geometrical considerations, as stated earlier. Similar atomic shift y in 4c Wyckoff positions has been reported[10, 32] in Ti-Nb system and y is found to increase with Nb, within the phase field of α”. Crystallographic symmetry based arguments [34] also support the view that α″ is a transition phase between hcp α' and bcc β.

It is clear from our studies that the extent of shuffle of atom positions in Ti-7Mo alloy, is not sufficient enough to directly transform the system from hcp α' to bcc β phase. The approach to equilibrium β phase has to be facilitated by either ‘thermal’ energy during aging or an intermediate phase like α″or ω, as is very often observed in titanium alloys.

4.4.2 Influence of charge density distribution in anisotropy of orthorhombic α″ phase

Titanium and its alloys are known to show high degree of anisotropy in many properties, as a result of bonding anisotropy along different crystallographic directions. The information of the charge density distribution in the unit cell of titanium alloys, of the present study, is very useful in providing evidence for the origin of the reported anisotropy of elastic constants and properties. This can be identified qualitatively by analyzing the integrated intensity along suitable crystallographic directions.

Dai *et. al.* [2] have calculated shear anisotropy factors, A1, A2 and A3, in α″ of Ti-Mo system, using first principle calculations. The shear anisotropy factors depend on the bonding anisotropy between atoms in different planes and are calculated by the following equations [2, 43]. Dai *et.al.* [2] reported that A1>A3>A2.

$$A_1 = \frac{4C_{44}}{C_{11}+C_{33}-2C_{13}} ----------(4.4)$$

$$A_2 = \frac{4C_{55}}{C_{22}+C_{33}-2C_{23}} ----------(4.5)$$

$$A_3 = \frac{4C_{66}}{C_{11}+C_{22}-2C_{12}} ----------(4.6)$$

These anisotropy factors are influenced by the charge density differences along specific directions in certain planes. Hence, the integrated intensity of the α″ structure along specific crystallographic directions in the following planes, corresponding to the reported anisotropies A1, A2 and A3 are calculated:

A1 – [011] and [010] directions in (100) plane,

A2 – [101] and [001] in (010) plane and

A3 – [110] and [010] in (001) plane.

Figure 17 shows the 2-D charge density distribution along the (100), (010) and (001) planes of α″ structure in Ti-7Mo alloy. The line profile of the charge density distribution along different crystallographic directions is shown as an insert in each figure. The integrated charge densities along different crystallographic directions are listed in Table 4.5. The charge density variations between different crystallographic directions are also calculated. These values are compared with anisotropy factors calculated based on elastic constants evaluated using DFT calculations. The reports suggest that anisotropy in A1 is maximum followed by A3 and A2 successively. It is observed that the difference in the integrated charge density along relevant crystallographic directions shows a similar trend with shear anisotropic factor along the corresponding crystallographic directions and planes: A1 > A3 > A2. Thus, it has been possible to obtain direct evidence for the origin of reported anisotropy in α″phase of Ti-Mo system, in the present study.

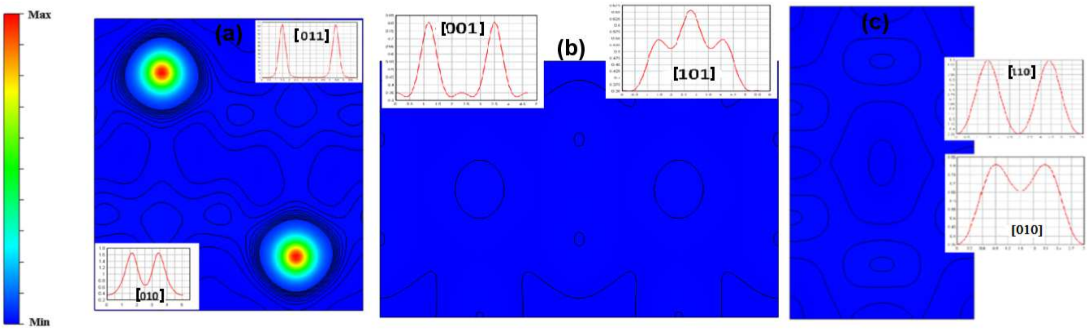

Figure 4.17 2D charge density distribution (0.5 to 5 e/Å^3 step of 0.5e/Å^3) α″ along (a). (100) plane with line profile charge density distribution along [011] and [010] (b). (010) plane with line profile charge density distribution along [101] and [001] (c). (001) plane with line profile charge density distribution along [110] and [010].

Table 4.5 Variation in the values of ρ_e in specific crystallographic directions in α'' phase in Ti-7Mo alloy

anisotropy factor	Plane	Direction	Integrated Charge density (along the direction)	Charge density Variation. $\Delta\rho_e$
A1	(100)	[011]	80.4471	75.856
		[010]	4.5906	
A2	(010)	[101]	2.6923	0.5248
		[001]	2.1674	
A3	(001)	[110]	3.9798	2.0975
		[100]	1.8823	
A1 > >A3 > A2				

4.4.3 Influence of crystal structure and bonding on modulus of Ti-Mo alloys

The recent spurt of research activities in β phase titanium alloys is driven by the need for replacing the current generation of α+ β Ti-Al-V base alloys for biomedical implants, with alloys of lower modulus to reduce the ‘stress shielding’ effect. Ti-Nb and Ti-Mo based alloys are being evaluated due to the lower modulus of β phase alloys, in addition to their non-toxic nature.

The present studies have demonstrated that the crystal structure, unit cell volume, e/a ratio, bond length and hence the bond strength varies with amount of molybdenum. The linear increase in e/a ratio and the observed reduction in bond length with molybdenum, suggests an increase in the bond strength with molybdenum. Hence, it would be expected that the modulus would increase with molybdenum amount. This behavior is consistent with the reported increase in Young's modulus with molybdenum [3, 44], in the β-phase field. However, as the amount of molybdenum in the alloy is reduced, the β phase becomes more and more unstable, leading to hcp α/α″ in Ti/Ti-1Mo and Ti-7Mo. The metastable phases lead to significant increase in modulus offsetting the anticipated reduction in modulus due to higher bond length in Ti and Ti-1Mo.

Thus, the results of the present study on structure and bonding nature are consistent with the reported changes in the young's modulus with amount of molybdenum in Ti-Mo alloys.

4.5 Summary

Rietveld analysis of X-ray diffraction patterns from titanium and Ti-Mo alloys was used for refining the crystal structure and calculate the charge density distribution within the unit cells of hcp α', orthorhombic α″ and bcc β phases. The major conclusions are as follows:

- The unit cell dimensions and atom positions of all product phases (hcp α', orthorhombic α″ and bcc β phases) in water quenched Ti-Mo alloys and titanium metal were obtained, with good reliability indices.

- The effective co-ordination length calculated using line profile of charge density along the nearest neighbors was found to reduce with amount of molybdenum. The reduction in unit cell volume, bond length and co-ordination number with molybdenum is identified as due to the reduction in effective atom size.
- The electron charge density distribution in α'' and β phases is more delocalized than α', thus demonstrating the tendency of molybdenum to promote metallic character of bonding.
- The α'' phase in Ti-7Mo alloy has been found to be a transition phase, closer to α' than β phase. The molybdenum added is not sufficient enough to introduce the required shuffle of the atoms along the ‘b’ axis, to transform directly from α' to β phase.
- Anisotropy in the charge distribution along crystallographic directions is calculated using one dimensional charge density distribution, in specific planes and directions in Ti-7Mo alloy, along which elastic anisotropy was reported in literature. This provides the direct evidence for the origin of anisotropy in reported values [2] of elastic constants of α'' phase.
- The results of present study on the crystal structure and bonding nature in Ti-Mo alloys are found to be consistent with the reported dependence of modulus on amount of molybdenum.

References

[1] C.-X. Li, H.-B. Luo, Q.-M. Hu, R. Yang, F.-X. Yin, O. Umezawa, L. Vitos, *Solid State Communications* **2013**, 159, 70.

[2] J. Dai, X. Wu, Y. Song, R. Yang, *Journal of Applied Physics* **2012**, 112, 123718.

[3] R. Sahara, S. Emura, S. Ueda, K. Tsuchiya, *Science and Technology of Advanced Materials* **2014**, 15, 35014.

[4] A. Devaraj, R. Williams, S. Nag, R. Srinivasan, H. Fraser, R. Banerjee, *Scripta Materialia* **2009**, 61, 701.

[5] D. Banerjee, J.C. Williams, *Acta Materialia* **2013**, 61, 844.

[6] S. Banerjee, P. Mukhopadhyay, Phase transformations: examples from titanium and zirconium alloys, Elsevier, 2010.

[7] M. Sabeena, R. Mythili, J. Basu, M. Vijayalakshmi, *Transactions of the Indian Institute of Metals* **2013**, 66, 401.

[8] W. Ho, *Journal of Medical and Biological Engineering* **2008**, 28, 47.

[9] H. Rietveld, *Journal of applied Crystallography* **1969**, 2, 65.

[10] S. Banumathy, R. Mandal, A. Singh, *Journal of Applied Physics* **2009**, 106, 093518.

[11] J.R.S. Martins Jr, C.R. Grandini, *Journal of Applied Physics* **2012**, 111, 083535.

[12] R. Saravanan, M.P. Rani, Metal and Alloy Bonding-An Experimental Analysis: Charge Density in Metals and Alloys, Springer Science & Business Media, 2011.

[13] N.T. Oliveira, G. Aleixo, R. Caram, A.C. Guastaldi, *Materials Science and Engineering: A* **2007**, 452, 727.

[14] M. Sabeena, S. Murugesan, R. Mythili, A. Sinha, M. Singh, M. Vijayalakshmi, S. Deb, *Transactions of the Indian Institute of Metals* **2015**, 68, 1.

[15] M. Sabeena, S. Murugesan, R. Mythili, A. Sinha, M. Singh, M. Vijayalakshmi, S. Deb, Influence of Mo in β phase stability of Ti-Mo system: Synchrotron based XRD studies, in:

Solid State Physics: Proceedings of the 58th DAE Solid State Physics Symposium 2013, AIP Publishing, 2014, pp. 119.

[16] F. Bruneseaux, E. Aeby-Gautier, G. Geandier, J.D.C. Teixeira, B. Appolaire, P. Weisbecker, A. Mauro, *Materials Science and Engineering: A* **2008**, 476, 60.

[17] F. Sun, J. Zhang, M. Marteleur, T. Gloriant, P. Vermaut, D. Laillé, P. Castany, C. Curfs, P. Jacques, F. Prima, *Acta Materialia* **2013**, 61, 6406.

[18] S. Malinov, W. Sha, Z. Guo, C. Tang, A. Long, *Materials characterization* **2002**, 48, 279.

[19] I. Lonardelli, N. Gey, H.-R. Wenk, M. Humbert, S. Vogel, L. Lutterotti, *Acta Materialia* **2007**, 55, 5718.

[20] M.T. Mohammed, Z.A. Khan, A.N. Siddiquee, *International Journal of Chemical, Nuclear,Materials and Metallurgical Engineering* **2014**, 8, 1123.

[21] R. Boyer, *Materials Science and Engineering: A* **1996**, 213, 103.

[22] Y.-L. Zhou, D.-M. Luo, *Materials Characterization* **2011**, 62, 931.

[23] J. Gonzalez, J. Mirza-Rosca, *Journal of Electroanalytical Chemistry* **1999**, 471, 109.

[24] J.I. Qazi, H.J. Rack, *Advanced Engineering Materials* **2005**, 7, 993.

[25] M. Geetha, A.K. Singh, R. Asokamani, A.K. Gogia, *Progress in Materials Science* **2009**, 54, 397.

[26] Y. Qiang, S. Jian, X. Hui, W.-y. Guo, *Transactions of Nonferrous Metals Society of China* **2007**, 17, 1417.

[27] W. Ho, C. Ju, J.C. Lin, *Biomaterials* **1999**, 20, 2115.

[28] M.-j. Lai, X.-y. Xue, Z.-b. Zhou, B. Tang, J.-s. Li, L. Zhou, *Journal of Shanghai Jiaotong University (Science)* **2011**, 16, 227.

[29] P.D.F. ICDD, *Powder Diffraction File"(Newtown Square, PA 19073, USA)* **1997**.

[30] A. Larson, R. Von Dreele, *There is no corresponding record for this reference*.

[31] W. Dollase, *Journal of Applied Crystallography* **1986**, 19, 267.

[32] A. Pathak, S. Banumathy, R. Sankarasubramanian, A. Singh, *Computational Materials Science* **2014**, 83, 222.

[33] M. Bönisch, M. Calin, L. Giebeler, A. Helth, A. Gebert, W. Skrotzki, J. Eckert, *Journal of Applied Crystallography* **2014**, 47, 1374.

[34] Y. Mantani, Y. Takemoto, M. Hida, A. Sakakibara, M. Tajima, *Materials transactions* **2004**, 45, 1629.

[35] R. Davis, H. Flower, D. West, *Journal of Materials Science* **1979**, 14, 712.

[36] R. Hake, D. Leslie, T. Berlincourt, *Journal of Physics and Chemistry of Solids* **1961**, 20, 177.

[37] Y. Motemani, M. Tan, T. White, W. Huang, *Materials & Design* **2011**, 32, 688.

[38] E. Wu, X. Xu, X. Yuan, X. Guo, S. Wang, *Journal of Alloys and Compounds* **2008**, 458, 161.

[39] T. Fawcett, J. Faber, S. Kabbekodu, F. McClune, D. Rafaja, *Microstruct. Anal. Mater. Sci.* **2005**.

[40] M. Hoch, R. Viswanathan, *Metallurgical Transactions* **1971**, 2, 2765.

[41] L. Cheng-Bin, L. Ming-Kai, Y. Dong, L. Fu-Qing, F. Xiang-Jun, *Chinese Physics* **2005**, 14, 2287.

CHAPTER 5

COMPETING PHASE TRANSFORMATION MECHANISMS AND PRODUCTS IN Ti-Mo ALLOYS

CHAPTER 5

COMPETING PHASE TRANSFORMATION MECHANISMS AND PRODUCTS IN Ti-Mo ALLOYS

5.1 Introduction

The influence of chemistry on transformation mechanism and product has been studied in detail in last two chapters. Another parameter which governs the transformation path is the cooling rate. Gil *et. al.* [1] studied the influence of cooling rate on the morphology of Widmanstätten structures and its effect on mechanical properties in Ti6Al4V alloy. Study of morphological characteristics of microstructure, which bear the signature of different modes of transformation, has been helpful to study the transformation mechanism in titanium alloys. As the cooling rate decreases, the size of Widmanstätten plate and α allotriomorphs increases due the increase in residence time at high temperatures. A similar observation of increase in the thickness of grain boundary α phase and coarse lamellae of α phase is reported in Ti-5Ta-1.8Nb alloy [2, 3]. At low cooling rates, the alloying elements get sufficient time to diffuse inside the β matrix. This enhances the nucleation and growth of the diffusional α phase. The competitive nature and morphological variations of martensitic to massive and diffusion controlled Widmanstätten transformation is reported for a cooling rate of >420°C/s, 420-20°C/s, and <20°C/s respectively for Ti-6Al-4V alloy[4]. An increase in the volume fraction of massive α with decrease in cooling rate is reported in the same study. The reason for this is the initiation of massive transformation at higher temperature.

Studies on Ti-Mo alloys demonstrated various modes of phase transformations in these alloys at various heat treatment conditions [5-11]. Ti-Mo binary alloys having Mo composition less than 8wt% undergo martensitic transformation under fast quenching of the order of few hundred K/s and leads to the formation of either hcp α' or orthorhombic α″ martensite depending on the Mo concentration of the alloy [8, 11-13], which has been discussed earlier.

In addition to the non-diffusional martensitic transformation, Ti-Mo system can undergo diffusional Widmanstätten transformation on very slow cooling from the β phase field or on aging in the α+β phase field. During slow cooling, the grain boundary allotriomorphs α form along the β grain boundary creating a concentration gradient of β stabilizing element (Mo in the present study) near the grain boundary. The high concentration of β stabilizing element stabilize the bcc structure and hence retard the further growth of GB α in the early stage of its formation itself. In this β rich region due to certain perturbation, Mo lean and rich regions are created. The region lean in Mo further grows inside the β grain rejecting the Mo, normal to the growth direction. This causes the formation of alternate lamellae of α and β structures, which is a typical Widmanstätten structure. Furuhara *et. al.* [14] studied the morphology and crystallography of α precipitate in the β matrix for various aging conditions in the Ti-Mo alloys of Mo composition 10-40%. Precipitation of α plate at the grain boundary and its further growth inside the β grain is observed for binary alloys of Ti for a Mo concentration of 10, 20 and 30 wt%. The detailed study of effect of composition and aging treatment on microstructure and mechanical behavior has been reported by Flavia *et. al.* [12] for a Mo concentration ranging from 3 to 15 wt%. The study confirms the formation of α' structure for alloys with 3 to 5wt% Mo and α″ structure in alloys with 6 to 7.5 wt% Mo on β quenching. Alloys with 8 to 10wt% Mo alloys show co-existence of α″ and β structure. The study further confirms that the phase variation influences the Young’s modulus of the alloy. High modulus of alloys forming martensitic structure like α' and α″ are low due to the low strain from the substitutional elements. However, the precipitation of ω phase in the 8wt% quenched alloy leads a higher modulus. The aging of the 5wt% and 7.5wt% Mo alloy at 573K leads the precipitation of ω phase and hence cause a higher hardness and Young's modulus. Similar behavior in Ti-Mo alloys with ω phase is reported by many investigators [8, 15, 16]. The present chapter would focus on the influence of cooling rate on the mechanism of phase transformation and the final products during decomposition of β in Ti-1Mo and Ti-7Mo alloys.

The chapter is organized as follows. Section 5.2 presents the influence of cooling rate on the transformation mechanism of Ti-xMo (x=1,7 wt%) alloys. This section includes identification of microstructure using conventional microscopic techniques and the crystal structure using Rietveld refinement of X-ray diffraction pattern of Cu Kα source. The influence of alloy composition and cooling rate on the crystal structure details of transformed phases is discussed in section 5.3. Basically, the Rietveld refined data of XRD patterns is presented to derive details regarding accurate lattice parameter, atom position and relative volume fraction of transformation products. Section 5.4 describes about the variations in the hardness of present alloys in the light of difference in the crystal structure/ microstructure of transformed product discussed in the preceding sections. Section 5.5, summarizes all the results presented in this chapter.

5.2 Transformation mechanism and products for different cooling rates in Ti-1 & 7 Mo alloys

The present section discusses the effect of cooling rates (900°C/s, 3.3°C/s and 0.13°C/s) on the transformation mechanism and product of high temperature parent β-bcc phase, in Ti-1Mo and Ti-7Mo alloys.

5.2.1 Studies in Ti-1Moalloy

Optical and SEM micrographs of Ti-1MoWQ alloy, (already presented in earlier chapters, is reproduced here for the sake of completion), in figure 5.1(a) and 5.1(b) respectively show the typical, characteristic plate morphology of martensitic structure. The grain boundary shown in figure 5.1(a) is devoid of grain boundary α, due to non-availability of time required for diffusional transformation above Ms. Rietveld refined XRD pattern shown in figure 1(c) confirms formation of 100% hcp α' structure in the water quenched alloy. There is no signature of the retention of parent bcc β phase, in the XRD pattern, as expected. In addition, EDX analysis in SEM confirmed the composition invariance of constituent elements from region to region. The result presented above confirms that water quenching of Ti-1Mo alloys promotes martensitic transformation of parent bcc β phase to hcp α'. The observation in the current study is consistent with results reported in literature for the quenched alloy of Ti-1Mo. The observation of martensite for a cooling rate of 900°C/s is in agreement with the reported critical cooling rate of 420°C/s, for martensitic transformation in Ti-1Mo alloy.

In order to understand the finer microstructural details, transmission electron microscopy was carried out. The microstructure of Ti-1MoWQ alloy is shown in figure 5.1(d). Fine plates of martensite with micro twins are clearly visible in the TEM micrograph. SAD pattern along $[\bar{1}101]$ zone axis of hcp α' corresponding to figure 5.1(d) given in figure 5.1(e), shows the presence of twin reflections. Both these observations confirm that the plate morphology observed in figure 5.1(d) is a result of formation of twin martensite.

The experimental results described above could only provide information about the room temperature product and the transformation mechanism. To understand the different stages of transformation during cooling, JMatPro calculations (figue 5.2) were carried out to arrive at relative phase fraction of Ti-1Mo alloy at different temperatures, based on TTT and CCT diagrams. The grain size used for the calculations was 1800 μm, based on β grain size after solutionising in the β phase field at 1173K.

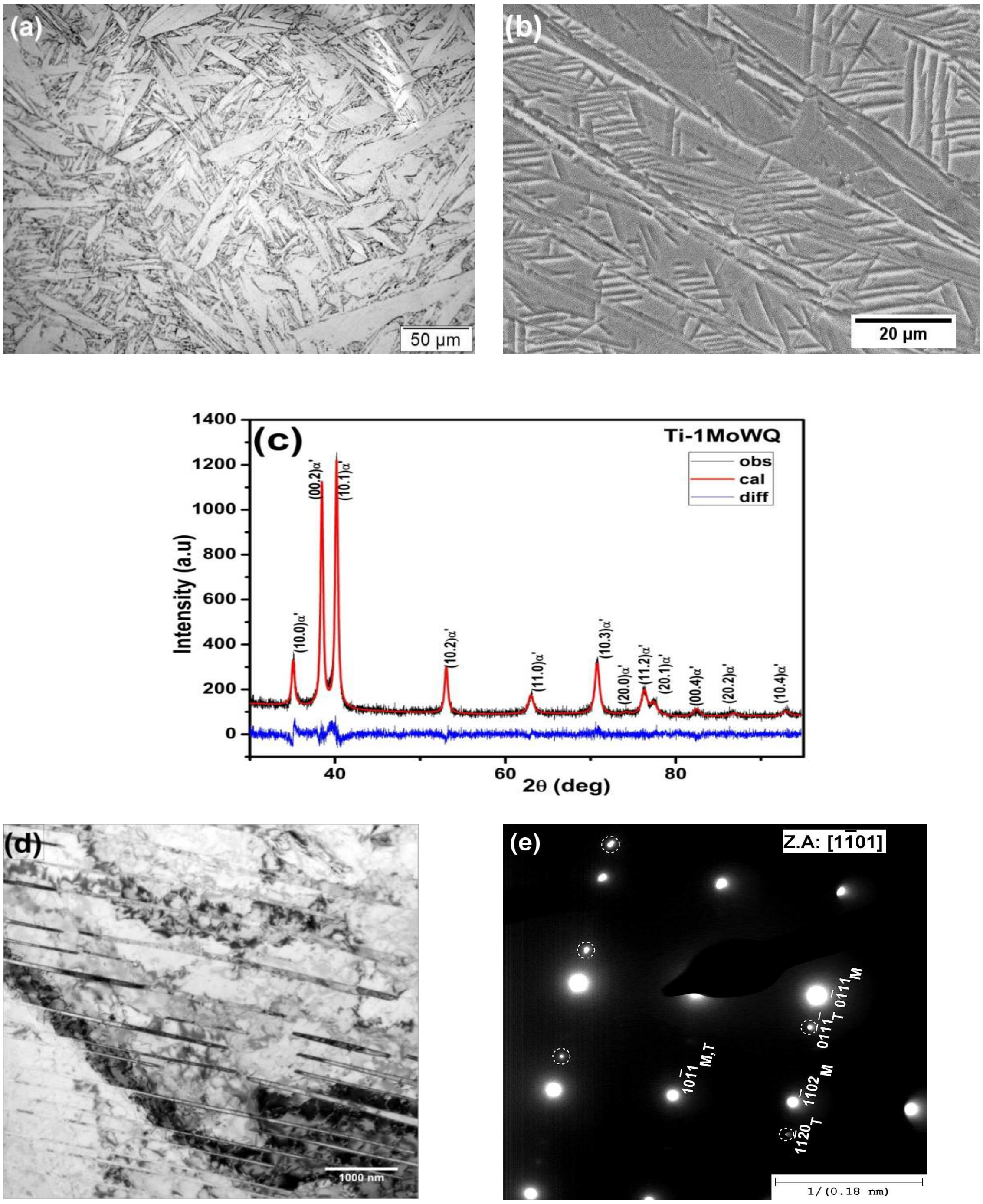

Figure 5.1 Evidence for formation of hcp α' in Ti-1Mo WQ alloy: (a) Optical (b).SEM micrograph of plate morphology of martensitic α' (c) Rietveld refined XRD pattern confirming formation of hcp α'.(d).Transmission electron micrograph of β quenched Ti-1Mo alloy showing hcp α' containing micro-twins, (e) SAD pattern from the same region along $[\bar{1}101]$ zone axis of α'(M), along with the twin reflections (T-circled).

Figure 5.2(a) shows the TTT curve, calculated based on classical nucleation and growth rate equations, for isothermal hold at various temperatures, for formation of grain boundary allotriomorph at high temperatures and β→α transformation at the lower temperatures. The CCT diagram of the alloy was calculated at different cooling rates of 1.0, 0.1, 0.01, 0.001C/s. The CCT diagram shows that the grain boundary α is a high temperature product, due to balance between the low driving force and the ease of nucleation along the grain boundaries. The room temperature product will consist of grain boundary allotriomorph only if the "residence time" of the system at high temperature is ~42s. A cooling rate of ~900°C/s, marked in the CCT diagram, shows clearly that the system does not encounter the nose of the CCT diagram.

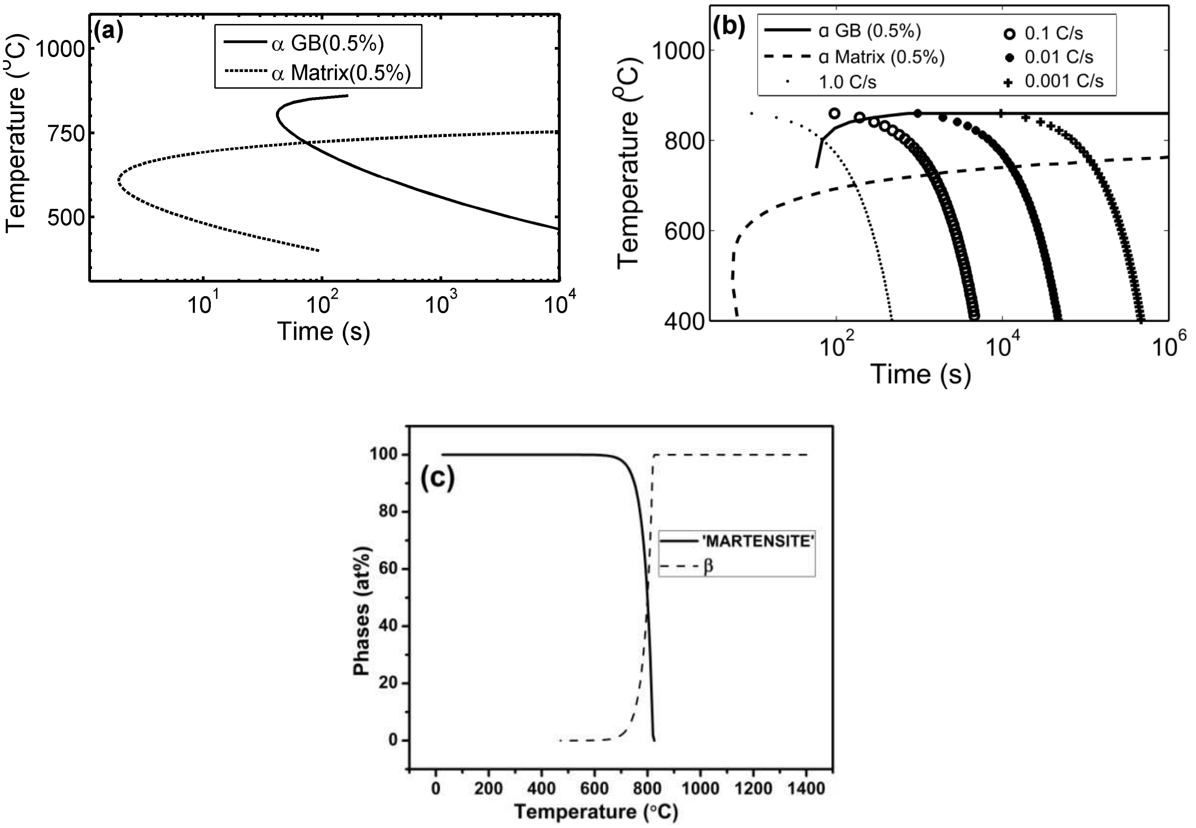

Figure 5.2 JMatPro calculations in Ti-1Mo alloy showing (a) TTT diagram (b)CCT diagram at various cooling rates and (c) phase fraction calculation confirming 100% martensitic transformation of high temperature bcc β phase, cooled at 900° C/s.

The phase fraction calculated using the CCT diagram, for 900°C/s is given in figure 5.2(c). This figure shows the formation of 100% martensite at temperatures below 821°C, thus in agreement with experimental observations and CCT, TTT diagram, presented above. Based on the above results, it is concluded that the high temperature bcc β phase in Ti-1Mo transforms completely to martensitic hcp α′ during water quenching and is in agreement with literature [8, 10].

Further reduction in cooling rate to 3.3°C/s, changes the transformation mode and product of β phase in Ti-1Mo alloy. The optical micrograph in figure 5.3(a) suggests mainly the presence of Widmanstätten transformation products. Scanning electron micrograph [figure 5.3(b)] shows the presence of grain boundary allotriomorph α and presence of fine α plates within the grains. The wide distribution of size of α plates is possibly due to its formation in a range of temperatures, during cooling. XRD experiments were carried out to confirm the crystal structure of product phase. Figure5.3(c) confirms the presence of predominantly hcp α. In addition, the XRD results provided unambiguous signature of bcc β phase also [Figure 5.3(c)]. A non-overlapping $(110)_\beta$ peak along with peaks overlapping with that of hcp α is clearly visible. However, the observed intensity of 100% intense $(110)_\beta$ peak is low. The amount of β phase calculated using Rietveld analysis of the pattern was identified as 5%. In order to confirm the presence of β phase, careful SEM/EBSD phase map studies were carried out. The uniform distribution of very fine particles of bcc β could be obtained using phase map in SEM/EBSD, as shown in figure 5.3(d). The amount of bcc β measured from phase map is ~3% [inset of figure 5.3(d)], which is of the same order of magnitude as that obtained from XRD analysis.

SEM/EDX spot analysis (see figure 5.4) was carried out to determine the chemistry of both α and β phases. However, many regions with Mo concentration ~1 wt% corresponding to α phase were identified. The area with higher concentration of Mo representing bcc β phase could not be identified. This is probably due to smaller size of β particles, which will be demonstrated below, in comparison with the incident probe size and the beam broadening within the specimen. These observations suggest that air cooling Ti-1Mo alloy from the β phase field leads to the transformation of β phase to a lamellar α+β microstructure. The formation of such a Widmanstätten α+β microstructure in Ti-1Mo alloy at a cooling rate of 3.3 °C/s is understandable, since this cooling rate is much less than the critical cooling rate for martensitic transformation, 420 K/s[10]. Optical micrograph of the Ti-1MoFC alloy is shown in figure 5.5(a).The presence of mixture of different morphologies of hcp α microstructure is observed. So, for resolving the finer micro structural details, transmission electron microscopy was carried out. The results presented earlier are reproduced here, again for the sake of completion. The bright field micrograph is shown in Figure 5.5(b) clearly shows the presence of alternate lamellae of α and β phases, typical of Widmanstätten transformation.

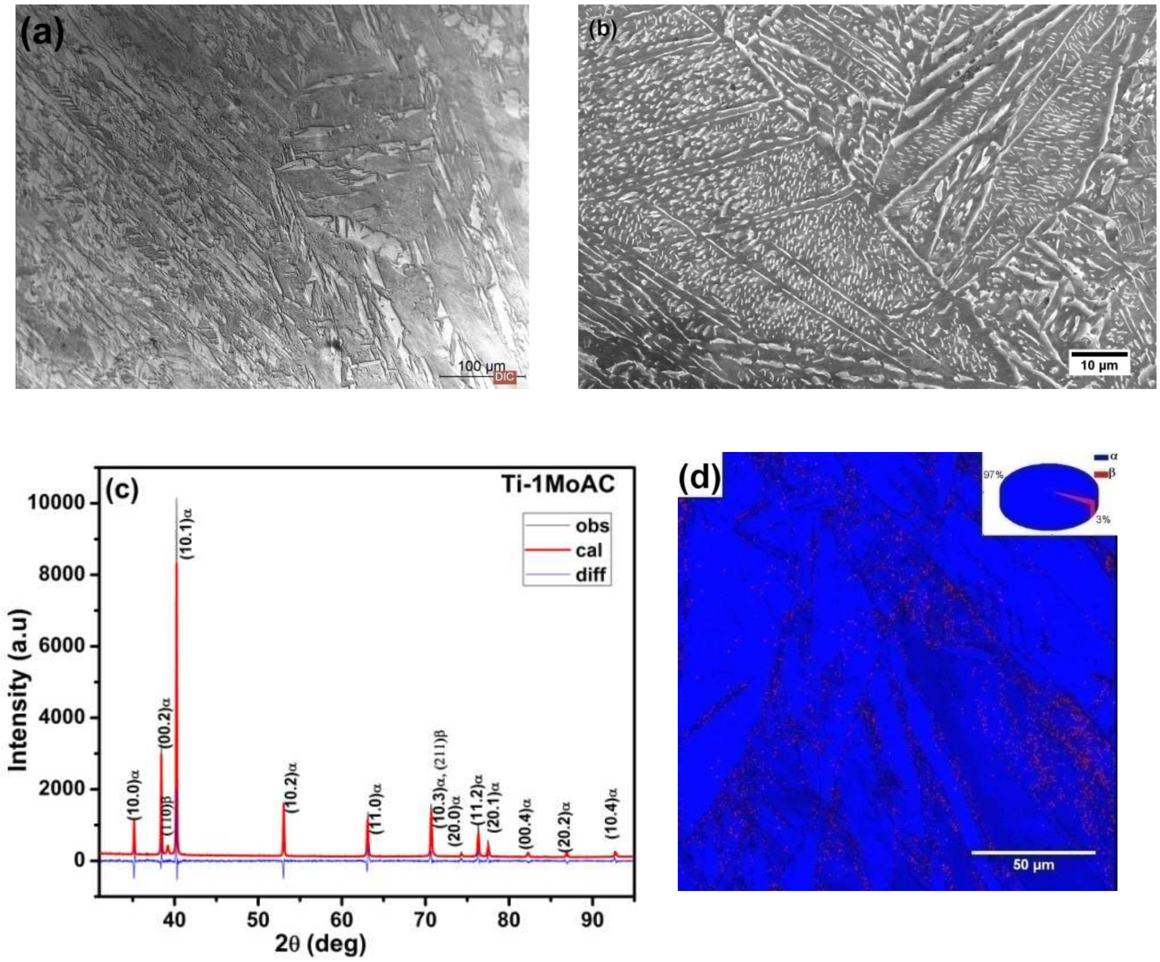

Figure 5.3 Microstructure of Ti-1Mo alloy air cooled from β phase field: (a) optical microscopy and (b) Scanning electron micrograph showing the α+β Widmanstätten structure (c) XRD pattern showing presence of α and β (d) Phase map using SEM/EBSD showing the stringers of bcc β (red) in the predominant hcp α phase (blue); inset shows the pi chart of α and β phase percentage.

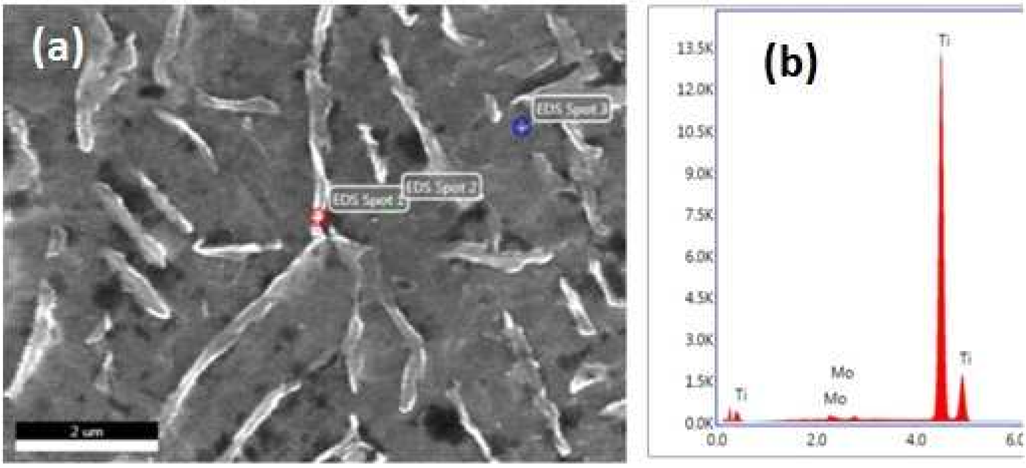

Figure 5.4 (a) SEM image of Ti-1MoAC alloy showing distribution of α plate (b) EDX spectrum taken from spot 1 in (a) indicting the chemistry of α phase.

Formation of coarse grain boundary allotriomorph of α along the prior β boundaries observed in figure 5.5(b), suggests that a diffusional transformation of parent β phase, precedes the Widmanstätten transformation. Similar observation for air/furnace cooled Ti-1Mo alloy has been reported by Flower et.al [17].

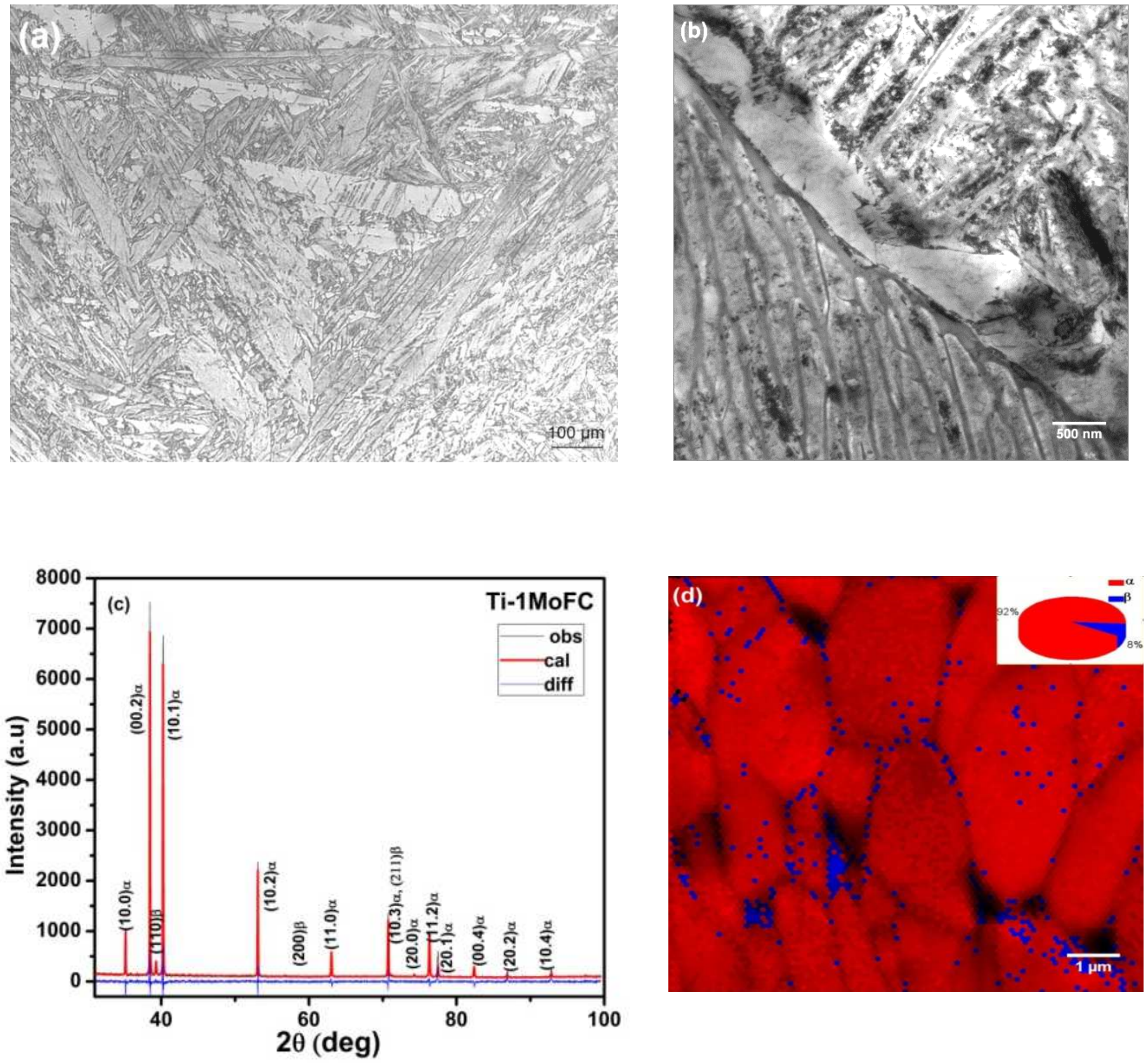

Figure 5.5 Transformation mechanism and products in FC Ti-1Mo alloy: (a) Optical micrograph showing mixture of different morphologies of α phase (b) TEM micrograph showing alternate lamellae of hcp α and bcc β of Widmanstätten product along with grain boundary α(c) Reitveld refined XRD pattern showing presence of α and β phases (d) Phase map using SEM /EBSD showing distribution of isolated fine particles of β phase (blue colour) around the α phase (red colour).

XRD studies [figure 5.5(c)] confirm the presence of both hcp α and bcc β. The phase map of EBSD analysis in figure 5.5(d) shows the distribution of fine β particles, around α grains. The amount of bcc β phase, determined using Rietveld refinement of XRD pattern and the phase map of SEM/EBSD [figure 5.5(d)] confirmed the formation of 7 and 8 % (by volume) of bcc β phase, respectively.

The increase in the amount of bcc β in furnace cooled sample compared to air cooled sample is consistent with the higher residence time for the transformation of parent bcc β phase of the alloy during furnace cooling. Figure 5.6(a) shows typical Widmanstatten structure obtained using TEM. The SAD pattern taken from the same region given in figure 5.6(b) confirms the formation of hcp α and bcc β phases along [41.-3] and [1-10] zone axis respectively. The microchemistry of α and β phases varied widely. TEM/EDX analysis from various regions in figure 5.6(a) shows 0.08-0.47 wt% Mo in α phase and 8.4 to 26.73 wt% Mo in β phase, suggesting the transformation to proceed in a wide range of temperatures, for varying times. Based on the above results, it is reasonable to conclude that the high temperature β bcc phase undergoes diffusional transformations on cooling at the rate of 0.13°C/s resulting in grain boundary α phase and Widmanstätten structure consisting of alternate lamellae of α + β phases.

Calculation of the amount of phases present in Ti-1Mo alloy, cooled at 1.1 C/s, using JMatPro shown in figure 5.2 (a), is in agreement with the above experimental results. Below this critical cooling rate, the mode of transformation changes to diffusional transformation. The results presented so far in the present study are in agreement with earlier observations [10, 12, 17, 18].

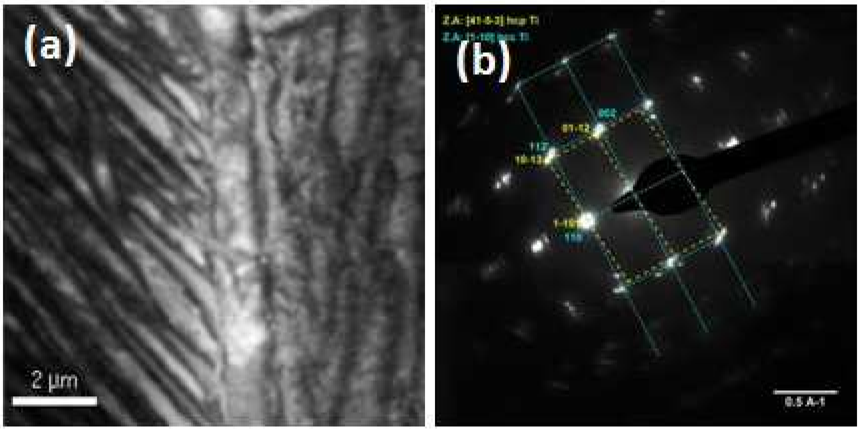

Figure 5.6 (a) TEM micrograph of furnace cooled Ti-1Mo alloy showing the typical Widmanstätten structure consisting of α and β phases. (b) SAD pattern corresponding to the marked area in figure (a) showing the presence of α and β phases.

5.2.2 Studies in Ti-7Mo alloy

The optical and SEM micrographs of Ti-7MoWQ alloy shown in figure 6.7(a) and (b) respectively shows distribution of coarse and fine plates with twin morphology. The prior β grain size, which dictates the martensite plate size, was estimated to be about 1.2 ± 0.2mm. EDX analysis in SEM showed compositional invariance throughout the sample as in Ti-1MoWQ. XRD pattern shown in figure 5.7(c) confirms the formation of 100% base centered orthorhombic α″ phase. The TEM micrograph shown in figure 5.7(d) shows the formation of orthorhombic α″ with plate morphology. The inset in figure 5.7(d) shows the SAD pattern along [010] zone axis of α″. The above observations confirm [8] the complete transformation of high temperature bcc β to martensitic base centered orthorhombic structure (α″) in the Ti-7MoWQ alloy.

JMatPro calculations have been carried out for Ti-7Mo alloy, for a cooling rate of 1000°C/s and grain size 1.2 mm. The result [figure 5.8] is in agreement with the experimental observations. The Ms temperature for Ti-7Mo alloy, calculated using JMatPro is 571° C and this matches with the value estimated based on literature [10].

Reduction in rate of cooling, to 3.3° C/s is expected to change the transformation mechanism of β phase in Ti-7Mo alloy. The optical microstructure shows the formation of finer grains than Ti-7MoAC. The grain size was evaluated to be 169µm. The size of parent β grains in air cooled Ti-7Mo alloy was observed to be significantly smaller (~100-200 µm) than water quenched samples (~mm), which is attributed to the deformation carried out prior to β solutionising.

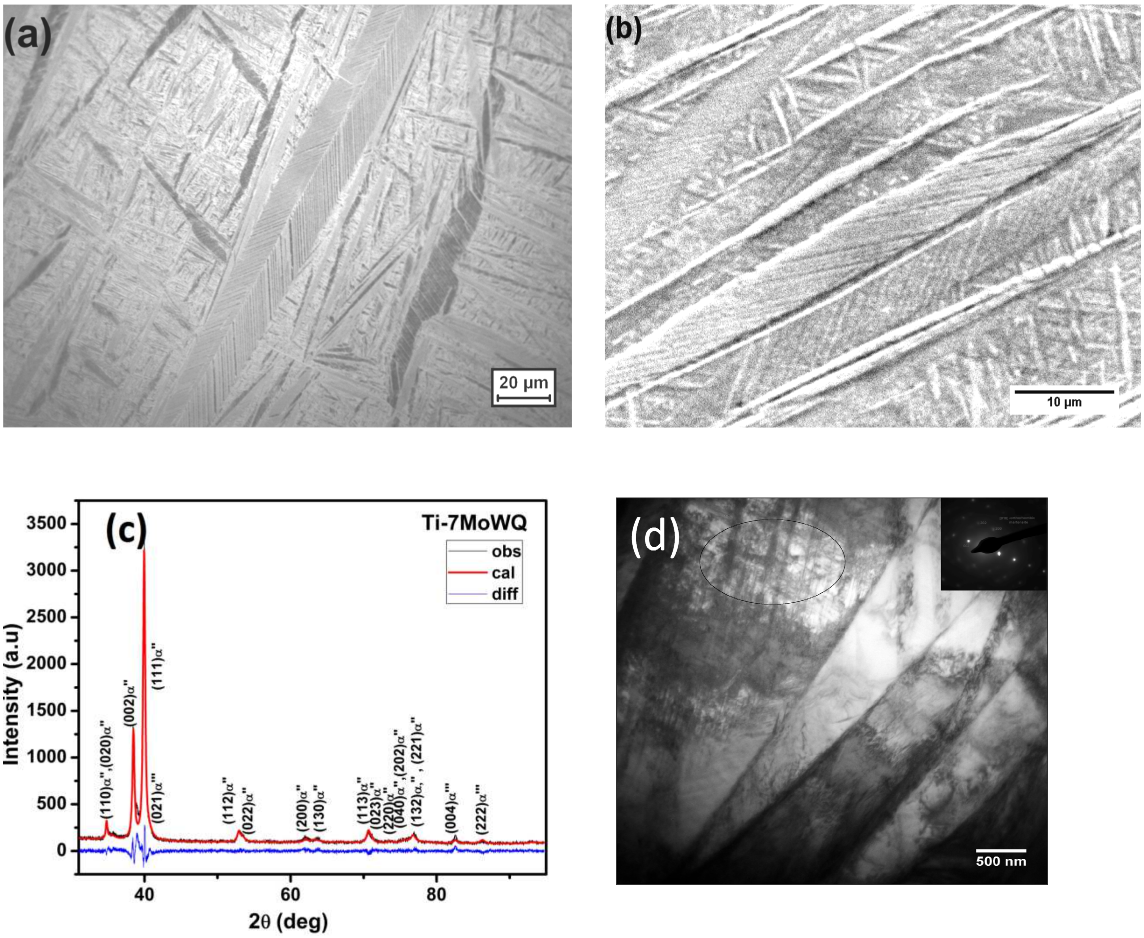

Figure 5.7 Phase transformation mechanism in ice-water quenched Ti-7Mo alloy: (a) Optical (b) SEM micrograph showing plates of martensite (c) Rietveld refined XRD pattern showing orthorhombic α" and (d) TEM micrograph showing orthorhombic plate martensite with inset showing SAD pattern along [010] zone axis.

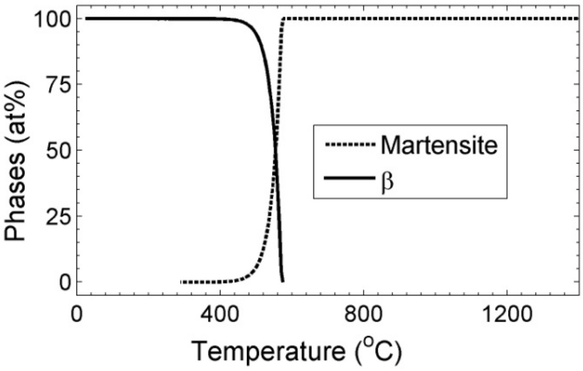

Figure 5.8 JMatpro calculations in Ti-7Mo alloy showing the phase evolution curve showing the transformation of bcc β phase to 100% martensitic structure at an Ms temperature of 571°C.

The SEM microstructure of Ti-7MoAC alloy is given in figure 5.9, which shows three different morphologies of transformation products: (1) primary α plates in the interior; (2) grain boundary allotriomorph of α and (3) occasionally, small packets of Widmanstätten product of α+β. Similar morphology of primary α is reported for many Ti based alloys [14, 17]. EDX analysis in SEM from various regions given in figure 9(a) showed that the concentration of Mo to be ~5wt%

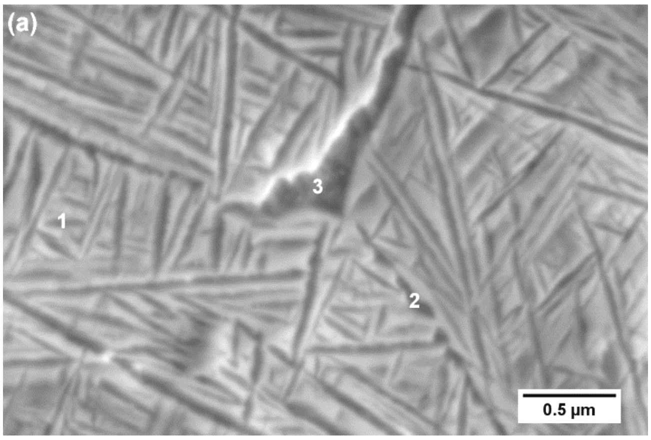

Figure 5.9 Transformation products in air cooled Ti-7Mo alloy: Scanning electron micrograph showing (1) primary α plates, in addition to (2) grain boundary allotriomorphs α and (3)Widmanstätten α+β.

Figure 5.10 shows the XRD pattern of Ti-7MoAC alloy, clearly confirming the presence of hcp α and bcc β phases. However, the hardness, as presented earlier is the highest, which could not have been contributed only by α and β phases. The weak unique peaks of ‘ω’ in Figure 5.10 suggest that the high hardness could be due to the formation of hard brittle, ω phase. It is reported in literature that for Mo content between 5 and 10, the hard ‘ω’ phase is expected to form on aging treatments [12], in the temperature regime of 250° to 450°C, though not during water quenching. The air cooling could have provided the residence time at lower temperatures, required for nucleation and growth of ω phase. Hence, it is concluded that air cooling of Ti-7Mo alloy has led to the formation of α and β phases, by diffusional and the Widmanstätten transformation, in addition to athermal ω phase. The formation of ω phase in the present cooling rate is probably due to the following reason: The diffusion followed by Mo enrichment of β phase is expected to occur at the higher temperature regime. It is possible that the enrichment of Mo in microscopic regions, could have reached the composition range, conducive for formation of ω phase. Under such circumstances, few regions of even Ti-7Mo could have undergone β to ω transformation. If the Mo concentration is very high, the β phase is retained without any transformation, in which case the hardness of the alloy will be low. The absence of α″ in Ti-MoAC suggests that lowering the cooling rate suppresses the martensitic transformation, in preference to diffusional and Widmanstätten transformation. It is reported in literature that cooling slower than the critical cooling rate changes the mode of shear transformation from martensitic to Widmanstätten. JMatPro calculations have not been carried out for Ti-7MoAC, since JMatPro does not take into consideration the formation of ω phase.

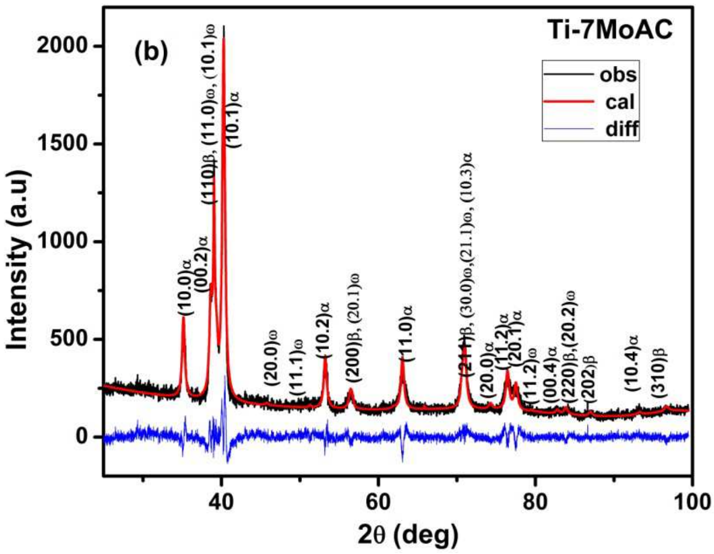

Figure 5.10 Rietveld refined XRD pattern showing the co existence of α, β, and ω phases in Ti-7MoAC alloy.

Further reduction in cooling rate of β phase in furnace cooled Ti-7Mo alloy, resulted in a microstructure (figure 5.11(a)) consisting of (a) the prior β grain boundary along with Widmanstätten structures and (b) an enlarged portion of Widmanstätten structures (c) the discrete plates of primary α homogeneously distributed inside the grain. The EBSD phase map [figure 5.11(b)] shows the well resolved individual alternate lamellae of hcp α and bcc β phases, confirming Widmanstätten transformation. Detailed TEM analysis revealed the presence of hcp α grains, within which coarse lenticular plates of β phase could be seen as shown in figure 5.11(c) and (d). EDX analysis in TEM has been carried out to study the composition of constituent phases. Figure 5.11(e) shows the EDX spectrum taken from α and β phases. The analysis could identify the concentration of Mo varies from 0.22 to 1.43 wt% in the regions identified as hcp α and 11.08 to 13.53 wt% in the regions corresponding to bcc structure. The XRD pattern of the furnace cooled Ti-7Mo alloy shown in figure 5.11(f) confirmed the formation of hcp α and bcc β phases, irrespective of whether they are formed *via* Widmanstätten or diffusional transformation. There was no signature of orthorhombic α″. The above observations confirm that furnace cooling of Ti-7Mo alloy promotes formation of

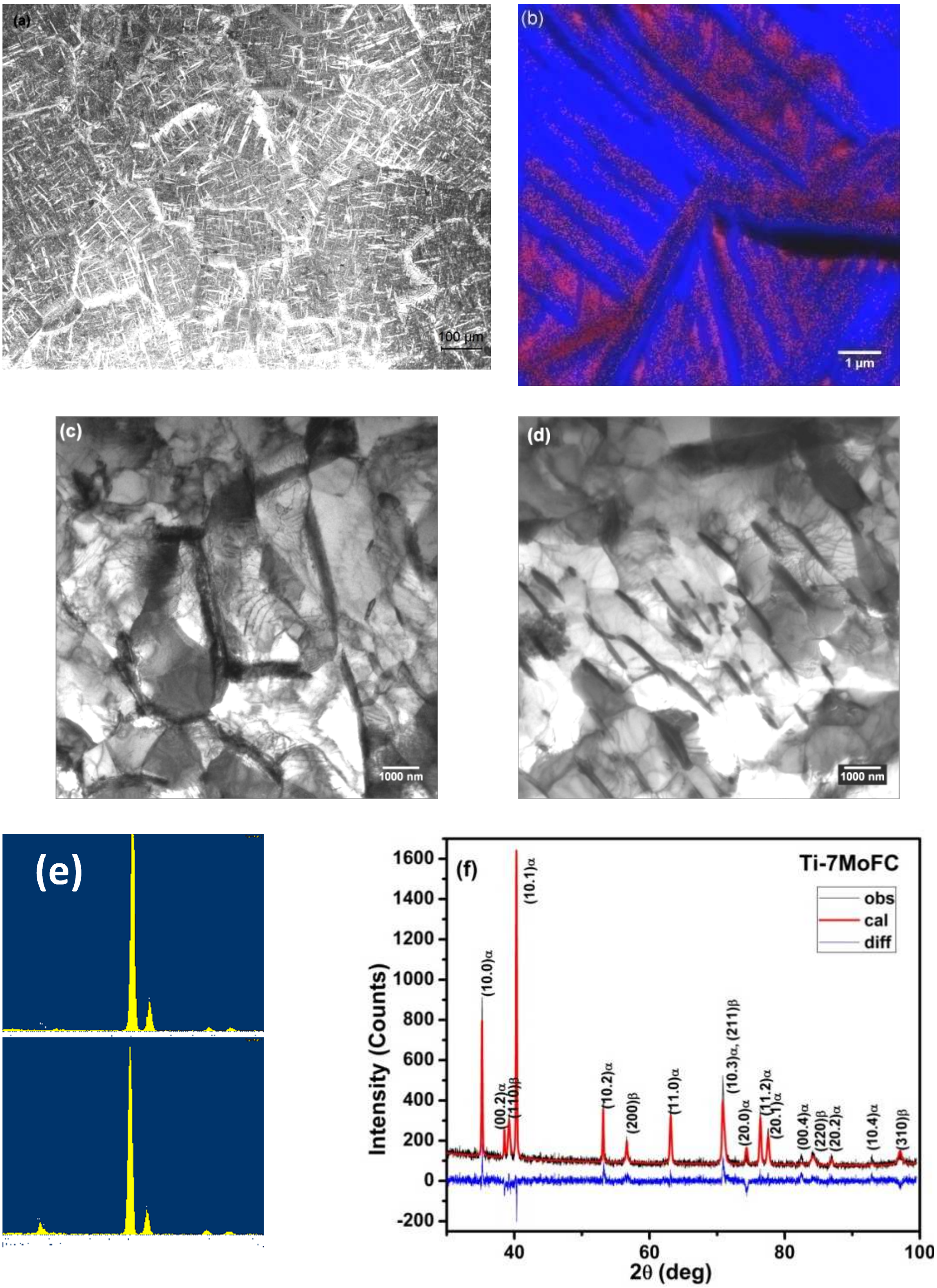

Figure 5.11 Transformation mechanism in furnace cooled Ti-7Mo alloy (a) Optical micrograph showing primary α plates, along with Widmanstätten products within the grains (b) SEM/EBSD phase map showing well resolved lamellae of α (blue) and β (red) of Widmanstätten products (c and d) Transmission electron micrograph showing growth of fine α grains and lenticular β phase within α grains. (e) TEM/EDX specta of α and β phases showing enrichment of Mo in β phase and (f) Rietveld refined XRD pattern confirming presence of α and β phases.

α″ phase. The above observations confirm that furnace cooling of Ti-7Mo alloy promotes formation of equilibrium α+β by the high temperature diffusional transformation, in addition to Widmanstätten transformation.

The experimental results described above match well with predictions of JMatPro, as shown in Figure 5.12 wherein the room temperature products are only α and β phases

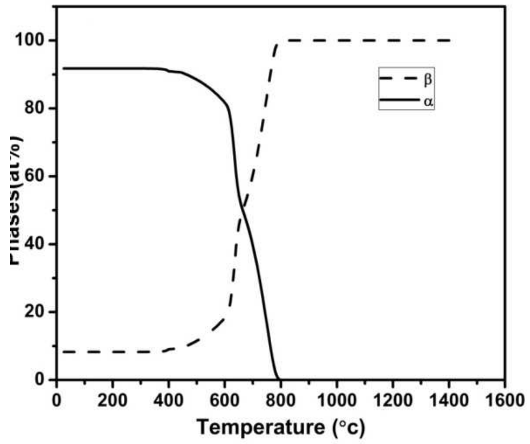

Figure 5.12. JMatpro calculations in Ti-7Mo alloy showing the phase evolution curve showing the transformation of bcc β phase to α+β.

5.3 Variations in crystal structure parameters

Based on morphology and crystal structure, the competing transformation mechanisms of parent β are identified as either martensitic or diffusional. The various transformation products were identified as hcp α', orthorhombic α″, diffusional hcp α and bcc β phases. A detailed examination of the Rietveld refined XRD pattern, in conjunction with microchemistry enables the identification of cooling rate dependence of volume fraction of phases and crystal structure parameters like unit cell dimensions. The results of Rietveld refinement of XRD pattern of Ti-Mo alloys are given in Table 5.1.

Table 5.1 Rietveld refined crystal structure details of Ti-Mo alloys

Alloy	Phase/space group	Lattice parameter (Å)	*Atomic position (x,y,z)*	Vol. fraction (%)	Reliability factors
Ti-1MoWQ	hcp P63/mmc	a=2.9475(2) c=4.6728(4)	*(1/3,2/3,1/4)*	100	Rp=0.07 wRp=0.09 GoF=1.16
Ti-1MoAC	hcp P63/mmc	a=2.9456(7) c=4.6845(1)	*(1/3,2/3,1/4)*	95	Rp=0.10 wRp=0.14 GoF=3.90
	Bcc Im-3m	a=3.2499 (4)	*(0,0,0)*	5	
Ti-1MoFC	hcp P63/mmc	a=2.9481(0) c=4.6810(0)	*(1/3,2/3,1/4)*	93	Rp=0.08 wRp=0.11 GoF=1.85
	bcc Im-3m	a=3.2425(2)	*(0,0,0)*	7	
Ti-7MoWQ	Orthorhombic Cmcm	a=2.9867(6) b=5.0471(21) c=4.6672(7)	*(0,0.18,0.25)*	100	Rp=0.10 wRp=0.07 GoF=1.53
Ti-7MoAC	hcp P63/mmc	a= 2.9483 (2) c= 4.6614 (4)	*(1/3,2/3,1/4)*	72	Rp=0.07 wRp=0.09 GoF=1.97
	bcc Im-3m	a= 3.2616 (3)	*(0,0,0)*	11	
	Hexagonal, ω P6/mmm	a=4.5765(15) c= 2.8368 (5)	*(0,0,0),* *(1/3,2/3,1/2)*	17	
Ti-7MoFC	hcp P63/mmc	a=2.9470(2) c=4.6798(4)	*(1/3,2/3,1/4)*	88	Rp=0.07 wRp=0.10 GoF=1.35
	bcc Im-3m	a=3.2530 (3)	*(0,0,0)*	12	

(1) Table 5.1 confirms the formation of 100% martensite α' and α″ in 1 and 7 wt% Mo alloys respectively on water quenching (~900°C/s). Though many papers deal with the different phase transformation aspects in titanium alloys, Rietveld refined details are available only for very few systems [18-22]. Chun-Xia Li *et. al.* [23] has reported that Rietveld refined parameters of orthorhombic α″ for Ti-Mo are rarely reported, unlike Ti-Nb. In this context, the calculations of the lattice parameter, relative shuffle of the atom along 'y' direction of the α″ phase of Ti-

7Mo alloys using Reitveld refinement of XRD data in the present study assumes importance.

(2) Reduction in cooling rate, leads to the formation of diffusional α and β phases, for both the alloys. However, the final products depend crucially on the chemistry, for intermediate cooling rate of 3.3°C/s: diffusional α+β for Ti-1Mo, while diffusional α + β, along with ω, as Mo content is increased to 7 %. This can be understood in terms of β stabilizing effect of Mo, which retards the growth rate of diffusional α with increase in Mo, leading to retention of untransformed β.

(3) There is no significant change in the 'a' and 'c' values of hcp α - irrespective of whether it is a product of diffusion less martensitic transformation (Ti-1MoWQ) or Widmanstätten product (Ti-7MoFC) or high temperature, diffusional transformation (Ti-1MoAC &FC and Ti-7Mo AC & FC). This observation is consistent with the weak temperature dependence of solubility limit of Mo in α (Mo^{max} -0.1 wt% at 695°C and Mo^{min} - 0.02 wt% at 876°C) obtained from phase diagram.

(4) A variation in the lattice parameter of bcc β phase is found to vary depend on both cooling rate and alloy composition: A reduction in lattice parameter (~0.01 Å) was observed in both alloys, as the cooling rate changes from 3.3°C/s to 0.11°C/s. The reduction in lattice parameter is probably due to the higher concentration of Mo in the bcc lattice during slow cooling. This could be attributed possibly due to the formation of most of β phase at lower temperature range, wherein the phase diagram dictates higher amount of Mo in β. This is understandable, based on 'higher residence time' in this temperature regime during slower cooling. A

decrease in lattice parameter of high temperature bcc β phase with increase in Mo content in Ti-Mo alloys has already been reported [10].

(5) Table 5.1 shows the variation in the relative volume fraction of various phases, for the two alloys, with three different cooling rates. As the Mo concentration changes from 1 to 7 wt%, an increase in the volume fraction of β phase was observed in both air and furnace cooling. This is due to the β stabilizing effect of Mo. However, there is no significant variation in the relative volume fraction of bcc β phase for a particular alloy composition between air and furnace cooling.

(6) The transformation products in Ti-7MoAC are α, β and ω. The amount of ω was estimated to be 17%, using Rietveld refinement of XRD data. It is known that 'ω' phase transforms to α phase, on prolonged aging [24].

(7) The volume fraction of hcp α in Ti-7MoAC sample (72%) is less in comparison with Ti-7MoFC alloy (88%). This is consistent with the higher residence time of the alloy during furnace cooling.

5.4 Microstructural map of transformation mechanism and products

The transformation paths and products for Ti-1Mo and Ti-7Mo alloys for different cooling rates, explained in section 5.1, can be summarized in a microstructural map as shown in figure 5.13 and understood in terms of basic thermodynamic and kinetic principles, as explained in this section.

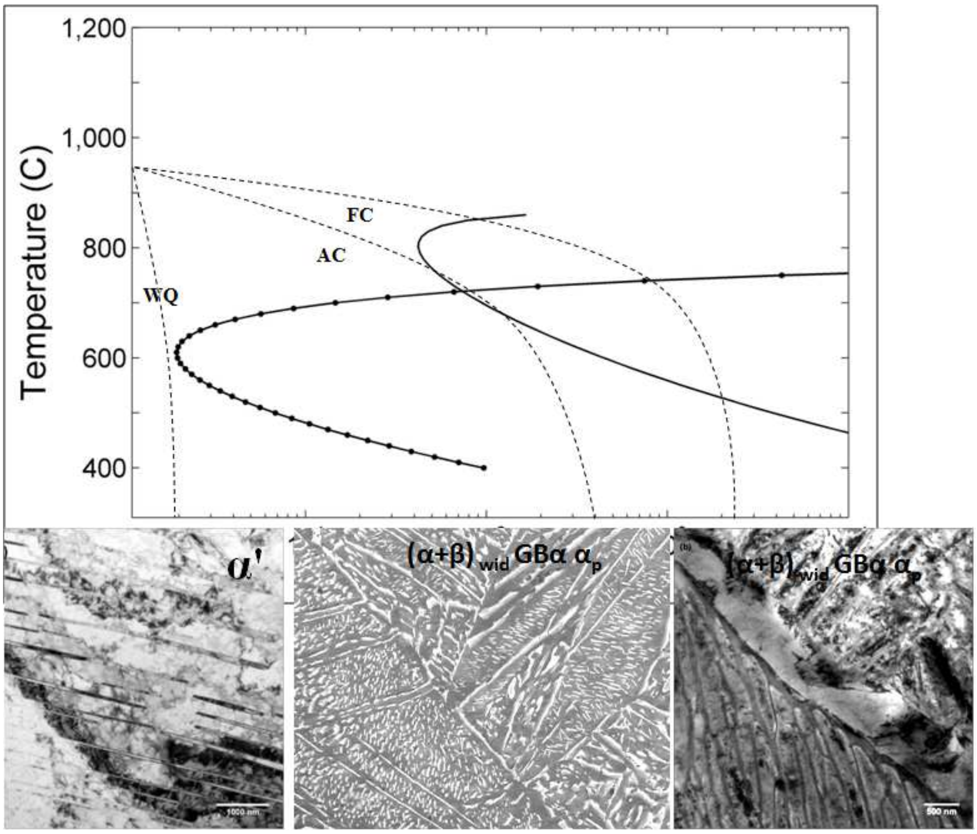

Figure 5.13 Schematic diagram showing the transformation mechanism of β phase in Ti-1Mo and Ti-7Mo alloys. For the purpose of depicting the mechanisms, schematic diagram does not show change in kinetics between 1 and 7 Mo alloys. The TTT diagram at high temperature range represents grain boundary α, while the low temperature one represents diffusional α.

The mechanism and product of transformation of β can be understood in terms of (1) the thermodynamic driving force, which keep continuously changing with temperature, as the system cools, (2) kinetics of competing transformation mechanisms which is dictated by amount of Mo and the (3) residence time of the system at various temperature intervals. Figure 5.14 represents the increase in the thermodynamic driving force, for any chosen alloy of initial composition C_0, at T_2 [figure 5.14(b)], when $T_2 << T_1$ [figure 5.14(a)]. Figure 5.14(b) represents similar concept of reduction in driving force for transformation of β→α, with increase in Mo, at a constant temperature.

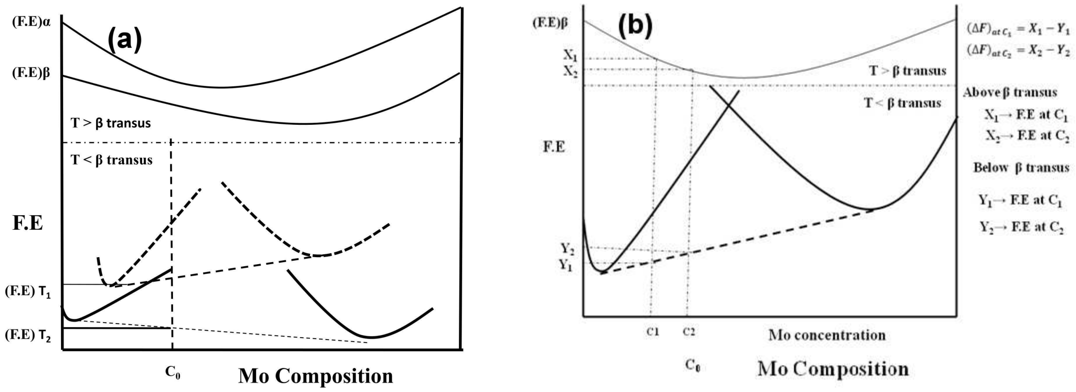

Figure 5.14 (a) A schematic diagram showing the variation in driving force for a given composition at two different temperatures.(b) for two different compositions C_1*and* C_2

For fast cooling rates, the above mentioned driving force is far too low compared to that of martensitic transformation of β to hcp α'. Hence, both systems, Ti-xMo(x=1,7wt%) choose the martensitic transformation in preference to diffusional α. Additionally, the "residence time" during fast cooling is not high enough for the diffusional α to nucleate and grow. The reduction in cooling rate introduces the kinetic factor through the combined role of diffusivity and the 'residence time' at various temperatures. A JMatPro calculation explained in the previous section has quantitatively captured these differences. Hence, TTT curves of both alloys for 0.5% transformation are used for understanding the combined role of chemistry, diffusivity and residence time. The shift of TTT diagram for diffusional matrix α, to larger time (~158s for 7Mo & vs ~2 s for 1) and lower nose temperature (991K for 7 Mo vs 889 K for 1 Mo) with increase in Mo content of the alloy is due to its β stabilizing effect.

Combination of the above two thermodynamic and kinetic factors, enables us to picturise the events that could have taken place in different temperature zones during different cooling rates and to arrive at the sequence of transformation mechanisms and products. A schematic diagram is shown in figure 5.15. In this diagram, critical cooling rate for martensitic transformation is shown. When the experimental cooling rate is faster than the CCR and intersects the Ms before encountering the isothermal TTT curves, martensitic transformation takes place, leading to hcp α' in Ti-1Mo and orthorhombic α″ in Ti-7Mo alloy. But, the transformation sequence in slowly cooled samples can be understood by the curve 3 in figure 5.15. When the system reaches temperatures just below the β transus the first product to form is the grain boundary allotriomorph α, so long as the residence time is at least 42 s at 1079 K for Ti-1Mo or 158s at 783K for Ti-7Mo.

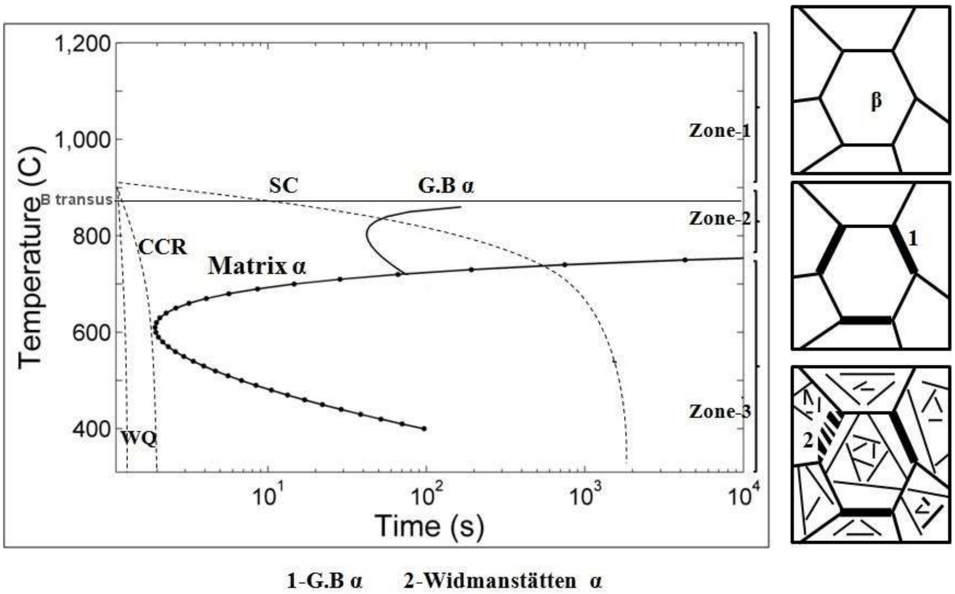

Figure 5.15 Schematic diagram depicting different phase transformation mechanisms for different cooling rates.

This zone can be named as temperature zone -2, while the β phase field is the first zone. The fraction of boundaries along which the α allotriomorphs have formed is dictated by the 'residence time' of the system in this range of temperature, which has been calculated using JMatPro software. At the end of zone 2, certain amount of parent β is expected to be retained. Subsequent cooling, allows the system to encounter the TTT curve for the β → diffusional / Widmanstätten α plates. Hence, the co-existence of primary α plates and Widmanstätten α+β microstructure is observed in slow cooled Ti-1Mo and Ti-7Mo alloys.

Thus, the transformation mechanisms and products discussed so far, can be understood in terms of three different temperature zones, as explained above. The selection of transformation mechanism of β phase in an alloy is dictated mainly by the intersection positions of the cooling curve with TTT curves for grain boundary α and diffusion/Widmanstatten α and the 'residence time' of the system in the three operative temperature zones or martensitic transformation if the cooling rate is above the CCR.

5.5 Influence of transformation mechanism and products on hardness of Ti-1Mo and Ti-7Mo alloys

The variations in the microstructure can influence the mechanical behavior of the alloy. The present section discusses the influence of cooling rate and chemistry on the hardness of the alloy.

The Vicker's microhardness of the Ti-1 and 7 Mo alloys, cooled from the β phase at three different cooling rates are depicted in figure 5.16 and listed in Table 5.2. The salient features are described below.

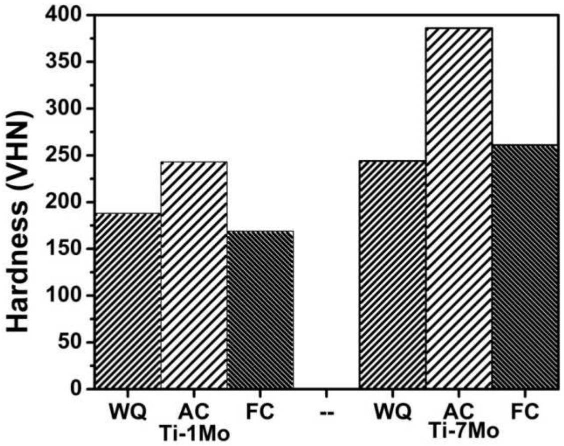

Figure 5.16 Variation in the Vicker's hardness of Ti-Mo(x=1,7wt%) alloys on various cooling conditions.

- For any given cooling rate, the hardness increased with amount of Mo.

Increase in molybdenum content, has increased the hardness of the alloy, as can be seen from the hardness value of Ti-1MoWQ (188 VHN) to Ti-7MoWQ (244 VHN). The possible reasons could be the solid solution strengthening by Mo and the difference in structure of hcp α' and orthorhombic α″ and the grain size. In the present study, the measured grain size of Ti-1Mo was 1.8 mm, in contrast to 1.2 mm in Ti-7Mo alloy.

Table 5.2 Variations in the hardness of Ti-Mo alloy with various cooling rate.

No	Alloy	Hardness (VHN)	Microstructure
1	Ti-1Mo WQ	188±10	martensite, α'
2	Ti-1Mo AC	243 ± 15	Fine Widmansttaten (α+β)
3	Ti-1Mo FC	169 ± 7	Course Widmanstätten (α+β) + grain boundary α
4	Ti-7Mo WQ	244 ± 4	martensite, α″
5	Ti-7Mo AC	384 ± 4	β grains (~μm) smaller than WQ(~mm) +fine ω + Widmanstätten (α+β).
6	Ti-7Mo FC	261± 6	β grains (~μm) smaller than WQ(~mm) + course Widmanstätten (α+β)+ grain boundary α

- For a given alloy composition, a variation in hardness is observed with cooling conditions and was maximum during air cooling.

The transformation mechanisms and products described above can be used to understand the hardening behavior of the alloys. The hardness in Ti-1MoWQ sample (Table 5.2), where 100% martensitic α' formed is lower than Ti-1MoAC, with Widmanstätten α + β. Generally, the martensitic transformation is expected to generate a high density of dislocations and high strain in the lattice and maximize the extent of hardening. However, the current observation is not in agreement with the above expectation. One of the reasons is that the substitutional Mo atoms introduce less strain in the lattice, reducing the extent of hardening. Another reason is that the homogeneous distribution of fine α lamellae in Ti-1MoAC alloy is expected to harden the alloy, much more efficiently than a martensitic microstructure. Flavia *et. al.* [8] reported an increase in the hardness in Ti-Mo alloys due to α phase precipitation during aging. Further reduction in cooling rate to FC of Ti-1Mo has led to a lower hardness, than air cooling. This is mainly contributed by the copious precipitation of “defect free” coarse grain boundary α, in addition to the formation of coarse α+β Widmanstätten structure of the matrix, due to higher ‘residence time’ in high temperature range. In Ti-7Mo alloy also, the grain size of AC and FC alloys is around 150 µm, in contrast to 1.2 mm for WQ alloy. The higher hardness of AC and FC alloys, therefore, is due to a lower grain size.

- The highest hardness is observed in Ti-7MoAC alloy.

The hardness is maximum for air cooling in Ti-7Mo, which is mainly due to the formation of ω phase. Several studies have reported an increase in hardness of Ti based alloys due to the precipitation of ω phase formation [5, 6, 8, 13, 16]. The hardness of Ti-7Mo alloy is less after furnace cooling than AC. The lower hardness is due to the absence of ω phase formation and formation of recrystallised α grains.

The current study has shown that the cooling rate influences the transformation mechanism and products in Ti-Mo alloys. The smaller grain size, fine α plates and formation of hard brittle ‘ω’ increase the hardness. The maximum hardness was obtained for an intermediate cooling rate of 3.3˚C/s.

5.6 Summary

The present study has examined the competing phase transformation mechanisms and products of high temperature parent β phase in Ti-1 and 7 Mo alloys. The selection criteria is understood in terms of thermodynamic and kinetic considerations, based on which the possible sequence of events that could have taken place during cooling have been arrived at. The variation in hardness with chemistry and cooling rate is understood in terms of the phase transformation mechanism and products.

Reference

[1] F. Gil, M. Ginebra, J. Manero, J. Planell, *Journal of Alloys and Compounds* **2001**, 329, 142.

[2] T. Karthikeyan, A. Dasgupta, R. Khatirkar, S. Saroja, I. Samajdar, M. Vijayalakshmi, *Materials Science and Engineering: A* **2010**, 528, 549.

[3] M. Behera, R. Mythili, S. Raju, S. Saroja, *Journal of Alloys and Compounds* **2013**, 553, 59.

[4] T. Ahmed, H. Rack, *Materials Science and Engineering: A* **1998**, 243, 206.

[5] S. Banerjee, P. Mukhopadhyay, Phase transformations: examples from titanium and zirconium alloys, Elsevier, 2010.

[6] M. Sabeena, A. George, S. Murugesan, R. Divakar, E. Mohandas, M. Vijayalakshmi, *Journal of Alloys and Compounds* **2016**, 658, 301.

[7] M. Sabeena, S. Murugesan, R. Mythili, A. Sinha, M. Singh, M. Vijayalakshmi, S. Deb, *Transactions of the Indian Institute of Metals* **2015**, 68, 1.

[8] M. Sabeena, R. Mythili, J. Basu, M. Vijayalakshmi, *Transactions of the Indian Institute of Metals* **2013**, 66, 401.

[9] M. Sabeena, S. Murugesan, R. Mythili, A. Sinha, M. Singh, M. Vijayalakshmi, S. Deb, Influence of Mo in β phase stability of Ti-Mo system: Synchrotron based XRD studies, in: Solid State Physics: Proceedings of the 58th DAE Solid State Physics Symposium 2013, AIP Publishing, 2014, pp. 119.

[10] R. Davis, H. Flower, D. West, *Journal of Materials Science* **1979**, 14, 712.

[11] R. Davis, H. Flower, D. West, *Acta Metallurgica* **1979**, 27, 1041.

[12] F.F. Cardoso, P.L. Ferrandini, E.S. Lopes, A. Cremasco, R. Caram, *journal of the mechanical behavior of biomedical materials* **2014**, 32, 31.

[13] W. Ho, C. Ju, J.C. Lin, *Biomaterials* **1999**, 20, 2115.

[14] T. Furuhara, T. Makino, Y. Idei, H. Ishigaki, A. Takada, T. Maki, *Materials Transactions, JIM* **1998**, 39, 31.

[15] Y. Hao, S. Li, S. Sun, C. Zheng, R. Yang, *Acta biomaterialia* **2007**, 3, 277.

[16] W. Ho, *Journal of Medical and Biological Engineering* **2008**, 28, 47.

[17] H. Flower, *Materials Science and Technology* **1990**, 6, 1082.

[18] S. Banumathy, R. Mandal, A. Singh, *Journal of Applied Physics* **2009**, 106, 093518.

[19] F. Sun, J. Zhang, M. Marteleur, T. Gloriant, P. Vermaut, D. Laillé, P. Castany, C. Curfs, P. Jacques, F. Prima, *Acta Materialia* **2013**, 61, 6406.

[20] J.R.S. Martins Jr, C.R. Grandini, *Journal of Applied Physics* **2012**, 111, 083535.

[21] E. Wu, X. Xu, X. Yuan, X. Guo, S. Wang, *Journal of Alloys and Compounds* **2008**, 458, 161.

[22] I. Lonardelli, N. Gey, H.-R. Wenk, M. Humbert, S. Vogel, L. Lutterotti, *Acta Materialia* **2007**, 55, 5718.

[23] C.-X. Li, H.-B. Luo, Q.-M. Hu, R. Yang, F.-X. Yin, O. Umezawa, L. Vitos, *Solid State Communications* **2013**, 159, 70.

[24]S.K Sikka, Y.K Vohra, R.Chidambaram, *Progress in Materials Science* **1982**, 27, 245.

CHAPTER 6

VARIANT SELECTION MECHANISM DURING TRANSFORMATIONS OF β PHASE IN Ti-Mo ALLOYS

CHAPTER 6

VARIANT SELECTION MECHANISM DURING TRANSFORMATIONS OF β PHASE IN Ti-Mo ALLOYS

6.1 Introduction

The previous chapters have demonstrated the occurrence of many types of phase transformations in Ti-Mo system: diffusional type, like grain boundary allotriomorph, primary α and the shear driven transformations like martensitic α'/α″. The variant selection mechanism normally pertains to the latter type of transformation, since the system strictly obeys the orientation relation between the parent and the product. These type of transformations are either martensitic or Widmanstätten products. In titanium/zirconium alloys, the specific OR *i.e.*, Burger's relation, in the above two transformation types can be stated as follows:

$$\{110\}_\beta // \{0001\}_\alpha \text{ and } <1\text{-}11>_\beta // <11\text{-}20>_\alpha.$$

The OR exhibited by titanium/zirconium alloys is illustrated in figure 6.1.

The product crystal in specific orientation relation with a single parent crystal is called a variant. The number of product crystals which can obey OR depends on the symmetry considerations and the OR. In titanium alloys, as shown earlier, $\{110\}_\beta \,||(00.1)_\alpha$ and $<1\text{-}11>_\beta \,||\, <11\text{-}20>_\alpha$. A typical example of formation of 12 different hcp-α crystals from a single bcc-β crystal, obeying the orientation relation in Ti alloys is shown [1] in figure 6.2.

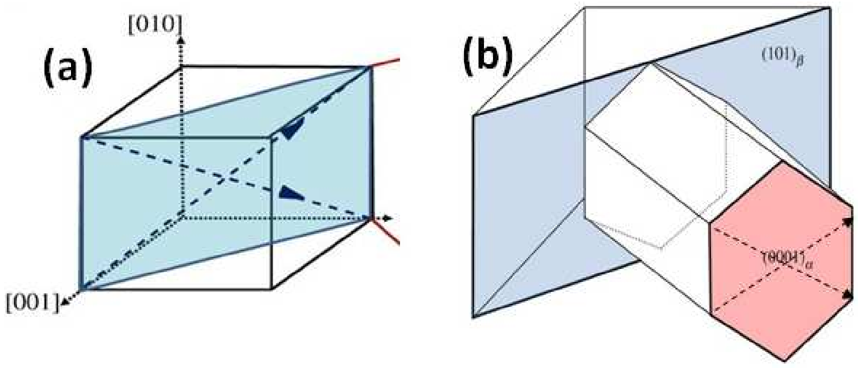

Figure 6.1 Illustration of OR $\{110\}_\beta // \{0001\}_\alpha$ *between parent bcc* β *and product hcp* α *in titanium alloys. (a)* $(101)_\beta$ *in the unit cell of bcc* β *and (b) growth of unit cell of hcp* α*, retaining (00.1)* $_\alpha$ *parallel to* $(101)_\beta$*. The directions* $<1\text{-}11>_\beta$ *marked in (a) is parallel to* $<11\text{-}20>_\alpha$*(arrow).*

If all the above 12 possible α variants from a given single β crystal form with equal probability, the β→α transformation is said to evolve without variant selection. On the other hand, if certain specific variants occur much more frequently than other variants, then the transformation is understood to proceed obeying variant selection mechanism.

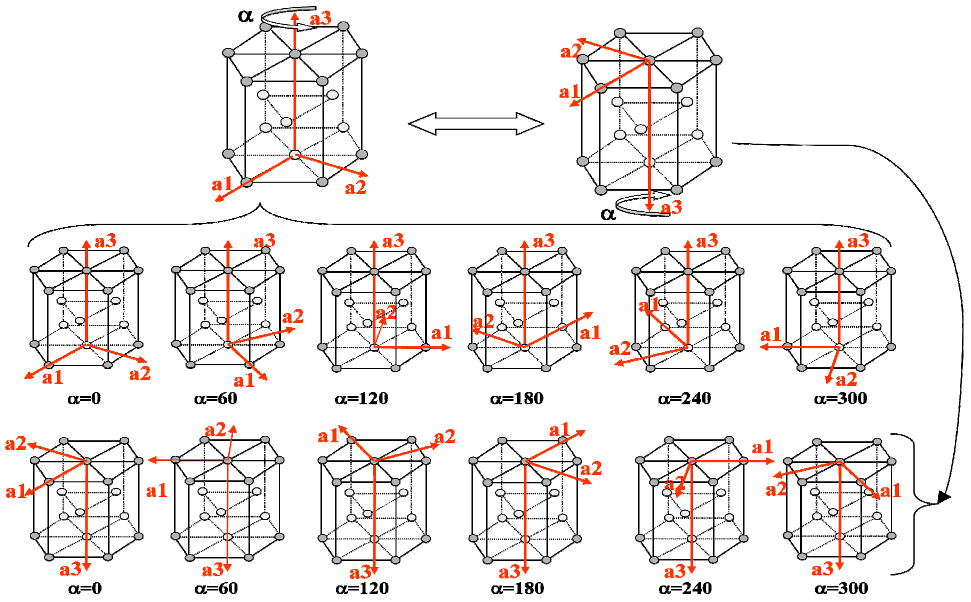

Figure 6.2 Possible twelve variants of hcp α*, for a given bcc* β *crystal, during* $\beta \rightarrow \alpha$ *transformation in Ti alloys.*

Several systems, especially Ti and Zr based systems are reported [2-6] to display variant selection mechanism, especially in the presence of external stress.

Energetically, the variant selection mechanism is preferred by a system, in order to minimize the elastic strain energy of the system. Patel and Cohen model [7] explains the energetic criterion for predicting the variant selection mechanism. The total driving force or the change in free energy is written as follows:

$$(\Delta \mathrm{G})_{\mathrm{Tot}} = (\Delta \mathrm{G})_{\mathrm{chem}} + (\Delta \mathrm{G})_{\mathrm{mech}}$$

The propensity for a system to display variant selection mechanism is minimized when the chemical driving force dominates. The extent of variant selection depends on the ratio of mechanical driving force to the total driving force ($(\Delta G)_{mech.} / (\Delta G)_{Tot.}$) for the transformation.

In the present context, it is interesting to examine if variant selection mechanism reported very often in Ti alloys is operative during β→α transformation in Ti-Mo alloys or not. It is well known that the β→α phase transformation, obeys the Burgers orientation relationship, $\{110\}_\beta||(00.1)_\alpha$ and $<1\text{-}11>_\beta||<11\text{-}20>_\alpha$ [2,9]. Based on crystal symmetry, it is possible to identify 12 crystallographically unique combinations of (110)/ [1-11] parent β phase. Similarly, for every single orientation of β crystal, 12 possible variants of product α crystals can also be identified. It is known that parameters like the chemistry, prior deformation, and cooling rate[1] can influence the probability of variant selection mechanism. Karthikeyan *et. al.* [1] reported the presence of deformation texture in cold rolled Ti-5Ta-1.8Nb alloy and transformation texture during β to α, in the alloy of same composition slow cooled from above the β transus. The presence of grain boundary allotriomorph α formed during slow cooling was found to promote variant selection mechanism during Widmanstätten transformation, to minimize the total strain energy [1].

In the present study, martensitic/Widmanstatten transformations in Ti-1Mo and Ti-7Mo alloys are used to examine the extent of variant selection mechanism, using emerging technique like the precession assisted orientation imaging in TEM and EBSD in SEM.

6.2. Orientation Imaging Microscopy studies

6.2.1 Ti-1Mo alloy

Bright field micrograph and orientation imaging map, both recorded using TEM from the same region of water quenched Ti-1Mo alloy is shown in figure 6.3. It is observed that the orientations of martensite plates in the two adjacent β grains on either side of the grain boundary are completely different. This suggests that variant selection mechanism is not operative. It is also interesting to note that the plates in each β grain are twin related which was also shown in Chapter 3 and 5.

It is generally well known that most of the titanium alloys display [1, 8] variant selection mechanism during martensitic / Widmanstatten transformations. However, on a careful study of the literature, it is found that almost all the alloys which show variant selection mechanism have experienced deformation. It is also known that the mechanical driving force has to be more dominant than chemical driving force for variant selection mechanism to be operative during β to α transformation. Hence, the absence of variant selection mechanism in Ti-1Mo alloy can be understood in terms of (1) high chemical driving force for β to α transformation being close to Ti and (2) absence of any external deformation.

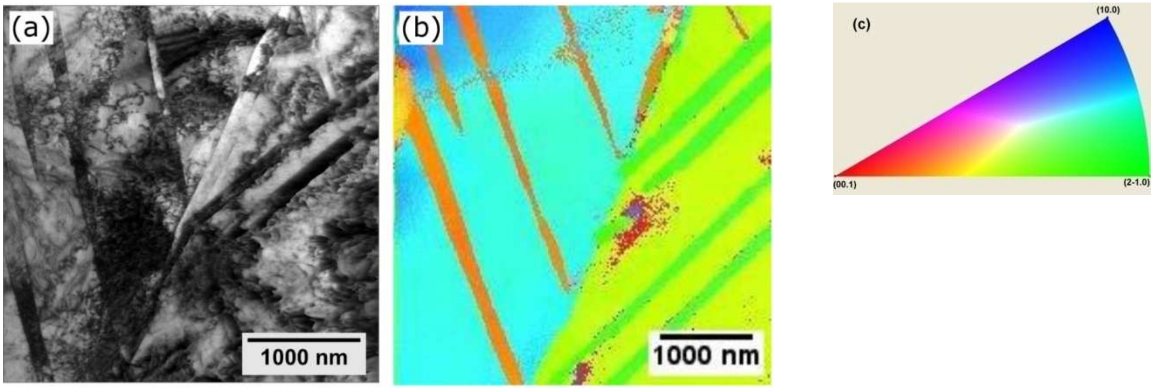

Figure 6.3 Martensite plates on either side of a grain boundary in Ti-1MoWQ alloy in (a) BF image showing hcp martensite (b) orientation map in TEM. The difference in color indicates change in orientation according to the IPF color code for hcp α *phase given in (c)*

In order to examine the influence of other competing reactions during slower cooling and to obtain more meaningful statistical information, EBSD/SEM was carried out in air cooled Ti-1Mo alloy. Figure 6.4 shows the band contrast image of a region near grain boundary, along with orientation and phase map. The results show that the transformation product is predominantly α, on either side of a grain boundary, as expected, in view of very small amount of alloying element, Mo. The orientation image map confirms that the orientations of all the different α packets are entirely independent of each other, confirming the absence of variant selection mechanism.

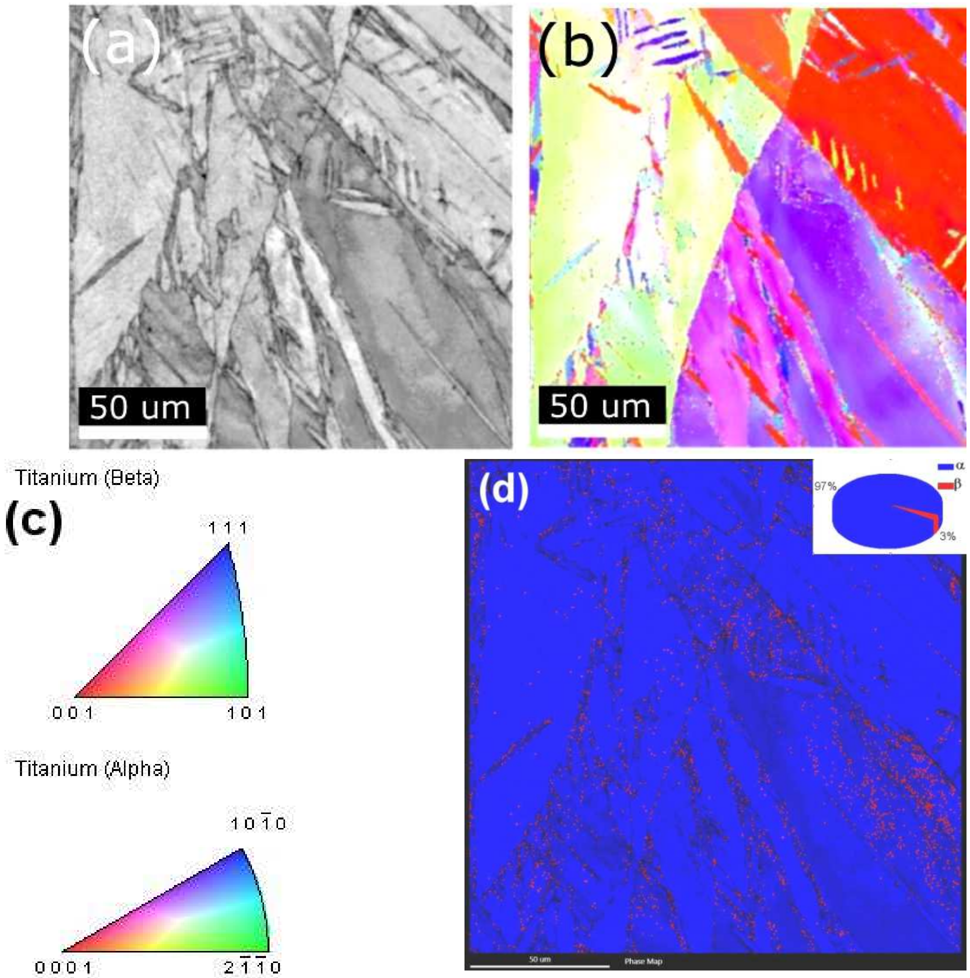

Figure 6.4 EBSD/SEM images of air cooled Ti-1Mo alloy: (a) Band contrast image showing the predominant α plates (b) Orientation imaging map, of same region as in (a) showing that the co-existing regions of α plates do not have same orientation; (c) IPF color code (d) Phase map showing the distribution of small amount of fine β particles (red) in α matrix and inset shows percentage of the two phases.

G.A.Sargent *et.al.* [9] have shown that cooling rate in a β solutionised alloy of titanium influences the variant selection mechanism, which is triggered by transformation strain during β→α transformation. The phase map, in the present study, shows the presence of "disjointed", fine, β particles probably in a lamellar morphology, sandwiched between wide α lamellae. SEM evidence shown in Chapter 5 confirms that the air cooled Ti-1Mo shows Widmanstätten transformation.

Further reduction in cooling rate to furnace cooling of Ti-1Mo alloy, resulted in formation of a Widmanstätten α+β, as shown earlier in Chapter 5. Figure.6.5(a) and 6.5(b) show the band contrast image and orientation map of furnace cooled Ti-1Mo alloy. The low magnification does not permit us to derive reliable inferences. A careful examination of phase map in Figure 6.5 d shows that the β particles in the Widmanstätten lamellae are fragmented. It is also seen that these fine β particles are along the boundaries of a α plate. In order to confirm this, same regions were examined at higher magnification. Figure 6.6 shows the results of these observations. It is clear that well grown α grains, along with uniform distribution of fine β particles along the interfaces, are seen in figure 6.6. More importantly, the orientations of the α grains are not the same. These fine grains are expected to have formed during fresh nucleation and growth of α grain, during the high residence time at higher temperature, during furnace cooling.

It was shown in the earlier Chapter 5 that reduction in the rate of cooling of the high temperature parent bcc β phase, promotes growth of grain boundary allotriomorph, α, Widmanstätten product of alternate lamellae of α+β, in addition to the diffusional α. In order to examine the nature of orientation between the grain boundary allotriomorph of α and Widmanstätten α+β, orientational imaging using PED in TEM with better resolution was more useful, as presented below.

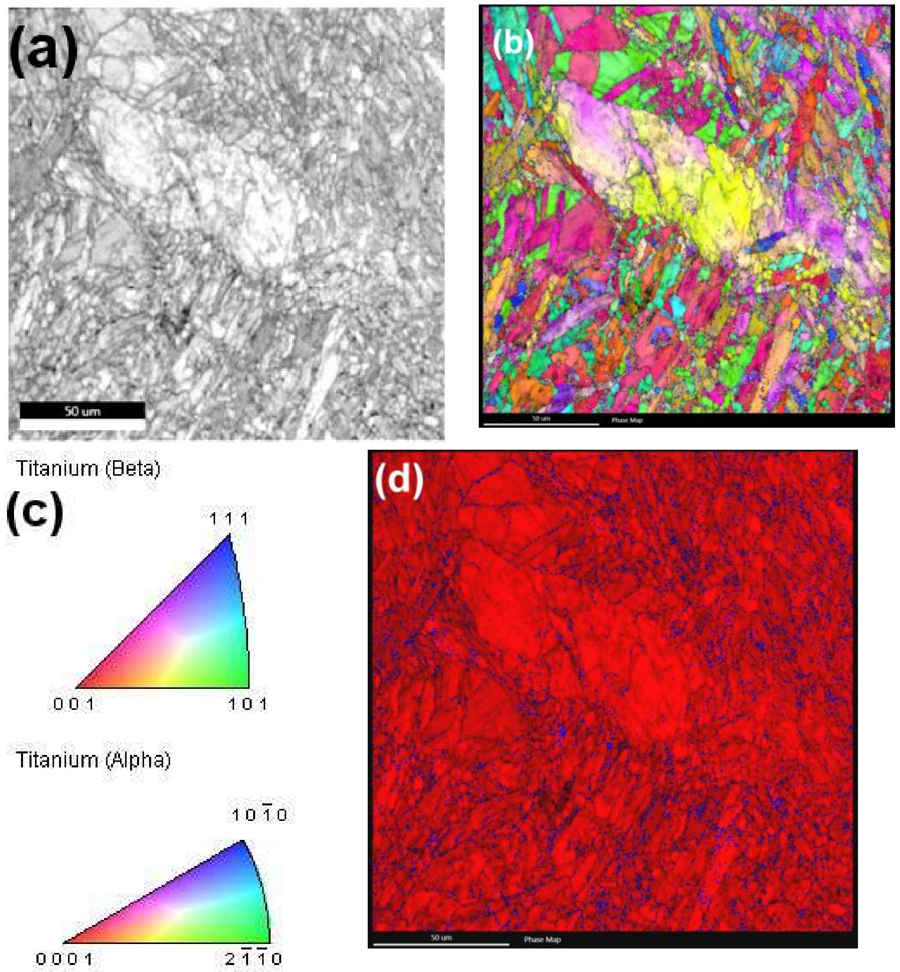

Figure 6.5 (a) Band contrast image of furnace cooled Ti-1Mo alloy showing broad grain boundary α and fine α plates (b) Orientation imaging map, of same region as in (a) showing that the co-existing regions of α with different orientations; (c) IPF colour codes of α and β phases (d) Phase map showing the distribution of small amount of fine β particles(blue) at the boundaries of α plates (red)

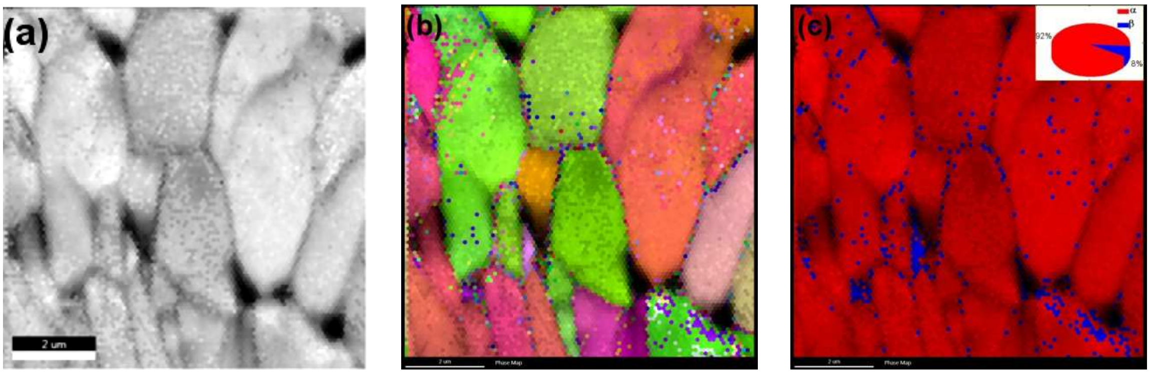

Figure 6.6 High magnification EBSD/SEM images of the same region shown in figure.6.5. (a) Band contrast image showing α grains; (b) Orientation image (c)phase map showing low amounts of fine β precipitates (blue) at the grain boundaries α phase (red)in furnace cooled Ti-1Mo alloy. IPF colour codes of α and β phases are given in figure 6.5 (c).

Figure 6.7 shows the results of orientation imaging studies in TEM of the furnace cooled Ti-1Mo alloy. The BF image is shown in figure 6.7(a), which shows the Widmanstätten lamellae is clearly resolved, though the grain boundary allotriomorph is not very convincing. In order to identify the phases, the phase map was imaged, which is shown in figure 6.7(b). The grain boundary allotriomorph is seen clearly. The orientation image is shown in figure 6.7(c), which shows that alternate lamellae of α and β, in the Widmanstätten colony have the same orientation, as expected.

The grain boundary α appears to have crystals of various orientations, none of which is the same as Widmanstätten α. It has been demonstrated [1, 10] in literature that the grain boundary α will choose that variant which has near Burger's OR with relation to at least one of the β grains. The variant selection is made to minimize deviation of OR with respect to the β grain, which is away from Burger's OR. Extending this line of approach, Karthikeyan *et.al.* [1] have shown that at slower cooling rates, the orientation of the grain boundary allotriomorph α influences the orientation of Widmanstätten α, which grows into the untransformed parent β grains. However, due to the high thickness of the regions, the reliability map of indexing, from these regions appear to be too very low as shown in figure 6.7(d), to draw any meaningful inference about the orientations in grain boundary α or Widmanstätten α, for which the reliability index is too low.

Based on the above studies, it can inferred that there is no strong evidence to support that variant selection mechanism is preferred by Ti-1Mo, during the various transformations of high temperature bcc β phase on cooling.

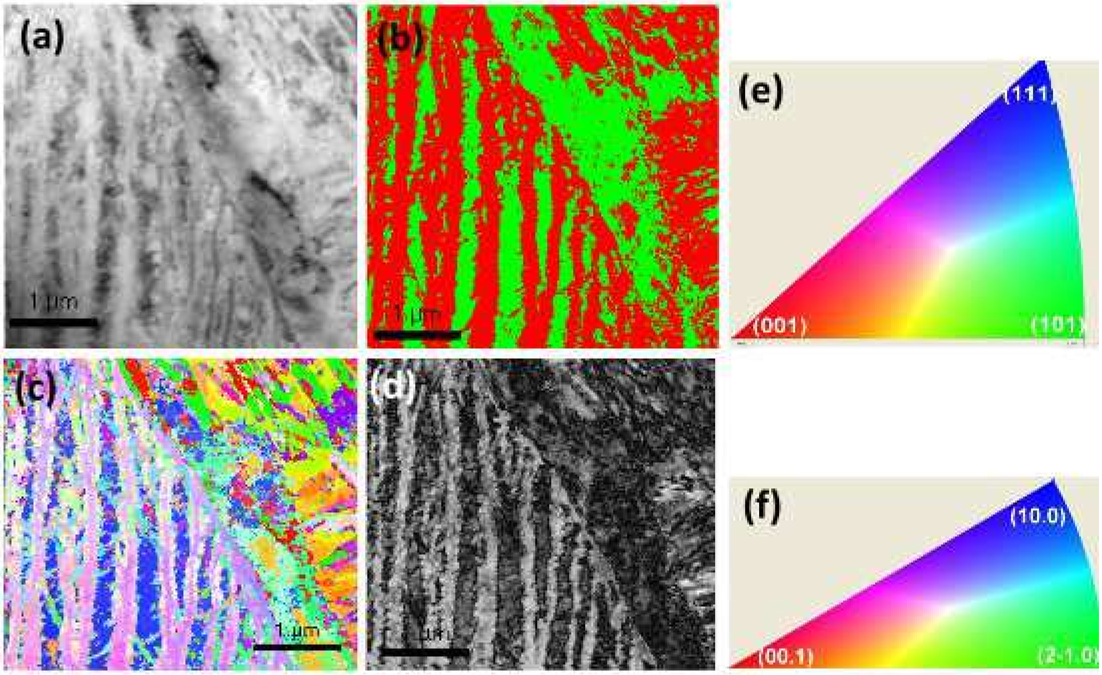

Figure 6.7 Orientation imaging microscopy of furnace cooled Ti-1Mo alloy: (a) BF image showing Widmanstatten structure; (b) phase map (red – bcc β and green – hcp α), showing grain boundary allotriomorph and Widmanstatten lamellae of α and β phases; (c) Orientation map of same region and (d) reliability map, suggesting the determination of orientation of Widmanstätten α alone is reliable.(e)and(f)represents IPF colour codes of α and β phases.

6.2.2 Ti -7Mo alloy

Experiments similar to Ti-1Mo were carried out for Ti-7Mo alloy. It is relevant to recall the fact that the Ti-7Mo alloys were compressed, prior to solutionising, unlike Ti-1Mo alloy. Since the results are more or less the same as that of Ti-1Mo, typical results of furnace cooled alloy alone are presented below.

Figures 6.8 and 6.9 show the series of images for two different types of products formed in the alloy: Widmanstätten $\alpha + \beta$ lamellae near grain boundary α in figure 6.8 and diffusional α grains in the interior of the grains in figure 6.9.

Figure 6.8 shows the band contrast image, orientation image with IPF, phase map along with the color code. Similar to Ti-1Mo alloy, it is seen a Widmanstätten lamellar α+β structure form and the orientation of alternate α lamellae within one colony remains the same, though different from adjacent colony. The results were carefully analyzed to see if the orientation of grain boundary α influences the selection of orientation of Widmanstätten α colony on either side of it. The orientation of unit cells in selected regions A, B and C are marked in figure 6.8(b). It is clearly seen that orientation of region A and B are similar, while it is different for regions A and C, as also shown by the colour scheme. Comparison of orientation

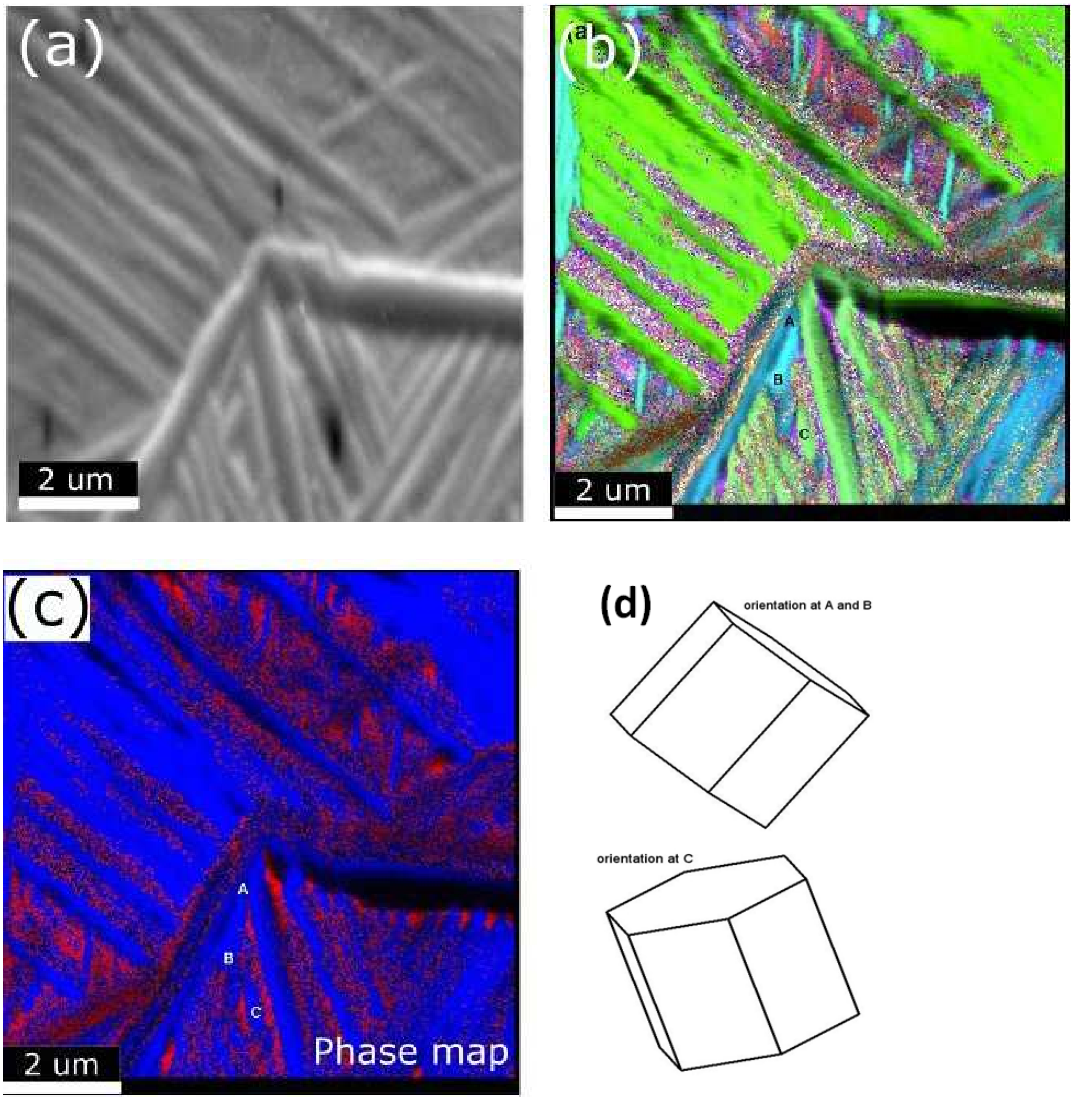

Figure 6.8 EBSD/SEM images of furnace cooled Ti-7Mo alloy (a)band contrast image of the transformation products (b) Orientation image of the same region in (a), showing that orientation of grain boundary α and Widmanstatten α is similar only when not interspersed by β, in between (c) Phase map of the same region (red indicate bcc β and blue indicate hcp α). The rotation of unit cells in A, B and C are also clearly superimposed. (Inverse Pole Figure is same as in figure 6.5(c).

map and phase map, suggests that similar orientations are selected between two regions if there is no bcc β in between. Hence, it can be concluded that there is a tendency for variant selection mechanism to operate in Ti-7Mo alloy, though there is no strong evidence for variant selection mechanism.

The orientation of the diffusional α grains in the interior of the high temperature β grains in furnace cooled Ti-7Mo alloy was studied high resolution by OIM in TEM. The results are shown in figure 6.9 (a-d). BF image in Fig. 6.9(a) shows the presence of lamellar α and β phases. The orientation map in fig. 6.9(b) shows the orientation of α and β phases. The identification of α and β phases is carried out using the phase map in figure 6.9(c).

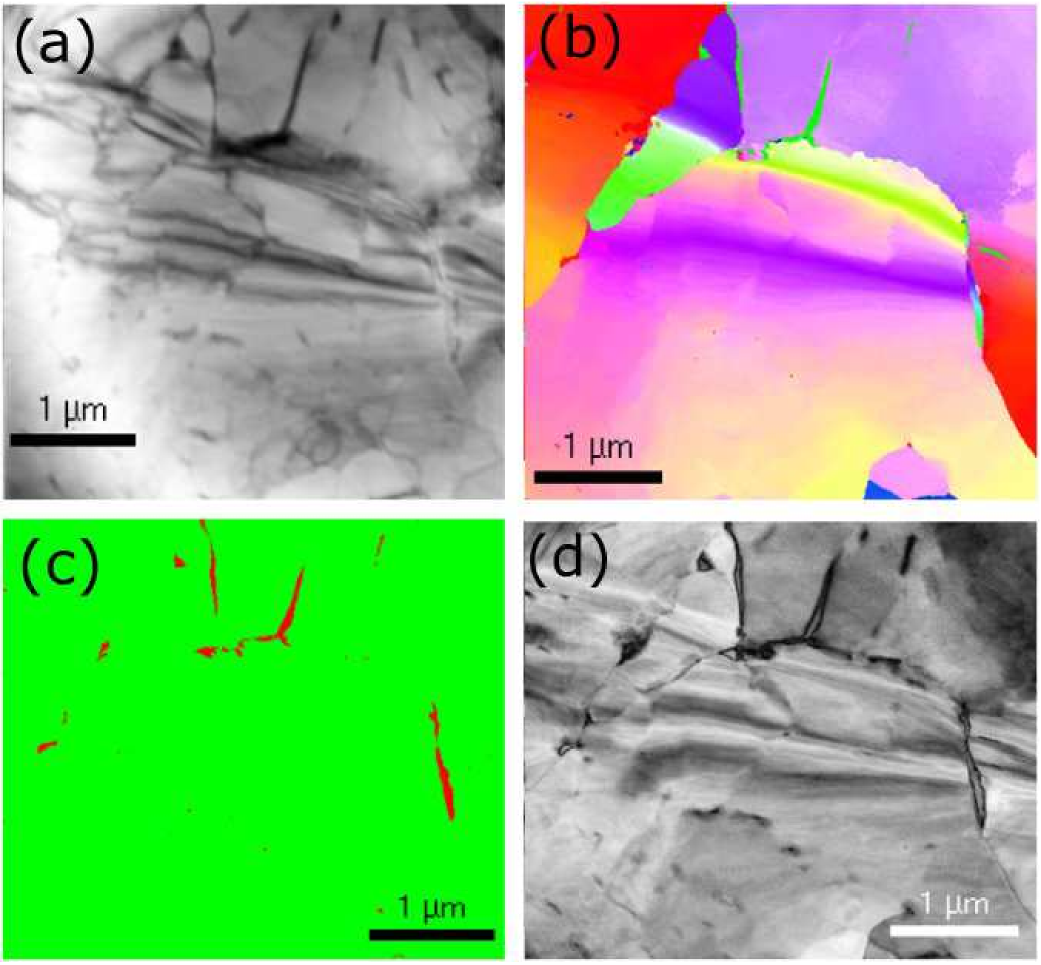

Figure 6.9 Orientation imaging studies in TEM for furnace cooled Ti-7Mo alloy, (a) BF image showing lamellae of α and β phases originating from grain boundary α, (b) orientation imaging map, (c) Phase map (green-α and red - β) and (d) reliability map.

The orientation of α phase is predominantly similar within a colony, with small misorientations. But adjacent α colonies have completely differing orientations as seen from figure 6.9(b). The reliability map in figure 6.9(d) suggests the reasonable indexing of α and β phases used for fig. 6.9(b) and 6.9(c). Confining to regions with high reliability index, it is clear that the orientation of all adjacent α colonies are different, thus reconfirming the absence of variant selection mechanism even during slow furnace cooling of Ti-7Mo alloy. This could be understood in terms of high residence time during furnace cooling, promoting diffusional transformations in this region.

6.3 Reasons for the possible absence of variant selection mechansim

The complete absence of variant selection mechanism in Ti-1Mo and weak tendency in Ti-7Mo can be understood based on relative role of chemical and mechanical driving forces for the β to α transformation. As stated in introduction, the variant selection mechanism is dominant when the 'mechanical' driving force for the transformation is dominant. In the present study, there was no external stress and the samples have not been subjected to any deformation, at any stage of the experiment for Ti-1Mo alloy. However, Ti-7Mo alloy was compressed prior to solutionising. Hence it appears that the different types of transformations are allowed to proceed predominantly by the 'chemical' driving force. It is expected that the advantage of lowering the strain energy *via.*, variant selection mechanism under the experimental conditions of the present study is not too high in terms of minimization of strain energy of the system. In Ti-7Mo alloy, where prior deformation was present, there is signature of weak variant selection mechanism, in regions which have undergone Widmanstatten transformation. Hence, the behavior of the two alloys studied, suggest that mechanical driving force has to be dominant for the variant selection mechanism to operate.

It has also been shown in literature [1, 9, 10] that the system has “memory” of the selection mechanism, during any stage prior to the specific phase transformation. Karthikeyan *et.al.* [1, 10] have shown that the deformation texture influences the subsequent recrystallisation and transformation textures. It is also shown that if the system is taken to liquid state, by erasing the memory of any type of previous history, variant selection mechanism is not operative. J. Romero [2] has observed hardly any variant selection during $\alpha \rightarrow \beta$ transformation in a Zr based alloy, when the β solutionising is carried out for very long time at temperatures far higher than β transus. This suggests that the recrystallisation texture of β could probably be due to incompleteness of $\alpha \rightarrow \beta$ transformation. Thus, variant selection mechanism is unlikely if the parent β grains have truly random orientations and no/not enough deformation is applied to the system, as has been the case in our present study.

6.4 Summay

The orientation imaging microscopy studies using SEM and TEM have confirmed that variant selection mechanism is not strongly operating in Ti-xMo alloys (x=1,7wt%) , for the cooling rates employed in the present study. The absence of variant selection mechanism is understood in terms of absence of / insufficient mechanical driving force and domination of chemical driving force for the transformation of high temperature parent bcc β phases.

References

[1] T. Karthikeyan, A. Dasgupta, R. Khatirkar, S. Saroja, I. Samajdar, M. Vijayalakshmi, *Materials Science and Engineering: A* **2010**, 528, 549.

[2] J. Romero, M. Preuss, J.Q. Da Fonseca, *Acta Materialia* **2009**, 57, 5501.

[3] N. Stanford, P. Bate, *Acta materialia* **2004**, 52, 5215.

[4] P. Gaunt, J. Christian, *Acta Metallurgica* **1959**, 7, 534.

[5] S. Kundu, *Materials Science and Technology* **2014**, 30, 867.

[6] H. Beladi, Q. Chao, G.S. Rohrer, *Acta Materialia* **2014**, 80, 478.

[7] J. Patel, M. Cohen, *Acta Metallurgica* **1953**, 1, 531.

[8] D. Banerjee, J.C. Williams, *Acta Materialia* **2013**, 61, 844.

[9] G. Sargent, K. Kinsel, A. Pilchak, A. Salem, S. Semiatin, *Metallurgical and Materials Transactions A* **2012**, 43, 3570.

[10] T. Karthikeyan, A. Dasgupta, S. Saroja, R. Khatirkar, M. Vijayalakshmi, I. Samajdar, *Materials Science and Engineering: A* **2008**, 485, 581.

CHAPTER 7

CHARACTERISTICS OF $\beta \rightarrow \omega$ TRANSFORMATION IN Ti-15Mo ALLOY

CHAPTER 7

CHARACTERISTICS OF β→ω TRANSFORMATION IN Ti-15Mo ALLOY

7.1 Introduction

β→ω transformation in Ti/Zr alloys has provided a paradise for physical metallurgists, due to the interesting insight that this transformation offers. Additionally, the necessity to develop titanium alloys for biomedical [1] applications has driven extensive research in the study of mechanical properties of ω forming titanium alloys.

The earliest detection of ‘ω’ in Ti and Zr under pressure was based on XRD studies [2]. The formation of ω was proposed based on similarity with the structural details of ‘ω’ in Ti-V, Zr-Nb and Zr-V, which generated intense interest in β→ω transformations subsequently. The extensive literature available so far have confirmed the conditions with respect to alloy chemistry, pressure, temperature and rate of cooling, under which the β→ω transformation in titanium and zirconium alloys is favoured [3]. These observations have been understood in terms of existence of favourable e/a ratio, and subsequent detailed rationalisation based on electronic structure [4, 5] and lattice dynamics [6, 7]. The β→ω transformation is understood in terms of “lattice collapse mechanism” and the onset and growth of “displacement wave vectors” due to minimization of free energy corresponding to specific displacement amplitude. It is shown that β→ω transformation proceeds by collapse of $\{111\}_\beta$ planes, wherein the extent of collapse dictates the ω to be either hexagonal [8] or trigonal [9], which is dictated by the amount of β stabiliser in the alloy. The morphology of ω in Ti/Zr alloys is either ellipsoidal or cuboidal, depending on the balance between misfit and interfacial energy.

The β→ω transformation can proceed either by a displacive mechanism during quenching from the β phase field, leading to athermal ω or by a diffusional mechanism resulting in isothermal ω. The degree of collapse and amount of displacive, athermal ω, increased with cooling rate. Strong diffuse scattering in neutron, electron and X-ray diffraction patterns, characteristic of athermal ω, confirmed the deviation from ideality in the expected lattice correspondence. The partial collapse of (222) β planes, in athermal ω, resulted in retention of trigonal symmetry along <111> direction of bcc, leading to incommensurate structure. In contrast, isothermal ω is found to grow around the embryos of athermal ω, by out-diffusion of β stabilising solutes, which subsequently act as nucleation centre for hcp α. The degree of collapse is complete leading to discrete diffraction intensity maxima, dividing the reciprocal lattice vector $\mathbf{g}_{112}$ of β phase into three equal parts. The completion of collapse yields a hexagonal symmetry to the product with a commensurate structure.

The 'ω' phase particles in titanium and zirconium alloys [3, 10-13] are known to significantly strengthen the alloys, with a concomitant reduction in ductility, leading to "ω - embrittlement". In early days, Silcock [11] proposed that the embrittlement could be due to one of the following three reasons: inhomogeneous slip or unfavourable orientations of three variants or the coherency strain of β introduced by ω. Wen-Fu Ho [12] have attributed ω - embrittlement to dispersion hardening of the alloys and found [3] to be significant for volume fraction of ω higher than 0.6. The micro-void coalescence mechanism of failure is reported [3] in ω containing alloys, wherein the dimple size was found to depend on ductility. The strengthening mechanism was found to be either by-passing [3] of ω particles, or "shearing mechanism". Of late, the emphasis on development of bio-medical implants has provided a large impetus for the development of low modulus alloys. The steep increase in modulus values in the 'ω' containing titanium alloys, has motivated recent spurt of modelling studies.

These studies have been successful in predicting the composition of titanium alloys, to avoid ω and achieve modulus compatible with bone.

One of the proposed reasons for the brittle nature of ω containing titanium alloys is its covalent nature of bonding, for which there is no direct confirmation, despite extensive studies on electronic structure of ω phase. Early studies have proposed two models for the electronic structure of 'ω' in Group IV transition metals and alloys: localization of 'd' electron model of Jamieson [2] and graphitic bonding model of Doherty and Gibbons [5]. The former is based on application of Pauling's valence bond model to the observed interatomic distances, which could explain the reported changes in volume and electrical resistance of Ti and Zr under pressure. The latter model is based on the different types of bonding in the two different sites of 'ω': one of metallic nature and the other of covalent nature using sd^2 hybridized orbital, similar to sp^2 in graphitic structure. However, both models suggest reduced metallic character of 'ω' phase compared to α or β phase. Subsequent studies on temperature and pressure dependence of electric field gradients, XPS studies and band structure calculations, support the graphitic bonding model, which could also explain the high hardness of 'ω' containing alloys and hence is widely accepted. Few ab initio calculations have extended [4] the calculations to the maps of electron localization function, which show only the non-spherical nature of electron density around atoms. Some of the first principle calculations have suggested the non-uniform strength of bonding in different planes of ω, based on correlations between crucial interatomic distances. There are very few studies on the nature of bonding of ω that too, only in pure titanium and Ti-V alloy [14-17]. In this context, the current study on bonding of various metastable phases using XRD in Ti-Mo appears to be the first experimental attempt.

The current chapter 7 on “Characteristics of β→ω transformation in Ti-15Mo alloy” presents the Rietveld analysis of XRD patterns using synchrotron and Cu-Kα sources and phase contrast microscopy of product phases of high temperature bcc β phase in Ti-15Mo alloy, after quenching the β phase at different cooling rates and isothermal exposure at 748K. The comparison in the characteristics of ω^{ath} and ω^{iso}, the nature of bonding in ω^{iso} and the strengthening mechanism by the formation of ω are highlighted based on unit cell dimensions, interatomic distances, 3-D strain distribution, electron density distribution maps and atomic column contrast images from hcp α, bcc β and hexagonal ω. The characteristics of ω^{ath} and ω^{iso} are compared with respect to the extent of displacement during the ‘lattice collapse mechanism’, symmetry of the phases and morphology, using Fourier filtering technique to image atomic column contrast, for the first time in literature. Identification of ‘graphite-like’ bonding in ω^{iso} based on the interatomic distances and electron density distribution is another novelty of the present studies.

7.2 Characteristics of ω phase

The results on Rietveld analysis of XRD patterns using synchrotron and Cu-Kα sources and phase contrast microscopy of product phases of high temperature bcc β phase in Ti-15Mo alloy, after quenching the β phase at different cooling rates and isothermal exposure at 748K are presented in the sequence of characteristics of ω^{ath} and ω^{iso}.

7.2.1 Characteristics of athermal ω phase

The unambiguous characterization of crystal structure details, micro structural parameters and bonding characteristics of ω phase requires high quality diffraction data. This is rendered difficult in XRD studies of Ti-Mo alloys, due to the low intensity of unique peaks of ω and overlap in high intensity peaks of β and ω phases. Hence, synchrotron XRD experiments have been carried out to enhance the intensity of unique, low intense peaks of ω. Another method to obtain reliable, measurable intensity of unique ω peaks is to promote β→ω transformation. Extensive studies have shown that, increase in the cooling rate promotes the β →ω transformation. Hence, different cooling rates of bcc β phase were employed, to study ω^{ath} in Ti-15Mo alloy. Figure 7.1(a-c) shows the optical micrographs of Ti-Mo quenched from β phase in three different media, like ice-water, brine and liquid nitrogen.

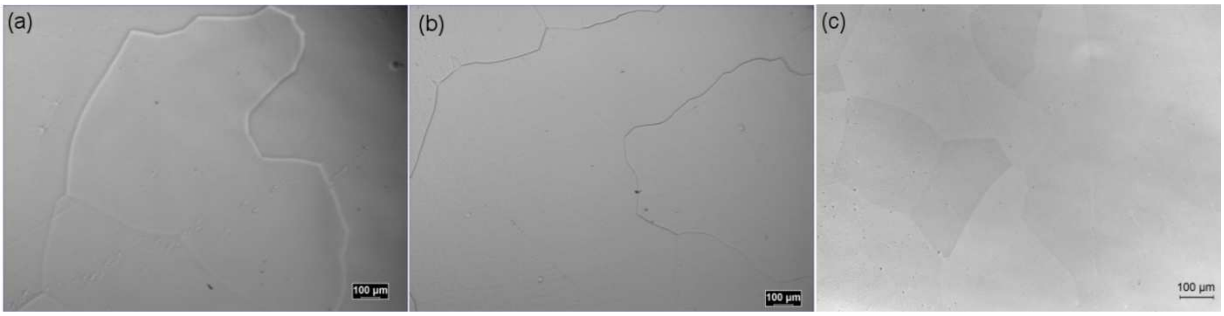

Figure 7.1 Optical micrograph of Ti-15Mo alloy quenched from β phase into (a) ice water (b) brine solution and (c) LN2 showing large grains of β.

The micrographs, as expected, do not show any evidence of phase transformation. Hence, further studies were carried out using synchrotron XRD and the results are described below.

7.2.1.a Synchrotron XRD studies of quenched Ti-15Mo alloys

The synchrotron XRD image plate data of brine quenched alloy of Ti-15Mo is given in figure 7.2.

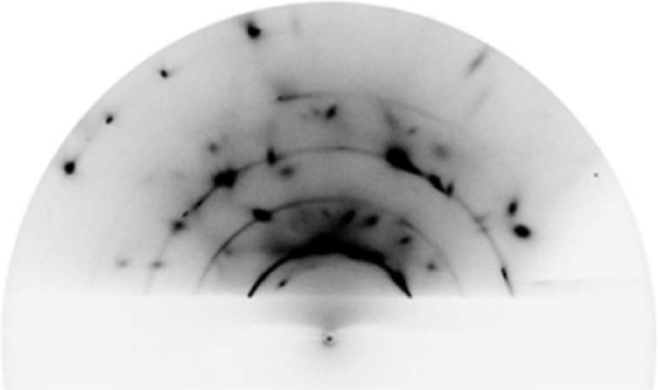

Figure 7.2 Synchrotron XRD from brine quenched Ti-15Mo alloy.

It is clearly evident that the few continuous rings that are visible are too broad, with non-uniform angular distribution of intensity. Additionally, the pattern is very noisy. These observations could be directly understood in terms of high lattice strain, overlap of β and ω peaks and possible texture. The large grain size (1-2 mm) and the static nature of the sample during data acquisition resulted in variations in the intensity of the peaks. The data acquisition time of ~10 to 20 seconds for the imaging plate was optimized after 4 to 5 runs, to enable detection of resolvable ω peaks. In the process, a certain degree of saturation in high intense β peaks was unavoidable. Hence, the Rietveld analysis could not be carried out, due to the inaccurate information on the intensities of diffracted peaks. Despite all these difficulties, synchrotron XRD was continued only for the confirmation of formation of ω, especially in view of the fact that existing literature could not confirm [12, 18, 19] the presence of ω in this composition of the alloy using conventional XRD, though expected based on TEM evidences [12]. Similar data was obtained for other two quenching rates also. These data were converted to I vs 2θ plot using fit2d software. The plots of I *vs* 2θ for the Ti-15Mo alloy β quenched at three different cooling rates are shown in figure 7.3.

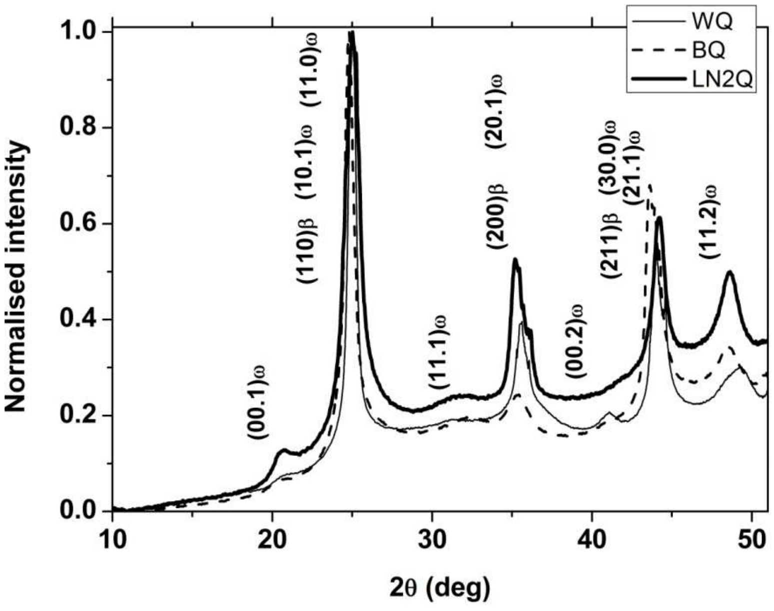

Figure 7.3 I vs 2θ plot of synchrotron XRD data, using fit2d software, for Ti-15Mo alloy quenched from the β phase at various cooling rates. Unique peaks of ω are clearly seen.

The detection of discernable (11.2) peak of ω phase, unambiguously confirms the presence of ω phase in these samples. Most of the high intensity peaks of β phase are coinciding with that of ω. However, unique low intensity peaks (00.1), (11.1), (00.2) (11.2) of ω phase are also clearly visible for all quenching conditions. However, reliable quantitative estimate of volume fraction using peak profile analysis of XRD patterns could not be carried out. In order to obtain convincing evidence for formation of ω phase, data acquisition time was optimized resulting in unavoidable saturation of β phase peaks, which made it difficult to calculate amount of ω phase.

The occurrence of β to ω transformation during quenching at temperatures where the self or solute mobility is too low suggests the displacive nature of transformation, as expected. The observation of unusually broad peaks of ω suggests that these particles are expected to be too fine, of nm size with high amount of locked in lattice strain. Additionally, it is observed that the $(00.1)_{\omega}$ peak is dominant for LN2 quenching less dominant for brine quench and almost invisible for water quench, while (00.2) peak does not follow the same trend. This could possibly be due to texture effects intensifying the $(00.1)_{\omega}$ peak, due to the β grain size (~0.6 mm) of the stationary sample being larger than the incident beam size (300×300μm). The synchrotron experiments on alloys with different cooling rates were useful to confirm the formation of athermal ω phase in Ti-15Mo alloy.

The reported composition range of Mo in Ti-Mo system, in which ω is known to form is ~10 to 20 wt% Mo [20-22], of which the low concentration range is more favorable. Most of the evidences in literature, for the formation of ω in β quenched Ti-Mo alloys, originate from electron diffraction studies. The XRD studies in literature could not detect the unique ω peaks and there are hardly any studies using synchrotron XRD to study this aspect. Conventional XRD analysis could be comfortably used to confirm the formation of ω phase in the low composition range. However, 15wt% Mo falls slightly above this composition range favorable for ω phase formation. Conventional X-ray diffraction studies have reported only the retention of β phase in Ti- 15Mo alloys, as it is unable to detect the unique ω phase peaks [23]. In this context, present synchrotron XRD studies confirming the formation of ω phase in parent bcc β matrix in the same alloy composition, where ω could not be detected, assumes relevance. The effect of rate of cooling in the ease of β to ω transformation has been demonstrated [3] as early as 1969, in Ti- 6 wt% Cr alloys. Cooling rates as high as 11000 K/s, could not prevent the formation of ω phase [10]. Electron diffraction studies have shown that the intensity of diffuse scattering decreases with appearance of discrete spots with cooling rate [7], suggesting an increase in the amount of ω phase. However, there is no systematic study of the unit cell dimensions of product phases with cooling rate.

The lattice parameter of ω and β phases at different quenching conditions could be retrieved based on analysis of figure 7.3. The lattice parameters were determined using MAUD (Material Analysis Using Diffraction) Java based profile fitting code [24]. The refined lattice parameters for both phases at different quenching conditions are given in Table 7.1 which does not show any significant change in their values.

Table 7.1 Lattice parameters of ω and β phases in β quenched Ti-15Mo alloy

quenching medium	Lattice parameter (ω phase)		Lattice parameter (bccβ)
	a_ω(Å)	c_ω(Å)	a_β (Å)
Ice water	4.5751	2.7828	3.2503
Brine	4.5451	2.8153	3.2387
LN2	4.5594	2.8413	3.2412

There are reports in literature, which show the influence of quenching conditions on β to ω transformation. De Fontain *et. al.* [7] observed change in the intensity of ω diffuse scattering in the SAD analysis depending on exposure conditions at different temperature in Ti-15Mo alloy. However, systematic XRD analysis of variations in the unit cell dimensions of ω with quenching rates is very few in literature. The influence of Rietveld refined lattice parameter on quenching conditions of athermal ω phase is established using synchrotron XRD in the present study, for the first time to the best of the existing knowledge.

The high background and discontinuity of the synchrotron XRD patterns in figure 7.2 restricted the analysis to only calculation of unit cell dimensions. Since the main purpose of the synchrotron XRD experiments was to identify ω phase, the data acquisition time of ~10 to 20 seconds for the imaging plate was optimized after 4 to 5 runs, mainly to enable detection of resolvable ω peaks. In the process, a certain degree of saturation in high intense β peaks was unavoidable. Hence, the Rietveld analysis could not be carried out, due to the inaccurate information on the intensities of diffracted peaks in the entire pattern. The detailed, reliable, quantitative Rietveld analysis could be carried out using conventional XRD of isothermal ω, i.e., ω^{iso}, which is explained later.

7.2.1.b Phase Contrast Microscopy Studies of quenched Ti-15Mo alloy

Having unequivocally established the formation of ω in the β matrix of Ti-15Mo alloy quenched in all cooling rates, detailed high resolution TEM studies were carried out in the water quenched alloy to complete the microstructural characterization. The details are presented below. Figure 7.4 (a&b) shows the bright field image and SAD pattern of the Ti-15Mo alloy, water quenched from above the β transus. The bright field image does not show any 'mottled' contrast, of ω. However, the SAD pattern in figure 7.4 (b), taken along the [110] zone axis of bcc β phase, shows clearly the presence of primary maxima and secondary maxima associated with diffuse scattering of their intensity along preferred orientations. The primary maxima clearly corresponds to bcc β matrix along [110] zone axis, as revealed by the indices of the reflections marked in the figure. The value of unit cell dimension of bcc β, measured based on the SAD is 3.47 Å, which is close to that of the value from synchrotron results (Table 7.1). The secondary maxima with streaking were analyzed to be from ω, with the zone axis along [2-1-10]. The diffuse scattering in the reciprocal lattice sections of ω has been confirmed as a strong 'signature' of the incomplete nature of $\beta \rightarrow \omega$ transformation [7], which is known to proceed through "lattice collapse" mechanism. In contrast, the SAD pattern shown in figure 7.4(c). from the alloy quenched in liquid nitrogen shows the reduction in the extent of diffuse scattering along with increase in the intensity of discrete spots at 1/3, 2/3 d_{112}. This observation suggests that liquid nitrogen quenching has promoted $\beta \rightarrow \omega$ transformation, in agreement with reported literature [7].

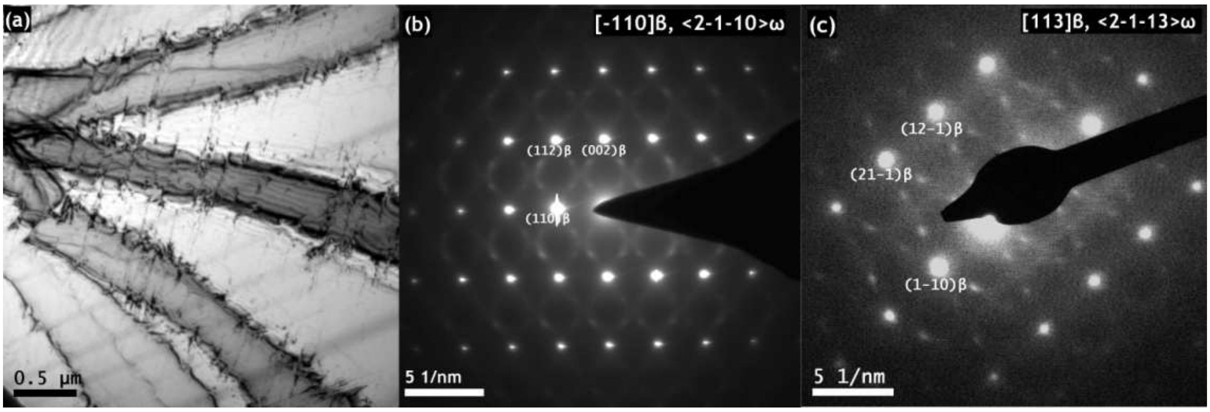

Figure 7.4 TEM micrographs of Ti-15Mo alloy (a) bright field image; the entire region corresponds to bcc β and the size of ω is below the detection limit and (b) SAD pattern along $[110]_\beta$ *for ice water quenched alloy and (c) SAD pattern along* $[113]_\beta$ *for LN2 quenched alloy.*

Figure 7.5(a) shows the SAD pattern taken from yet another zone axis of β phase in the water quenched Ti-15Mo alloy. The diffraction pattern is analyzed to be along the zone axis of $<102>_\beta$. The secondary maxima in this SAD pattern could be analyzed to be from [2-1-16] zone axis of ω phase. The SAD pattern shows that the spots with intensity less than the primary β spots divide the g_{-211} vector into three equal distances. The dark field image in figure 7.5(b) is imaged using $(20.\text{-}1)_\omega$ reflection [circled in figure 7.5(a)], confirming the uniform distribution of nm sized ω particles, in tune with the very broad peaks observed in the synchrotron XRD patterns of figure 7. 3. It is clearly seen that second phase particles of nm size, of various shapes are uniformly distributed throughout the matrix.

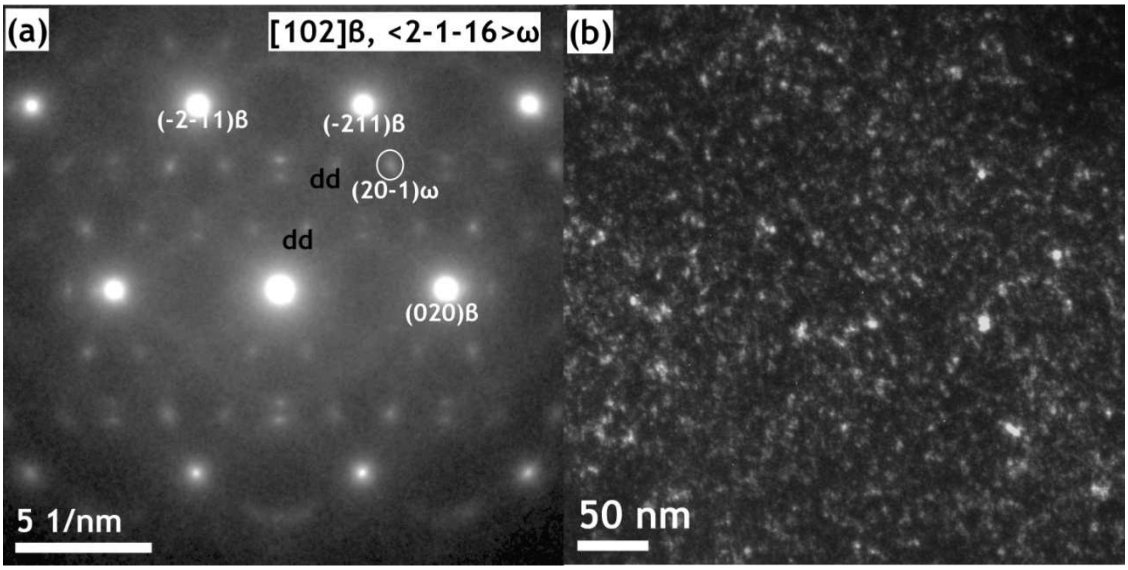

Figure 7.5 TEM results of ice water quenched Ti-15Mo alloy. (a) The SAD pattern along [102] zone axis of β. (b) The dark field micrograph imaged using (20-1) spot (circled in 4a) from<2-1-16>ω.

In order to image the lattice planes of the constituent phases, phase contrast microscopy was carried out. As per the previously reported HRTEM results, it is stated that resolving of the collapsed atom pairs along the <111> direction of the parent β matrix individually is difficult due to the resolution limit of the microscope used [25, 26]. Even though Sukedai *et. al.* [27, 28] attempted to show the coexistence of regions of ω structure as well as regions with two-dimensionally-ordered linear defects, the atomic displacement for the ω transformation in β matrix could not be imaged perfectly. In the present study, it is demonstrated that the well resolved images of atomic columns of single variant of ω could be obtained to study the 'lattice collapse' mechanism, by using advanced filtering techniques. This method chooses Inverse Fourier Transform images using reflections from only one variant of the ω to image the lattice planes of ω phase.

Figure 7.6 (a) shows the HRTEM image recorded along the $[-110]_{\beta}$ zone axis. The inset shows the FFT of the entire image in figure 7.6(a). It is difficult to distinguish the lattice fringes corresponding to β and ω phases from figure 7.6(a). However the FFT unambiguously confirms the presence of the two types of lattices. The similarity between the inset in figure 7.6(a) and figure 7.4(b) also is clearly observed, as expected.

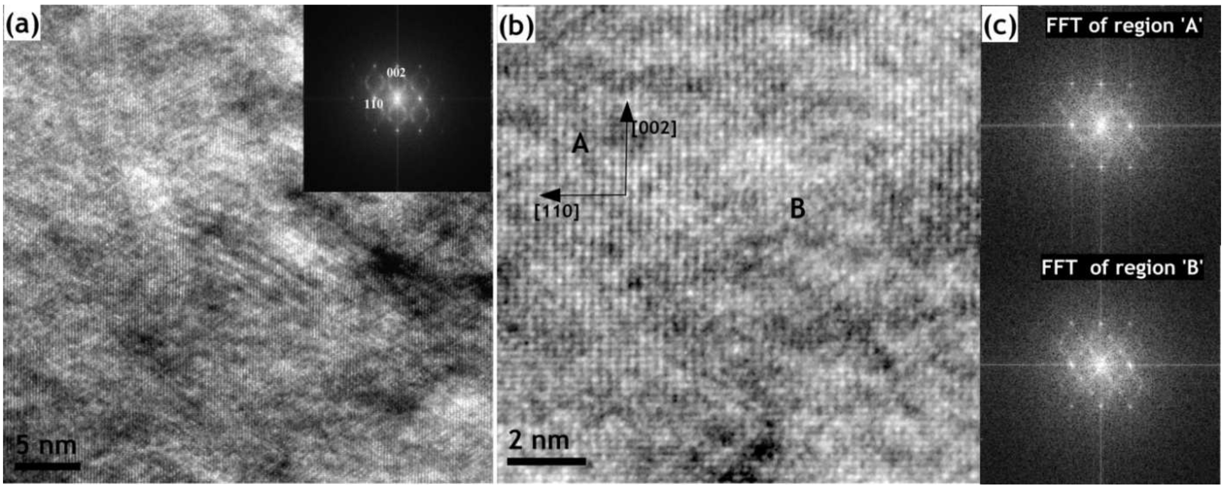

Figure 7.6 HRTEM images of Ti-15MoWQ alloy. (a) HRTEM lattice image recorded along the [-110]$_\beta$ zone axis; inset shows the FFT of this image; (b) magnified image showing atomic column contrast variation in different regions. The regions A and B show bcc β matrix contrast in [110] zone axis; (c) The FFT is taken from region A and B in figure 7.6(b).

An attempt was made to identify the lattice planes of the two phases in figure 7.6(a) by magnifying a chosen region of figure 7.6(a), which is shown in figure 7.6(b). This figure reveals the presence of different atomic column contrast in different areas of the image. The left top region (marked as A) in figure 7.6(b) shows the well resolved atomic column contrast, revealing the presence of two sets of planes, perpendicular to each other. The intensity profile along the two perpendicular directions, yielded the average interplanar spacing of the two sets of planes to be d_{110} = 2.366 Å and d_{200} =1.659 Å. These values agree reasonably well with the expected ‘d’spacings of $(110)_\beta$ and $(002)_\beta$. Based on this observation, the directions are marked in the region A of figure 7.6(b). The FFT of region A shown in figure 7.6(c) shows that the intensity of reflections corresponding to β is far too high compared to that of ω. The analysis of the intense spots in FFT taken selectively from region A [shown in figure 6(c)] enables the identification of region A to be mainly from bcc β matrix, as expected. After properly aligning the FFT with the lattice image, the (002) and

(110) planes of β matrix could be unambiguously identified and marked in figure 7.6(b). In the same image, region B (the right part) shows a fuzzy contrast, where the atomic columns are not well resolved. The FFT of region B, also shown in figure 7.6(c) shows that the intensity of ω reflections is far too higher than that of region A and intensity of reflections of β has reduced considerably compared to region A. The analysis of reflections stronger than corresponding FFT of region A, confirms that these correspond to ω phase. Thus, the results of the present study shows that it is impossible to obtain phase contrast image form only either β or ω and the observed phase contrast image always contains contributions from both ω and β phases. This is mainly due to the fine size of ω particles, leading to sandwiching of ω particles in β matrix, within the thickness of the thin foil. Hence, additional filtering and inverse FFT procedures are essential to image the lattice planes of only ω and these are discussed below.

An attempt to image the lattice planes of ω, needs to take into account another factor, namely existence of four major variants of ω (ω_1 to ω_4). Of these variants, the SAD pattern along $<110>_\beta$, would contain reflections from two variants, ω_1 and $\omega_{2,}$ due to the presence of two <111> directions at an angle of 70.5°, in the (110) plane. The reflections from ω_3 and ω_4 overlap with reflections of β phase which get filtered, when β reflections are filtered out, to image single variant of ω phase. Hence, viewing the lattice planes of single variant of ω requires simulation of diffraction patterns and filtering from the reconstructed FFT patterns.

As a first step, the diffraction pattern of $<110>_\beta$ and <2-1-10> of ω_1 and ω_2 are simulated [figure 7.7(a) -7.7(c)], using the input parameters (figure 7.6(c)) from the FFT of the experimental phase contrast image. The superposition of all the above three simulated SAD patterns were carried out based on information about orientation relationships between β & ω and ω_1 & $\omega_{2.}$

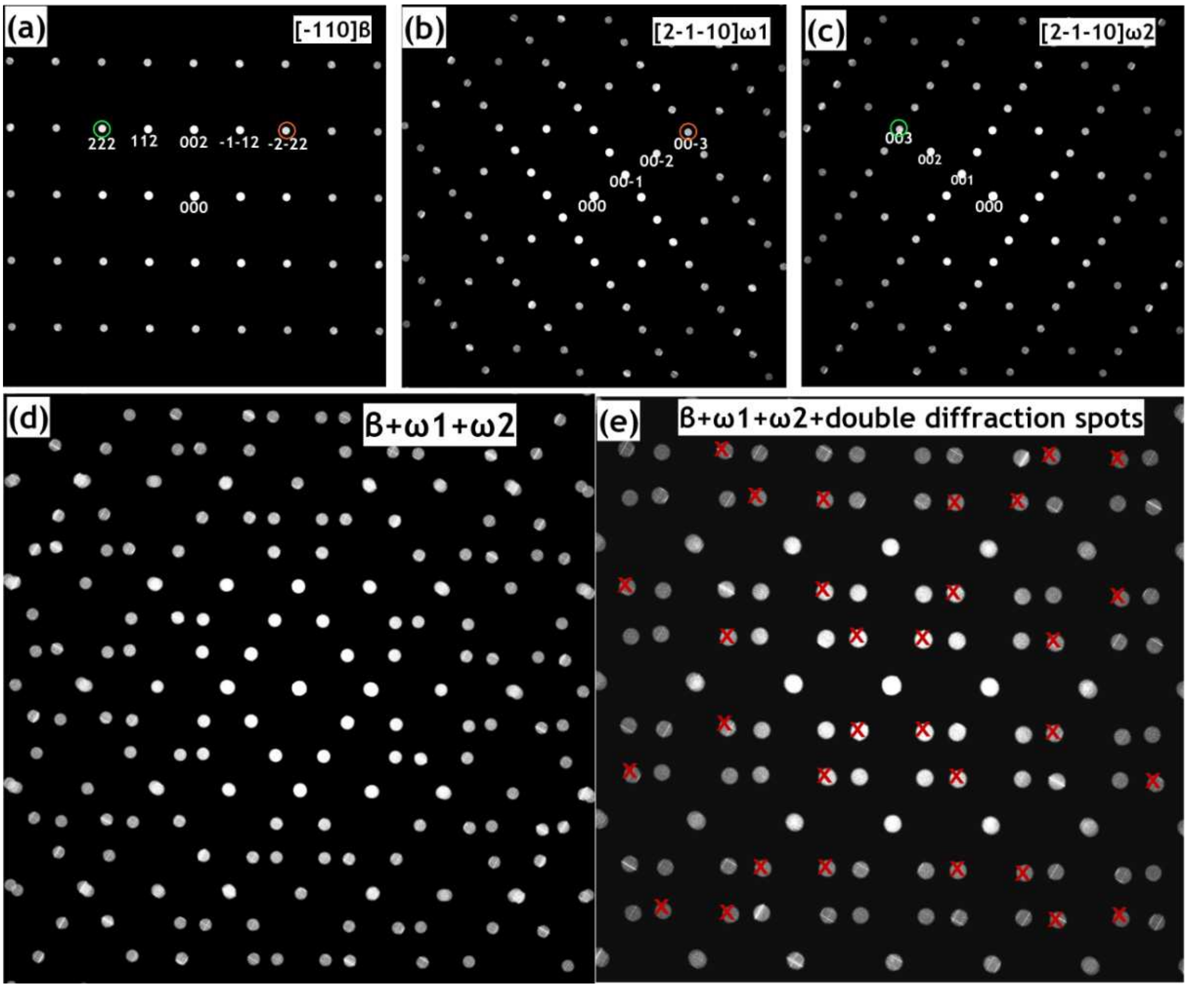

Figure 7.7 Simulation of diffraction patterns of β and ω phases. (a) diffraction pattern of $[110]_{\beta}$*; (b and c) diffraction patterns of* ω_1 *and* ω_2 *along <2-1-10> zone axis, oriented at 70˚ with each other;(d) The superimposed diffraction pattern of β with* ω_1 *and* ω_2 *and (e) Final SAD pattern including double diffraction spots (marked as x). Notice that figure 7.7(e) matches well with the experimental pattern in figure 7.4(b).*

The circles in figures 7.7(a) to 7.7(c) show the overlapping reflections of <222>β and <0003>ω in the individual SAD patterns. Figures 7.7(b&c) are oriented at 70˚ with each other. Figure 7.7(d) shows the superimposed SAD pattern containing β and the two variants of ω phase. The final reconstructed SAD pattern along <110>β shown in figure 7.7(e) includes the double diffraction spots (marked as x) also, as has already been observed during the analysis of figure 7.4(b). Figure 7.7(e) is found to match well with experimental SAD pattern in figure 7.4(b). However, the diffuse streaking observed in the experimental pattern in figure7.4 could not be reproduced in the simulation, since the different degrees of lattice collapse in ω domains are not incorporated in the simulation.

The last step is to view the lattice planes of only one variant of ω, using the inverse FFT of the reflections corresponding to only one variant of ω. The Fourier filtered image of figure 7.6(a), corresponding to only one variant of ω, is shown in figure 7.8(a).

The circled regions in figure 7.8(a), correspond to ω phase, embedded in the remaining β matrix. The co-existence of β and ω phases, as has been discussed earlier, is responsible for the well resolved lattices of both, seen in figure 7.8(a). The viewing plane corresponds to $\{110\}_\beta$. These circled regions correspond to the embryos of ω. In order to view the displacement of lattice planes of ω more clearly, the circled region is enlarged and shown in figure 7.8(b). Comparison of two lines along <002>β, one within β and another including the regions of β and ω, clearly reveals the atomic displacement within ω, leading to the observed difference in the contrast. The unit cell of β and ω are also marked in the figure 7.8(b). The orientation relations are clearly followed in the lattice images shown in figure 7.8. The ω like embryos of size 2- 5 nm embedded in the β matrix shows coherent nature with the matrix, as shown in the line profile [figure.7.8 (c)] of intensities of atomic columns along line marked in figure 7.8(b). The experimental image shown in figure 7.8(b) was compared with image simulated using multislice simulation. The best matching of the simulated and experimental image could be obtained only if trigonal symmetry of ω is considered.

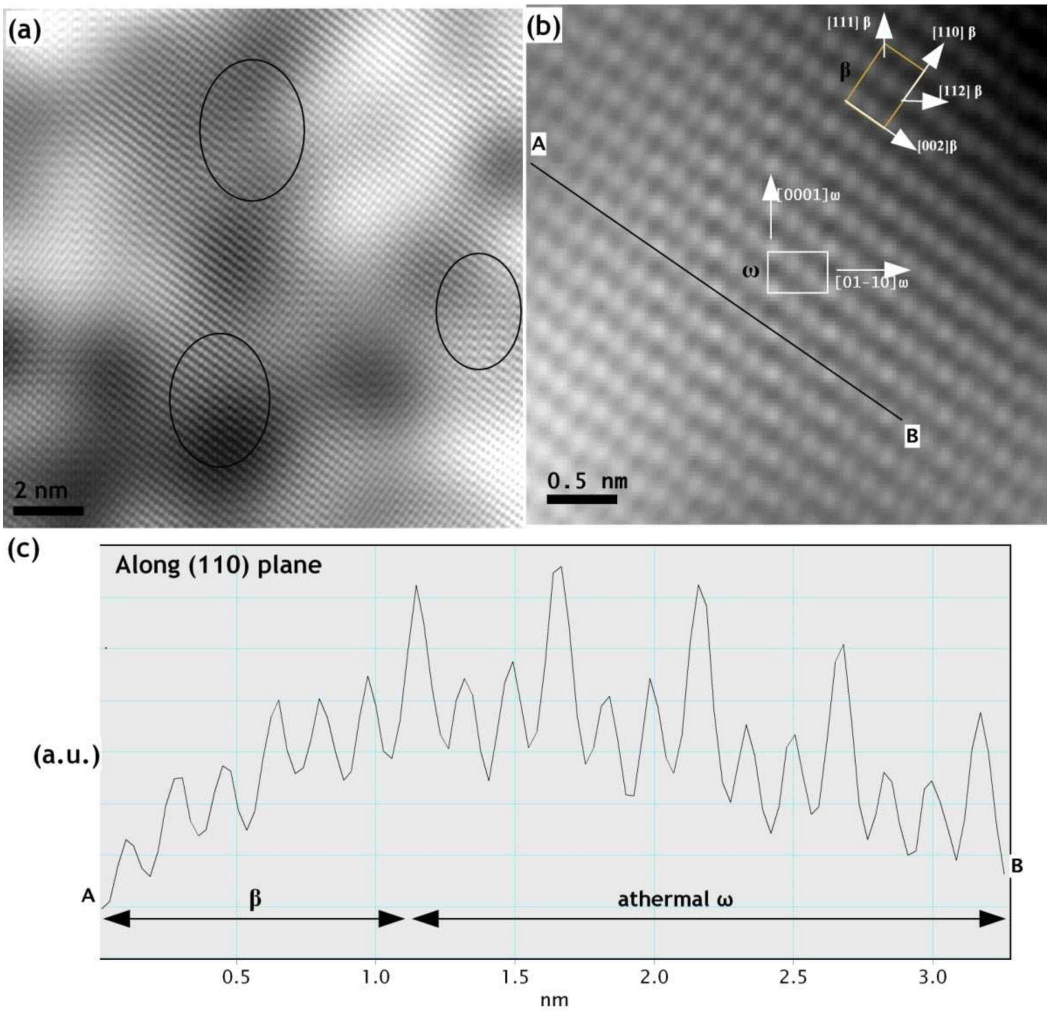

Figure 7.8 (a) The Fourier filtered image of ω1 reflections. The encircled region shows ω like embryos (b) Enlarged image of ω like embryos shows the unit cell of ω with orientation relationship with β (c) Intensity line profile taken along AB marked in b.

Thus the phase contrast microscopy of water quenched Ti-15Mo alloy enabled the direct imaging of lattice planes of ω and β lattices, showing the adherence to the proposed orientation relation, displacement of atoms inside ω embryos and the coherent nature of the interface.

The synchrotron XRD and HRTEM results presented above on ω^{ath}, can be summarized as follows:

1. ω^{ath} phase formation is confirmed using synchrotron XRD in Ti-15Mo alloy, quenched from the β phase at three different rates of quenching.

2. Homogeneous distribution of 2-3 nm sized ω clusters in the β matrix is demonstrated.

3. Phase contrast microscopy was carried out to image atomic column contrast, from single variant of ω^{ath}, confirming orientation relation with β matrix, atomic displacement inside ω^{ath} and the coherent nature of interface between β and ω.

7.2.2 Characteristics of isothermal ω phase

The equilibrium phase diagram of Ti-Mo system confirms that the alloy of interest (Ti-15Mo) to the present study exists in the two phase field of hcp α and bcc β, up to a temperature of approximately 1073 K. However, quenching followed by shorter durations of exposures at temperatures ~ less than 773K, suggests the formation of isothermal ω, i.e., ω^{iso}. It is expected that the thermal activation could promote the kinetics and extent of β→ω phase transformation. In order to arrive at the Rietveld refined accurate lattice parameters, the microstructural 'strain' parameters and the bonding nature, conventional XRD studies were carried out on the Ti-15Mo alloy, isothermally aged at 748K for 24 hours after ice-water quenching from β phase. In order to compare the extent of transformation with ω^{ath}, phase contrast microscopy was carried out and the results are presented below.

7.2.2.a Rietveld Analysis of XRD of aged Ti-15Mo alloy

The optical microstructure of Ti-15Mo alloy aged at 748K for 24 hours following β quenching is shown in figure 7.9. The β grains of size in the mm range are clearly visible in the optical micrograph of the alloy. Usually, the grain size of β in titanium based alloys is known to be very high and is understood in terms of exceptionally high self and solutes diffusion coefficients, in the high temperature β phase.

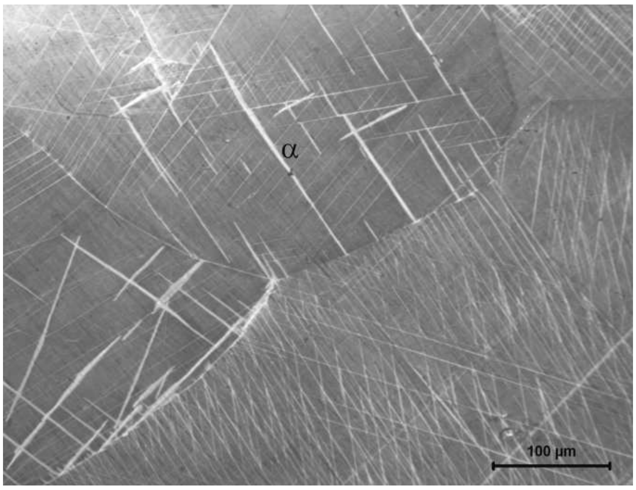

Figure 7.9 Microstructure of Ti-15Mo aged alloy showing isothermal ω phase formation inside the large grains of β phase.

The uniformly distributed equilibrium α phase is marked in figure 7.9. The Rietveld refined XRD pattern from aged Ti-15Mo alloy is shown in figure 7.10.

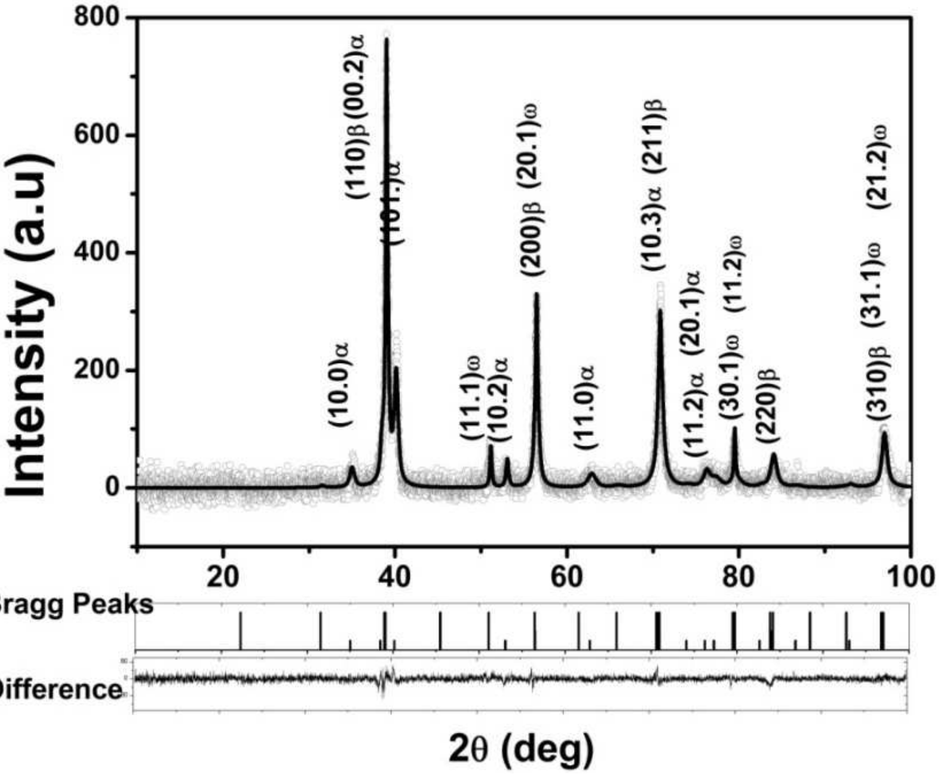

Figure 7.10 Rietveld refined XRD pattern of Ti-15Mo aged 748 K/24 hours showing presence of α, β, and ω phases.

The input parameters for the initial model for ω are as follows (ICDD # 04-007-2125)[29]: space group symmetry: P6/mmm, lattice parameters as a=b=4.625A° and c=2.813A° and atomic position as(000) (1/3, 2/3,1/2). The values for equilibrium α and β were the same as that referred by Sabeena *et. al.* [30]. It may be noticed that the hexagonal symmetry for ω has yielded Rp and wRp values as small as 0.08 and 0.10, confirming the symmetry of ω^{iso} to be hexagonal. Care has been taken to derive amount of co-existing phases from a textured sample during the refinement. The crystal structure details with weight fraction of all phases obtained during Rietveld refinement of conventional XRD analysis of Ti-15Mo aged sample are given in Table 7.2. Based on the unit cell dimensions in Table 7.2 and the geometry of the relevant planes of parent bcc β and hexagonal ω, the complete degree of displacement is estimated as 0.3 Å.

Table 7.2 ***Rietveld refined crystal structure details of Ti-15Mo alloy aged at 748 K for 24 hours.***

PHASE	Space group	Lattice parameter (Å)			Atomic Position	wt fraction(%)
		A	b	c		
HCP	$P6_3$/mmc	2.9483 (6)	2.9483 (6)	4.6618 (9)	(1/3, 2/3,0.25)	52
BCC	Im-3m	3.2506 (2)	3.2506 (2)	3.2506 (2)	(0,0,0)	23
Omega	P6/mmm	4.5899 (10)	4.5899 (10)	2.8254 (3)	(0,0,0) (1.3, 2/3,0.5)	24
Reliability factors : Rp=0.0837, wRp=0.1086, GoF= 1.3						

The unit cell of ω was found to contract during $\beta \rightarrow \omega$ transformation. The atom positions in ω listed in the Table 7.2 correspond to 1a and 2d Wyckoff notations, corresponding to the one atom in position ‘a’ and two atoms in‘d’ position. However, the present diffraction data could not identify if the titanium and molybdenum atoms preferentially occupy these atom sites.

The volume fractions of α β and ω phases, were calculated using peak profile analysis of XRD pattern. The analysis confirmed the presence of 52% of α, 23% of β and 24% of ω phases. If equilibrium is achieved, the amount of co-existing α and β phases, as per the phase diagram, at 748K happens to be around ~75% of α phase and ~25% of β phase. However, the presence of ~24% of ω suggests that the system has not achieved equilibrium. It is known that the metastable ω, being depleted of Mo acts as nucleation sites for α and will transform finally to α. If this is also accounted for, the amount of co-existing phases measured experimentally, match reasonably well with the expectation from phase diagram.

The next step is to calculate the charge density distribution of the three phases using the structure factors calculated using the refined intensity of diffraction peaks. Since the bonding in equilibrium phases, hcp α and bcc β are conventional 'metallic' in nature, the current discussion would confine to that of only hexagonal ω. The nature of bonding is known to influence the bond lengths and interatomic distances. For this purpose, the nomenclature used in literature is extrapolated: Assuming the two atoms in Wyckoff 2d positions to be a sub lattice of B atoms and that of 1a to be of A atoms (not based on 'chemistry'), the relevant interatomic distances $d_{A\text{-}A}$, $d_{A\text{-}B}$ and $d_{B\text{-}B}$ and co-ordination numbers are measured and given in Table 7.3 and indicated in figure 7.11(a). These values have certain implication on the type of bonding in ω unit cell, which will be discussed in section 7.4.2.

Table 7.3 Bond Length (BL) and Effective Co-ordination Number (ECN) of the product phases

Comp. wt%	hexagonal ω		bcc β		hcp α	
	BL	ECN	BL	ECN	BL	ECN
Ti-15Mo	$d_{B\text{-}B}$ - 2.6518(3), $d_{A\text{-}A}$ - 2.8265(4) $d_{A\text{-}B}$ 3.0049(3)	9	2.81640(16)	8	2.8877(5)2 .9501(4)	First Neighbors: 6; Second Neighbors :11.9156
Ti-25Mo			2.81348(3)	8		

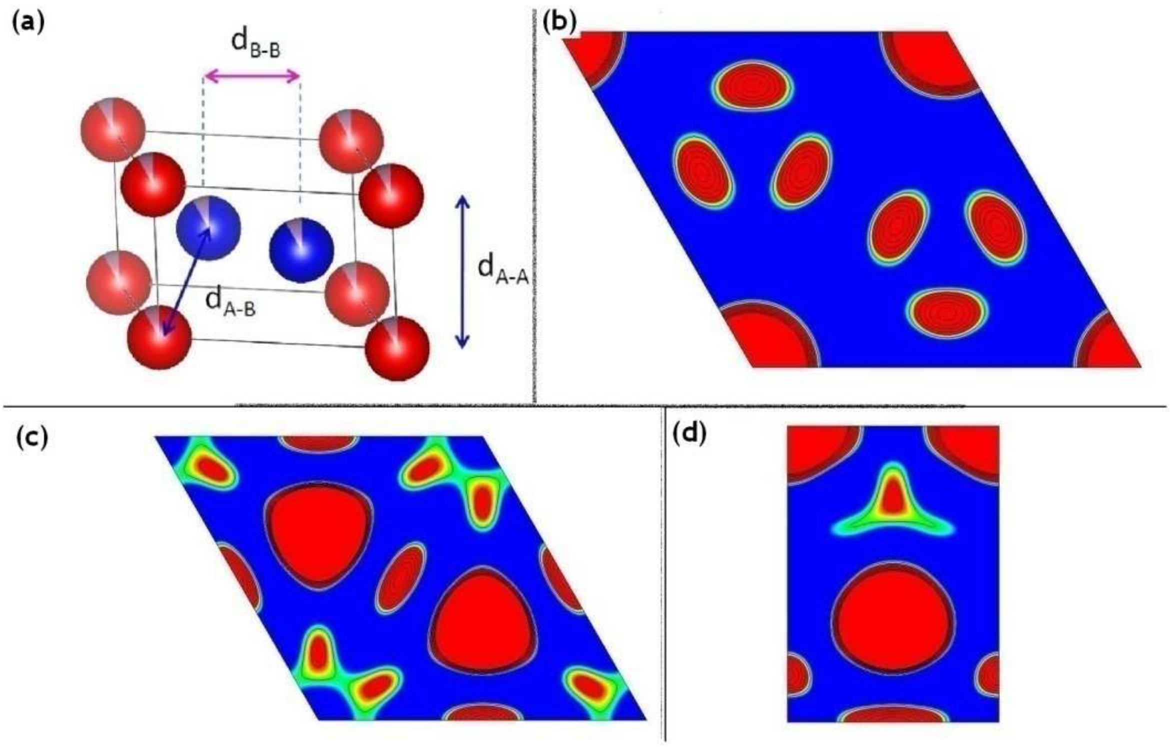

Figure 7.11(a) ω unit cell; The effective bond length and charge density distribution of (b) (00.1) (c) (00.2) and (d) (12.0) atomic planes in ω^{iso} phase of aged Ti-15Mo.

The direct information on nature of bonding within ω^{iso} in Ti-15Mo alloy could be obtained using electron density distribution maps, as stated earlier. Figure 7.11(b-d) shows the two dimensional electron density distribution maps in three planes: (001) with A-A atoms, (002) with B-B atoms and (1-20) with A-B atoms. It is quite clear that the bonding in (001) and (1-20) planes is predominantly metallic, with most of the charge density distributed spherically around atom centers and low uniform distribution between atom centers. However, the charge distribution in (002) plane is strikingly different, with a strong non-spherical distribution of charge around the centers of B atoms. This suggests a strong anisotropy in the nature of bonding. However, the vertices of the triangular shape of the charge density are not 'touching' each other, which would be expected preferably along with a region of overlap of charge density, if the bonding between B atoms were covalent in nature. Hence, current study suggests that there is no clear evidence for strong covalent bonding between the atoms in the ω phase. This aspect will be discussed later in connection with the interatomic distances.

As stated earlier, there is very little literature concerning the direct evidence for the nature of bonding. The interatomic distances and their correlation to certain bond lengths have been used to derive inferences regarding the nature of bonding and even the type of atoms in the A and B sublattices, which will be further discussed in section 7.4.2.

Rietveld analysis of XRD peaks of aged Ti-15Mo alloy can also be used for deducing microstructural parameters like the size of coherent domains of co-existing phases and the microstrain locked up within the lattice of the three phases. While an attempt was made to calculate the microstructural parameters, it was found that the large grain size, overlap of intensity from three different phases made the analysis very difficult, to obtain reliable coherent domain size. However, the 3-D distribution of microstrain could be arrived at using the experimental data. The Williamson – Hall plots for the three co-existing phases α, β and ω phases are shown in figure 7.12.

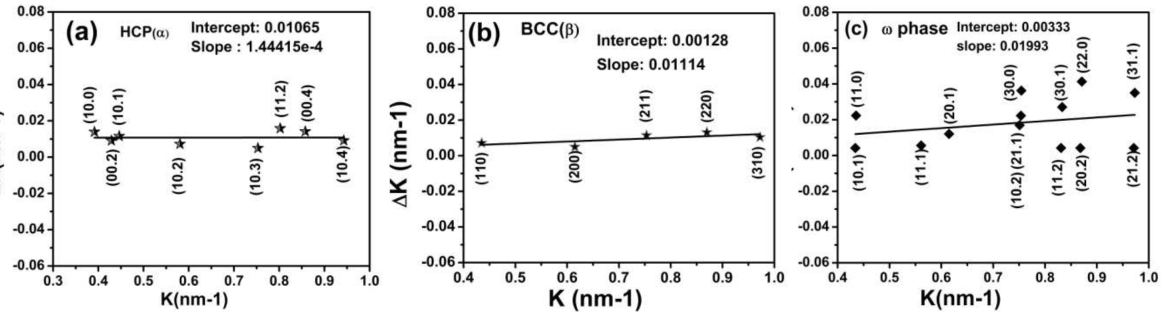

Figure 7.12 The Williamson Hall plots for the three co-existing phases, α, β and ω.

It is observed that the plots are linear with very little scatter for α and β phases, while the ω phase shows a lot of scatter in the data, suggesting an anisotropic strain for ω phase. Generally, the values of slopes for all the phases are small. However, the equilibrium lattice of α shows very low strain, as expected. The ω and β phase lattices appear to have higher locked in strain relative to α phase. The actual values of the total strain in the three lattices are marked in the figure.

An attempt was made to identify the anisotropic nature of strain in the three lattices of α, β and ω. The 3-dimensional strain distribution in the three co-existing phases α, β and ω are shown in figure 7.13.

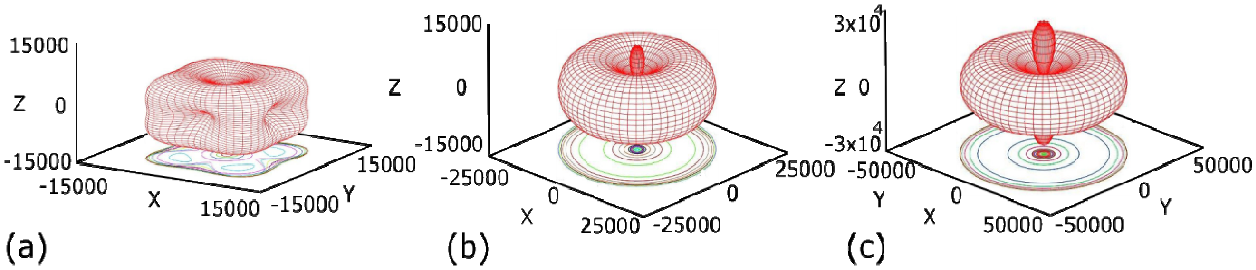

Figure 7.13 The 3D microstrain ellipsoid with 2D contour of (a) ω (b) α (c) β phase. Strain is more for ω phase comparing the other two phases. The scale of the plot is $\delta d/d$ *X* 10^{-6}.

Similar results have not been so far reported in literature for the titanium based alloys. It is clearly seen that the strain distribution is not isotropic. The variation in the strain distribution is a combined effect of anisotropy in elastic constants and the microscopic stress field caused by the matrix in which the three phases are co-existing.

7.2.2.b Phase Contrast Microscopy Studies of aged Ti-15Mo alloy

The microstructural characterization of ω^{iso} was carried out using conventional TEM and phase contrast microscopy, which is explained below. Figure 7.14(a) is the SAD pattern of the aged alloy, showing the presence of β and ω. It is clear that the SAD is along <110> zone axis of the bcc β matrix and <2-1-10> of ω. The unit cell dimensions, measured using figure 7.14(a) are as follows: a_β = 3.263 Å; a_ω = 4.655 Å; c_ω = 2.845 Å. In this orientation, the non-overlapping reflections of ω phase, along the zone axis <2-1-10>ω are clearly observed. A comparison of a similar pattern for the ω^{ath} in figure 7.4(b) shows that there are distinct differences between the SAD patterns of ω, before and after the isothermal annealing. After isothermal annealing, the secondary intensity maxima corresponding to ω phase have become stronger than that of athermal ω. The diffuse intensity has completely disappeared suggesting the completion of the displacement/collapse of atoms in $(111)_\beta$ planes and hence the formation of ω phase. In continuation of the presence of two variants of ω, discussed earlier, it can be seen from figure 7.14(a) that it consists of only one variant of ω and the reflections of the second variant are very weak. Figure 7.14(b) shows the dark field micrograph imaged using (01.1) reflection of the SAD pattern along $<2\text{-}1\text{-}10>_{\omega}$ (encircled in figure 7.14 a). The uniform distribution of 50-100 nm size elliptical particles of ω, in the β matrix is clearly seen. The major axis of all the ellipsoids which are imaged are parallel and lie along $<222>_{\beta}$, correspond to a single crystallographic variant of ω, out of the four possible variants, expected as explained earlier. Thus, it is confirmed that the isothermal exposure of the water quenched Ti-15Mo alloy results in the formation of plates of α and uniform, fine, ellipsoidal particles of ω in β-bcc matrix.

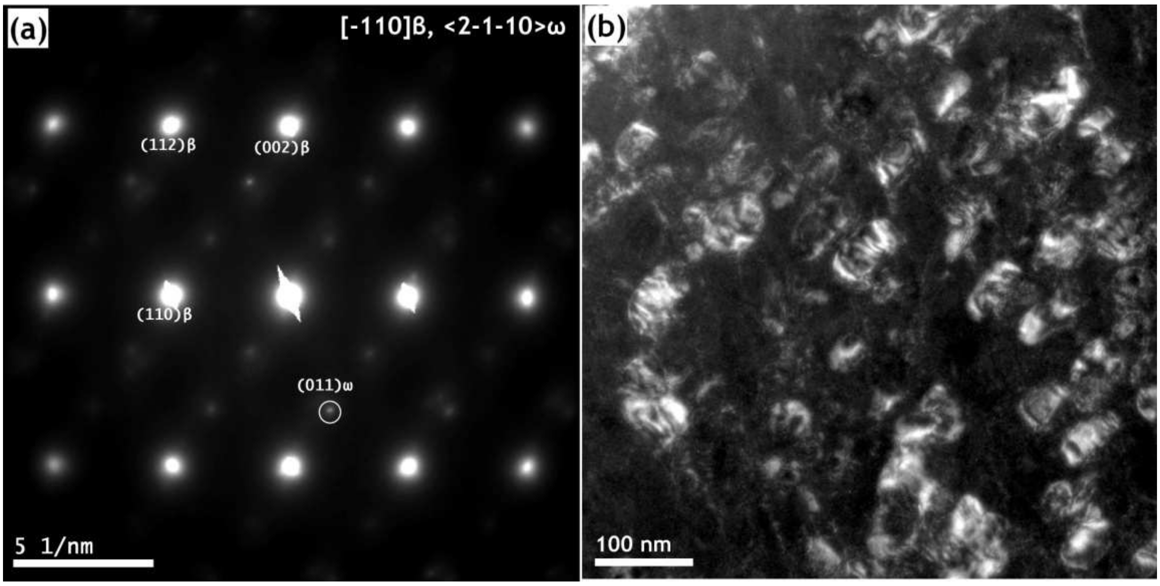

Figure 7.14 (a) The SADP taken along <110> of β matrix; (b) The dark field image with $(01.1)_{\omega}$ reflection (circled in a) showing the ω phase particles.

HRTEM study was carried out to understand the atomic column contrast from the isothermal ω^{iso} and hence the degree of displacement of atomic rows in $(111)_{\beta}$. Figure 7.15(a) shows the high resolution phase contrast image taken along $<110>_{\beta}$. The FFT (inset) shows the presence of both β and ω phases, as expected based on the fine size of ω^{iso}. Following the same procedure as explained in section 7.2.1.b, for athermal ω, atomic column contrast for β and ω is derived and shown in figure 7.15(b). The crystallographic directions parallel to the β and ω are clearly marked in the figure.

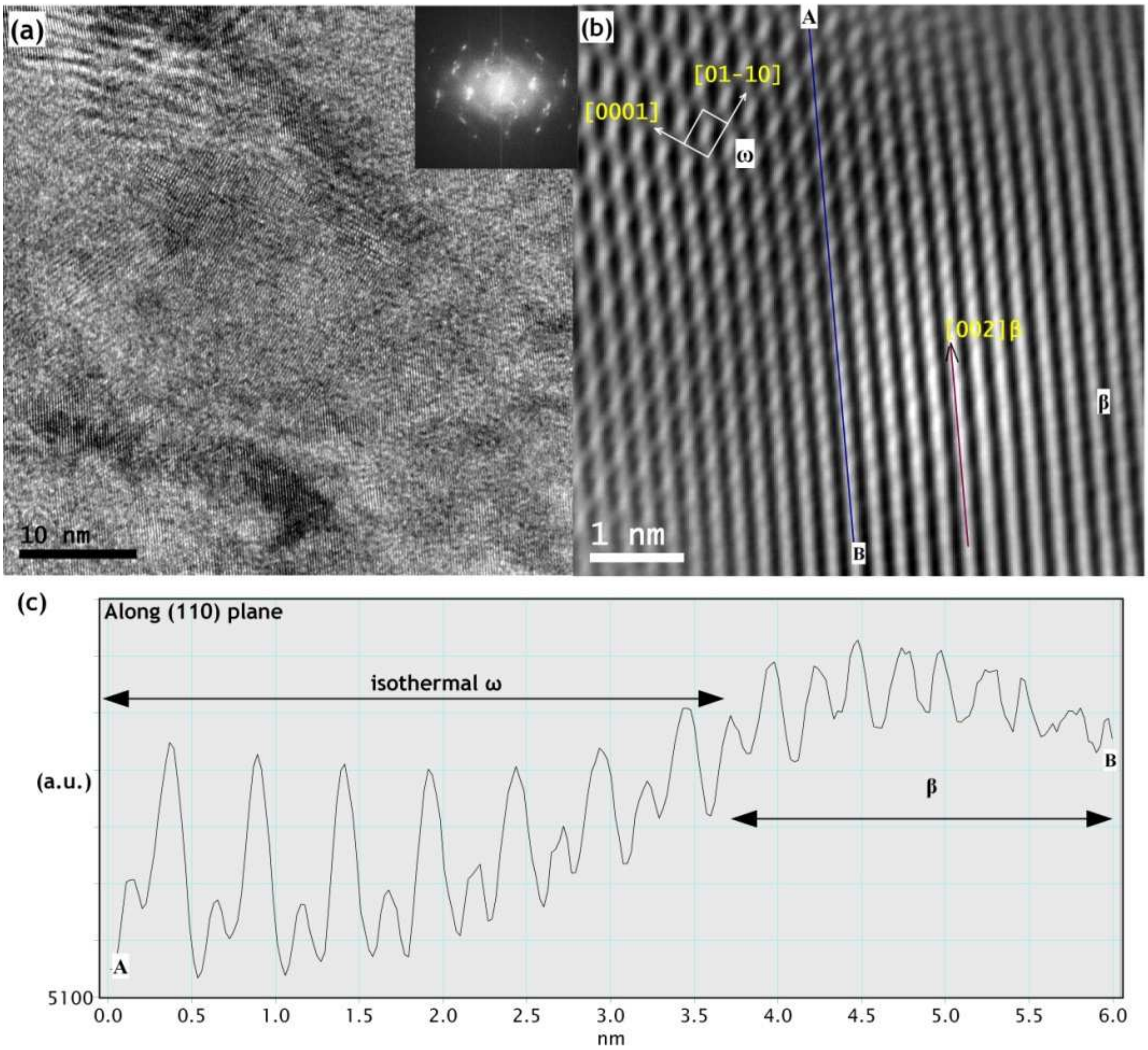

Figure 7.15 HRTEM micrographs (a) The high resolution phase contrast image taken along <110> zone axis of β; (b) The Fourier filtered image shows the boundary between 'ω' and 'β'region (c) Line profile showing the contrast variation of atomic columns of ω and β in (110)β plane along [002]β direction taken from the line marked as AB from figure 15(b).

The line profile of projected intensity is shown in figure 7.15(c) confirming the completion of collapse in ω phase. The multislice simulated image of ω^{iso} matches well with experimental image only if hexagonal symmetry is assumed. Another relevant observation is that there is no distinct, easily recognizable interface between the two lattices of ω and β, as shown in figure 7.15(b). This observation suggests the coherent nature of ω in β matrix, which would influence the strength or the hardness of the alloy, as would be discussed later.

7.3 Influence of ω phase formation on the mechanical properties of the material

Table 7.4 shows the hardness value of Ti-15Mo alloy in different heat treated conditions. It is observed that the hardness for all quenched alloys is less than aged alloy. The XRD results discussed above show that while the ω peaks in quenched alloys is extremely difficult to detect, necessitating Synchrotron XRD, the isothermal ω could be easily detected with conventional XRD.

Table 7.4 Variation in hardness of Ti-15Mo alloy with different heat treatments

Serial No.	Heat treatment	Hardness(VHN)
1	Ice water quenched	295±8
2	Liquid N2 quenched	338±5
3	Brine quenched	340±11
4	Aged	450±7

This suggests an increase in amount of ω in aged alloy in contrast to quenched alloys. In addition, while there is extensive diffuse scattering in the electron diffraction patterns of ice water quenched alloy, the aged alloy showed the presence of discrete spots of ω. Similar trend has been shown for LN2 quenched alloys as compared to ice water quenched alloy. This suggests that aging or lowering of quenching temperature promotes the β to ω transformation. This is the cause for the observed high hardness in aged alloy compared to quenched alloy and LN2 quenched alloy as against ice water quenched alloy.

It is reported [10-12] that the observed variation in the hardness of ω-forming titanium or zirconium alloys could simply be a manifestation of increase in the amount of nm sized ω particles, due to either increasing the cooling rate or the isothermal exposure. However, additional insight could be obtained in the present studies, regarding the contribution of ω to strength of the alloy, based on information about the bonding nature inside ω, presence of variants of ω and the nature of interface between ω and β, which will be discussed later.

7.4. Discussion of results

The results presented above are useful in arriving at inferences regarding the (a) comparison of characteristics of ω^{ath} and ω^{iso}, (b) bonding nature within ω^{iso} and (c) origin of observed increase in hardness.

7.4.1 Characteristics of ω^{ath} and ω^{iso}

The results presented so far, provide multiple evidences for arriving at the difference in the evolution of ω^{ath} and ω^{iso} , which are presented below:

- The well known orientation relation [10] between co-existing β and ω phases, during the formation of ideal ω, suggest the following relation between unit cell dimensions:

$$a_\omega = \left(\sqrt{2}\right) a_\beta \quad \text{and} \quad c_\omega = \left(\frac{\sqrt{3}}{2}\right) a_\beta$$

Table 7.5 lists the unit cell dimensions of β and ω, for quenched and aged samples, thus revealing the deviation from ideality for athermal and isothermal ω phases. This suggests that the extent of deviation from ideality is more for athermal ω phase than for isothermal ω phase.

- Diffuse streaking was observed in the SAD patterns of ω^{ath} in contrast to discrete spots in diffraction pattern of ω^{iso}. The presence (figure 7.14a) of discrete reflections at simple fractions (1/3 and 2/3) of $<222>_\beta$ in the reciprocal lattice sections of ω^{iso} suggesting trebling of unit cell of ω along that <222>of β confirms the existence of a commensurate superstructure. This is to be contrasted with the observation (figure 7.4b) of diffuse streaking in the SAD pattern of ω^{ath}, suggesting loss of translational symmetry along $<222>_\beta$ and hence, an incommensurate structure, with a loss of translational periodicity.
- The atomic column contrast images (figures 7.8 and 7.15) on both the ω's show that the degree of displacement is incomplete in ω^{ath}, while it is complete in the case of ω^{iso}.

Table 7.5 Deviation from ideality for athermal and isothermal ω

S. N.	Heat treatment	Experimental lattice parameter (Å)			Calculated lattice parameter(Å)		Deviation of experimental from calculated (Å)	
		a_ω	c_ω	a_β	a_ω ($\sqrt{2}a_\beta$)	c_ω ($\sqrt{3}/2\ a_\beta$	A	c
1.	WQ	4.58	2.78	3.25	4.596	2.815	0.016 (0.35%)	0.035 (1.24%)
2.	LN2	4.56	2.84	3.24	4.58	2.806	0.02 (0.44%)	0.034 (1.21%)
3.	aged	4.59	2.83	3.25	4.59	2.815	0.0	0.015 (0.53%)

- Another feature characteristic of ω^{ath} and ω^{iso} concerns the symmetry of ω. In the case of ω^{ath}, excellent agreement between experimental and JEMS simulated image could be obtained only if trigonal symmetry is considered [31]. Similar inference could not be drawn using Rietveld analysis of Synchrotron XRD for ω^{ath}, for reasons stated earlier. In the case of ω^{iso}, best Rietveld refinement of laboratory XRD pattern and agreement between experimental and simulation images in HRTEM could be obtained only if hexagonal symmetry is assumed. These results suggest change from trigonal symmetry of ω, in the 'as-quenched' state to hexagonal with progress in aging, in tune with available literature

Based on these evidences also, it is reasonable to conclude that ω^{ath} is non-ideal characterized by incomplete collapse of the lattice planes, while the collapse mechanism is nearly completed in ω^{iso}, which has approached close to the ideal configuration.

The extensive literature on β→ω transformation in Ti-Mo system has shown that the extent of collapse or the degree of displacement of <222> lattice planes of β to form ω embryos and its further growth, depends on the solute content. In Ti-Mo system, with Mo, a strong β stabilizer, it restricts the degree of displacement, resulting in three fold, trigonal symmetry of ω. On aging, out-diffusion of Mo from ω into surrounding β matrix is expected [26] to occur, leading to completion of collapse. When the collapse is more or less complete, reaching a value of ½ d_{222}, six fold hexagonal ω forms. It is also reported that the embryos of ω formed during quenching act as nucleation site for their conversion to equilibrium, hcp α, on prolonged aging [32].

The last feature which differentiates ω^{ath} and ω^{iso} concerns the morphology of the particles. The present study has shown that in Ti-Mo system, the uniform distribution of nm sized ω particles were either elliptical (figure 7.14b) in the isothermal case, with the major axis parallel to $<111>_{\beta}$ while a similar morphology was not observed (figure 7.5b.) in the case of athermal ω. This observation is consistent with the reported literature [33]. The arrangement of ω particles in β matrix is known to be a combined effect of interaction between elastic strain due to atomic displacement and slight volume change associated with the 4 variants of ω. The solute rich, β isomorphous alloys with low misfit strain favors elliptical particles with their major axis along $<111>_{\beta}$, while the solute lean, β eutectoid systems with high misfit strain promotes particles, along $<110>_{\beta}$, with a cuboidal shape driven by a reduction in matrix elastic energy. The misfit strain calculated in the present study is 0.36%, which is less than the critical misfit value for ellipsoidal morphology, which is in tune with the expectation. The arrangement of ω particles in β matrix is also known to be a combined effect of interaction between elastic strain due to atomic displacement and slight volume change associated with the four variants of ω.

7.4.2 Correlation between interatomic distances, bond lengths and bonding nature in ω^{iso}

The values of interatomic distances, d_{A-A}, d_{B-B} and d_{A-B} in ω^{iso}, were provided in section 7.2.2a. An examination of these values suggest that the d_{B-B} the distance between atoms at (1/3,2/3,1/2) and (2/3,1/3,1/2) in ω is the lowest. More importantly, this value is close to the shortest distance, D(1)or Pauling's single bond length in α-Ti, which happens to be 2.648 Å. In the present study, d_{B-B} is found to be 6% shorter than shortest bond length (BL1) in bcc- β of Ti-15Mo alloy. In addition, Table 7.3 shows that d_{B-B} is shorter than the shortest distance in the A-B plane, $d_{A-B.}$ Similar correlations about interatomic distances have been reported in many ω forming systems. These correlations have been related to the nature of bonding in the B-plane of ω and the electronic structure of ω. These correlations suggest that the bonding between B atoms is stronger than A atoms in plane above and below, making the plane containing B atoms act like a graphite-like layer.

The manifestation of the proposed electronic structure of ω in many physical properties like electrical resistivity, internal friction and magnetic susceptibility has been studied supporting the 'graphite-like' bonding in ω. There are few computational efforts to study the electron localization function, mostly in Ti, Zr, Ti-V and Zr-Nb alloys, the classic systems in which the above proposal is examined for many decades. The current study is the first of its nature to provide an experimental confirmation of the directional nature of electron density distribution in the B-B plane and metallic or spherical nature of charge density distribution in the A-A and A-B plane, in ω of Ti-Mo alloys. The charge density distributions (figure 7.11) provide the direct confirmation of the differences in the bonding in the three different planes discussed above. Similar correlations have also been arrived at in many systems like Ti, Zr, Ti-V and Zr-Nb alloys. Computational studies have also yielded electron localization functions of β and ω phases, though this feature has not been clearly brought out. However, the direct experimental evidence about the differences in the bonding has been provided in the present study for the first time in literature.

Our studies, both based on correlations between interatomic distances with bond lengths and charge density distribution in different plans of ω phase, support the view that the atoms in the plane (002), the middle plane of ω, are more strongly bonded than that of (001). The attraction across the parallel planes is rather weak. There is no evidence for covalent bonding in ω phase of Ti-15Mo alloy, though there is strong evidence for anisotropy of charge density distribution.

Neutron diffraction evidence exists [15] for "bond induced configurational ordering" within ω, in Ti-V alloys. The strong bonding in the middle 'B' layer of ω is found to promote ordering of titanium atoms in this plane. It has also been independently shown [26] that the composition of ω could be around 4% Mo, in Ti-Mo alloys. However, the present results are not sufficient to probe this question of configurational ordering within ω in Ti-15Mo alloy.

7.4.3 Mechanisms of hardening in ω of Ti-15Mo alloy

It is shown in section 3.3 that the hardness of the Ti-15Mo alloy increases with rate of cooling from the β phase field and isothermal exposure to elevated temperature. In Chapter 3, it is also shown that the hardness is maximum for the composition of 15%Mo compared to other alloys which were studied like 1, 7 and 25%Mo, which has been attributed to the presence of ω phase. Extensive literature is available on the strengthening mechanisms and embrittlement in titanium alloys, due to formation of ω phase [33]. The three major reasons, proposed in literature [11, 13] are as follows: Rupture of close neighbors in strongly bonded ω than β, along the slip direction $[111]_\beta$ in allowed slip planes or presence of three of the four variants of ω with irrational directions parallel to $[111]_\beta$ or the coherency strains. Most of the studies in literature attribute the increase in strength and loss of ductility of ω containing Ti alloys to the covalent bonding in ω phase. However, our studies do not support this view. An analysis of electron diffraction patterns confirm the presence of both variants of ω, expected if exact orientation relation were to exist. Hence, an attempt was made to understand the increase in hardness in terms of the coherency strains introduced by ω in the alloy. All the phase contrast images, of both quenched and isothermally aged alloy suggest that the interface between β and ω are coherent [see figures 7.8(c) and 7.15(c)].

The 3-D distribution of lattice strain, in the bcc β matrix of water quenched Ti-15Mo &Ti-25Mo alloy~~s~~ is shown in figure 7.16. It was noticed that the absolute value of strain along anyone of the three axes, is higher for alloy containing 15%Mo (figure 7.16(a)) than 25 % Mo.

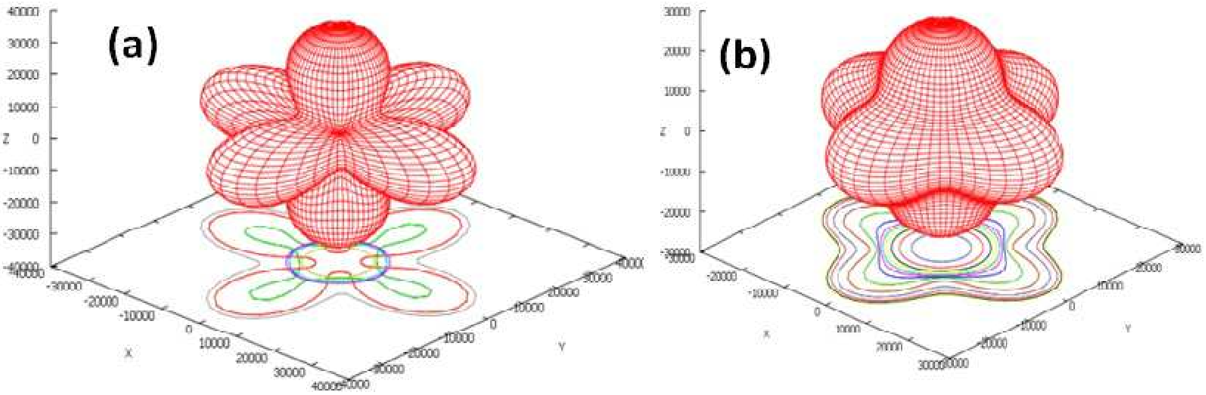

Figure 7.16 3-D strain distribution and their 2D contour in water quenched alloy of (a) Ti-15%Mo and (b) Ti-25%Mo. Note that the maximum value of strain in x,y and z axis is +40,000 for 15%Mo alloy and 30,000 for 25%Mo alloy.The scale of the plot is δd/d X 10^{-6}

Similar observation was also observed for the alloy cooled in LN2. It may be recalled that the phase transformation products during cooling of β phase have been identified as β + ω in Ti-15%Mo alloy and β in Ti-25%Mo alloy. Hence, the observation suggests that the locked up strain in β lattice is higher in the presence of ω, than in ω -free β lattice.

Additionally, the difference in the interplanar distances of the ω regions embedded in the β matrix are too very small suggesting the coherency between the two phases. It has been shown based on the atomic column contrast in figure 7.15(b) that the interface between β and ω phases is coherent in nature. These two observations suggest that the strain in the β lattice originates due to the coherency strains introduced by ω. Therefore, it is reasonable to conclude that the major strengthening contribution in Ti-15Mo alloy due to the presence of ω, arises due to the coherent nature of the interface with β, than the bonding nature.

7.5 Summary

This chapter on "Characteristics of β→ω transformation in Ti- 15Mo alloy" has presented the Rietveld analysis of synchrotron and laboratory XRD pattern and phase contrast microscopy results in Ti-15Mo alloy, on cooling from the β phase field at different cooling rates and also after isothermally aging at 748K, following β quenching. Synchrotron XRD studies could confirm the $\beta \rightarrow \omega^{ath}$ transformation in this alloy for all cooling rates. The unit cell dimensions, and the degree of displacement along $<111>_{\beta}$ to form ω suggest that ω^{iso} has reached the ideal structure, while ω^{ath} is far away from ideality. The correlations between interatomic distances in ω phase, suggest stronger bonding in the plane containing atoms at (1/3,2/3,1/2) and (2/1,1/3,1/2) in ω phase. This is also confirmed by examination of charge density distribution in various planes of ω phase. Three dimensional distribution of strain of Ti-15 Mo alloys confirm that the ω containing alloy is stronger than ω-free lattice of bcc β lattice in Ti-25 Mo alloy. Coherency strain has been identified as the cause of strengthening, which is supported by the observed increase in hardness in isothermally aged alloy where in there is higher amount of ω phase.

References

[1] M. Geetha, A. Singh, R. Asokamani, A. Gogia, *Progress in Materials Science* **2009**, 54, 397.

[2] J.C. Jamieson, *Science* **1963**, 140, 72.

[3] B.S. Hickman, *Journal of Materials Science* **1969**, 4, 554.

[4] Y.K. Vohra, S.K. Sikka, R. Chidambaram, *Journal of Physics F: Metal Physics* **1979**, 9, 1771.

[5] J.E. Doherty, D.F. Gibbons, *Acta Metallurgica* **1971**, 19, 275.

[6] B.A. Hatt, J.A. Roberts, *Acta Metallurgica* **1960**, 8, 575.

[7] D. De Fontaine, N.E. Paton, J.C. Williams, *Acta Metallurgica* **1971**, 19, 1153.

[8]M.H.Davis, J.M. Silcock, H.K. Hardy, Symposium on the Mechanism Phase Transformations in Metals in: Institute of Metals, 1955

[9] Yu.A. Bagaryatskiy, G.I. Nosova, T.V. Tagunova, Doklady Akad. Nauk. SSSR 105 **1955**, 1225.

[10]P. Mukhopadhyay, S.Banergee Phase Transformation: Examples from Titanium and Zirconium Alloys, in, Pergamon Press, Oxford, United Kingdom, 2004.

[11] J.M. Silcock, *Acta Metallurgica* **1958**, 6, 481.

[12] W. Ho, *Journal of Medical and Biological Engineering* **2008**, 28, 47.

[13] J.C. Williams, B.S. Hickman, H.L. Marcus, *MT* **1971**, 2, 1913.

[14] G. Aurelio, A. Fernández Guillermet, *Journal of Alloys and Compounds* **1999**, 292, 31.

[15] G. Aurelio, A. Fernández Guillermet, *Scripta Materialia* **2000**, 43, 665.

[16] G. Aurelio, A.F. Guillermet, *Journal of Alloys and Compounds* **2000**, 298, 30.

[17] G.B. Grad, G.M. Benites, G. Aurelio, A. Fernández Guillermet, *Materials Science and Engineering: A* **1999**, 273–275, 175.

[18] W.F. Ho, C.P. Ju, J.H. Chern Lin, *Biomaterials* **1999**, 20, 2115.

[19] M. Sabeena, S. Murugesan, R. Mythili, A.K. Sinha, M.N. Singh, M. Vijayalakshmi, S.K. Deb, *Transactions of the Indian Institute of Metals* **2015**, 68, 1.

[20] M. Hida, E. Sukedai, C. Henmi, K. Sakaue, H. Terauchi, *Acta Metallurgica* **1982**, 30, 1471.

[21] S.K. Sikka, Y.K. Vohra, R. Chidambaram, *Progress in Materials Science* **1982**, 27, 245.

[22] E. Sukedai, W. Liu, M. Awaji, T. Horiuchi, *Ultramicroscopy* **1994**, 54, 192.

[23] N.T.C. Oliveira, G. Aleixo, R. Caram, A.C. Guastaldi, *Materials Science and Engineering: A* **2007**, 452–453, 727.

[24] L. Lutterotti, P. Scardi, P. Maistrelli, *Journal of Applied Crystallography* **1992**, 25, 459.

[25] D. Schryvers, L. Tanner, High Resolution Electron Microscopy Observations of Athermal Omega Phase in Ti-Mo Alloys, in: Materials Science Forum, Trans Tech Publ, 1991, pp. 329.

[26] A. Devaraj, S. Nag, R. Srinivasan, R. Williams, S. Banerjee, R. Banerjee, H. Fraser, *Acta Materialia* **2012**, 60, 596.

[27] E. Sukedai, Y. Kitano, A. Ohnishi, *Micron* **1997**, 28, 269.

[28] E. Sukedai, H. Yagi, D. Yoshimitsu, H. Matsumoto, T. Ando, W.F. Xu, H. Hashimoto, *Ultramicroscopy* **2004**, 98, 209.

[29] P.D.F. ICDD, *Powder Diffraction File"(Newtown Square, PA 19073, USA)* **1997**.

[30] M. Sabeena, A. George, S. Murugesan, R. Divakar, E. Mohandas, M. Vijayalakshmi, *Journal of Alloys and Compounds* **2016**, 658, 301.

[31] S.M. Alphy George, Divakar R., E. Mohandas, M. Vijayalakshmi, **To be published**.

[32] S. Nag, R. Banerjee, R. Srinivasan, J.Y. Hwang, M. Harper, H.L. Fraser, *Acta Materialia* **2009**, 57, 2136.

[33] S. Banerjee, P. Mukhopadhyay, Phase transformations: examples from titanium and zirconium alloys, Elsevier, 2010.

CHAPTER 8

SUMMARY

CHAPTER 8

SUMMARY

8.1 Summary

Solid state phase transformations, in general, have invoked tremendous interest for many decades in the past. Phase transformations in titanium alloys, in particular, have attracted attention of many industries and researchers since 1970. Despite the intense research of the past, research in phase transformations in titanium alloys continue to remain active even today, mainly due to the advent of many investigative techniques, both experimental and theoretical, to solve unresolved issues. In this backdrop, a careful selection of problems in Ti-Mo alloys in the current thesis, could lead to following new additions to the existing literature:

(1) Application of synchrotron XRD for the accurate identification of amount of titanium stabilizing bcc β phase.

(2) Complete analysis of XRD results of all metastable phases in Ti-Mo alloys, to not only give information about crystal structure, but also about co-ordination number, bond length, charge density distribution and three dimensional strain distribution.

(3) Established that the orthorhombic α'' phase is intermediate between α' and β for the first time in Ti-Mo, though has been carried out in Ti-Nb system for various compositions inside α'' phase field.

(4) Demonstrated that the elastic anisotropy reported in literature based on first principle calculations correlates well with anisotropy in charge density distribution.

(5) Provided evidence for the first time for graphite-like bonding in ω of Ti-15 Mo alloys, based on interatomic distances in different planes of ω phase.

(6) Precession electron microscopy has been used for the first time in Ti-Mo alloys to examine if variant selection mechanism is operative or not.

Above all, the studies have provided an excellent learning ground for basic aspects of various types of phase transformation mechanisms, in addition to good exposure to both experimental and theoretical research methodologies.

The salient features of the studies on Phase "Transformations in Ti-Mo alloys" can be summarized as follows: The stability of various metastable phases with increase in molybdenum as alloying element has been established, using conventional and synchrotron XRD. In addition, Miedema model was learnt to predict the relative stability of amorphous over solid solution phases. While most of the XRD studies in Ti-Mo are confined to structure determination, current studies could obtain additional information about atomic co-ordinates, co-ordination number, bond length, strain and charge density distribution in the metastable phases using detailed Rietveld refinement methods. The experimentally determined charge density distributions agreed well with first principle DFT based VASP calculations. The presence of competing phase transformation mechanisms always provides ample scope for tuning the thermal treatment to preferentially favor one mechanism over the other, which has been studied in Ti-1Mo and Ti-7Mo alloys for different cooling rates. The experimental observations are in agreement with JMatPro calculations. The β→ω transformations in Ti-15Mo alloy has been studied in detail, with respect to the mechanism of formation, signatures of difference between athermal and isothermal ω and graphite-like bonding nature, The absence of ω in Ti-25Mo alloy had manifested in lower hardness and less 3-D strain distribution, as calculated from XRD studies. A new emerging technique called the precession electron diffraction in TEM has been used to examine if the β→α'/α" in Ti-1Mo and Ti-7Mo *via* martensitic transformation displayed variant selection mechanism, which was found to be absent.

8.2 Scope for future work

While doing the project on phase transformations in Ti-Mo alloys, several interesting situations were encountered, for which additional, more sophisticated experiments were required which could be scope for future work:

The atomic number of Ti and Mo being very different, the system provides enough scope for detailed work on the atomic nature of ω phase in the alloy. There are many speculations in the literature that out diffusion of Mo is expected from ω phase, thus acting as strong nucleating sites for the hcp α. With advanced microscopy techniques, it may be possible to confirm this in future.

Ti-Mo is one of the possible basis for development of β phase alloys and hence extensive work has been carried out in predicting the modulus of the alloys. It would be possible to make meaningful correlations between microstructure and modulus to understand the role of Mo in influencing elastic properties through phase transformations.

Search for ternary and quaternary alloying additions to the basis of Ti-Mo to optimize the modulus to be as close to human bone as possible will be an excellent contribution to human society.